

**MULTI-SCALE MODELING OF WET GRANULATION
PROCESSES**

by

DANA BARRASSO

A dissertation submitted to the
Graduate School—New Brunswick
Rutgers, The State University of New Jersey
in partial fulfillment of the requirements

for the degree of

Doctor of Philosophy

Graduate Program in Chemical & Biochemical Engineering

written under the direction of

Rohit Ramachandran

and approved by

New Brunswick, New Jersey

October 2015

© 2015

Dana Barrasso

ALL RIGHTS RESERVED

ABSTRACT OF THE DISSERTATION

Multi-scale modeling of wet granulation processes

By DANA BARRASSO

Dissertation Director:

Rohit Ramachandran

Wet granulation is a particle design process used to create larger granules from fine powder, improving flowability, compactibility, and homogeneity. Although it is widely used in the food, pharmaceutical, detergent, and fertilizer industries, it is often operated inefficiently, with high recycle ratios in continuous processes and high rejection rates in batch processes. In pharmaceutical applications, wet granulation is a critical step in tablet manufacturing that affects the uniformity and compactibility of the final dosage form. A model-based approach can be used to understand the effects of process parameters and material properties on critical quality attributes, developing a knowledge space for Quality by Design. Population balance modeling (PBM) provides a fundamental framework for tracking changes in particle properties over time, though it requires rate expressions and empirical parameters that cannot easily be measured. Discrete element modeling (DEM) is more mechanistic, tracking particles as they move through space and collide, but does not consider the complex mechanisms involved in wet granulation. Through this thesis, a multi-dimensional PBM for a continuous wet granulation process is presented. Model calibration and validation are performed using experimental data. A multi-scale PBM-DEM framework is developed and demonstrated using mechanistic rate expressions to enhance predictive capabilities. The multi-scale model is applied to realistic systems using computationally efficient techniques.

Acknowledgements

I would first like to thank my advisor, Dr. Rohit Ramachandran, for his guidance and support. I would also like to thank my committee members for their thoughtful feedback: Dr. Meenakshi Dutt, Dr. Marianthi Ierapetritou, and Dr. Jim Litster.

Co-authors contributing to the publications featured in this dissertation include Dr. Ravindra Aglave (CD-adapco), Dr. Sean Bermingham (PSE), Dr. Kristian Debus (CD-adapco), Dr. Arwa El Hagrasy (Purdue), Dr. Thomas Eppinger (CD-adapco), Dr. Jim Litster (Purdue), Dr. Frances Pereira (PSE), Dr. Rohit Ramachandran (Rutgers), Ashutosh Tamrakar (Rutgers), and Samjit Walia (Cooper Union).

The following group members and colleagues at Rutgers have influenced this work: Dr. Anwesha Chaudhury, Dr. Savitha Panikar, Dr. Amanda Rogers, Dr. Maitraye Sen, Dr. Ravendra Singh, Anik Chaturbedi, Sarang Oka, Ashutosh Tamrakar, Anuj Varghese, Samjit Walia, and Reginald Wilbourn.

Collaborators who contributed to discussions on this work include Dr. Atul Dubey (Tridiagonal Solutions), Dr. Shantenu Ja (Rutgers), Dr. Jianfeng Li (PSE), Dr. David Slade (PSE), Dr. Huiquan Wu (FDA), and Ridade Sayin (Purdue).

This work was financially supported by the NSF Engineering Research Center for Structured Organic Particulate Systems and by Process Systems Enterprise. In addition to their financial support, both ERC-SOPS and PSE have given me countless opportunities to present my work, challenge my thought processes, and launch my career, for which I am truly grateful. In particular, I sincerely thank Dr. Sean Bermingham and Dr. Jim Litster for their active interest and involvement in my research and career.

Lastly, I would like to thank my family and friends, who never fail to support, encourage, and inspire me. This thesis is dedicated to Travis Heithoff, who took every step of this journey with me, and to my mother, who is a constant source of inspiration.

Table of Contents

| | |
|---|---------------|
| Abstract | ii |
| Acknowledgements | iii |
| List of Tables | x |
| List of Figures | xi |
| 1. Introduction | 1 |
| 1.1. Wet granulation processes | 1 |
| 1.2. A model-based approach to Quality-by-Design | 3 |
| 1.3. Powder process modeling techniques | 5 |
| 1.3.1. Population balance modeling | 7 |
| 1.3.2. Discrete element modeling | 10 |
| 1.4. Specific Aims | 12 |
| Specific Aim I: Multi-dimensional population balance modeling of wet granulation processes | 13 |
| 2. A comparison of model order reduction techniques for a four-dimensional population balance model describing multi-component wet granulation processes | 14 |
| 2.1. Background | 14 |
| 2.1.1. Multi-dimensional population balance modeling | 14 |
| 2.1.2. Multi-component granulation | 15 |
| 2.1.3. Reduced order models | 16 |

| | |
|--|-----------|
| 2.1.4. Objectives | 17 |
| 2.2. Model development | 17 |
| 2.2.1. Rate kernels and process parameters | 17 |
| 2.2.2. Numerical and computational techniques | 22 |
| 2.2.3. Model reduction methodology | 23 |
| 2.3. Results and discussion | 25 |
| 2.3.1. Validation of numerical methods | 25 |
| 2.3.2. Comparison of reduced order models | 27 |
| 2.3.3. Computation time reduction | 32 |
| 2.4. Summary | 33 |
| | |
| 3. Multi-component population balance modeling of continuous granulation processes: A parametric study and comparison with experimental trends. | 34 |
| 3.1. Background | 34 |
| 3.1.1. Population balance modeling of continuous particulate processes . . | 35 |
| 3.1.2. Objectives | 37 |
| 3.2. Model development | 38 |
| 3.2.1. Spatial coordinates and particle flow | 39 |
| 3.2.2. Rate processes | 41 |
| 3.2.3. Discretization and numerical techniques | 45 |
| 3.3. Results and discussion | 46 |
| 3.3.1. Validation of numerical methods | 46 |
| 3.3.2. Parametric study | 49 |
| 3.3.3. Comparison with experimental trends | 58 |
| 3.4. Summary | 60 |
| | |
| Specific Aim II: Parameter estimation and population balance model validation using experimental data from a twin-screw granulator | 62 |

| | |
|--|-----------|
| 4. Multi-dimensional population balance model development and validation for a twin-screw granulation process | 63 |
| 4.1. Background | 63 |
| 4.1.1. Objectives | 64 |
| 4.2. Experimental methods | 65 |
| 4.3. Model development | 65 |
| 4.3.1. Spatial compartments and flow | 68 |
| 4.3.2. Liquid addition | 69 |
| 4.3.3. Consolidation | 69 |
| 4.3.4. Aggregation | 70 |
| 4.3.5. Breakage | 72 |
| 4.3.6. Multiple solid components | 72 |
| 4.3.7. Numerical method | 73 |
| 4.3.8. Parameter estimation and validation | 74 |
| 4.4. Results and discussion | 76 |
| 4.4.1. Experimental results | 76 |
| 4.4.2. Parameter estimation and predictive modeling | 76 |
| 4.4.3. Sensitivity analysis of adjustable parameters | 81 |
| 4.4.4. Simulated dynamic behavior | 82 |
| 4.4.5. Multi-component interactions | 83 |
| 4.5. Summary | 84 |

Specific Aim III: Development of a multi-scale model using bi-directional coupling of discrete element modeling and population balance modeling **85**

| | |
|--|-----------|
| 5. Multi-scale modeling of granulation processes: Bi-directional coupling of PBM with DEM via collision frequencies | 86 |
| 5.1. Background | 86 |

| | | |
|-----------|--|------------|
| 5.1.1. | Comparison of PBM and DEM | 87 |
| 5.1.2. | Objectives | 89 |
| 5.2. | Model development | 89 |
| 5.2.1. | Population balance model | 89 |
| 5.2.2. | Discrete element model | 91 |
| 5.2.3. | Bi-directional coupling | 94 |
| 5.3. | Results and discussion | 96 |
| 5.3.1. | Effect of particle size distribution on collision rates | 96 |
| 5.3.2. | Hybrid model results | 99 |
| 5.4. | Summary | 106 |
| | | |
| 6. | A multi-scale, mechanistic model of a wet granulation process using a novel bi-directional PBM-DEM coupling algorithm | 109 |
| 6.1. | Background | 109 |
| 6.1.1. | Objectives | 111 |
| 6.2. | Model development | 112 |
| 6.2.1. | Population balance model development | 112 |
| 6.2.2. | Discrete element method simulations | 122 |
| 6.2.3. | Bi-directional coupling of PBM and DEM | 125 |
| 6.3. | Results and discussion | 127 |
| 6.3.1. | Characterizing the DEM simulations | 127 |
| 6.3.2. | PBM-DEM simulations: Base case | 131 |
| 6.3.3. | PBM-DEM simulations: Sensitivity analysis | 135 |
| 6.4. | Summary | 139 |
| | | |
| | Specific Aim IV: Applications of multi-scale models to simulate realistic wet granulation processes | 140 |

| | |
|---|-----|
| 7. A reduced order PBM-ANN model of a multi-scale PBM-DEM description of a wet granulation process | 141 |
| 7.1. Background | 142 |
| 7.1.1. Reduced order models and artificial neural networks | 142 |
| 7.1.2. Objectives and approach | 145 |
| 7.2. Model development | 146 |
| 7.2.1. Population balance model development | 146 |
| 7.2.2. Discrete element method | 149 |
| 7.2.3. Artificial neural network architecture and training techniques | 153 |
| 7.2.4. Bi-directionally coupled PBM-DEM model | 156 |
| 7.3. Results and discussion | 157 |
| 7.3.1. Particle size distributions and collision rate functions from DEM | 157 |
| 7.3.2. ANN training and predictability | 158 |
| 7.3.3. PBM-ANN simulation results | 159 |
| 7.3.4. Comparison of PBM-DEM and PBM-ANN results | 162 |
| 7.4. Summary | 163 |
| | |
| 8. Qualitative assessment of a multi-scale, compartmental PBM-DEM model of a continuous twin-screw wet granulation process | 165 |
| 8.1. Background | 165 |
| 8.1.1. Objectives | 167 |
| 8.2. Population balance model development | 168 |
| 8.2.1. Particle properties | 171 |
| 8.2.2. Compartments and flow | 173 |
| 8.2.3. Liquid addition | 174 |
| 8.2.4. Nucleation | 176 |
| 8.2.5. Aggregation | 177 |
| 8.2.6. Breakage | 178 |
| 8.2.7. Consolidation and layering | 179 |

| | |
|---|------------|
| 8.2.8. Numerical techniques | 181 |
| 8.3. Discrete element method simulations and coupling to PBM | 182 |
| 8.3.1. Screw element geometries and configurations | 183 |
| 8.3.2. Multi-compartment simulations and residence times | 183 |
| 8.3.3. Single-compartment simulations and bi-directional coupling | 187 |
| 8.4. Results and discussion | 188 |
| 8.4.1. Residence time results | 189 |
| 8.4.2. PBM-DEM simulations: Mechanisms by compartment | 191 |
| 8.4.3. PBM-DEM simulations: Effect of number of kneading elements | 196 |
| 8.4.4. PBM-DEM simulations: Reverse configuration | 198 |
| 8.4.5. PBM-DEM simulations: Liquid distribution | 199 |
| 8.5. Summary | 202 |
| 9. Conclusions and future perspectives | 204 |
| Appendix A: Cell average technique and model order reduction | 208 |
| Appendix B: Hertz-Mindlin contact model | 214 |
| Acknowledgment of previous publications | 216 |
| Bibliography | 217 |

List of Tables

| | |
|---|-----|
| 2.1. Process parameters and initial conditions | 18 |
| 2.2. Four-dimensional and reduced order models | 24 |
| 2.3. Summary of results and computation time for each model | 29 |
| 3.1. Granule properties and dependent rate processes | 39 |
| 3.2. Process parameters and initial conditions used in simulations for the baseline case | 40 |
| 4.1. Summary of parameter estimation results | 77 |
| 5.1. Parameters and initial conditions for simulation | 92 |
| 5.2. Summary of results for different coupling intervals | 101 |
| 6.1. Values of input parameters representing the base case | 116 |
| 6.2. Data exchanged between gPROMS and STAR-CCM+ | 126 |
| 6.3. Summary of results of coupled PBM-DEM simulations | 132 |
| 7.1. Parameter values used in PBM simulations | 147 |
| 7.2. Parameter values and equipment geometry used in DEM simulations | 150 |
| 7.3. Four ANN alternatives for describing collision frequencies | 155 |
| 7.4. Coefficients of determination for each ANN, by data set | 158 |
| 8.1. Parameter values used in simulations | 172 |
| 8.2. Screw element configurations simulated in PBM-DEM framework | 186 |

List of Figures

| | | |
|-------|--|----|
| 2.1. | Total volume of each component over time | 26 |
| 2.2. | Ratios of formation to depletion | 27 |
| 2.3. | Effect of grid size | 27 |
| 2.4. | Average diameter and moles of particles over time | 28 |
| 2.5. | Particle size distribution | 29 |
| 2.6. | Particle size and composition distributions | 30 |
| 2.7. | Particle size and liquid content distributions | 31 |
| 2.8. | Particle size and porosity distributions | 31 |
| 2.9. | Effect of dimensionality and grid size on computation time | 32 |
| 3.1. | Continuous granulator with three zones | 41 |
| 3.2. | Time trajectories demonstrating conservation of material and particles . . . | 47 |
| 3.3. | Validation of numerical techniques | 48 |
| 3.4. | Effect of heterogeneous liquid distribution | 50 |
| 3.5. | Evolution of particle properties within the granulator | 51 |
| 3.6. | Effect of liquid-to-solid ratio | 52 |
| 3.7. | Effect of spray zone length | 54 |
| 3.8. | Effect of axial length of the twin screw granulator | 55 |
| 3.9. | Effect of particle velocity distribution | 57 |
| 3.10. | API-excipient interactions and compositional distributions | 59 |
| 3.11. | Experimentally observed effects of liquid-to-solid ratio | 60 |
| 4.1. | Three regions of the twin-screw granulator based on the experimental setup | 66 |
| 4.2. | Experimental size distributions of initial blend and product at various liquid-to-solid ratios (El Hagrasy et al., 2013) | 77 |

| | |
|---|-----|
| 4.3. Experimental and simulated quartile parameters using Madec kernel | 78 |
| 4.4. Experimental and simulated quartile parameters using Wauters kernel | 79 |
| 4.5. Measured and fitted steady-state product size distributions | 79 |
| 4.6. Measured and predicted steady-state product size distributions | 80 |
| 4.7. Measured and predicted or fitted porosity of granules in the 1-1.4 mm size class | 80 |
| 4.8. Sensitivity of product attributes to adjustable parameters | 81 |
| 4.9. Sensitivity of product attributes to adjustable liquid-dependency exponents | 82 |
| 4.10. Simulated dynamic behavior of median diameter | 83 |
| 4.11. Average composition of 0.5-1.5 mm size class versus interaction parameter . | 84 |
| 5.1. Schematic of multi-scale model and data transfer | 94 |
| 5.2. Size distributions used to determine collision rates | 97 |
| 5.3. Collision frequency versus particle size for each distribution based on DEM simulations | 99 |
| 5.4. Conservation of solid and liquid volume | 100 |
| 5.5. DEM images of particles, colored by liquid fraction | 101 |
| 5.6. Evolution of volume-weighted average diameter | 102 |
| 5.7. Size dependence of liquid content over time | 103 |
| 5.8. Reproducibility of coupled model results with respect to data transfer frequency | 103 |
| 5.9. Evolution of the particle size distribution | 104 |
| 5.10. Distributions of particle size and liquid content | 105 |
| 6.1. Schematic of bi-directional coupling approach | 113 |
| 6.2. 3-D CAD models of axial section of a twin-screw granulator | 122 |
| 6.3. Time trajectories from DEM simulation demonstrating stabilization of results | 128 |
| 6.4. DEM results showing the effects of size distribution | 129 |
| 6.5. DEM results showing the effects of particle wetness and porosity | 130 |
| 6.6. DEM results showing the effects of screw element type and rotational speed | 131 |
| 6.7. Snapshots of the DEM simulations during execution of coupled model | 133 |

| | |
|--|-----|
| 6.8. PBM-DEM results for the base case and a replicate simulation | 134 |
| 6.9. PBM-DEM results showing effects of equipment geometry and screw speed | 136 |
| 6.10. PBM-DEM results showing effects of process parameters and material prop- erties | 138 |
| 7.1. Schematic of bi-directional coupled PBM-DEM and PBM-ANN models . . | 146 |
| 7.2. Equipment geometry, DEM snapshot, and size distributions used in DEM . | 150 |
| 7.3. Collision frequencies obtained from DEM simulations | 152 |
| 7.4. DEM results and ANN predictions | 153 |
| 7.5. Regression plots for artificial neural network | 159 |
| 7.6. Collision frequencies predicted by ANN | 160 |
| 7.7. PBM and PBM-ANN results demonstrating effects of impeller speeds . . . | 160 |
| 7.8. Comparison of PBM-ANN and PBM-DEM model results | 162 |
| 8.1. Flowchart of coupled PBM-DEM modeling approach | 169 |
| 8.2. Schematic of four-compartment model of the TSG | 173 |
| 8.3. Geometries of individual sections of conveying and kneading elements . . . | 184 |
| 8.4. Screw element configurations for residence time DEM simulations | 185 |
| 8.5. Snapshots of DEM simulations after a steady state is reached | 189 |
| 8.6. Average residence time in each compartment based on steady-state DEM simulations of the full screw | 191 |
| 8.7. Snapshots of the fourth compartment after the final DEM iteration | 192 |
| 8.8. Evolution of granule properties in each compartment simulated by PBM- DEM model | 194 |
| 8.9. Effect of number of kneading elements on granule attributes | 197 |
| 8.10. Effect of kneading element orientation on granule attributes | 199 |
| 8.11. Liquid distribution simulated by PBM-DEM framework | 200 |

Chapter 1

Introduction

1.1 Wet granulation processes

Granulation is a particle design process in which fine powder particles agglomerate to form larger granules with improved properties, such as flowability, reduced dust formation, and composition uniformity. In wet granulation processes, aggregation is facilitated with the addition of a liquid binder. Wet granulation is governed by three rate processes; wetting and nucleation, consolidation and aggregation, and attrition and breakage (Iveson et al., 2001; Cameron et al., 2005).

Granulation processes are utilized in various process industries, such as food, pharmaceuticals, and fertilizers (Iveson et al., 2001). Because a narrow size distribution is often desired, industrial granulation processes are typically inefficient, with large recycle ratios of up to 6:1 (Wang and Cameron, 2002). As a result, design, scale up, and control of granulation processes is usually based on heuristic experimentation. Particularly in the pharmaceutical industry, granule composition, in addition to other granule properties such as liquid content and porosity, must be controlled to ensure product uniformity that meets strict regulatory guidelines (Vervaet and Remon, 2005).

Wet granulation is a particle design process used to create larger granules from fine powder, improving flowability, compactibility, and homogeneity while reducing dust formation. Although it is widely used in the food, pharmaceutical, detergent, and fertilizer industries, it is often operated inefficiently, with high recycle ratios in continuous processes and high rejection rates in batch processes (Wang and Cameron, 2002). The design and control of granulation processes is primarily performed via heuristic experimentation, and a more mechanistic approach is required to improve operational efficiency (Cameron et al.,

2005).

The wet granulation process is highly complex, governed by the rate processes of wetting and nucleation, aggregation and consolidation, and breakage and attrition (Iveson et al., 2001). In wetting and nucleation, the fine powder comes into contact with the liquid binder and forms granule nuclei. When wet particles collide, they can form liquid bridges, resulting in aggregation. Collisions with vessel walls and/or impellers also result in consolidation, leading to a reduction in the porosity of a granule. Breakage and attrition occur when large particles are subjected to shear, compressive, and tensile forces and break to form fragments.

Based on these sub-processes, a single granule can be described by three internal properties. The size, related to the solid volume, is a critical product attribute. The liquid content, related to the amount of liquid within and on the surface of a particle, affects the aggregation rate. The porosity, related to the air volume, affects the surface liquid and as it decreases, liquid is forced out of the pores and onto the particles, further affecting aggregation rates (Cameron et al., 2005). The product porosity also affects the compactibility of the granules, which is critical to tablet manufacturing (Vervaet and Remon, 2005). In multi-component granulation processes, the composition of each granule is also important, and segregation can occur, affecting the final product (Vervaet and Remon, 2005).

Pharmaceutical manufacturing processes are almost exclusively operated in batch configurations. However, continuous processing has gained recent attention due to its numerous potential advantages over batch processes (Leuenberger, 2001, 2003; Plumb, 2005; Vervaet and Remon, 2005; Schaber et al., 2011). For instance, Schaber et al. (2011) predicted substantial economic benefits of continuous manufacturing. However, Vervaet and Remon (2005) caution against the common misconceptions surrounding continuous processing in the pharmaceutical industry, such as the idea that continuous processes on their own cannot always consistently meet the quality requirements of the highly regulated industry. Instead, they argue that real-time monitoring using in-line process analytical techniques (PAT) would result in better process control, higher efficiencies, and less destruction of product due to failed specifications.

Furthermore, continuous granulation has been proposed as an alternative to batch granulation in the pharmaceutical industry (Vervaet and Remon, 2005). Transitioning towards continuous granulation would require substantial efforts in process design. Schaber et al. (2011) argued that continuous processing has economic benefits over to batch processing. As demonstrated by Boukouvala et al. (2012a), Boukouvala et al. (2011), and Boukouvala et al. (2012b), data-driven models can facilitate continuous process design. Glaser et al. (2009), Ramachandran and Chaudhury (2012), and Ramachandran et al. (2011) have proposed model-based control methods that utilize population balance models for continuous granulation. Ramachandran and Chaudhury (2012) demonstrated the current method's inability to control granule size and the potential for model-based methods to solve this problem. Significant research focuses on developing useful models of granulation to accomplish these goals.

Continuous wet granulation processes can be categorized into four types: fluidized bed, high shear, drum, and twin screw granulation (TSG). TSG is well-suited to pharmaceutical processes for its optimal throughput, short residence times, design flexibility, and ability to mix ingredients (El Hagrasy et al., 2013; Vervaet and Remon, 2005). Note that TSG is different from twin screw extrusion, where the granules fall from the open end of the screw conveyor in the TSG configuration, rather than being extruded through a die.

1.2 A model-based approach to Quality-by-Design

In the pharmaceutical industry, recent efforts focus on implementing Quality by Design (QbD). QbD involves developing a strong process understanding and defining a design space, a set of operating parameters that will result in a quality product (Yu, 2008). In contrast, a Quality by Testing (QbT) approach involves sampling the products of empirically designed processes and rejecting batches that do not meet specifications, often wasting expensive active ingredients. Current research and development efforts aim to shift from batch to continuous processing in tablet manufacturing in order to improve controllability, scalability, and profitability. In order to successfully transition to continuous processing, a QbD approach is desired, and a more mechanistic understanding of powder processes is

needed.

Over the past decade, QbD has gained importance in the pharmaceutical industry to manage risk, reduce costs, and satisfy regulatory requirements. In 2006, QbD was introduced in the ICH Q8 guidance document and later was defined as “a systematic evaluation, understanding and refining of the formulation and manufacturing process” (U.S. Food and Drug Administration, 2006, 2009). In contrast, the traditional approach of Quality by Testing (QbT) involves empirical design and operation of manufacturing processes and relies on testing and rejection of failed batches to assure quality, which can lead to sub-optimal product quality.

Wet granulation is often used in pharmaceutical manufacturing as an intermediate step in the tablet-manufacturing process. While tablet manufacturing is primarily operated in batch mode, continuous processing is being investigated for its potential advantages in cost, controllability, and scalability (Schaber et al., 2011). Currently, the design and control of pharmaceutical powder processes is primarily based on heuristic experimentation. To implement QbD in these processes, a design space must be defined such that the CQAs of the product meet desired specification, if the process is operated within this space. In order to make the transition to continuous manufacturing, a better process understanding is needed to predict the effects of material and process parameters on CQAs. A model-based approach can be used to validate, optimize, and design these processes.

To implement QbD, predictive process understanding must be established to quantify the effects of process parameters and material properties on the critical quality attributes (CQAs) of the product. From this knowledge base, a design space can be identified, defining the multi-variate combination of process parameters and material properties that result in a product of acceptable quality. Experimental approaches to QbD often rely on large sets of experimental data and statistical models, but provide little insight beyond the experimental design space.

Alternatively, a model-based approach can be taken to describe the behavior of the process from a more scientific perspective. The underlying mechanisms driving the process are described mathematically, and a limited number of experiments are required to calibrate

and validate the model (Kayrak-Talay et al., 2013). The development of truly predictive pharmaceutical process models is challenging because many of these processes involve powders. Powder processes are often operated empirically and inefficiently due to a poorer understanding of their behavior compared to that of liquid and gas processes.

A model-based approach to design and control of continuous powder processes has been proposed to tackle this challenge (Faure et al., 2001; Wang and Cameron, 2002). This approach can be used to define a design space, and if the process variables are kept within the design space, the product will be of acceptable quality, a concept known as Quality by Design (QbD). For instance, Glaser et al. (2009) and Ramachandran and Chaudhury (2012); Ramachandran et al. (2011) have demonstrated model-based control methods for continuous granulation using population balance modeling. Additionally, Boukouvala et al. (2012a, 2011, 2012b) have developed data-driven models for continuous powder processes.

These data-driven techniques have limited ability to predict process behavior beyond an experimental design space. More mechanistic approaches, such as population balance modeling (PBM) and discrete element method (DEM) modeling, lend better insight into the mechanisms driving the process, requiring fewer experiments to calibrate the model and demonstrating predictive capabilities beyond the experimental design space.

1.3 Powder process modeling techniques

Two modeling frameworks are predominantly used to simulate particulate processes: the semi-empirically-driven PBM and the more mechanistic DEM.

PBMs have been extensively used to model particulate processes including granulation, crystallization, mixing, milling and drying applications of pharmaceutical products (Reynolds, 2010; Griffin et al., 2010; Mortier et al., 2013; Barrasso and Ramachandran, 2012; Sen and Ramachandran, 2013). The PBM groups the particles into a set of classes based on one or more properties, such as size, liquid content, and porosity. The number of particles in each of these classes, or bins, is tracked over time by evaluating rate processes, such as aggregation, breakage, nucleation, and growth. These rate expressions are often empirical and require ample experimental data to estimate unknown parameters, resulting

in poor predictability outside the experimental design space and limited understanding of the effects of process parameters and material processes on the critical quality attributes of the process (Barrasso et al., 2015a; Chaudhury et al., 2014a).

In contrast, DEM models track each individual particle as it moves through space, colliding with equipment walls, blades, and other particles. Using Newton's laws of physics and supplemental contact models, such as the Hertz-Mindlin model, net forces are calculated and applied to each particle. Although recent studies have demonstrated that DEM can be used to obtain detailed mechanistic information such as collision frequencies, impact velocities and forces (Yang et al., 2003; Gantt and Gatzke, 2005; Hassanpour et al., 2011), more direct investigations are needed to decisively validate these collision-level predictions from DEM. In the study by Freireich et al. (2009), the justification of collision-scale DEM predictions through verification of particle velocity and solid fraction fields using experimental techniques such as particle image velocimetry or positron emission particle tracking was shown to be an insufficient validation. Nevertheless, at flow-level the measured macroscopic trends were well captured by DEM models despite the difference in collision-level behavior (Freireich et al., 2009; Renzo and Maio, 2004). Under these circumstances, the use of DEM simulations to obtain necessary granular flow information in this study has been restricted to approximate only the net collision frequencies between particle size combinations at a flow-scale level. Besides collision frequencies, DEM simulations can provide additional flow-level information such as shear stresses and spatial inhomogeneities. In addition, DEM simulations are highly computationally intensive and generally unsuitable for practical applications such as parameter estimation, control, and optimization (Ketterhagen et al., 2009).

A critical difference between PBM and DEM is the treatment of the rate processes: while DEM simulations cannot independently simulate particle size and property changes resulting from the subprocesses in wet granulation, PBM models also cannot independently capture the detailed granulation behavior without empirical parameters inherent in its kernels. As a result, recent studies have focused on coupling PBM and DEM to take advantage

of both models individual strengths. In the study by Reinhold and Briesen (2012), for instance, the aggregation kernel is developed by coupling discrete element simulations with a PBM. Wang et al. (2012) similarly utilizes DEM to obtain collision and dissipation energies during the granule breakage processes in a ball milling operation to link with PBM. Other coupled models have investigated coupling PBM and DEM with computational fluid dynamics (CFD) for particle-fluid interactions in fluidized bed granulation processes (Rajniak et al., 2009; Fries et al., 2011; Sen et al., 2014).

1.3.1 Population balance modeling

The PBM is a class of integro-differential equations that describe the change in the number of particles within each class over time as the particles are subjected to rate processes, such as liquid addition, consolidation, aggregation, and breakage. A general form of the population balance equation is given in Equation 1.1 (Ramkrishna, 2000).

$$\frac{\partial F(\mathbf{x}, t)}{\partial t} + \frac{\partial}{\partial \mathbf{x}} \left[F(\mathbf{x}, t) \frac{d\mathbf{x}}{dt}(\mathbf{x}, t) \right] = \mathfrak{R}_{formation}(\mathbf{x}, t) - \mathfrak{R}_{depletion}(\mathbf{x}, t) \quad (1.1)$$

Here, F represents the number of particles or particle density as a function of particle class and time. The set of particle properties can include size, wetness, porosity, and composition, as well as spatial coordinates. This vector is represented by \mathbf{x} . The first term in Equation 1.1 is the temporal component, representing changes over time. The second term accounts for changes in each property, such as an increase in liquid volume due to liquid addition or a decrease in porosity due to consolidation. This term can also account for particle fluxes when the property is a spatial coordinate. The source terms $\mathfrak{R}_{formation}$ and $\mathfrak{R}_{depletion}$ represent the change in particles within each class from aggregation, breakage, or nucleation.

PBMs have been used to model various powder processes, such as crystallization (Gerstlauer et al., 2002), powder mixing (Sen and Ramachandran, 2013), and milling (Bilgili and Scarlett, 2005), and wet granulation (Cameron et al., 2005; Verkoeyen et al., 2002). Most PBMs found in the literature are one-dimensional; they only consider distributions with respect to one particle property, typically size. Because wet granulation is a complex process facilitated by a liquid binder, 1-D PBMs have limited accuracy in representing real processes

(Iveson, 2002). As a consequence, multi-dimensional PBMs have been developed using three internal coordinates: solid, liquid, and gas volume (Poon et al., 2008). Some studies have also used multiple internal coordinates to model two solid components, which may result in inhomogeneous distributions (Matsoukas and Marshall Jr., 2010; Matsoukas et al., 2009; Marshall Jr. et al., 2011, 2013). Although these models can simulate more complex behavior, they are more computationally expensive and require many empirical expressions and parameters (Barrasso and Ramachandran, 2012). These models may be unsuitable for iterative calculations, such as parameter estimation and optimization. Reduced order modeling has been proposed as an alternative, representing one or more particle properties as a lumped parameter within the remaining internal coordinate system to reduce the dimensionality of the problem (Barrasso and Ramachandran, 2012; Hounslow et al., 2001; Biggs et al., 2003). This technique drastically reduces the computational time, but it may result in a loss of information and fail to represent wide distributions in lumped properties (Barrasso and Ramachandran, 2012).

Additionally, spatial coordinates are not inherent in traditional PBMs. Spatial compartments can be defined to simulate inhomogeneities within the equipment. The equipment is divided into geometric regions, often related to zones of liquid addition, impeller, and chopper action. A three compartment PBM for a fluidized-bed granulator was developed by Maronga and Wnukowski (1997), dividing the granulator into spraying, drying, and inactive zones using empirical values for the rate of transfer between the domains. Similarly, a two-compartment PBM for a Wurster fluidized bed is presented by Borner et al. (2013), based on spraying and drying zones. In horizontal, continuous operation, granules develop along the axial coordinate. A continuous wet granulator has been simulated using axial spatial compartments by Barrasso et al. (2013b). A drawback of compartmental modeling is that an additional model is required to describe the flux between neighboring compartments since the PBM cannot independently describe particle flow. Some studies have used DEM to complete the compartmental model, using flux data from DEM simulations as input data to the PBM (Sen and Ramachandran, 2013; Freireich et al., 2011; Sen et al., 2012; Li et al., 2013).

Various rate expressions are needed to describe the sub-processes of consolidation, liquid addition, breakage, and aggregation. An exponential decay function is often used to describe the consolidation rate, but this approach contains multiple empirical parameters and does not account for the effect of liquid binder content on consolidation, which has been observed experimentally (Verkoeijen et al., 2002; Iveson et al., 1996). Similarly, liquid addition rates require assumptions about the distribution of liquid to the particles. A homogeneous distribution based on particle mass or surface area is often assumed, although heterogeneity has been observed (Scott et al., 2000; Stepanek et al., 2009). Empirical and mechanistic expressions have been developed to describe the breakage rate (Pandya and Spielman, 1983; Pinto et al., 2007; Ramachandran et al., 2009) as it depends on particle properties and process parameters, but these kernels contain additional empirical parameters or particle data that is not inherently known in PBMs, such as particle shear forces.

The aggregation rate is the most investigated, with empirical and semi-empirical rate kernels describing the effect of size on the rate of aggregation. Hounslow et al. (2001) proposed a size-independent kernel (SIK), Smoluchowski's shear kernel (SSK) and the equipartition of kinetic energy kernel (EKE). Numerous alternative size-dependent kernels have also been proposed (Cameron et al., 2005). Fewer aggregation kernels describe the effect of the liquid binder content. The kernel presented by Madec et al. (2003), accounts for size and liquid content, containing three empirical parameters. Additionally, Wauters (2001) proposed a simple kernel based on size and liquid content that categorizes particles as large or small and wet or dry, defining a rate of zero or one for each combination.

Mechanistic or semi-mechanistic aggregation kernels have also been developed. Typically, the aggregation rate is broken into two multiplicative factors. The collision frequency describes the transport of particles, or the rate of collisions between each pair of particle sizes. DEM simulations have been used to analyze the collision frequency distribution by Gantt et al. (2006). The second factor, the collision efficiency, determines whether two colliding particles will aggregate based on particle sizes and surface wetness, relative velocities, and material properties. Expressions for coalescence criteria have been developed (Gantt et al., 2006; Liu and Litster, 2002; Chua et al., 2013). Both the collision frequency

and efficiency require information that is unknown in PBMs, such as the collision frequency distribution, particle surface liquid, and relative velocities. DEM simulations can be useful in obtaining this information.

In order to obtain realistic values for the unknown parameters in empirical and semi-empirical rate expressions, parameter estimation has been performed using experimental data (Darelius et al., 2006; Poon et al., 2009; Braumann et al., 2010; Ramachandran and Barton, 2010). Parameter estimation has also been used with 1-D PBMs for other powder processes, such as milling (Capece et al., 2011; Barrasso et al., 2013a). When many parameters are used, substantial experimental data is required, or the model is computationally intensive, this approach is not ideal. Further, these models may not fully capture the complex nature of granulation processes. In order to reduce the number of unknown parameters and capture complex trends, a more mechanistic approach is required, such as multi-scale modeling using DEM.

1.3.2 Discrete element modeling

In contrast to the PBM, DEM simulations track each particle as it moves through space, collides with equipment and other particles, and is subject to force fields, such as gravity. These models primarily use Newton’s laws of motion, expressed in Equations 1.3 (Cameron et al., 2005).

$$m_i \frac{dv_i}{dt} = F_{i,net} \quad (1.2)$$

$$F_{i,net} = F_{i,coll} + F_{i,ext} \quad (1.3)$$

In these equations, the mass of particle i is given by m_i , and the velocity is given by v_i . $F_{i,net}$ is the net force acting on the particle, which is the sum of the forces due to collisions ($F_{i,coll}$) and the external forces ($F_{i,ext}$), such as gravity. When coupled with Navier-Stokes equations or computational fluid dynamics (CFD), fluid-particle forces are also included. Various contact models can be implemented to describe the collision behavior, such as the hard-sphere model, the Hertz-Mindlin model, and the Johnson-Kendall-Roberts (JKR) model. The non-linear elastic Hertz-Mindlin contact model is used in this study.

Commercial DEM software is available, such as EDEM (DEM Solutions), which contain graphical user interfaces for easy use. However, DEM is highly computationally intensive, with single simulations taking hours or days to solve. Parallel computing can be used to reduce computation time (Solutions, 2013). However, DEM is not suitable for iterative calculations, such as parameter estimation or optimization. Furthermore, the number of particles is a limiting factor, and many DEM simulations contain a drastically reduced number of particles compared to those observed in real systems, often with larger particles used to represent a fixed number of smaller particles (Hassanpour et al., 2009). Collision detection is the limiting calculation in DEM, and smaller particles require a finer grid to perform this operation (Solutions, 2013). Periodic sectioning can also be used to reduce the number of particles in a simulation (Gao et al., 2011).

Microscale DEM simulations involve fewer particles in order to obtain mechanistic results. Lian et al. (1998) simulated two-particle interactions and impact coalescence between wet agglomerates using DEM, and Kafui and Thornton (2000) performed simulations of impact breakage. While these studies provide micro-scale insight into granulation mechanisms, they are not directly applicable to process-level simulations. Gantt et al. (2006) studied the interactions of 5000 particles with a mean size of 1.7 mm within a periodic boundary and extracted data to provide statistical estimates of coalescence rates and efficiencies. These results can help connect mechanistic, micro-scale modeling with process-level models, such as the population balance. However, these simulations do not incorporate the rate processes observed in granulation, but can serve as input data for a PBM. The effects of size distribution, segregation, liquid distribution, and process parameters are not captured by this approach. At the process level, DEM simulations for powder flow and mixing have also been used to generate reduced order models for use in flowsheet simulations by Boukouvala et al. (2013). A similar approach can be used to overcome the computational limitations of DEM within process-level simulations.

1.4 Specific Aims

Through this dissertation, four research objectives are addressed to advance the mechanistic understanding of wet granulation processes and to develop predictive models that describe process behavior. These specific aims are:

- I. Multi-dimensional population balance modeling of wet granulation processes
- II. Parameter estimation and validation using experimental data from a twin-screw granulator
- III. Development of a multi-scale model using bi-directional coupling of discrete element modeling and population balance modeling
- IV. Applications of multi-scale models to simulate realistic wet granulation processes

The specific aims are supported by seven chapters, each an original research study published in the literature. PBM techniques are used extensively and combined with experimental data, DEM models, and reduced order modeling approaches to create useful tools that advance the understanding of wet granulation processes. In each chapter, a unique PBM is developed and presented. While these models are similar, their subtle differences are intentional as the modeling framework is tailored to meet the unique needs of each application, from experimental validation to multi-scale modeling.

Specific Aim I

Multi-dimensional population balance modeling of wet granulation processes

While population balance modeling has been used extensively to describe granulation processes, these are often over-simplified and unable to capture the effects of process parameters on critical quality attributes. A detailed, multi-dimensional population balance model is presented for continuous wet granulation processes, and a parametric study is performed. Numerical solution techniques are developed, validated, and implemented.

The goals of this specific aim are to:

- Develop a PBM, allowing for variations in size, liquid content, porosity, and solid composition, and including spatial compartments.
- Demonstrate theoretical effects of process parameters on critical quality attributes.
- Use and validate numerical techniques to reduce the computation time while allowing for a large size change, such as the cell average technique and the lumped parameter approach.

These works were originally published in:

- Barrasso, D., Ramachandran, R., 2012. A comparison of model order reduction techniques for a four-dimensional population balance model describing multi-component wet granulation processes. *Chemical Engineering Science* 80, 380 – 392
- Barrasso, D., Walia, S., Ramachandran, R., 2013b. Multi-component population balance modeling of continuous granulation processes: A parametric study and comparison with experimental trends. *Powder Technology* 241, 85 – 97

Chapter 2

A comparison of model order reduction techniques for a four-dimensional population balance model describing multi-component wet granulation processes

Three-dimensional (3-D) population balance equations have been used to model wet granulation processes, simulating distributions in particle size, liquid binder content, and porosity. In multi-component granulation, two or more solid components are present, and granule composition becomes a fourth distributed parameter. In this study, a four-dimensional (4-D) population balance model for multi-component wet granulation is presented and solved. Population balance models of high order are computationally expensive, limiting their applicability in analysis and design. The 4-D model was reduced to a combination of lower-dimensional models using the lumped parameter technique, in which one or more particle characteristics is assumed to be fixed within the remaining distributions. The reduced order models were compared with the full 4-D model for accuracy and computation time. Significant time savings were observed for all reduced order models. The 3-D model with gas volume as the lumped parameter showed the most promising results as an alternative to the 4-D model, which is attributed to the limited influence of gas volume on aggregation and breakage rates.

2.1 Background

2.1.1 Multi-dimensional population balance modeling

One-dimensional (1-D) population balance models, which characterize granules according to one intrinsic property, are traditionally used to model granulation processes (Iveson, 2002; Biggs et al., 2003). These models operate under the assumption that a granule

can be described sufficiently by its size alone, and there are no considerable variations in other characteristics within a size class. This approach has certain limitations; it cannot account for variations in binder content and porosity within a given size class (Iveson, 2002; Verkoeyen et al., 2002).

Heterogeneous distributions of liquid binder content have been observed, and binder content variations have been found within size classes (Scott et al., 2000; Stepanek et al., 2009; Reynolds et al., 2004). As the rate of aggregation is strongly dependent on liquid binder content, the 1-D population balance model fails to adequately describe this behavior (Iveson, 2002).

A three-dimensional(3-D) population balance model has been widely used to account for concurrent distributions in size, liquid binder content, and porosity (Immanuel and Doyle III, 2005; Poon et al., 2009; Ramachandran et al., 2008; Poon et al., 2008; Ramachandran and Barton, 2010; Ramachandran et al., 2012). Based on the general form presented in Equation 1.1, the 3-D population balance equation is given by

$$\begin{aligned} \frac{\partial}{\partial t} F(s, l, g, t) + \frac{\partial}{\partial s} \left[F(s, l, g, t) \frac{ds}{dt} \right] + \frac{\partial}{\partial l} \left[F(s, l, g, t) \frac{dl}{dt} \right] + \frac{\partial}{\partial g} \left[F(s, l, g, t) \frac{dg}{dt} \right] \\ = \mathfrak{R}_{nuc}(s, l, g, t) + \mathfrak{R}_{agg}(s, l, g, t) + \mathfrak{R}_{break}(s, l, g, t), \end{aligned} \quad (2.1)$$

where (s, l, g) is the vector that represents the solid, liquid, and gas volumes of a granule. $F(s, l, g, t)$ is the population density of a granule described by that vector, varying over time. The three growth terms represent the state changes due to solid layering, liquid addition, and gas consolidation, respectively. \mathfrak{R}_{nuc} , \mathfrak{R}_{agg} , and \mathfrak{R}_{break} represent the net rates of nucleation, aggregation, and breakage, respectively.

2.1.2 Multi-component granulation

Many granulation processes involve multiple solid components. In pharmaceutical granulation processes, an active pharmaceutical ingredient is often granulated with one or more excipients (Lee et al., 2008). With a second solid component, composition becomes an important granule characteristic. An interest in understanding and modeling multi-component granulation is apparent in the literature (Lee et al., 2008; Matsoukas and Marshall Jr., 2010;

Matsoukas et al., 2009; Marshall Jr. et al., 2011, 2013).

Particularly in the pharmaceutical industry, an inhomogeneous composition distribution is severely undesired because it can educe the uniformity of the final dosage form (Iveson, 2002; Lee et al., 2008). For these purposes, a model that assumes a homogeneous composition distribution is inadequate. A fourth dimension must be added to the 3-D population balance model to account fully for granule composition (Iveson, 2002). For each additional solid component used, a new dimension must be added to the population balance model. While this approach may work in theory, its increased computation time and complexity limit its applicability (Pinto et al., 2007).

2.1.3 Reduced order models

A high-dimensional population balance model can be reduced to simpler models of lower dimension (Biggs et al., 2003; Hounslow et al., 2001). In a reduced order model, one or more granule characteristics are lumped into the remaining distributions. By assuming that all of the granules of a given size have the same liquid content, a two-dimensional (2-D) model can be reduced to two 1-D equations, as shown in Equations 2.2 and 2.3.

$$\frac{\partial}{\partial t}n(v, t) = \frac{1}{2} \int_0^v \beta(v - v', v)n(v - v', t)n(v', t)dv' - n(v, t) \int_0^\infty \beta(v, v')n(v', t)dv \quad (2.2)$$

$$\frac{\partial}{\partial t}M(v, t) = \frac{1}{2} \int_0^v \beta(v - v', v)M(v - v', t)n(v', t)dv' - M(v, t) \int_0^\infty \beta(v, v')n(v', t)dv \quad (2.3)$$

Here, $n(v, t)$ represents the number of particles as a function of size and time, and $dM = M(v, t)dv$ is the mass of binder in the size range $(v, v + dv)$ (Biggs et al., 2003; Hounslow et al., 2001). The factor β is the kernel describing the rate of aggregation. Reduced order models simplify the solution of the model, but they are not exactly equivalent to the full model. Hounslow et al. (2001) warn against model order reduction for parameters that influence the rates, such as binder content.

2.1.4 Objectives

Multi-component wet granulation presents unique modeling challenges. Two approaches include (1) the four-dimensional (4-D) population balance equation and (2) the reduced order model using lumped parameters. The purposes of this study are to:

- Propose a 4-D population balance model for multi-component granulation.
- Present and solve reduced order models using the lumped parameter method, taking into account aggregation, breakage, liquid addition, and consolidation.
- Demonstrate that the models conserve mass and result in the appropriate ratios of particle formation to depletion for breakage and aggregation.
- Compare the results of the reduced models with the fully distributed model, in terms of accuracy and time savings.

2.2 Model development

The 4-D population balance was developed by modifying Equation 2.1. As nucleation and layering effects were not included in this model, the resulting population balance is presented in Equation 2.4, where s_1 and s_2 represent the volumes of the two solid components in each granule.

$$\frac{\partial}{\partial t} F(s_1, s_2, l, g, t) + \frac{\partial}{\partial l} \left[F(s_1, s_2, l, g, t) \frac{dl}{dt} \right] + \frac{\partial}{\partial g} \left[F(s_1, s_2, l, g, t) \frac{dg}{dt} \right] = \mathfrak{R}_{agg}(s_1, s_2, l, g, t) + \mathfrak{R}_{break}(s_1, s_2, l, g, t) \quad (2.4)$$

2.2.1 Rate kernels and process parameters

To evaluate the terms in Equation 2.4, the aggregation, breakage, and consolidation rates were modeled with semi-empirical kernels from the literature, and the liquid addition was approximated with a constant spray rate over a time interval. The process parameters and initial conditions used with these kernels are presented in Table 2.1.

Table 2.1: Process parameters and initial conditions used in simulations.

| Parameter name | Value |
|--|--|
| Granulation time | 900 <i>s</i> |
| Time step size | 0.5 <i>s</i> |
| Volume of first bin, solid component 1 $s_{1,1}$ | $1 \times 10^{-13} \text{ m}^3$ |
| Volume of first bin, solid component 2 $s_{2,1}$ | $1 \times 10^{-13} \text{ m}^3$ |
| Volume of first bin, liquid binder l_1 | $2 \times 10^{-14} \text{ m}^3$ |
| Volume of first bin, gas g_1 | $1 \times 10^{-14} \text{ m}^3$ |
| Total number of bins of in each dimension | 8 |
| Initial particle count F in bin (1, 2, 1, 2) | $3 \times 10^{-13} \text{ mol}$ |
| Initial particle count F in bin (2, 1, 1, 2) | $7 \times 10^{-13} \text{ mol}$ |
| Aggregation constant β_0 | $1 \times 10^{19} \text{ mol}^{-1} \text{ s}^{-1}$ |
| Aggregation constant α | 1 |
| Aggregation constant δ | 1 |
| Aggregation constant a_{ab} | 1 |
| Breakage constant P_1 | 1 m^{-1} |
| Breakage constant P_2 | 1 |
| Shear rate G_{shear} | 85 s^{-1} |
| Consolidation rate constant c | $1 \times 10^{-7} \text{ s}^{-1}$ |
| Minimum porosity ϵ_{min} | 0.1 |
| Liquid binder spray interval | $120 \text{ s} < t < 360 \text{ s}$ |
| Liquid binder spray rate \dot{V}_{spray} | 25 mL/s |

Aggregation

The formation and depletion of granules due to aggregation is represented by \mathfrak{R}_{agg} , which can be determined using the semi-empirical aggregation kernel β , as shown in Equations 2.5-2.7.

$$\mathfrak{R}_{agg}(s_1, s_2, l, g, t) = \mathfrak{R}_{agg}^{form}(s_1, s_2, l, g, t) - \mathfrak{R}_{agg}^{dep}(s_1, s_2, l, g, t) \quad (2.5)$$

$$\begin{aligned} \mathfrak{R}_{agg}^{form}(s_1, s_2, l, g, t) &= \frac{1}{2} \int_0^{s_1} \int_0^{s_2} \int_0^l \int_0^g \beta(s_1-s'_1, s_2-s'_2, l-l', g-g', s'_1, s'_2, l', g') \\ &\quad \times F(s_1-s'_1, s_2-s'_2, l-l', g-g', t) F(s'_1, s'_2, l', g', t) dg' dl' ds'_2 ds'_1 \end{aligned} \quad (2.6)$$

$$\begin{aligned} \mathfrak{R}_{agg}^{dep}(s_1, s_2, l, g, t) &= F(s_1, s_2, l, g, t) \int_0^\infty \int_0^\infty \int_0^\infty \int_0^\infty \beta(s_1, s_2, l, g, s'_1, s'_2, l', g') \\ &\quad \times F(s'_1, s'_2, l', g', t) dg dl ds_2 ds_1 \end{aligned} \quad (2.7)$$

The aggregation rate is known to depend on liquid binder content and granule size. Since the reduced order models employ average values for these parameters, a kernel that accounts for both is most appropriate for comparing their results and identifying accuracy losses. The aggregation kernel proposed by Madec et al. (2003) was implemented, given by

$$\beta(s_1, s_2, l, g, s'_1, s'_2, l', g') = \beta_0(V + V') \left((LC + LC')^\alpha \left(100 - \frac{LC + LC'}{2} \right)^\delta \right)^\alpha \quad (2.8)$$

where the two colliding particles are described by (s_1, s_2, l, g) and (s'_1, s'_2, l', g') . V and LC represent the total volume and fractional liquid binder content of the particles, given by Equations 2.9 and 2.10. β_0 , α , and δ are adjustable parameters, whose values can be found in Table 2.1.

$$V(s_1, s_2, l, g) = s_1 + s_2 + l + g \quad (2.9)$$

$$LC(s_1, s_2, l, g) = \frac{l}{s_1 + s_2 + l + g} \times 100 \quad (2.10)$$

In a real multi-component system, dissimilar solid particles can attract or repel one another. A composition-dependent aggregation kernel is desired to simulate this behavior and investigate limitations of the reduced order models, some of which treat composition as a lumped parameter. A composition-dependent factor first proposed by Matsoukas et al. (2009) is given by

$$\psi(s_1, s_2, s'_1, s'_2) = \exp(-a_{ab}(x + x' - 2xx')), \quad (2.11)$$

where x is the mass fraction of the first solid component in the particle. In this study, the two solid components were assumed to have equal density, so the volume fraction was used as shown in Equation 2.12.

$$x(s_1, s_2) = \frac{s_1}{s_1 + s_2} \quad (2.12)$$

The interaction parameter a_{ab} relates the attraction or repulsion of the two components. A positive value of a_{ab} indicates repulsion between the two components, and a negative value

indicates attraction (Matsoukas et al., 2009). This factor can be used to modify any size-dependent kernel by multiplication, and it was used with Equation 2.8 to obtain a kernel with size, liquid content, and composition dependences. The overall aggregation kernel is shown in Equation 2.13.

$$\beta(s_1, s_2, l, g, s'_1, s'_2, l', g') = \beta_0(V + V') \left((LC + LC')^\alpha \left(100 - \frac{LC + LC'}{2} \right)^\delta \right)^\alpha \times \exp(-a_{ab}(x + x' - 2xx')) \quad (2.13)$$

Breakage

Breakage occurs when particles disintegrate into two or more fragments due to impact and attrition. The breakage rate consists of the depletion of larger granules ($\mathfrak{R}_{break}^{dep}$) and the formation of smaller particles ($\mathfrak{R}_{break}^{form}$), as shown in Equations 2.14-2.16.

$$\mathfrak{R}_{break}(s_1, s_2, l, g, t) = \mathfrak{R}_{break}^{form}(s_1, s_2, l, g, t) - \mathfrak{R}_{break}^{dep}(s_1, s_2, l, g, t) \quad (2.14)$$

$$\mathfrak{R}_{break}^{form}(s_1, s_2, l, g, t) = \int_0^\infty \int_0^\infty \int_0^\infty \int_0^\infty K_{break}(s'_1, s'_2, l', g') b(s'_1, s'_2, l', g', s_1, s_2, l, g) \times F(s'_1, s'_2, l', g', t) dg' dl' ds'_2 ds'_1 \quad (2.15)$$

$$\mathfrak{R}_{break}^{dep}(s_1, s_2, l, g, t) = K_{break}(s_1, s_2, l, g) F(s_1, s_2, l, g, t) \quad (2.16)$$

The breakage kernel $K_{break}(s'_1, s'_2, l', g')$ describes the rate at which particles break, and the probability distribution function $b(s'_1, s'_2, l', g', s_1, s_2, l, g)$ determines the properties of the daughter particles. The fragments of a broken particle can vary in volume but must be smaller than the parent particle. For the purposes of this study, a uniform probability distribution was assumed for all possible daughter particle bins, given by

$$b(s'_1, s'_2, l', g', s_1, s_2, l, g) = \frac{1}{(h-1)(i-1)(j-1)(k-1)} \quad \text{for } (s_1, s_2, l, g) < (s'_1, s'_2, l', g'), \quad (2.17)$$

where h , i , j , and k are the first and second solid component, liquid, and gas bin numbers of the parent particles, respectively. According to this distribution, a parent particle is equally

likely to break into fragments that can be described by each smaller bin. A semi-empirical breakage kernel was used in this study, as given by

$$K_{break}(s_1, s_2, l, g) = \frac{P_1 G_{shear} (D(s_1, s_2, l, g))^{P_2}}{2}, \quad (2.18)$$

where G is the shear rate, $D(s_1, s_2, l, g)$ is the particle diameter, and P_1 and P_2 are adjustable parameters (Pandya and Spielman, 1983). The values for G_{shear} , P_1 and P_2 are included in Table 2.1.

Consolidation

Consolidation is the decrease in porosity (ϵ) due to the compaction of particles. Particle porosity is given by

$$\epsilon(s_1, s_2, l, g) = \frac{l + g}{s_1 + s_2 + l + g} \quad (2.19)$$

Consolidation is represented by an exponential decay of porosity, resulting in the equation

$$\frac{dg}{dt} = -c \frac{(s_1 + s_2 + l + g)(1 - \epsilon_{min})}{s_1 + s_2} \left[l - \frac{\epsilon_{min}(s_1 + s_2)}{1 - \epsilon_{min}} + g \right], \quad (2.20)$$

where ϵ_{min} is the minimum granule porosity, and c is a rate constant (Verkoeijen et al., 2002). The values used for these parameters are given in Table 2.1.

Liquid Addition

In wet granulation, liquid binder is sprayed on dry particles to increase the aggregation rate. After a period of dry mixing, liquid is added at a constant rate of \dot{V}_{spray} . When the liquid addition period ends, granulation continues. It was assumed that each particle receives the same volume of binder, resulting in Equation 2.21.

$$\frac{dl}{dt} = \frac{\dot{V}_{spray} F(s_1, s_2, l, g)}{\int_0^\infty \int_0^\infty \int_0^\infty \int_0^\infty F(s_1, s_2, l, g) ds_1 ds_2 dl dg} \quad (2.21)$$

The values used for the spray rate and time intervals are included in Table 2.1. Prior to liquid addition, the aggregation and breakage rates were assumed to be negligible. Since the rate of liquid addition into each bin depends on the number of particles in that bin, it

is recalculated at each time point during the liquid addition interval.

2.2.2 Numerical and computational techniques

The resulting population balance equation was solved numerically. The descriptive particle parameters were discretized into bins according to the granule volume of each solid component, liquid, and gas. Because the 4-D model is so computationally expensive, a small number of bins was necessary to solve this model in an acceptable amount of time. A linear grid would require a very large number of bins to cover the size ranges observed industrially. Instead, a non-linear grid was used to define these bins, as presented in Equations 2.22-2.25.

$$s_{1,h} = s_{1,1} \times 3^{h-1} \quad (2.22)$$

$$s_{2,i} = s_{2,1} \times 3^{i-1} \quad (2.23)$$

$$l_j = l_1 \times 3^{j-1} \quad (2.24)$$

$$g_k = g_1 \times 3^{k-1} \quad (2.25)$$

The indices h , i , j , and k represent the bin numbers in the four dimensions. In the (h, i, j, k) bin, the volume per particle of each component is given by $(s_{1,h}, s_{2,i}, l_j, g_k)$. In the reduced models, lumped parameters are not discretized, and one or more of these equations are not needed. The initial population density is distributed over two bins, designated by $(1, 2, 1, 2)$ and $(2, 1, 1, 2)$. The two bins are used to allow for a distribution in particle composition, simulating initial particles of separate API and excipient. Since all bins have finite volumes of each component, the initial particles are not pure API or excipient, but have different mass fractions. The initial particles are assigned to the second gas bin to allow for gas consolidation, which transfers a fraction of particles to a lower bin. For the reduced models, the initial value for the lumped parameters is assigned to be consistent with the 4-D model. The component volumes in the first bin $(s_{1,1}, s_{2,1}, l_1, g_1)$ are given in Table 2.1, along with the total number of bins in each dimension and initial particle distribution.

Numerical integration of the population balance equation over the was performed using the discrete bins using the finite difference method, reducing the equation to a system of ordinary differential equations. Each bin was assumed to have uniform particle distributions. The cell average method was used to distribute particles with volumes that lie between bins into the surrounding populations, a technique developed for the 1-D case by Kumar et al. (2006) and for the 3-D case by Chaudhury et al. (2013a). Detailed equations describing the application of the cell average method are presented in Appendix 9.

First-order explicit Euler integration was performed to track the population distribution over time, with a time step size of 0.5 seconds. As with any explicit numerical solution to partial differential equations, numerical instability can occur if the selected time step is too large. The Courant-Friedrichs-Lewis (CFL) condition, shown in Equation 2.26, must be satisfied (Ramachandran and Barton, 2010).

$$\frac{GR\Delta t}{\Delta s_1} + \frac{GR\Delta t}{\Delta s_2} + \frac{GR\Delta t}{\Delta l} + \frac{GR\Delta t}{\Delta g} = CFL < 1 \quad (2.26)$$

In this case, the growth rate GR is the rate of change in volume due to consolidation or liquid addition. This condition indicates that the time step must be less than the time required for particles to travel to adjacent grid points.

The computations were performed on an Intel Core i7-2600 CPU processor (3.4 GHz) with 16 GB of RAM using MATLAB. The codes were parallelized to run on four cores using the Parallel Computing Toolbox in MATLAB. The majority of the computational time was spent calculating formation rate for the aggregation process, which involves many nested for-loops. The outermost for-loop was divided into four sections, each assigned to a core to run simultaneously.

2.2.3 Model reduction methodology

Since models of high dimension are computationally expensive, the 4-D model was reduced to models of lower order. In each reduced model, one or more particle characteristics are lumped into the remaining distributions. Five reduced order models were created, as summarized in Table 2.2.

Table 2.2: Four-dimensional and reduced order models.

| Dimensions | Lumped Parameters | Distributed Parameters |
|------------|-------------------|------------------------|
| 4 | none | s_1, s_2, l, g |
| 3 | s_2 | s_1, l, g |
| 3 | l | s_1, s_2, g |
| 3 | g | s_1, s_2, l |
| 2 | l, g | s_1, s_2 |
| 1 | s_2, l, g | s_1 |

The reduced population balance equations have some key differences from the 4-D equation. The lumped parameters are treated as properties of the bins, similar to the particle density function F . A new equation must be created for each lumped parameter to track its changes over time. Taking gas volume as the lumped parameter, the 3-D reduced model is presented in Equations 2.27 and 2.28.

$$\frac{\partial}{\partial t} F(s_1, s_2, l, t) + \frac{\partial}{\partial l} \left[F(s_1, s_2, l, t) \frac{dl}{dt} \right] = \mathfrak{R}_{agg} + \mathfrak{R}_{break} \quad (2.27)$$

$$\frac{\partial}{\partial t} [G(s_1, s_2, l, t)] = F(s_1, s_2, l, t) \frac{dg}{dt} + \mathfrak{R}_{agg,gas} + \mathfrak{R}_{break,gas} \quad (2.28)$$

Equation 2.27 is the reduced population balance equation, and Equation 2.28 is the gas balance equation. The total volume of gas in each bin is given by $G(s_1, s_2, l, t)$, while the volume of gas in each particle is denoted by $g(s_1, s_2, l, t)$. The gas balance equation includes the consolidation term, which is no longer needed in the population balance. Additionally, the aggregation and breakage terms in the gas balance equation ($\mathfrak{R}_{agg,gas}$, $\mathfrak{R}_{break,gas}$) account for the addition and subtraction of gas volume from each bin, instead of counting individual particles. The reduced order aggregation functions for this case are given in Equations 2.29 and 2.30.

$$\begin{aligned} \mathfrak{R}_{agg}(s_1, s_2, l, t) = & \frac{1}{2} \int_0^{s_1} \int_0^{s_2} \int_0^l \beta(s_1-s'_1, s_2-s'_2, l-l', s'_1, s'_2, l', t) \\ & \times F(s_1-s'_1, s_2-s'_2, l-l', t) F(s'_1, s'_2, l', t) dl' ds'_2 ds'_1 \\ - F(s_1, s_2, l, t) & \int_0^\infty \int_0^\infty \int_0^\infty \beta(s_1, s_2, l, s'_1, s'_2, l', t) F(s'_1, s'_2, l', t) dl ds_2 ds_1 \end{aligned} \quad (2.29)$$

$$\begin{aligned}
\mathfrak{R}_{agg,gas}(s_1, s_2, l, t) &= \frac{1}{2} \int_0^{s_1} \int_0^{s_2} \int_0^l \beta(s_1-s'_1, s_2-s'_2, l-l', s'_1, s'_2, l', t) F(s_1-s'_1, s_2-s'_2, l-l', t) \\
&\times F(s'_1, s'_2, l', t) (g(s_1-s'_1, s_2-s'_2, l-l', t) + g(s'_1, s'_2, l', t)) dl' ds'_2 ds'_1 \\
&- G(s_1, s_2, l, t) \int_0^\infty \int_0^\infty \int_0^\infty \beta(s_1, s_2, l, s'_1, s'_2, l', t) F(s'_1, s'_2, l', t) dl ds_2 ds_1
\end{aligned} \tag{2.30}$$

While the aggregation function \mathfrak{R}_{agg} relates to the number of particles forming and depleting in each bin, the gas aggregation function $\mathfrak{R}_{agg,gas}$ transfers the total amount of gas contained in the aggregating particles to the larger particle's bin. In addition, the aggregation kernel β is calculated from Equations 2.8 and 2.11 using the lumped parameter $g(s_1, s_2, l, t)$. The kernel is now a function of time and must be updated throughout the calculation. The breakage function is modified similarly, as shown in Equations 2.31 and 2.32.

$$\begin{aligned}
\mathfrak{R}_{break}(s_1, s_2, l, t) &= \int_{s_1}^\infty \int_{s_2}^\infty \int_l^\infty K_{break}(s'_1, s'_2, l', t) b(s'_1, s'_2, l', s_1, s_2, l) \\
&\times F(s'_1, s'_2, l', t) dl' ds'_2 ds'_1 - K_{break}(s_1, s_2, l, t) F(s_1, s_2, l, t)
\end{aligned} \tag{2.31}$$

$$\begin{aligned}
\mathfrak{R}_{break,gas}(s_1, s_2, l, t) &= V(s_1, s_2, l, t) \int_{s_1}^\infty \int_{s_2}^\infty \int_l^\infty K_{break}(s'_1, s'_2, l', t) b(s'_1, s'_2, l', s_1, s_2, l) \\
&\times \frac{G(s'_1, s'_2, l', t)}{V(s'_1, s'_2, l', t)} dl' ds'_2 ds'_1 - K_{break}(s_1, s_2, l, t) G(s_1, s_2, l, t)
\end{aligned} \tag{2.32}$$

The gas breakage function $\mathfrak{R}_{break,gas}$ accounts for volumes of gas transferred due to breakage. As gas is a lumped parameter, it is assumed that the volume fraction of gas in the daughter particles is the same as that of the breaking particle. Like the aggregation kernel, the breakage kernel K_{break} is evaluated using the lumped parameter, and is a function of time.

The governing equations for the remaining reduced order models are presented in Appendix 9.

2.3 Results and discussion

2.3.1 Validation of numerical methods

The results support the accuracy of the numerical techniques used in this study. As presented in Figure 2.1, the total amount of each solid component is constant over time in all

six simulations. The liquid volume is conserved, taking into account the liquid added during granulation. As expected, the total volume of gas decreases over time due to consolidation.

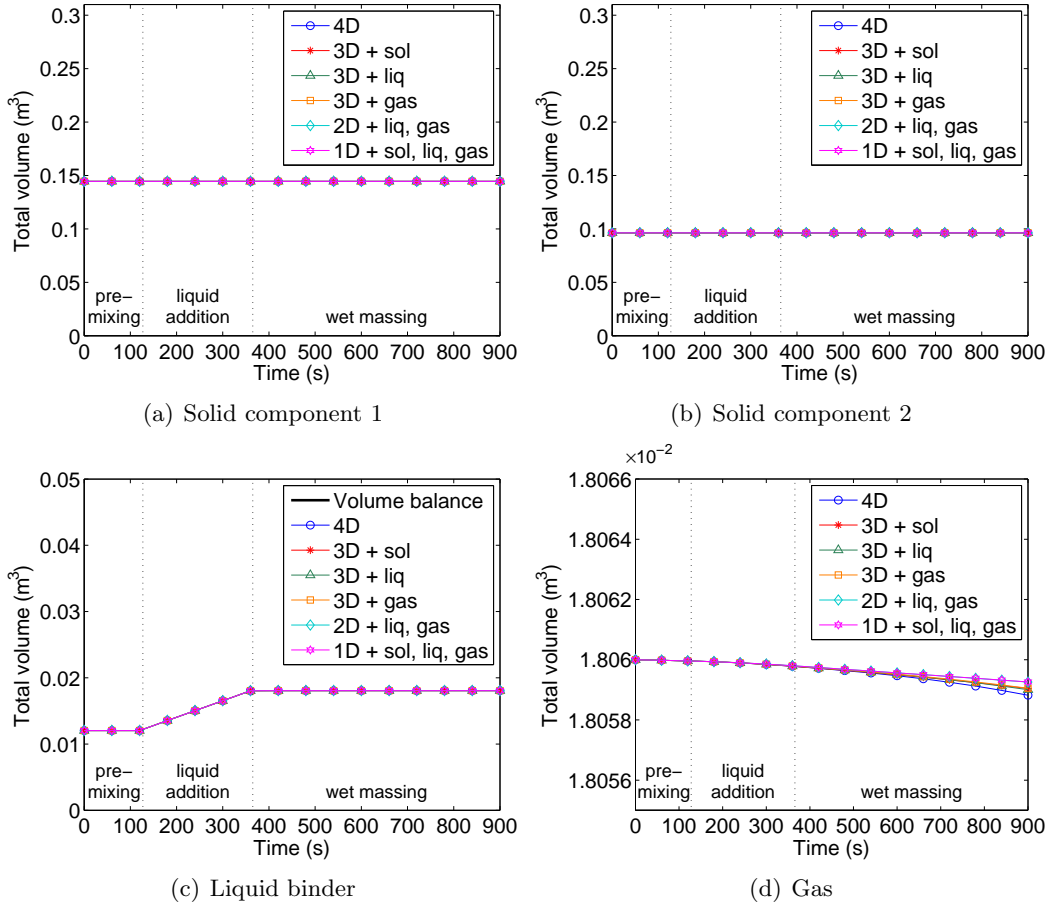


Figure 2.1: Total volume of each component over time, demonstrating conservation. The liquid volume changes due to liquid addition. The volume balance in (c) shows initial volume of liquid plus the volume of liquid added.

Further, the birth and depletion of particles due to aggregation and breakage are consistent with each other. In aggregation, two particles collide to form one larger particle. At all time points, the total aggregative depletion due must be twice the total aggregative birth of particles. For breakage, a single particle forms two daughter particles, so the ratio of total particles depleted to total particles born must equal $\frac{1}{2}$ at all times. These conditions were met in all simulations, as shown in Figure 2.2.

The simulations were repeated using different grid sizes to demonstrate the grid independence of the results. The volumes of the smallest and largest bins were held constant,

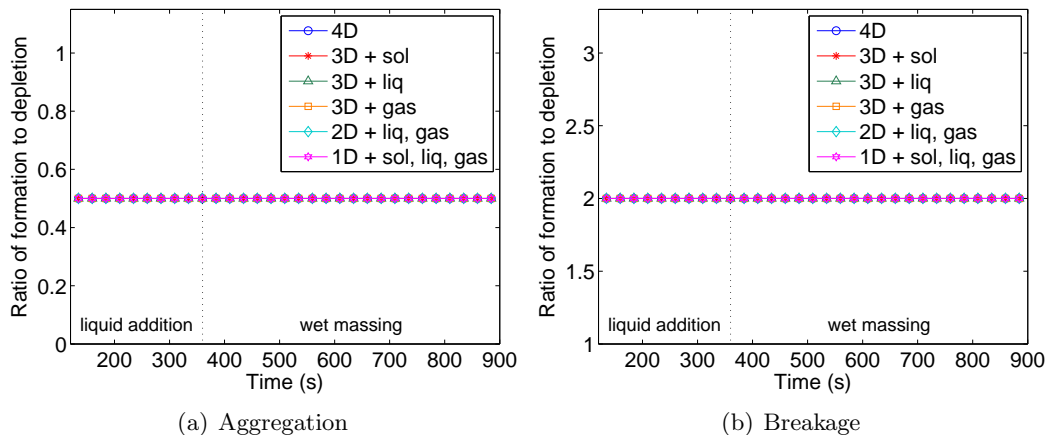


Figure 2.2: Ratio of formation to depletion vs. time due to (a) aggregation and (b) breakage.

and the grid spacing was adjusted to position the remaining bins by changing the base value in Equations 2.22-2.25. Figure 2.3 shows the average diameter over time for the 3-D model with a lumped solid volume using different grid sizes. These curves are similar, suggesting grid independent results. When using a lower number of bins, a greater error is expected.

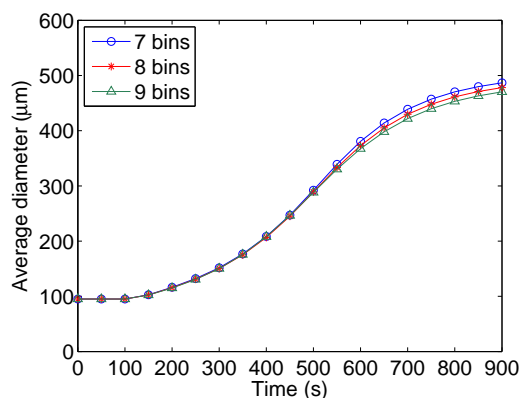


Figure 2.3: Average diameter over time for the 3-D model with lumped solid volume, weighted by volume, using various grid sizes.

2.3.2 Comparison of reduced order models

Figures 2.4(a) and 2.4(b) show the time profiles for the average granule diameter and total number of particles, respectively. The average diameter is weighted by particle volume. During granulation, the average diameter increased from under 100 μm to around 500 μm , while the total number of particles dropped to around 7×10^{-13} moles from 1×10^{-11}

moles. The PBM accurately predicts the initial rapid growth during the liquid addition phase followed by a reduction in the rate of increase in particle diameter during the wet-passing period.

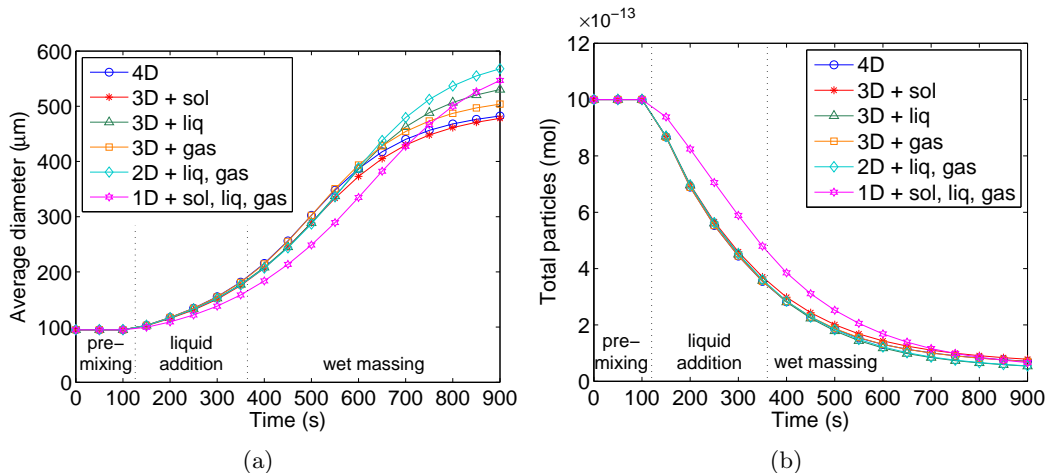


Figure 2.4: (a) Average diameter over time, weighted by volume and (b) total moles of particles over time.

The reduced order models had slightly different results from the 4-D model, as summarized in Table 2.3. The reduced order models with the largest differences were the 3-D model with lumped liquid volume, the 2-D model, and the 1-D model. All three of these models represented liquid as a lumped parameter, and they overestimated the final average diameter by 10-20%. Since liquid binder content has the largest effect on aggregation rate, it is logical that the largest error resulted from lumping the liquid distribution. This observation is consistent with the statement by Hounslow et al. (2001) that order reduction may result in error when the lumped parameters influence the aggregation rates. The 3-D model with gas as the lumped parameter overestimated the final diameter by less than 5%. Gas volume has a minor effect on the aggregation kernel, only through its effect on the overall particle volume. Finally, the 3-D model with a lumped solid volume underestimated the final diameter by 1.3%.

The particle size distribution after granulation, weighted by volume and normalized, is presented in Figure 2.5. The six models have similar, but not equal, size distributions. The 3-D models with solid or gas as the lumped parameter had size distributions that were the most similar to the 4-D model. However, the size distributions of the models with lumped

Table 2.3: Average diameter, total number of particles, and computation time at the end of granulation, as predicted by each model. Percent differences, in parentheses, are based on the predicted value from the 4-D model. Time savings percentages are based on the computation time for the 4-D model.

| Model | $d_{4,3}$ (μm) | Total Particles (mol) | Computation Time (s) | Savings |
|------------------|--------------------------------|---------------------------------|-------------------------|---------|
| 4-D | 482 | 7.13×10^{-13} | 121840 (33.84 hr) | — |
| 3-D+ s_2 | 478 (-0.89%) | 7.81×10^{-13} (9.54%) | 5584 (1.55 hr) | 95.4% |
| 3-D+ l | 530 (9.94%) | 5.40×10^{-13} (-24.3%) | 5686 (1.58 hr) | 95.3% |
| 3-D+ g | 503 (4.45%) | 7.03×10^{-13} (-1.33%) | 5508 (1.53 hr) | 95.5% |
| 2-D+ l, g | 567 (17.7%) | 5.46×10^{-13} (-23.4%) | 74.3 | 99.94% |
| 1-D+ s_2, l, g | 546 (13.4%) | 6.66×10^{-13} (-6.59%) | 3.36 | 99.997% |

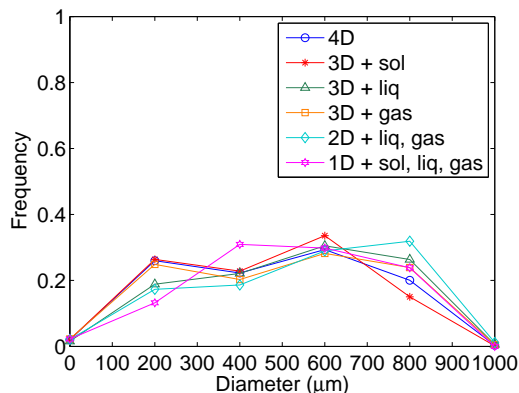


Figure 2.5: Particle size distribution after granulation ($t = 900$ s), weighted by volume and normalized.

liquid volume were skewed. Smaller particles were under-represented, while larger granules had higher frequencies. This discrepancy can be explained by the aggregation kernel, since wetter particles aggregate more readily than dryer particles. When liquid is represented as a distributed parameter, some particles of the same size are dryer than others and are less likely to aggregate, while other particles are wetter and more likely to aggregate. Since the relationship between liquid content and aggregation rate is non-linear (Equation 2.13), these effects do not negate each other.

The two-dimensional distributions of size with composition, liquid content, and porosity indicate additional differences between the fully-dimensional and reduced order models. Figure 2.6 shows the size and composition distributions. As expected, the 1-D model fails to depict this distribution accurately. The 3-D models with lumped liquid or gas volumes

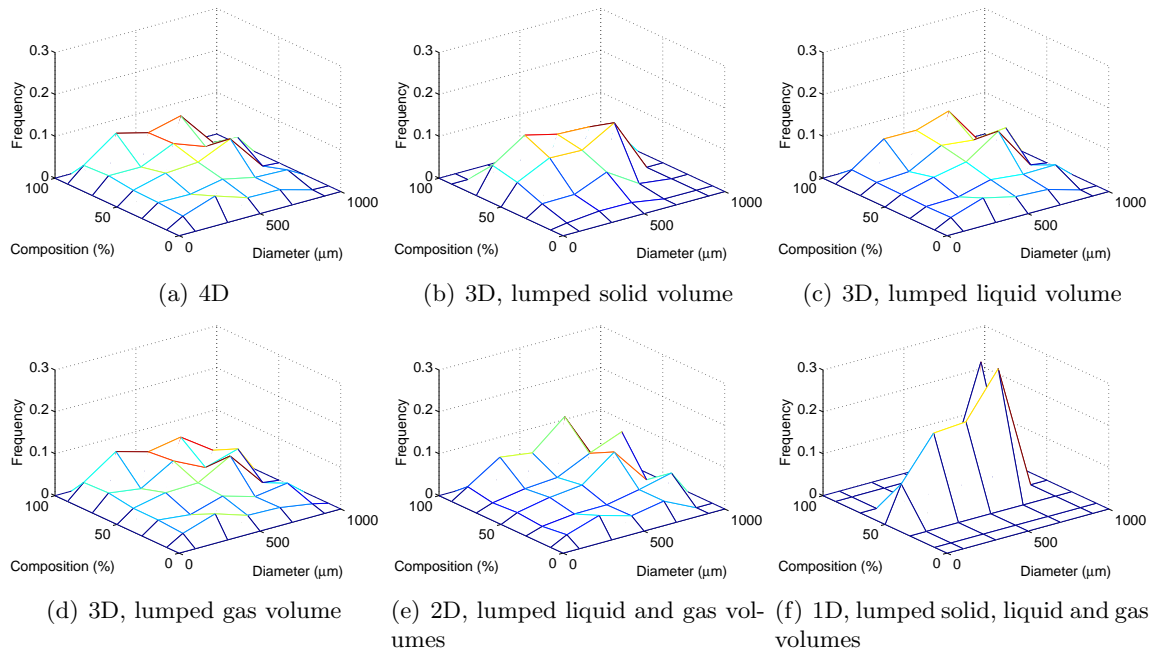


Figure 2.6: Particle size and composition distributions after granulation ($t = 900$ s) for fully dimensional and reduced models.

have size and composition distributions that most closely match that of the 4-D model. However, the distribution for the 3-D model with a lumped solid volumes is clearly different, with more exaggerated peaks and valleys.

The concurrent size and liquid content distributions are shown in Figure 2.7. All three models with liquid volume as a lumped parameter show different distributions from the 4-D model, with peaks at different values of size and liquid content. This result indicates a significant loss in accuracy. The 2-D size and liquid content distributions of the remaining reduced order models more closely resemble that of the 4-D model.

The size and porosity distributions (Figure 2.8) show similar trends. The 1-D model does not adequately simulate the two-dimensional distribution, with only one value of porosity represented at each size. For this distribution, the closest match to the fully-dimensional model is the 3-D model with lumped solid volume. The reduced order models with lumped liquid or gas volume showed different distributions, which can be explained by the relationship between porosity and liquid and gas volumes.

Overall, every reduced order model predicted a final average size that is comparable to that of the fully-dimensional model. The models with lumped liquid volume tended to

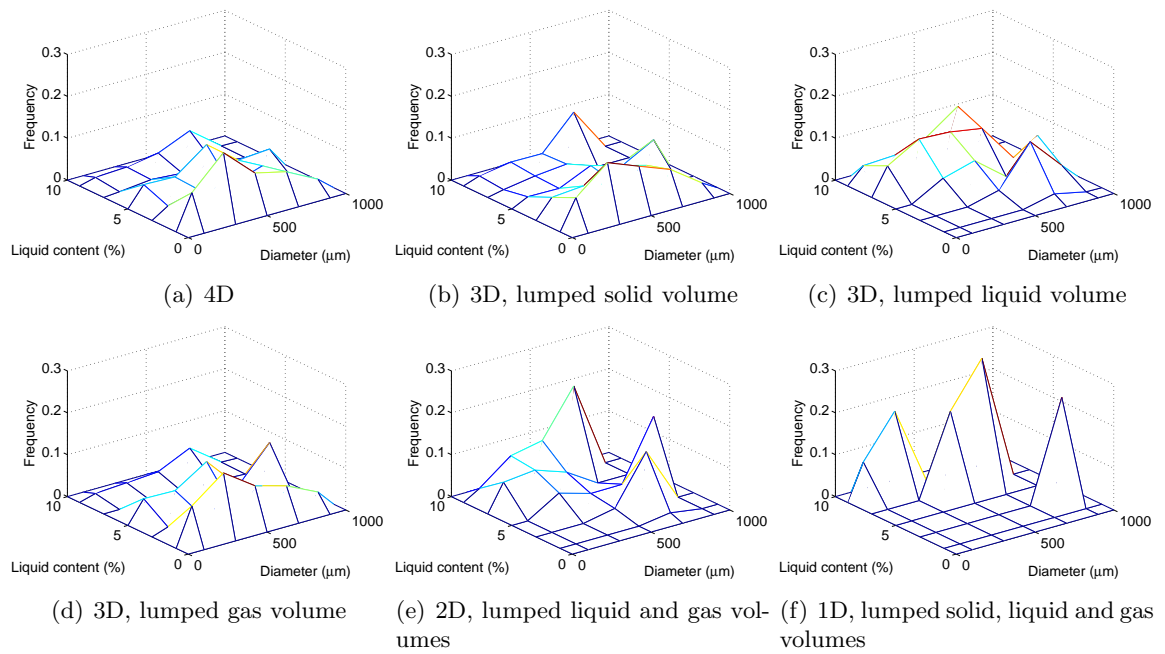


Figure 2.7: Particle size and liquid binder content distributions after granulation ($t = 900\text{ s}$) for fully dimensional and reduced models.

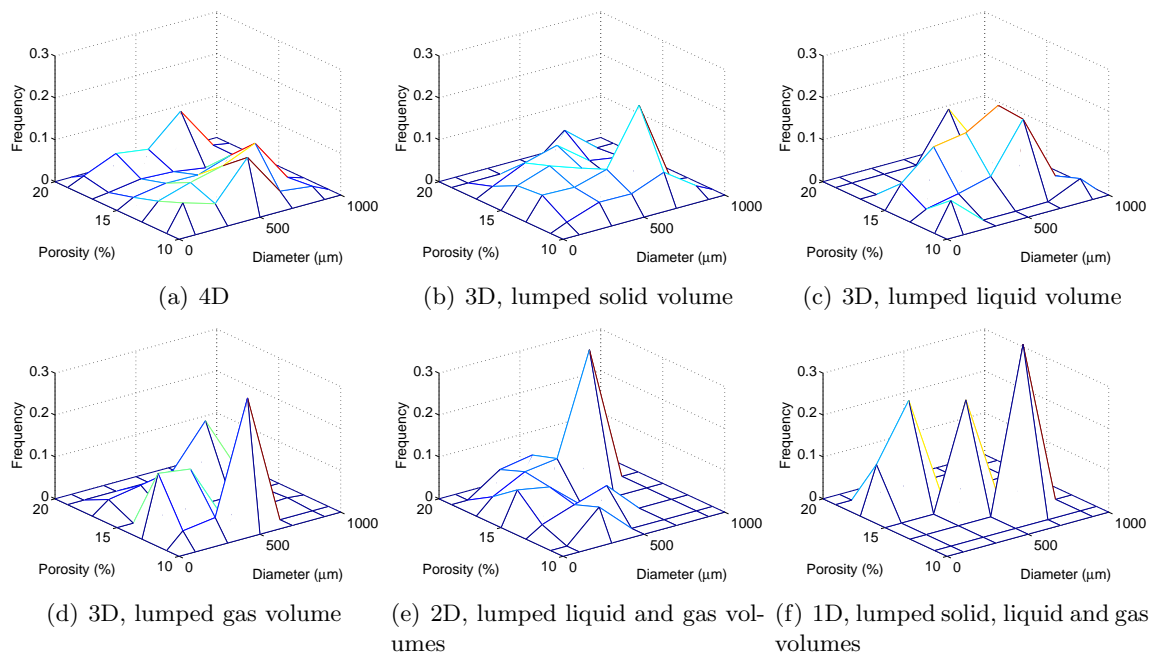


Figure 2.8: Particle size and porosity distributions after granulation ($t = 900\text{ s}$) for fully dimensional and reduced models.

overestimate the granule size, which can be attributed to the strong effect of liquid content on aggregation rates. Although the aggregation rate also depends on composition, the 3-D model with a lumped solid volume yielded similar results to the full model but showed some differences in the distribution of composition with diameter. This drawback may be significant because composition is of particular importance in multi-component granulation. For these reasons, the most sufficient order reduction for the 4-D model is the 3-D model with a lumped gas volume.

2.3.3 Computation time reduction

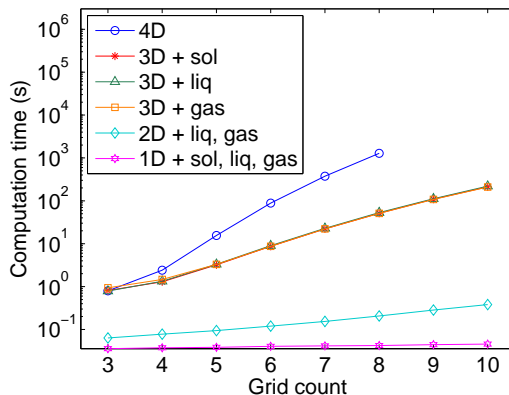


Figure 2.9: Exponential increase of computation time with grid size. Simulations were performed on one core for five time steps each. Grid count represents the total number of bins in each dimension.

The 3-D and 4-D simulations were parallelized to run on four cores. Because the 1-D and 2-D computations were much faster, they were processed on one core. As presented in Table 2.3, all reduced order models showed significant time savings over the 4-D model. The 3-D simulations were completed about 95% more quickly than the 4-D simulation, and the 1-D and 2-D simulations reduced the computation time by over 99%.

The computation time is sensitive to the number of bins. To demonstrate this effect, simulations were run with varying numbers of bins in each dimension for 5 time steps ($t = 2.5$ s). Since the outermost for-loop is divided into equal sections in parallel processing, the number of cores used must be a factor of the number of bins, so these computations were performed on one core. As shown in Figure 2.9, the computation time was found

to increase exponentially with the number of bins. Further, the higher order models had steeper increases in computation time.

2.4 Summary

In this study, modeling approaches for multi-component wet granulation were investigated. Multi-component granulation is of particular interest in the pharmaceutical industry, as excipients and APIs are often granulated in the tablet manufacturing process. Because the composition of these products is critical to their success, a useful model for multicomponent granulation processes must simulate distributions in composition.

Two modeling approaches were presented and solved for multi-component wet granulation. A 4-D population balance model was developed to account for simultaneous distributions of size, solid composition, liquid binder content, and porosity. Liquid addition, gas consolidation, aggregation, and breakage were represented in this model. In order to simulate the effects of multiple distributions, the aggregation kernel selected was size, liquid content, and composition dependent. This model was computationally expensive, particularly with large grids.

As an alternative, analogous reduced order models were developed using the lumped parameter technique. These models exhibited significant time savings over the fully-dimensional model, with some accuracy losses. Since the aggregation kernel selected was strongly influenced by liquid binder content, the models that represented liquid volume as a distribution were the most successful. Order reduction of higher order population balance models can be used to obtain realistic, but not exact, results in a short amount of time. While a finer grid can yield more accurate results, solving the 4-D model for a finer grid may be infeasible, and model reduction may be necessary.

Chapter 3

Multi-component population balance modeling of continuous granulation processes: A parametric study and comparison with experimental trends.

In the recent few years, continuous processing has been considered as a promising process alternative to batch processing in pharmaceutical manufacturing. Via a novel population balance model framework, a multi-dimensional multi-component model for a continuous granulation process was developed, describing time evolutions of distributions with respect to granule size, liquid distribution and granule composition. A parametric study was performed to analyze the effects of various process and design parameters, including granulator size and configuration, liquid spray rate and particle velocity, on evolutions and distributions of key granule properties. Simulation results capture experimentally observed sensitivities and trends thus demonstrating the use of a model-based framework for granulation process design, control and optimization to enable QbD in drug product development.

3.1 Background

A typical continuous horizontal granulator is divided into three zones. The first zone is the premixing zone, where dry powder particles are fed and mixed to achieve blend homogeneity. The particles then move into the spray zone, where liquid binder is sprayed onto the particles, and they begin to nucleate and aggregate to form larger granules. After the spray zone, the particles pass through a wet-massing zone, where they continue to aggregate and consolidate due to residual liquid and collisions, forming larger and denser granules. Other mechanisms such as breakage and layering may also occur concurrently in the spray and wet massing zone.

Continuous wet granulation processes can be categorized into four types: fluidized bed,

twin screw, high shear, and drum granulation. Horizontal fluidized bed granulators are often used in industries with high product volumes, such as the food industry (Vervaet and Remon, 2005). These machines can include dryers, removing the need for a separate drying step.

In twin screw granulation, two screws transport the particles through an extruder, mixing them in the process. This technique has been widely studied for pharmaceutical applications (Keleb et al., 2004; Vervaet and Remon, 2005; El Hagrasy et al., 2013), particularly because it is suitable for various capacities (Vervaet and Remon, 2005). However, a separate drying step is necessary to produce dry granules. Additionally, the screw configuration can become an important design parameter.

A high shear mixer can also be used for granulation with the addition of sprayers. This process is similar to twin screw granulation, using an impeller to transport the particles instead of screws. High shear granulation also produces wet granules, and it often is operated at a higher capacity than twin screw granulation (Vervaet and Remon, 2005).

Finally, a continuous drum granulator consists of a rotating cylinder, operating at a lower shear rate than high shear granulation. The cylinder is slightly inclined to transport the material. Continuous drum granulation is commonly used in the fertilizer industry (Walker, 2007).

3.1.1 Population balance modeling of continuous particulate processes

The population balance model (PBM) framework tracks the number of particles with a given set of properties (e.g. size) as they are subject to rate processes, such as aggregation, nucleation, and breakage. PBMs are often used to model powder processes, such as crystallization, mixing, milling, and granulation.

A three-dimensional (3-D) PBM has also been employed to model granulation processes (Immanuel and Doyle III, 2005; Poon et al., 2009; Ramachandran et al., 2008; Poon et al., 2008; Ramachandran and Barton, 2010; Ramachandran et al., 2012). As shown in Equation

3.1, this model accounts for simultaneous distributions of solid, liquid, and gas volumes.

$$\begin{aligned} \frac{\partial}{\partial t} F(s, l, g, t) + \frac{\partial}{\partial s} \left[F(s, l, g, t) \frac{ds}{dt} \right] + \frac{\partial}{\partial l} \left[F(s, l, g, t) \frac{dl}{dt} \right] + \frac{\partial}{\partial g} \left[F(s, l, g, t) \frac{dg}{dt} \right] \\ = \mathfrak{R}_{nuc} + \mathfrak{R}_{agg} + \mathfrak{R}_{break} \end{aligned} \quad (3.1)$$

This model includes terms for solid layering ($\frac{ds}{dt}$), liquid addition ($\frac{dl}{dt}$), gas consolidation ($\frac{dg}{dt}$), net rates of nucleation (\mathfrak{R}_{nuc}), aggregation (\mathfrak{R}_{agg}), and breakage (\mathfrak{R}_{break}). To fully model multi-component granulation, a fourth dimension must be added for the second solid component. However, higher-order PBMs are computationally expensive, and a four-dimensional PBM can take days or weeks to solve (Barrasso and Ramachandran, 2012). Higher-order PBMs can be reduced by assuming that one or more properties that are less significant are lumped within the other distributions (Barrasso and Ramachandran, 2012).

The PBM can be extended to include spatial coordinates to model non-uniform batch processes and continuous processes (Ramkrishna, 2000). As shown in Equation 3.2, a vector of external coordinates (\mathbf{z}) is added, accounting for spatial distributions in particle frequencies and properties.

$$\begin{aligned} \frac{\partial F(\mathbf{x}, \mathbf{z}, t)}{\partial t} + \frac{\partial}{\partial \mathbf{x}} \left[F(\mathbf{x}, \mathbf{z}, t) \frac{d\mathbf{x}}{dt}(\mathbf{x}, \mathbf{z}, t) \right] + \frac{\partial}{\partial \mathbf{z}} \left[F(\mathbf{x}, \mathbf{z}, t) \frac{d\mathbf{z}}{dt}(\mathbf{x}, \mathbf{z}, t) \right] = \\ \mathfrak{R}_{formation}(\mathbf{x}, \mathbf{z}, t) - \mathfrak{R}_{depletion}(\mathbf{x}, \mathbf{z}, t) + \dot{F}_{in}(\mathbf{x}, \mathbf{z}, t) - \dot{F}_{out}(\mathbf{x}, \mathbf{z}, t) \end{aligned} \quad (3.2)$$

The term $\frac{d\mathbf{z}}{dt}$ represents the particle velocity, and \dot{F}_{in} and \dot{F}_{out} are the inflow and outflow rates.

One-dimensional (1-D) PBMs are most commonly used for batch and continuous modeling because they are easy to solve and computationally inexpensive (Iveson, 2002; Biggs et al., 2003; Barrasso and Ramachandran, 2012). These models account for distributions with respect to one particle property, usually size. For granulation processes, this assumption has been found to be inefficient since other particle properties such as liquid content and porosity can significantly affect aggregation rates (Iveson, 2002; Verkoeyen et al., 2002; Barrasso and Ramachandran, 2012). Additionally, 1-D PBMs cannot represent distributions of key product quality attributes such as granule composition.

Most previous multi-dimensional PBM studies of wet granulation have involved batch

processes (Poon et al., 2008, 2009; Chaudhury et al., 2013b). These PBMs often focus on distributions in size, porosity, and liquid content, without simulating multiple solid components. However, Matsoukas and Marshall Jr. (2010) have developed a solid composition-dependent aggregation rate kernel. Marshall Jr. et al. (2013) presented a multi-component PBM for batch granulation to analyze the effects of binder content distribution, and Lee et al. (2008) have investigated segregation of solid components in batch granulation. In a previous study, Barrasso and Ramachandran (2012) presented a four-dimensional model for batch granulation, considering size, porosity, liquid content, and composition.

Fewer models of continuous granulation have been developed. Heinrich et al. (2002b,a) presented a dynamic 1-D PBM of continuous fluidized bed granulation, which did not include spatial coordinates. Further, Vreman et al. (2009) developed dynamic and steady state 1-D models for fluid bed granulation. Wang and Cameron (2002) reviewed the progress in modeling continuous drum granulation for control applications. Although these 1-D models are useful for design and optimization, they cannot capture inhomogeneities and spatial effects. For use in a control study, Ramachandran and Chaudhury (2012) have developed a 3-D PBM of continuous drum granulation that models spatial coordinates in three compartments. PBMs have also been used to model other continuous powder processes, such as crystallization and mixing (Gerstlauer et al., 2002; Sen and Ramachandran, 2013). No studies were found that use a PBM to simulate a twin-screw granulation process.

In this study, a 3-D continuous PBM for multi-component twin-screw granulation processes will be presented, accounting for distributions in size, liquid content, and solid composition that vary throughout the granulator.

3.1.2 Objectives

The purpose of this study is to propose a multi-dimensional model for continuous granulation processes. In particular, the following objectives will be addressed:

- Develop a dynamic 3-D PBM for multi-component, continuous granulation with two spatial dimensions, accounting for the rate processes of aggregation, breakage, liquid addition, and consolidation.

- Demonstrate this models ability to capture experimental trends and observations based using data from a twin-screw granulator.
- Perform a parametric study to analyze the effects of various input parameters on steady-state product distributions and start-up dynamics.

3.2 Model development

In this study, a 3-D PBM was developed to account for simultaneous distributions in size, composition, and liquid binder content, as given in Equation 3.3. For the purposes of this study, nucleation and layering effects were neglected. Although nucleation occurs during granulation, aggregation is the primary mechanism of particle growth (Marshall Jr. et al., 2011). However, it can be easily incorporated based on previous work by the second author (Poon et al., 2009). Layering was neglected due to previous experimental work ascertaining the layering is minimal in viscous regimes that result in aggregation being the dominant mechanism (Ramachandran et al., 2008).

$$\frac{\partial}{\partial t} F(s_1, s_2, l, t) + \frac{\partial}{\partial l} \left[F(s_1, s_2, l, t) \frac{dl}{dt} \right] = \mathfrak{R}_{agg} + \mathfrak{R}_{break} \quad (3.3)$$

Here, s_1 and s_2 represent the volumes of excipient and API in each granule, respectively. This model does not include a distributed gas volume. Instead, gas is represented as a lumped parameter under the assumption that all granules of the same size, composition, and liquid binder content have the same averaged porosity. In a previous study, this technique was found to reduce the computational expense significantly with minimal effect on accuracy (Barrasso and Ramachandran, 2012). The volume of gas in each particle is represented as a function of the API, excipient, and liquid binder volumes and is determined from Equation 3.4.

$$\frac{\partial}{\partial t} [G(s_1, s_2, l, t)] + \frac{\partial}{\partial l} \left[G(s_1, s_2, l, t) \frac{dl}{dt} \right] = F(s_1, s_2, l, t) \frac{dg}{dt} + \mathfrak{R}_{agg,gas} + \mathfrak{R}_{break,gas} \quad (3.4)$$

In this equation, G represents the total volume of gas in a bin, and g is the average volume of gas per particle in that bin. $\mathfrak{R}_{agg,gas}$ and $\mathfrak{R}_{break,gas}$ correspond to the amount of gas transferred due to aggregation and breakage.

The internal coordinates of API, excipient, liquid, and gas volumes are related to key granule properties, such as size, porosity, liquid binder content, and solid composition. A homogeneous product is desired, with narrow distributions in these attributes. The relationships between the internal coordinates and granule properties are given in Table 3.1.

Table 3.1: Granule properties and dependent rate processes.

| Property | Definition | Dependent Rate Processes |
|-------------------|---|--------------------------------------|
| Size (volume) | $V = s_1 + s_2 + l + g$ | aggregation, breakage, consolidation |
| Size (diameter) | $d = \left[\frac{6V}{\pi}\right]^{(1/3)}$ | aggregation, breakage, consolidation |
| Solid composition | $x = \frac{s_1}{s_1 + s_2}$ | aggregation |
| Liquid content | $l_s = \frac{l}{V}$ | aggregation |
| Porosity | $\epsilon = \frac{l+g}{V}$ | consolidation |

3.2.1 Spatial coordinates and particle flow

By adding external coordinates, the 3-D model was adapted to suit continuous granulation processes. The granulator was represented by two spatial dimensions, as done in previous mixing and powder flow studies (Portillo et al., 2007; Sen and Ramachandran, 2013). The resulting continuous PBEs are given in Equations 3.5 and 3.6.

$$\begin{aligned} \frac{\partial}{\partial t} F(s_1, s_2, l, x, y, t) + \frac{\partial}{\partial l} \left[F(s_1, s_2, l, x, y, t) \frac{dl}{dt} \right] + \frac{\partial}{\partial x} \left[F(s_1, s_2, l, x, y, t) \frac{dx}{dt} \right] + \\ \frac{\partial}{\partial y} \left[F(s_1, s_2, l, x, y, t) \frac{dy}{dt} \right] x = \dot{F}_{in}(s_1, s_2, l, x, y, t) - \dot{F}_{out}(s_1, s_2, l, x, y, t) + \\ \mathfrak{R}_{agg} + \mathfrak{R}_{break} \end{aligned} \quad (3.5)$$

$$\begin{aligned} \frac{\partial}{\partial t} G(s_1, s_2, l, x, y, t) + \frac{\partial}{\partial l} \left[G(s_1, s_2, l, x, y, t) \frac{dl}{dt} \right] + \frac{\partial}{\partial x} \left[G(s_1, s_2, l, x, y, t) \frac{dx}{dt} \right] + \\ \frac{\partial}{\partial y} \left[G(s_1, s_2, l, x, y, t) \frac{dy}{dt} \right] = F(s_1, s_2, l, x, y, t) \frac{dg}{dt} + g_{in} \dot{F}_{in}(s_1, s_2, l, x, y, t) \\ - g_{out} \dot{F}_{out}(s_1, s_2, l, x, y, t) + \mathfrak{R}_{gas,agg} + \mathfrak{R}_{gas,break} \end{aligned} \quad (3.6)$$

The axial and radial dimensions refer to the location of the particles within the granulator and are represented by x and y , respectively. These bins span the length of the granulator, covering all three zones. The terms $\frac{dx}{dt}$ and $\frac{dy}{dt}$ represent the axial and radial particle

velocities, which can vary over time and position. Additionally, the inflow and outflow of particles in the feed and product are given by \dot{F}_{in} and \dot{F}_{out} , respectively. The inflow term is based on an overall mass flow rate, \dot{m}_{in} , and feed particle distribution p_{in} , as well as the powder density ρ , as shown in Equation 3.7.

$$\dot{F}_{in}(s_1, s_2, l) = \frac{\dot{m}_{in} p_{in}(s_1, s_2, l)}{\rho V(s_1, s_2, l)} \quad (3.7)$$

The inlet flow rate, distribution, and density are given in Table 3.2. The outlet flow rate is based on the particle velocity and distribution in the last axial bin. All simulations are performed from process startup, so the initial number of particles within the granulator is zero.

Table 3.2: Process parameters and initial conditions used in simulations for the baseline case.

| Parameter name | Symbol | Baseline Value |
|--|-----------------------------------|------------------------------------|
| Mass flow rate of feed particles | \dot{m}_{in} | 4 kg/hr |
| Mass fraction of excipient particles in feed | $\dot{p}_{in}(2, 1, 1)$ | 0.75 |
| Mass fraction of API particles in feed | $\dot{p}_{in}(1, 2, 1)$ | 0.25 |
| Density of feed particles | ρ | 1525 kg/m ³ |
| Volume of gas per particle in feed | g_{in} | $2.67 \times 10^{-13} \text{ m}^3$ |
| Mean axial velocity (standard deviation) | v_x | 0.03 m/s (0.01 m/s) |
| Mean radial velocity (standard deviation) | v_y | 0 m/s (0.003 m/s) |
| Granulator length | x_f | 0.32 m |
| Granulator diameter | y_f | 0.016 m |
| Axial bounds on spray zone | x_1, x_2 | 0.08 m, 0.16 m |
| Radial bounds on spray zone (homogeneous) | y_1, y_2 | 0 m, 0.016 m |
| Radial bounds on spray zone (heterogeneous) | y_1, y_2 | 0.012 m, 0.016 m |
| Time at which sprayer turns on | t_{spray} | 5 s |
| Liquid-to-solid ratio | $L : S$ | 0.15 |
| Aggregation constants | $\beta_0, \alpha, \delta, a_{ab}$ | 300, 1, 1, 0 |
| Breakage constants | P_1, P_2 | 1, 1 |
| Shear rate | G_{shear} | 20 s ⁻¹ |
| Consolidation constant | c | 0.001 s ⁻¹ |
| Minimum porosity | ϵ_{min} | 0.1 |
| Volume of smallest excipient bin | $s_{1,1}$ | $2 \times 10^{-13} \text{ m}^3$ |
| Volume of smallest API bin | $s_{2,1}$ | $2 \times 10^{-13} \text{ m}^3$ |
| Volume of smallest liquid binder bin | l_1 | $1 \times 10^{-13} \text{ m}^3$ |
| Number of bins | $(i, j, k)_{max}$ | (8, 8, 8) |
| Time step | Δt | 0.01 s |

The geometry of the granulator was defined to be consistent with the EuroLab 16mm

twin screw granulator (L:D of 40:1) located at the Purdue University National Science Foundation (NSF) Engineering Research Center for Structured Organic Particulates (ERC-SOPs) facility. A diagram of this geometry is presented in Figure 3.1. This approach can also be used for high shear or fluidized bed granulation, and differences between the granulator types appear in input parameters such as particle velocity profiles, shear rates, and granulator geometry.

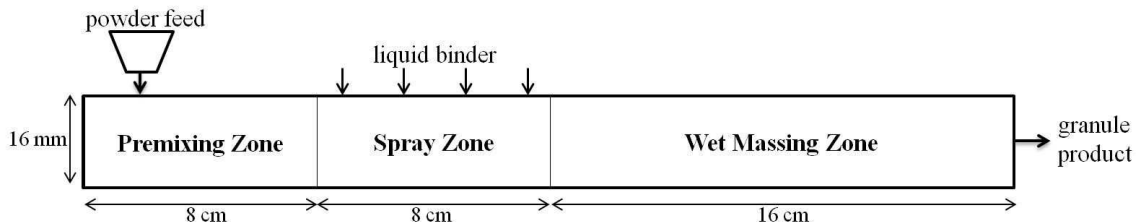


Figure 3.1: Continuous granulator with three zones.

To determine the particle velocities, the PBM can be coupled with discrete element modeling (DEM) (Sen and Ramachandran, 2013). For this study, an average axial velocity was assumed based on experimentally observed residence times in the granulator (El Hagrasy et al., 2013). A normal distribution of random numbers was used to vary this velocity at each time point and position. The average values and standard deviations are given in Table 3.2. Future work is needed to better understand the particle velocity profiles inside the granulator either via particle velocimetry or DEM studies.

3.2.2 Rate processes

Liquid addition

In continuous wet granulation, liquid binder is sprayed on dry particles within the spray zone, as shown in Figure 3.1. Liquid is added at a constant rate of \dot{V}_{spray} , and as the particles pass through the spray zone, their liquid content increases, resulting in higher aggregation rates. The expression for the liquid addition term is given in Equation 3.8.

$$\frac{dl}{dt} = \frac{\dot{V}_{spray}}{\int_{y_1}^{y_2} \int_{x_1}^{x_2} \int_0^{\infty} \int_0^{\infty} F(s_1, s_2, l, x, y, t) ds_1 ds_2 dl dx dy} \quad (3.8)$$

$\frac{dl}{dt}$ is the volumetric rate of liquid addition per particle, which was assumed to be equal for all particles within the spray zone, and $F(s_1, s_2, l, x, y, t)$ is the full distribution of particles with respect to API, excipient, and liquid volume as well as the spatial position. The liquid spray rate is described by a liquid-to-solid ratio, where $L : S = \rho \dot{V}_{spray} / \dot{m}_{in}$. In these simulations, the sprayer is turned on shortly after the process begins so that some particles reach the spray zone before liquid is added. Aggregation and breakage rates of wet granules were considered negligible prior to the start of liquid addition, due to the absence of liquid binder.

The spatial limits of integration (x_1 , x_2 , y_1 , and y_2) describe the axial and radial boundaries of the spray zone. While the axial boundaries are defined by the position of the sprayer, the radial boundaries depend on how well the liquid is distributed throughout the powder. For continuous twin screw granulation, Dhenge et al. (2013) found that low viscosity liquids are distributed more uniformly than high viscosity liquids. El Hagrasy et al. (2013) demonstrated the need to improve liquid distribution in twin screw granulation and showed that poor liquid binder distribution resulted in wide granule size distributions. To investigate this issue, two cases are modeled. The first case assumes that the liquid is evenly distributed in the radial direction, and the interval from y_1 to y_2 encompasses all radial bins. The second case simulates poor liquid binder distribution, such that only one radial bin receives liquid. The liquid spreads to the other bins through radial movement of particles.

The values used for the spray rate, the time at which spray is added (t_{spray}), and the spray zone for both cases are included in Table 3.2. Since the liquid addition rate depends on the number of particles in each bin, it is recalculated at each time step.

Aggregation

In the aggregation process, two particles collide and merge to form one larger particle. The rate of aggregation depends on the number of particles and their properties. As shown in Equation 3.9, the net aggregation rate can be broken into formation and depletion rates.

$$\mathfrak{R}_{agg}(s_1, s_2, l, t) = \mathfrak{R}_{agg}^{form}(s_1, s_2, l, t) - \mathfrak{R}_{agg}^{dep}(s_1, s_2, l, t) \quad (3.9)$$

These rates are determined using the particle distribution function F and a semi-empirical aggregation kernel β and are defined in Equations 3.10 and 3.11.

$$\begin{aligned} \mathfrak{R}_{agg}^{form}(s_1, s_2, l, t) &= \frac{1}{2} \int_0^{s_1} \int_0^{s_2} \int_0^l \beta(s_1 - s'_1, s_2 - s'_2, l - l', s'_1, s'_2, l') \\ &\times F(s_1 - s'_1, s_2 - s'_2, l - l', t) F(s'_1, s'_2, l', t) dl' ds'_2 ds'_1 \end{aligned} \quad (3.10)$$

$$\begin{aligned} \mathfrak{R}_{agg}^{dep}(s_1, s_2, l, t) &= \\ F(s_1, s_2, l, t) \int_0^\infty \int_0^\infty \int_0^\infty &\beta(s_1, s_2, l, s'_1, s'_2, l') F(s'_1, s'_2, l', t) dl ds'_2 ds'_1 \end{aligned} \quad (3.11)$$

The aggregation kernel takes particle properties into account. For example, a high liquid binder content is known to increase the aggregation rate. A variety of aggregation kernels are available in the literature (Cameron et al., 2005). Shown in Equation 3.12, the aggregation kernel presented by Madec et al. (2003) was selected because of its liquid content and size dependencies.

$$\beta(s_1, s_2, l, s'_1, s'_2, l') = \beta_0(V + V') \left((l_s + l'_s)^\alpha \left(100 - \frac{l_s + l'_s}{2} \right)^\delta \right)^\alpha \quad (3.12)$$

The two colliding particles are described by the internal coordinates (s_1, s_2, l) and (s'_1, s'_2, l') , and V and l_s represent their respective volumes and liquid contents. Selected values for the three adjustable parameters, β_0 , α , and δ , are given in Table 3.2.

This kernel does not account for interactions between the two solid components, which can be attractive or repulsive. Because the product composition distribution is a key quality attribute of this process, a composition dependent aggregation kernel is desired to simulate these interactions. To modify a size-dependent aggregation kernel, a composition-dependent multiplicative factor was proposed by Matsoukas et al. (Matsoukas et al., 2009), as given by Equation 3.13.

$$\psi(s_1, s_2, s'_1, s'_2) = \exp(-a_{ab}(x + x' - 2xx')) \quad (3.13)$$

The adjustable interaction parameter a_{ab} describes the attraction or repulsion of the two components. If a_{ab} is greater than zero, the solid components are repulsive, and if a_{ab} is less than zero, they are attractive (Matsoukas et al., 2009). This factor was used with the size-

and liquid content-dependent aggregation kernel (Equation 3.12) to introduce composition dependence, resulting in the overall aggregation kernel shown in Equation 3.14.

$$\beta(s_1, s_2, l, s'_1, s'_2, l') = \beta_0(V + V') \left((l_s + l'_s)^\alpha \left(100 - \frac{l_s + l'_s}{2} \right)^\delta \right)^\alpha \times \exp(-a_{ab}(x + x' - 2xx')) \quad (3.14)$$

Breakage

When particles are subject to impact or attrition, they can break into two or more fragments. Like the aggregation rate, the breakage rate can be broken into formation and depletion terms, as shown in Equation 3.15. The formation rate of smaller fragments, $\mathfrak{R}_{break}^{dep}$, and the depletion rate of larger granules, $\mathfrak{R}_{break}^{form}$, are presented in Equations 3.16-3.17.

$$\mathfrak{R}_{break}(s_1, s_2, l, t) = \mathfrak{R}_{break}^{form}(s_1, s_2, l, t) - \mathfrak{R}_{break}^{dep}(s_1, s_2, l, t) \quad (3.15)$$

$$\mathfrak{R}_{break}^{form}(s_1, s_2, l, t) = \int_0^\infty \int_0^\infty \int_0^\infty K_{break}(s'_1, s'_2, l') b(s'_1, s'_2, l', s_1, s_2, l) F(s'_1, s'_2, l', t) dl' ds'_2 ds'_1 \quad (3.16)$$

$$\mathfrak{R}_{break}^{dep}(s_1, s_2, l, t) = K_{break}(s_1, s_2, l) F(s_1, s_2, l, t) \quad (3.17)$$

The breakage kernel, K_{break} , describes the likelihood of breakage for a parent particle, and the probability distribution function, b , determines the size of the resulting fragments.

A semi-empirical breakage kernel was used, as shown in Equation 3.18 (Pandya and Spielman, 1983).

$$K_{break}(s_1, s_2, l) = \frac{P_1 G_{shear} d^{P_2}}{2} \quad (3.18)$$

This kernel is dependent on the diameter of the parent particle, d , as a larger particle is more likely to break than a smaller one. It is also dependent on the shear rate, G_{shear} . The shear rate can vary throughout a continuous granulator, particularly in a twin-screw granulator that includes various screw elements. For this study, a constant and uniform shear rate was used, given in Table 3.2. Further research is needed to model the shear rate distribution more accurately. P_1 and P_2 are adjustable constants whose values are also

provided in Table 3.2.

In this study, it was assumed that all breakage events result in two fragments. The probability distribution is given by Equation 3.19.

$$b(s'_1, s'_2, l', s_1, s_2, l) = \frac{1}{(i-1)(j-1)(k-1)} \text{ for } (s_1, s_2, l) < (s'_1, s'_2, l') \quad (3.19)$$

The indices i , j , and k represent the parent particle bin numbers of each solid component and the liquid binder, respectively. This distribution assumes the fragment particles have an equal likelihood of forming in each bin smaller than the parent particle.

Consolidation

As the particles are compacted, consolidation occurs and the volume of gas contained within the particles decreases. The rate of consolidation is described by Equation 3.20, which is consistent with an exponential decrease of porosity (Verkoeijen et al., 2002).

$$\frac{dg}{dt} = -c \frac{(s_1 + s_2 + l + g)(1 - \epsilon_{min})}{s_1 + s_2} \left[l - \frac{\epsilon_{min}(s_1 + s_2)}{1 - \epsilon_{min}} + g \right] \quad (3.20)$$

The minimum granule porosity, ϵ_{min} , and the consolidation rate constant, c , are given in Table 3.2 based on the work of Immanuel and Doyle III (Immanuel and Doyle III, 2005).

3.2.3 Discretization and numerical techniques

To solve the population balance equation numerically, a finite difference method was used. The spatial and internal dimensions were discretized, creating a system of ordinary differential equations. The granulator was divided into discrete spatial bins, using eight evenly-spaced axial bins, covering the three zones, and four evenly-spaced radial bins. A non-linear grid was used for the internal coordinates in order to accommodate particles of large sizes with a minimal number of bins. These grids are described by Equations 3.21-3.23.

$$s_{1,i} = s_{1,1} \times 3^{i-1} \quad (3.21)$$

$$s_{2,j} = s_{2,1} \times 3^{j-1} \quad (3.22)$$

$$l_k = l_1 \times 3^{k-1} \quad (3.23)$$

In these equations, i , j , and k represent the indices of the first solid component, second solid component, and liquid bins, respectively, and $s_{1,i}$, $s_{2,j}$, and l_k represent the corresponding volumes of each component per particle. The volume of the smallest bin, $(s_{1,1}, s_{2,1}, l_1)$, and the number of bins can be found in Table 3.2. The inlet population density was distributed over two internal bins, $(1, 2, 1)$ and $(2, 1, 1)$, to simulate particles of two different solid compositions, such as an API and an excipient. Because the volumes of each component in the first bin are nonzero, the feed particles are not represented as pure components. The lumped parameter, the gas volume, does not require discretization. The inlet gas volume per particle is also provided in Table 3.2.

Because a nonlinear grid was used, aggregating or breaking particles can have volumes that lie between bins. The cell average method was used to allocate these particles into the surrounding bins, as demonstrated by Kumar et al. (2006) for the 1-D case and by Chaudhury et al. (2013a) for multi-dimensional cases. This method conserves the volume of all components.

The system of equations was integrated numerically using first-order Euler integration. Since an explicit integration technique was used, the Courant-Friedrichs-Lewis (CFL) condition must be satisfied for numerical stability (Ramachandran and Barton, 2010). The CFL condition states that the time step must have a maximum value above which the solution will be inaccurate. In this case, the time step must be less than the time required for particles to travel to adjacent grid points. The selected time step is given in Table 3.2.

These computations were performed using MATLAB on an Intel Core i7-2600 CPU processor (3.4 GHz) with 16 GB of RAM.

3.3 Results and discussion

3.3.1 Validation of numerical methods

Several techniques were used to demonstrate the effectiveness of the numerical methods. First, the simulations demonstrated conservation of API, excipient, and liquid binder, as

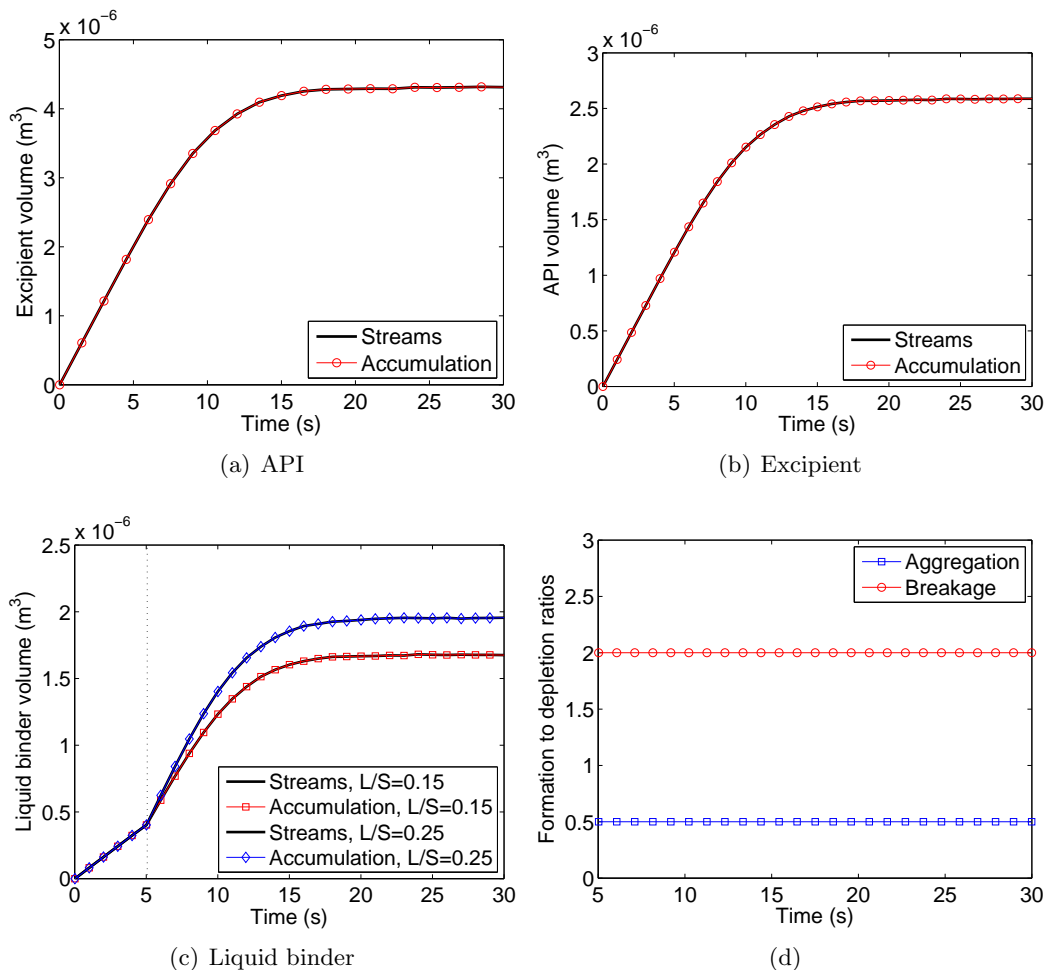


Figure 3.2: (a)-(c) Total volume of each component within the granulator over time, calculated from the inlet and outlet streams and the distribution of particles accumulated within the granulator for the baseline case with heterogeneous liquid distribution. The vertical dotted line indicates the time at which spraying begins. (d) Ratios of formation to depletion for aggregation and breakage for the baseline case with heterogeneous liquid distribution.

shown in Figure 3.2 for the baseline case. The streams curves are the net volume of material transferred from the inlet and outlet streams to the granulator, and the accumulation curves represent the total volume of material within the granulator, based on the particle distributions. The streams and accumulation curves are consistent, demonstrating that the volumes of these components are conserved.

Additionally, the ratios of birth to depletion for aggregation and breakage must be consistent with the assumptions in the problem, which stated that two particles aggregate to form one larger particle during aggregation, and each fracturing particle forms two particles.

As shown in Figure 3.2(d), the ratios of birth to depletion for aggregation and breakage are 0.5 and 2, respectively.

First-order explicit Euler integration was used to solve this system of ordinary differential equations. This integration technique requires only one function evaluation at each time step, whereas multistep, adaptive, and implicit methods require multiple function evaluations or iterations at each time step. An explicit, second-order Runge-Kutte method (RK2) was used to solve the baseline case for comparison with Euler integration. At the selected time step size, Euler integration produced nearly the same results as RK2, demonstrating sufficient accuracy. Figure 3.3(a) shows the number of particles in three specific bins over time using Euler and RK2 integration. Euler integration solved the problem 50.03% more quickly than RK2 integration. Therefore, the Euler integration method was utilized in this study.

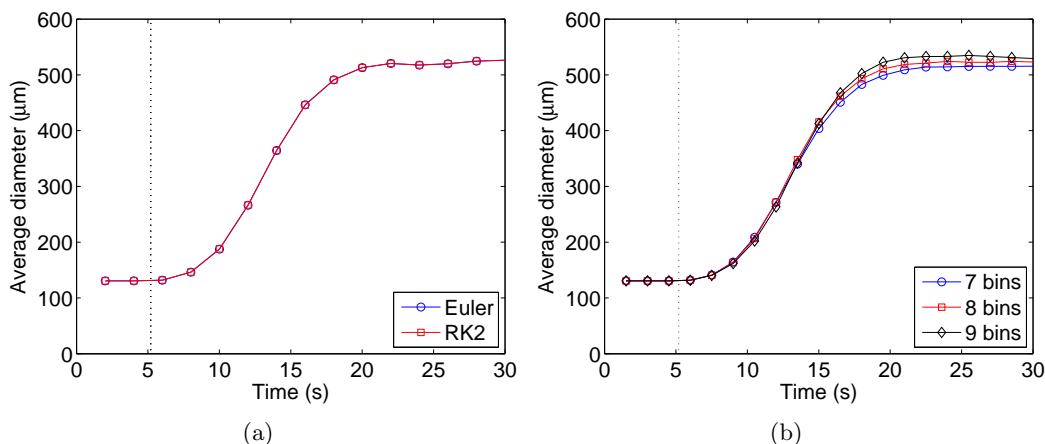


Figure 3.3: Average diameter at the outlet vs. time (a) using different integration techniques and (b) for the baseline case with poor liquid distribution, with varying grid sizes. The vertical dotted line indicates the time at which spraying begins.

Finally, the grid independence of the model was investigated. Keeping the upper and lower bounds constant, the grid size was varied by changing the base value in Equations 3.21-3.23. Plots of the steady-state particle size distribution with various grid sizes are shown in Figure 3.3(b). A marginal difference was observed, with a difference of approximately 1.2% between the steady-state diameters predicted using 8 and 9 bins. More accurate results are expected when using a finer grid width and smaller time step. However, this can drastically

increase computation time.

3.3.2 Parametric study

A parametric study was performed to evaluate the effects of material, process, and design parameters, including the liquid binder distribution, liquid-to-solids ratio, spray zone position and granulator lengths, particle velocities, and API-excipient interactions. In all simulations, the average product particle size increased over time before reaching a steady state. The start-up behavior and steady-state particle size distributions were analyzed, in addition to two-dimensional distributions, such as size and composition. The simulations also showed the granule properties at each position within the granulator. Finally, a pulse change in the powder feed was simulated to analyze the residence time distribution (RTD) for each simulation.

Liquid binder distribution

Two cases for the liquid binder distribution were simulated. In the homogeneous case, the binder was sprayed uniformly on all particles within the spray zone. For the heterogeneous case, liquid binder only reached particles in the highest radial bin, or the top 25% of the granulator. The liquid binder was transferred to other locations and particles through radial movement and aggregation. The same total liquid volume and spray rate was used in each case.

Figure 3.4 shows the average product diameter over time for each case. At steady state, the homogeneous case produced slightly larger granules than the heterogeneous case, with average diameters of 548 μm and 523 μm , respectively. Steady-state particle size distributions are given in Figure 3.4. The heterogeneous case shows a larger frequency of small particles than the homogeneous case. These results are as expected and can be explained by the aggregation rates. If the liquid is not distributed evenly, some particles remain dry and are less likely to aggregate, represented in the model by the liquid-dependent aggregation kernel. The liquid content particle distributions support this explanation, as shown in Figure 3.4.

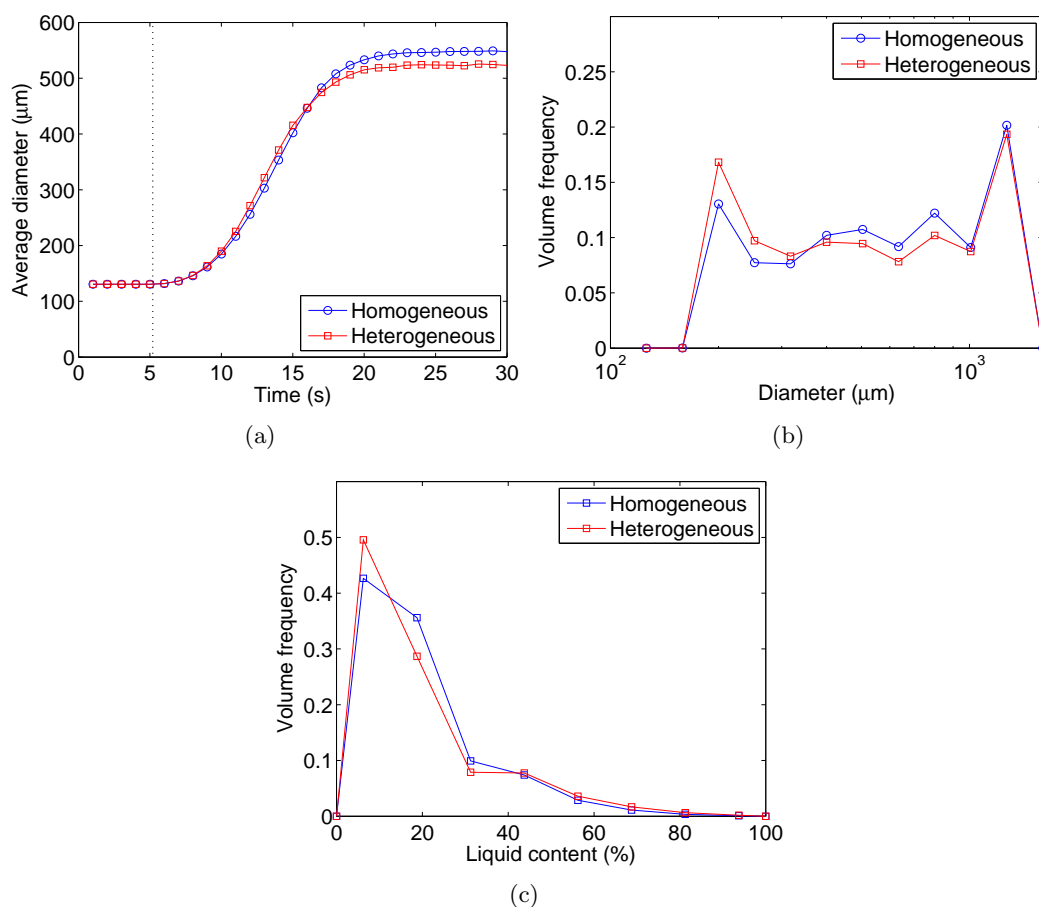


Figure 3.4: (a) Average diameter at the outlet vs. time (b) steady-state particle size distributions at the outlet and (c) steady-state liquid content distribution at the end of the spray zone for the baseline case with both liquid distribution models. The vertical dotted line indicates the time at which spraying begins.

In Figure 3.5, contour plots of size and liquid content versus position within the granulator show that the homogeneous case resembles a plug flow process, while the heterogeneous case has strong variations in both size and liquid content with radial position. In the heterogeneous case, the particles located near the sprayer collect most of the liquid and grow faster than particles located far from the sprayer. Further, the physical separation between the wet and dry particles contributes to the size difference. For the heterogeneous case, the dry particles are near other dry particles, resulting in very low aggregation rates and slow growth. When the liquid distribution is homogeneous, a dry particle can aggregate with a nearby wet particle, and this interaction has a higher aggregation rate than the interaction between two dry particles.

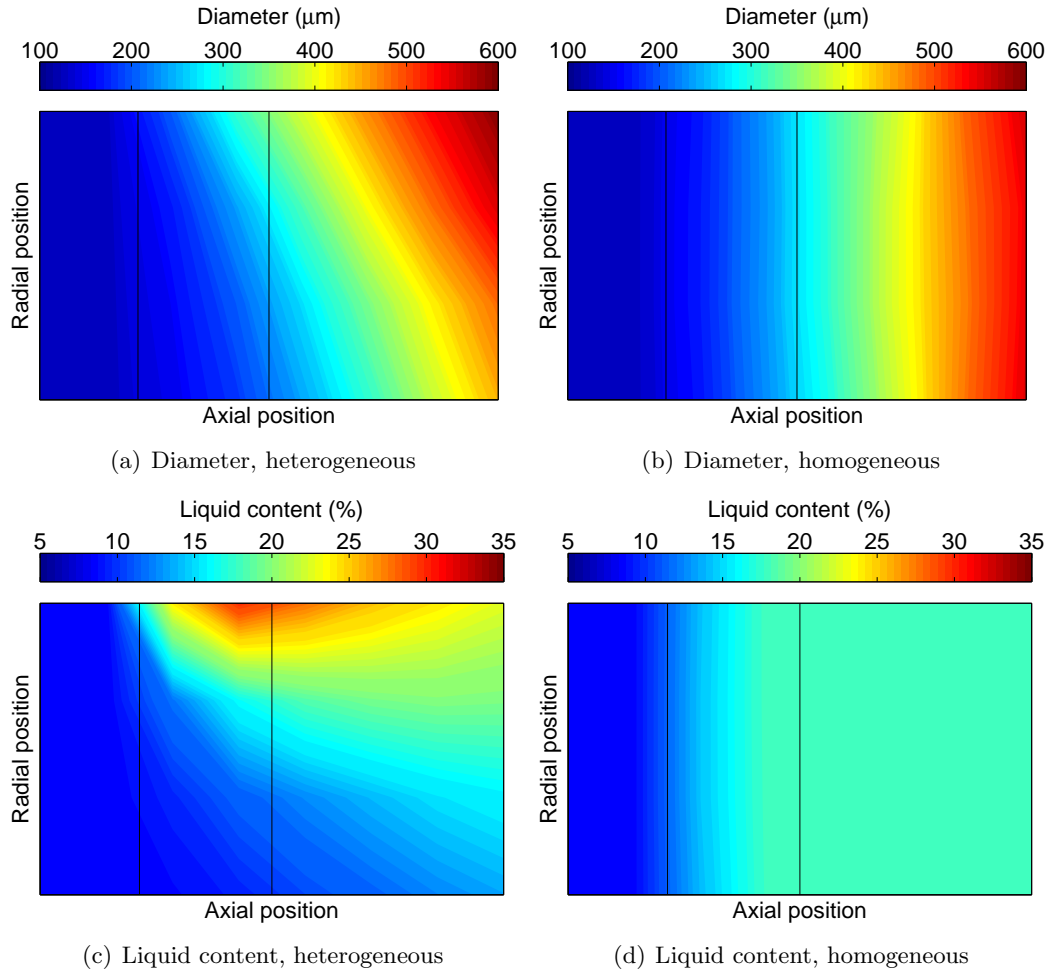


Figure 3.5: Average diameter (a-b) and liquid content (c-d) versus position at steady state for the baseline case with heterogeneous and homogeneous liquid distributions. The vertical lines indicate the axial bounds of the spray zone.

Liquid-to-solids ratio

For both the homogeneous and heterogeneous cases, simulations were performed with varying liquid binder spray rate at three liquid-to-solid ratios: 0.05, 0.15 and 0.25. These ratios are typically used in experimental studies (El Hagrasy et al., 2013). Figure 3.6 shows the average diameter over time for each simulation. As expected, the simulations with a higher liquid spray rate produced larger granules. Because the aggregation rate is dependent on the liquid content, wetter particles aggregate more quickly. The steady-state average diameters at the highest liquid-to-solid ratio were $562 \mu\text{m}$ and $597 \mu\text{m}$, for the heterogeneous and homogeneous cases, respectively, compared with sizes of $472 \mu\text{m}$ and $482 \mu\text{m}$ for the

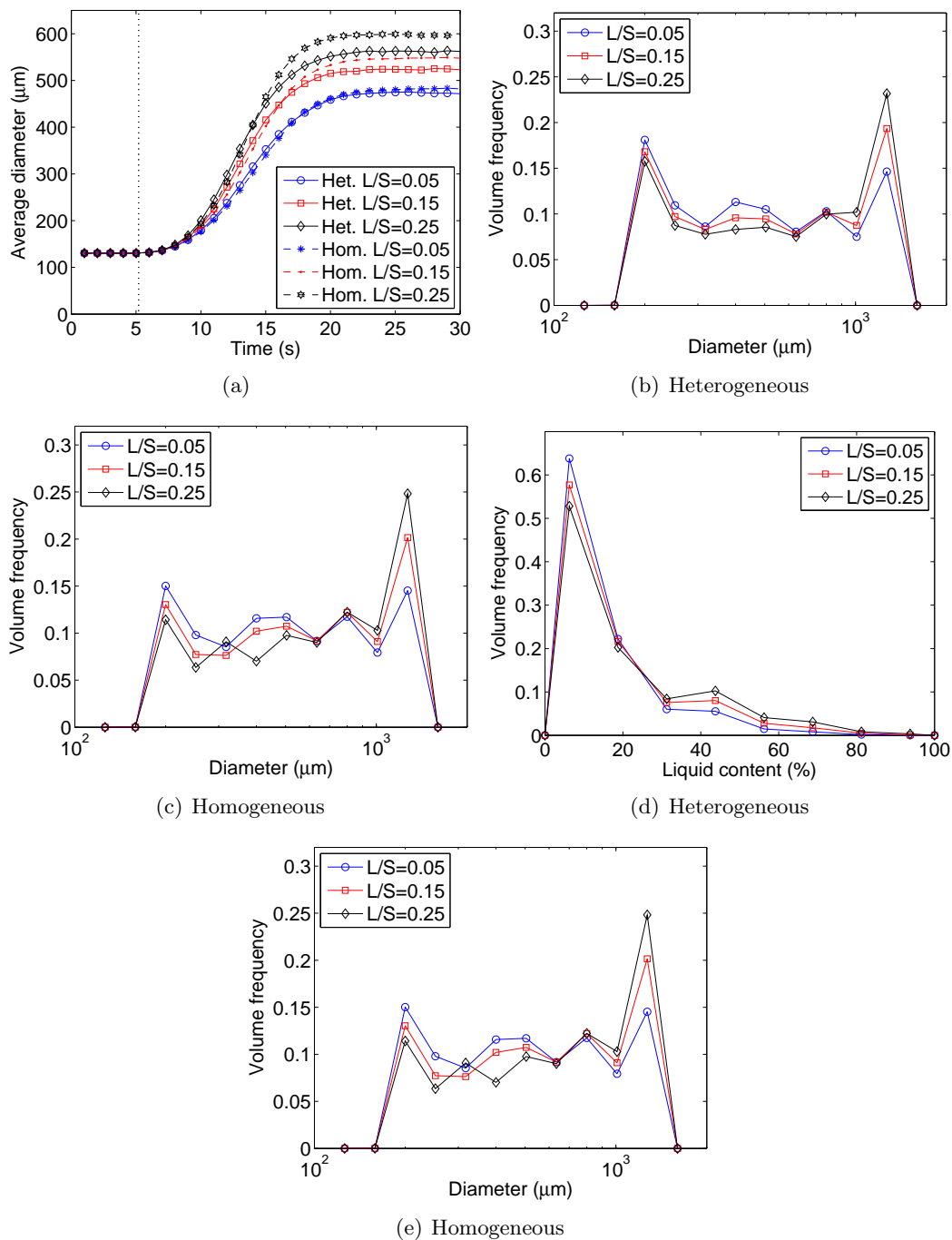


Figure 3.6: (a) Average diameter at the outlet vs. time for varying liquid-to-solid ratios, with a heterogeneous liquid distribution. The vertical dotted line indicates the time at which spraying begins. Steady-state (b-c) particle size and (d-e) liquid content distributions and for the baseline case with both liquid distribution models.

lowest liquid-to-solid ratio.

In all cases, the homogeneous liquid distribution produced a larger average diameter than the heterogeneous liquid distribution because in the heterogeneous case, some particles remained dry and were less likely to aggregate. This difference increased with increasing liquid-to-solid ratio, which can be attributed to the bimodal liquid content distribution observed for the heterogeneous case, shown in Figure 3.6. As the liquid-to-solid ratio increased, the difference in liquid content between the wet and dry particles was greater, resulting in a larger difference between the two liquid distribution cases.

Spray zone

In addition to the spray rate, the length of the spray zone was also varied to simulate configurations with multiple sprayers, representing different process design options. Spray zone lengths of 4, 8, and 12 cm were simulated. The overall length of the granulator was held constant, as was the total spray rate. The length of the wet massing zone varied to accommodate these changes.

As seen in Figure 3.7, a broader spray zone corresponded to smaller granules. The same total amount of liquid was added for each spray zone length. When the spray zone was small, the particles received the same amount of liquid more quickly, and when the spray zone was large, the liquid addition was spread across a larger region of particles. The sudden increase in liquid content that occurred in the 4-cm spray zone resulted in a rapid increase in diameter due to aggregation, while the size increase in the 12-cm spray zone was more gradual. Because the granulator with a 12-cm spray zone had a shorter wet massing zone, the granule size did not reach that of the 4-cm spray zone by the end of the granulator. In addition, the breakage rate was not substantial enough to mitigate the increase in diameter.

Granulator length

The effect of granulator length on the product was also observed to simulate another process design option. Three granulator lengths were simulated: 24, 32, and 40 cm. These changes

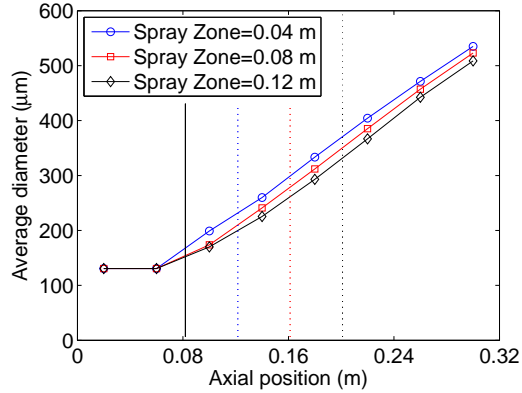


Figure 3.7: Steady-state average diameter vs. position with varying spray zone lengths. The solid vertical line indicates the beginning of the spray zone, and the dotted vertical lines represent the ends of the spray zone for each length.

were performed by varying the length of the wet massing zone, while keeping the lengths of the premixing and spray zones constant.

For these simulations, the residence time distribution (RTD) was evaluated. The RTD is important for blend homogeneity and compression characteristics. A longer residence time typically results in more consolidation and denser particles. Additionally, a narrower RTD could result in the granules being too porous hence resulting in tablets that are too hard because granules of low bulk density have a lower resistance to deformation during compression (Vercruyssen et al., 2012). Therefore, RTD is an important characteristic to optimize. The residence time distribution was determined by simulating a pulse change in inlet composition after the process has reached a steady state. The initial inlet solid composition (x_0) was changed to a new composition (x_{pulse}) for one second by changing the fraction of feed particles in bin (1, 2, 1) from 0.25 to 1. The outlet composition (x_{out}) was recorded over time to calculate the exit age distribution, as shown in Equation 3.24.

$$E(t) = \frac{x_{out} - x_0}{\int_0^{\infty} x_{out} - x_0 dt} \quad (3.24)$$

The mean residence time (\bar{t}) was determined according to Equation 3.25.

$$\bar{t} = \int_0^{\infty} tE(t)dt \quad (3.25)$$

As shown in Figure 3.8, a higher granulator length corresponded with a longer residence time. The mean residence times for granulators of length 24, 32, and 40 cm were 8.53 s, 11.2 s, and 13.9 s, respectively. Because of the greater residence time, longer granulators produced larger granules. Figure 3.8 shows the particle size distributions at steady state with different granulator lengths, as well as the particle size distributions at the inlet and at the end of the spray zone. These distributions show some size enlargement in the spray zone, with bimodal distributions within the wet massing zone. While some larger particles form in the spray zone, most of the agglomeration seems to occur within the wet massing zone.

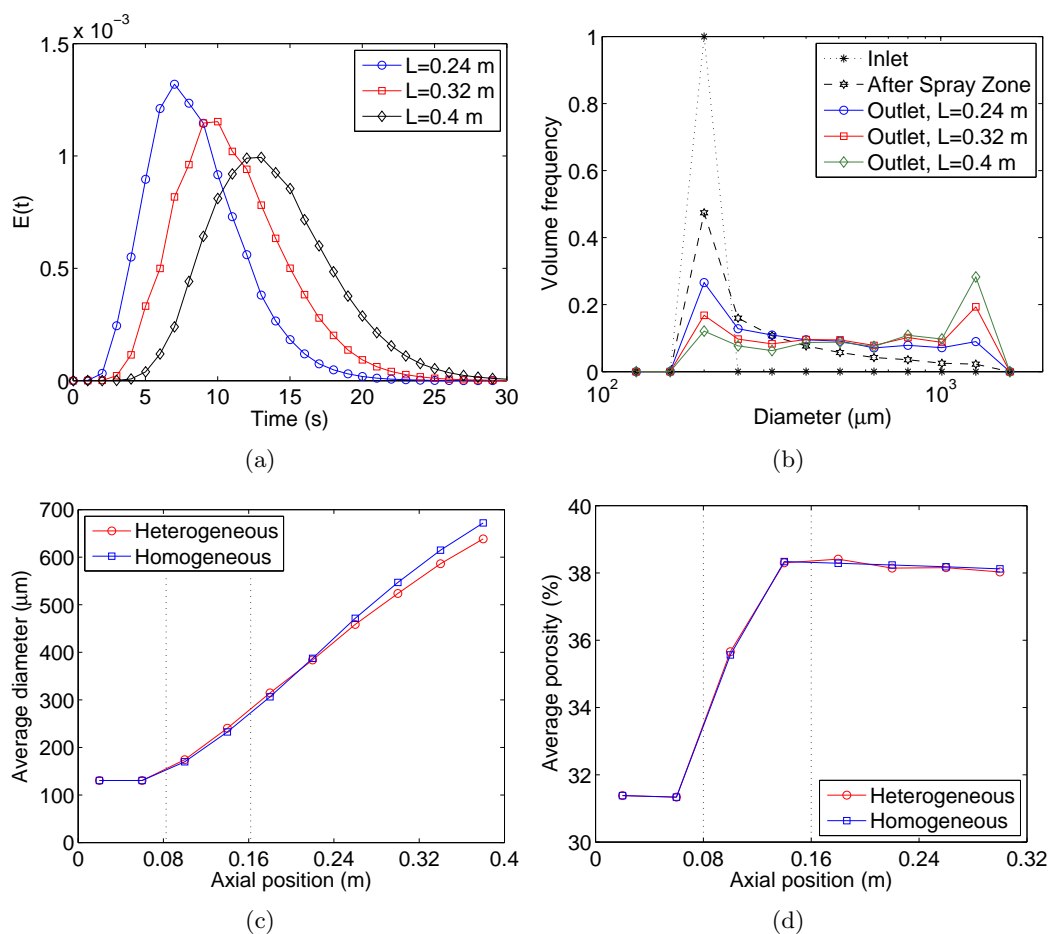


Figure 3.8: (a) Residence time distributions for varying lengths. (b) Steady-state particle size distributions for varying lengths at the inlet, after the spray zone, and at the outlet. (c) Average diameter and (d) average porosity vs. axial position. The vertical lines indicate the axial bounds of the spray zone.

Additionally, greater length corresponds to a larger average diameter. This relationship is shown in Figure 3.8. While the case with heterogeneous liquid distribution shows a larger average diameter within the spray zone, the homogeneous case shows a larger average diameter at the outlet. This result can be attributed to a higher amount of dry, fine particles that do not participate in aggregation for the heterogeneous case. A plot of porosity versus position in Figure 3.8 shows that the average porosity decreases in the premixing and wet massing zones, and increases in the spray zone. Because the porosity includes the liquid volume, an increase in liquid content results in an increased porosity. The average product porosity decreases with increased length because more consolidation occurs in the wet massing zone, due to the presence of residual liquid and minimal breakage and consolidation.

Particle velocities

The axial particle velocities were varied to simulate different screw speeds, an important process parameter. The baseline axial velocity was taken from the average residence time observed experimentally at a screw speed of 400 RPM (El Hagrasy et al., 2013). By varying the radial velocity, different degrees of radial mixing are simulated. The particle velocity profiles are unknown, and a simple velocity model was assumed for this study. DEM simulations can be performed to better understand particle velocity profiles (Gantt and Gatzke, 2005; Gantt et al., 2006; Portillo et al., 2007). Future work will involve coupling DEM results with this model.

The values used for the axial velocity were 0.015, 0.03, and 0.045 m/s . The axial velocity was found to have a large effect on the product diameter, as shown in Figure 3.9. A smaller axial velocity corresponded to a larger average particle size. This effect can be attributed to the larger residence time of slower-moving particles, also shown in 3.9. The evolution of granule size throughout the length of the granulator was affected by the velocity, also shown in Figure 3.9. At higher velocities, the average diameter increases slightly in the spray zone, and more significantly in the wet massing zone. At lower velocities, the granule size increases more drastically in the spray zone, and at a lower rate in the wet massing

zone, approaching a maximum value. Breakage rates are also reduced. Since there was

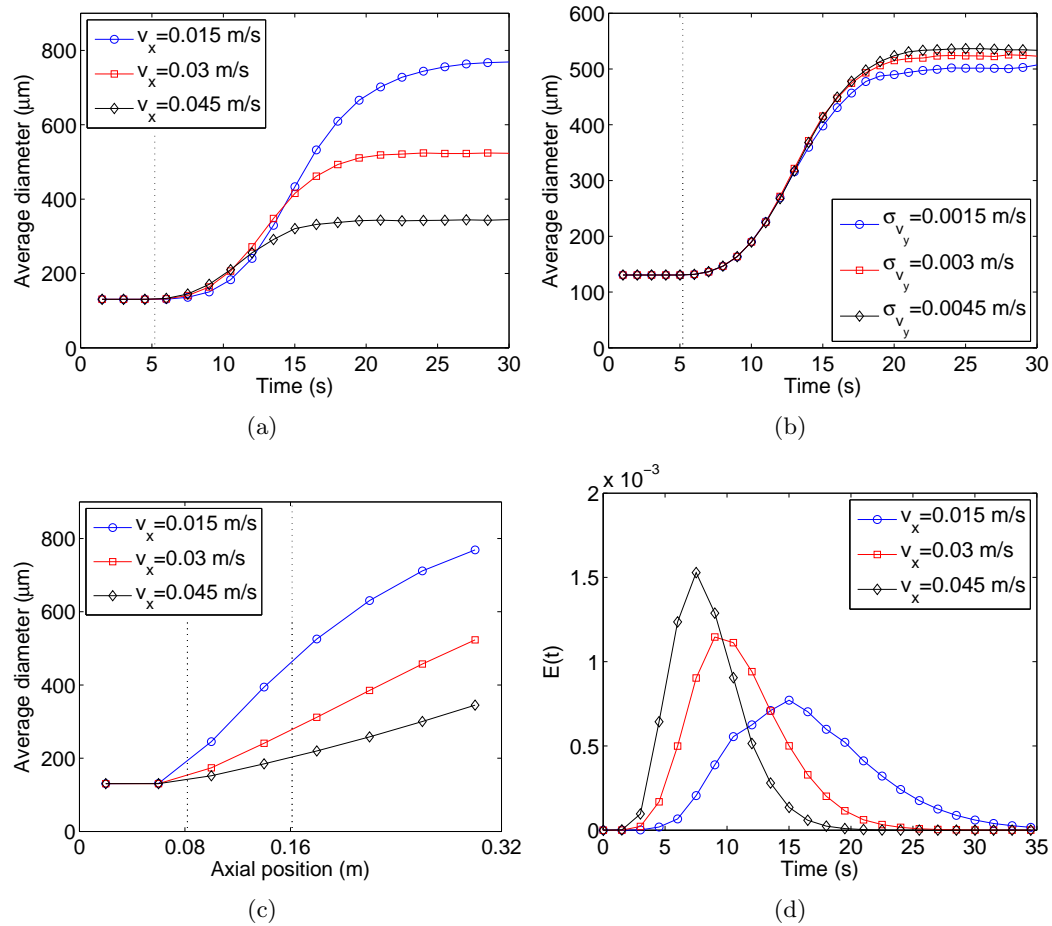


Figure 3.9: Average diameter at the outlet vs. time for varying (a) axial and (b) radial velocities with heterogeneous liquid distribution, where vertical lines indicate the time at which spraying begins. (c) Average diameter vs. axial position for varying axial velocities, where vertical lines represent the axial bounds of the spray zone. (d) Residence time distributions for varying axial velocities.

no net flux in the radial direction, the radial velocity was varied by changing the standard deviation of the randomly generated radial velocity. Values of 0.0015, 0.003, and 0.0045 m/s were selected. As shown in Figure 3.9, the heterogeneous simulations with a smaller radial velocity resulted in smaller granules. When the radial velocity is high, there is a large amount of mixing between bins along the radial axis, spreading the liquid binder throughout the granulator more evenly.

API-excipient interaction

To represent multi-component granulation, interactions between the API and excipient particles were taken into account. Repulsion between the API and excipient can cause segregation and inhomogeneous granule composition, which can affect the final product. By varying the parameter a_{ab} in the aggregation kernel with values of -2 and 2, attractive and repulsive interactions were simulated. In the baseline case, no interaction was assumed, and this parameter was equal to zero. The aggregation coefficient β_0 was adjusted to yield the same aggregation rate for the initial powder particles with particles of the same type across the three cases. In practice, the interaction parameter would be evaluated experimentally for the specific API and excipient in question.

As expected, Figure 3.10 shows that the average diameter is smaller when the components are repulsive and larger when they are attractive. The aggregation rates between dissimilar particles is greater for attractive interactions than repulsive interactions. As a result, attractive interactions between the API and excipient result in larger particles with more uniform compositions. Further, distributions in composition, presented in Figure 3.10 show that the case involving attraction produces more granules with even compositions, while the repulsive case has a slightly larger fraction of purer particles, at the extreme ends of composition. In the case with no interaction, two peaks are still present, indicating that some of the API and excipient particles remain segregated as particles, though they are spatially mixed. Due to the short residence time in the granulator, some of the primary particles did not aggregate significantly, and remained in the product stream as fine API or excipient particles.

3.3.3 Comparison with experimental trends

The simulated bulk and distributed profiles are consistent with experimental results for twin screw granulation. Similar to the model results, Keleb et al. (2004) and El Hagrasy et al. (2013) observed bimodal particle size distributions. Further, Keleb et al. (2004) found that an increase in screw speed resulted in a decrease in granule yield. The model demonstrates that an increase in axial velocity decreases the residence time, resulting in a larger fraction

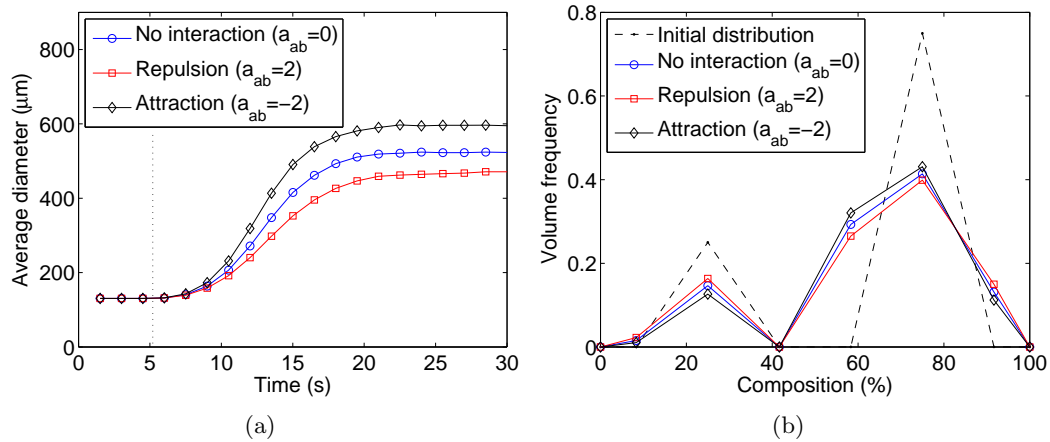


Figure 3.10: (a) Average diameter over time with varying API-excipient interactions and (b) steady-state compositional distributions. The vertical dotted line indicates the time at which spraying begins.

of unaggregated fines.

Dhenge et al. (2010) and El Hagrasy et al. (2013) demonstrated a correlation between the liquid-to-solid ratio and granule size. Larger granules form at higher liquid-to-solid ratios, consistent with the liquid-dependent aggregation kernel implemented in the model. Figure 3.11 shows the size distributions observed experimentally by El Hagrasy et al. (2013) at different liquid-to-solid ratios. They found a reduced fraction of powder fines at high liquid-to-solid ratios, as well as a wider size distribution. While our simulated results show a wide size distribution at high liquid-to-solid ratios, the fraction of fines decreases, and the peak within the granule size range becomes more prominent, as shown in Figure 3.6.

El Hagrasy et al. (2013) found that some very large granules were produced, even at low liquid-to-solid ratios. They attribute this observation to the kneading blocks of the screws, which were unable to adequately distribute the liquid binder. Similarly, in the simulations, poor liquid distribution resulted in wide size distributions, with some very large particles and a high fraction of fines.

In order to establish a more quantitatively accurate model, a more detailed understanding of the flow behavior of the granules must be developed. It was observed that the particle velocities and distribution of the liquid binder have large effects on the granule size distributions. Additionally, semi-empirical rate kernels were implemented, which contain

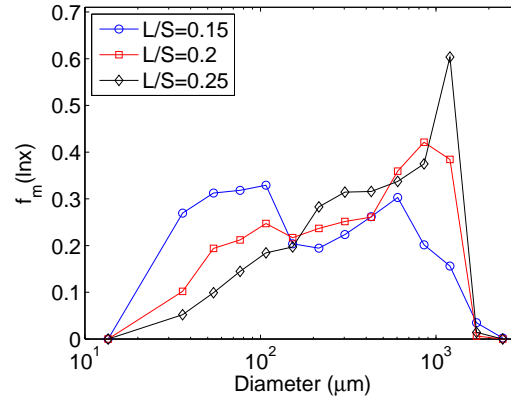


Figure 3.11: Experimentally observed granule size distributions using pharmatose 200M lactose in a twin screw granulator with varying liquid-to-solid ratios (El Hagrasy et al., 2013).

some adjustable parameters. These parameters can be estimated using experimental data to develop a more robust model.

The model provides additional insight into the experimental results, demonstrating variations in time and space. The particle size distribution can be predicted at each position, illustrating the effects of each zone. Multi-dimensional distributions can be modeled, enabling inhomogeneities in size, composition, and liquid distribution to be simulated.

3.4 Summary

Continuous granulation processes have potential advantages over batch processes in pharmaceutical manufacturing. Continuous granulation can be simulated using PBMs with spatial coordinates. These models are useful in process development, validation, and control.

For the first time, a developed model was able to simulate particle distributions in size, composition, liquid binder content, and evolution of porosity, taking into account the rate processes of aggregation, liquid addition, consolidation, and breakage. It also considers the interactions between multiple solid components and the incorporation of particle flux information.

The results show good agreement with experimental trends, such as the bimodal size distributions, the relationship between granule size and liquid spray rate, and the affects

of poor liquid distribution. For more quantitatively accurate predictions, a better understanding of the flow properties within the granulator is needed.

Additionally, future work will investigate the rate kernels and their adjustable constants. Parameter estimation using experimental data can be used to evaluate adjustable constants in the rate kernels. A variety of empirical rate kernels are used in the literature (Cameron et al., 2005), and mechanistic kernels have also been developed (Poon et al., 2008; Ramachandran et al., 2009). With substantial experimental data, these kernels can be compared and evaluated within the framework of this model.

There are various practical uses for a validated, accurate model of continuous granulation processes, particularly in pharmaceutical process design. As a part of the ERC-SOPs, a pilot plant for continuous tablet manufacturing is being assembled at Rutgers University. This approach has potential advantages over traditional batch methods in process control, efficiency, and cost. As continuous processing is investigated as an alternative to batch processes, the developed process model is useful in design and optimization, particularly to define a design space and implement QbD. In addition, these models can be used to develop model-based process control and optimization strategies.

Specific Aim II

Parameter estimation and population balance model validation using experimental data from a twin-screw granulator

The PBM provides a framework to track particles as they are subjected to various rate processes. Empirical or mechanistic rate expressions are needed to complete the PBM, often introducing unknown or adjustable parameters. Parameter estimation is required to calibrate the PBM and describe real process behavior.

The purposes of this aim are to:

- Demonstrate the effect of liquid-to-solid ratio on two critical quality attributes of the product: porosity and size distribution.
- Fit a PBM to experimental data by estimating unknown parameters in the rate expressions for aggregation, breakage, and consolidation.
- Use the calibrated model as a predictive tool and compare results to additional experimental data.
- Identify limitations of the model that can be solved with multi-scale modeling.

This work was originally published in:

Barrasso, D., El Hagrasy, A., Litster, J. D., Ramachandran, R., 2015a. Multi-dimensional population balance model development and validation for a twin screw granulation process. *Powder Technology* 270, Part B, 612 – 621

Chapter 4

Multi-dimensional population balance model development and validation for a twin-screw granulation process

In this study, a novel multi-component population balance model (PBM) for the twin-screw granulation (TSG) process was developed, taking into account the rate processes of aggregation, breakage, liquid addition, and consolidation. Interactions between multiple solid components (e.g. active pharmaceutical ingredient and excipient) and the amount of liquid were accounted for in quantifying the aggregation and breakage rates. Experimental data were obtained for the TSG process, whereby the effect of initial particle size distribution and liquid-to-solids ratios on key granule properties was studied. The data was used to estimate adjustable parameters in the proposed mechanistic kernels and to validate the calibrated process model as a predictive tool. The simulation results showed a good agreement with experimental data.

4.1 Background

Population balance models (PBM) can be used to track particle distributions as they evolve due to aggregation, breakage, and other rate processes. One-dimensional (1-D) PBMs are typically implemented, only considering variations in particle size. While these models are computationally inexpensive, they do not account for other particle properties, such as liquid content and porosity (Iveson, 2002). Particle liquid content strongly influences aggregation rates, and porosity is a CQA that affects the compactibility of the granules (Poon et al., 2008; Vercruyssen et al., 2012). A lumped-parameter approach was used to take advantage of the computation speed of 1-D PBMs while considering additional particle properties (Biggs et al., 2003; Barrasso and Ramachandran, 2012). Previously, a multi-dimensional PBM was used to model TSG, demonstrating the theoretical effects of various process parameters

(Barrasso et al., 2013b). This study used hypothetical values for unknown parameters within the model, qualitatively capturing experimental trends.

The ability to explain and predict experimental observations is of particular importance in the highly-regulated pharmaceutical industry. Few studies quantitatively relate PBMs to measured results. Parameter estimation has been performed by Ramachandran and Barton (2010), who used a multi-dimensional PBM to compare optimization techniques. In addition, Braumann et al. (2010) used response surface methodology to estimate rate parameters in a multi-dimensional model for batch granulation.

In this study, a two-dimensional (2-D) PBM for a continuous TSG process is presented to track particles size and liquid distributions along an axial coordinate, while taking into account the rate processes of aggregation, breakage, liquid addition, and consolidation, as well as powder flow. The lumped-parameter approach was used to track the liquid content and porosity of each particle size class.

Experimental data was collected to measure the effect of the liquid-to-solid ratio on the product size distribution and porosity. This data was used to estimate unknown rate parameters in the model. Parameter estimation was performed for two liquid-dependent aggregation kernels to compare their abilities to match the experimental trends. The calibrated model was used to predict additional data points, thus quantifying the predictive capability of the model.

Additionally, a three-dimensional (3-D) PBM is presented that accounts for an additional solid component, representing an active pharmaceutical ingredient (API). A composition-dependent term was added to the aggregation kernel to simulate attractive or repulsive effects between the excipient and API.

4.1.1 Objectives

The purposes of this study are to:

- Present a multi-dimensional PBM framework for continuous TSG processes.
- Calibrate and validate the model using experimental data.

- Use the model to predict additional experimental results.

4.2 Experimental methods

The experimental data was originally published in El Hagrasy et al. (2013), which provides additional details on the experimental set-up and analytical methods. Product size distributions and porosity data were collected from a continuously-operated TSG in order to validate the model. A Thermo Pharma 16 TSG, 40:1 L:D, Thermo Fisher Scientific, Karlsruhe, Germany, was used to produce the granules used in the study. The screw configuration of the granulator with the sequence of elements from the drive end was 3 spacer elements, 16 conveyer elements, 5 kneading elements, and 8 conveyer elements.

A formulation of Impalpable grade lactose (73.5%), Avicel PH101 (20%), hypromellose (5%), and Ac-Di-Sol (1.5%) was fed at a constant rate of 4 kg/hr. The screw speed was fixed at 400 rpm. Water was used as the binding liquid, and the liquid-to-solid ratio was varied from 0.15 to 0.35. Particle size analysis of the raw material was performed using laser light diffraction (Malvern Mastersizer 2000, Malvern Instruments, Westborough, MA), and this data was used as an input to the model.

The process was allowed to reach a steady state, and the granulated product was collected for analysis. Sieve analysis was used to measure the granule size distributions, with sieve trays from 45 μ m to 8 mm. The granule porosity of the 1-1.4 mm size class was measured using a GeoPyc Density Analyzer. The residence time was measured by feeding a pulse of dye to the TSG. Product samples were collected over time and analyzed by color. The arithmetic mean residence time of 9.9 seconds was used to estimate the average axial velocity within the granulator, and this value was used in the model.

4.3 Model development

As shown in Figure 4.1, the twin-screw granulator can be divided into three axial zones. In the first zone, dry particles are added, and mixing occurs, but the particles do not begin to aggregate. The second zone is the liquid addition zone, where liquid binder is added to the particles. Aggregation begins in this zone. The final zone is the wet massing

zone, where the wet particles continue to aggregate and consolidate. The wet massing zone consists of 5 kneading blocks followed by a length of screw conveyor (El Hagrasy et al., 2013). The lengths of the three zones were 8 cm, 8 cm and 16 cm, respectively. In order to model this granulator, a compartment approach was used, dividing the liquid addition and wet massing zones into three equally spaced regions. The premixing zone was neglected because the effects of this zone on the granule attributes were assumed to be negligible. It was assumed that the residence time in each of the three compartments was equal and constant. Future work will involve characterizing the size of the liquid distribution region using multi-scale modeling and experimental validation.

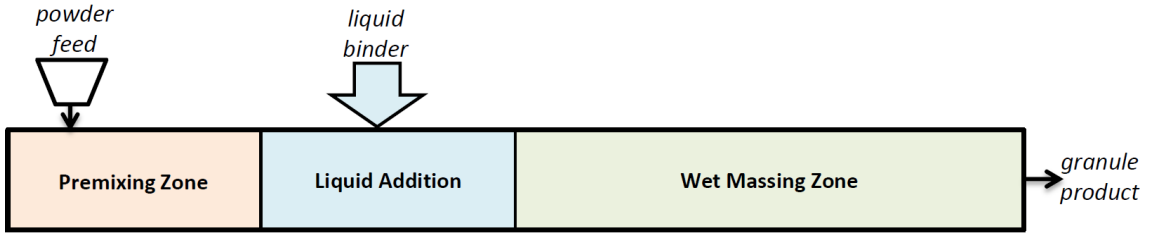


Figure 4.1: Three regions of the twin-screw granulator based on the experimental setup.

A dynamic, two-dimensional PBM was developed to represent twin screw granulation processes. As shown in Equation 4.1, the particle distribution was tracked at three locations within the granulator over time from start-up until a steady state was reached.

$$\frac{dF(s, z, t)}{dt} = \mathfrak{R}_{agg}(s, z, t) + \mathfrak{R}_{break}(s, z, t) + \dot{F}_{in}(s, z, t) - \dot{F}_{out}(s, z, t) \quad (4.1)$$

F represents the number of particles in each bin, and the bins were defined by the solid volume of each particle, s , and the spatial compartment, z . \mathfrak{R}_{agg} and \mathfrak{R}_{break} represent the net aggregation and breakage rates, respectively. The inlet and outlet flow rates for each compartment are given by \dot{F}_{in} , and \dot{F}_{out} .

Equation 4.1 alone only accounts for the amount of solid in the granule. However, other granule properties such as liquid content and porosity are known to have strong effects on aggregation and breakage rates. To simulate these properties, a lumped-parameter approach was used, making the assumption that all particles of the same solid content and position have the same porosity and liquid content (Biggs et al., 2003; Barrasso and Ramachandran,

2012). Equations 4.2 and 4.3 were developed to track the liquid and gas content of each bin in each compartment.

$$\begin{aligned} \frac{d}{dt} (F(s, z, t)l(s, z, t)) &= \mathfrak{R}_{liq,agg}(s, z, t) + \mathfrak{R}_{liq,break}(s, z, t) \\ + \dot{F}_{in}(s, z, t)l_{in}(s, z, t) - \dot{F}_{out}(s, z, t)l(s, z, t) + F(s, z, t)\dot{l}_{add}(s, z, t) \end{aligned} \quad (4.2)$$

$$\begin{aligned} \frac{d}{dt} (F(s, z, t)g(s, z, t)) &= \mathfrak{R}_{gas,agg}(s, z, t) + \mathfrak{R}_{gas,break}(s, z, t) \\ + \dot{F}_{in}(s, z, t)g_{in}(s, z, t) - \dot{F}_{out}(s, z, t)g(s, z, t) - F(s, z, t)\dot{g}_{cons}(s, z, t) \end{aligned} \quad (4.3)$$

The volumes of liquid and gas, per particle, are given by l and g , respectively. Similar to Equation 4.1, these equations account for axial flow between compartments, the inlet and outlet streams, aggregation and breakage. The net change in liquid and gas volumes due to aggregation and breakage are represented by $\mathfrak{R}_{liq,agg}$, $\mathfrak{R}_{liq,break}$, $\mathfrak{R}_{gas,agg}$, and $\mathfrak{R}_{gas,break}$. The lumped-parameter equations also account for the liquid added to the particles and consolidation. \dot{l}_{add} represents the volumetric rate of liquid addition, per particle, and \dot{g}_{cons} is the rate of consolidation.

The lumped-parameter approach was used because it combines the computational speed of a 1-D PBM with the ability to simulate multiple granules properties. By including the liquid and gas volumes as lumped parameters, additional granule properties can be evaluated and used in the main population balance. The total volume of each particle, V , and its diameter, d , are shown in Equations 4.4 and 4.5. It was assumed that all particles are spherical.

$$V(s, z, t) = s + l(s, z, t) + g(s, z, t) \quad (4.4)$$

$$d(s, z, t) = \left(\frac{6V(s, z, t)}{\pi} \right)^{1/3} \quad (4.5)$$

Furthermore, the average liquid content in each bin, LC , is given in Equation 4.6.

$$LC(s, z, t) = \frac{l(s, z, t)}{V(s, z, t)} \quad (4.6)$$

The porosity of each particle is given by ϵ , as shown in Equation 4.7.

$$\epsilon(s, z, t) = \frac{g(s, z, t) + l(s, z, t)}{V(s, z, t)} \quad (4.7)$$

The initial conditions were fixed such that the granulator was initially empty.

4.3.1 Spatial compartments and flow

There are two equivalent ways to represent the spatial behavior of particles in this model. The first states that the PBM is solved for three separate, well-mixed compartments, and transfer between the compartments is described based on the residence time of each compartment. The second representation states that the particles move along the axial dimension with a certain velocity, and the axial domain is discretized to solve the resulting PDE. Boundary conditions must be provided to describe transfer into and out of the system at the end points. If the forward difference method is used to solve the partial differential equation, the flow rate of particles at each discrete spatial coordinate is equal to the number of particles at that coordinate times the axial velocity divided by the distance between that coordinate and the subsequent coordinate. Assuming that the residence time is equal in each compartment or that the average axial velocity is constant along the length of the granulator, these two approaches are equivalent. The compartmentalization of the granulator or discretization of the spatial grid results in the same solution. For the purposes of this study, the model is presented using a three-compartment approach, though it must be emphasized that the spatial discretization approach is equivalent if the number of compartments is equal to the number of axial grid points.

The pre-mixing effects on granule attributes are assumed to be negligible. Therefore, the liquid addition and wet massing zones were divided into three equally-sized compartments. The inlet and outlet flow rates for each compartment were evaluated.

The flow into the system was equal to the inlet particle flow rate for the first compartment, as given in Equation 4.8.

$$\dot{F}_{in}(s, z_1, t) = \frac{p_{in}(s)\dot{m}_{in}}{\rho s} \quad (4.8)$$

Here, p_{in} is the experimentally-determined size distribution of the inlet particles, ρ is the density (1575 kg/m^3), and \dot{m}_{in} is the fixed mass flow rate used experimentally (4 kg/h). The inlet particles were assumed to be perfectly dry, with a bed porosity of 0.67. As a

result, the inlet terms for Equations 4.2 and 4.3 state that the transfer rate of liquid into this compartment is zero, and the transfer rate of gas is equal to $\dot{F}_{in}g_{in}$, where g_{in} is the volume of gas, per particle, corresponding to a porosity of 0.67.

The outlet flow rate from each compartment was evaluated using Equation 4.9.

$$\dot{F}_{out}(s, z_i, t) = \frac{F(s, z_i, t)}{\tau(z_i)} = \dot{F}_{in}(s, z_{i+1}, t) \quad (4.9)$$

Here, τ is the average residence time in each compartment, assumed to be constant with a value of 2.67 s based on the experimentally observed residence time distribution. The flow rate out of each compartment is equal to the flow rate into the subsequent compartment, and the outlet flow rate from the last compartment is the product stream flow rate.

4.3.2 Liquid addition

The rate of liquid addition, per particle, is given by Equation 4.10.

$$\dot{l}_{add}(s, z_{liq}, t) = \frac{s\dot{V}_{liq}}{\int_0^\infty F(s', z_{liq}, t)ds'} \quad (4.10)$$

where z_{liq} represents the axial region to which the liquid is added and \dot{V}_{liq} is the total volumetric rate of liquid addition, as determined from the liquid-to-solid ratio, LS , and the total rate of solid addition, shown in Equation 4.11.

$$\dot{V}_{liq} = LS \int_0^\infty \dot{F}_{in}(s')ds' \quad (4.11)$$

The liquid addition period began five seconds after particle flow began to allow particles to fill the granulator.

4.3.3 Consolidation

As the particles aggregate, they are compacted to form denser granules. The consolidation rate was determined from Equation 4.12 (Verkoeijen et al., 2002).

$$\dot{g}_{cons}(s, z, t) = c \left(\frac{LS}{0.3} \right)^\gamma V(s, z, t) \frac{1 - \epsilon_{min}}{s} \left[g(s, z, t) - s \frac{\epsilon_{min}}{1 - \epsilon_{min}} + l(s, z, t) \right] \quad (4.12)$$

This rate contains three adjustable parameters that were estimated from experimental data. c is a rate coefficient, and ϵ_{min} is the minimum granule porosity that can be obtained. Some studies have observed a liquid dependence of the consolidation rate, explained by the change in collision frequency in the presence of liquid (Iveson et al., 1996). The third adjustable parameter, γ , accounts for this effect.

It was assumed that liquid addition did not increase the overall porosity of the particle, and any liquid that entered the particle replaced the gas that occupied that space.

4.3.4 Aggregation

As the liquid binder is added to the particles, they begin to aggregate and form larger granules. The net aggregation rate is given by Equation 4.13.

$$\begin{aligned} \mathfrak{R}_{agg}(s, z, t) = & \frac{1}{2} \int_0^s \beta(s', s - s', z, t) F(s', z, t) F(s - s', z, t) ds' \\ & - F(s, z, t) \int_s^\infty \beta(s, s' - s, z, t) F(s' - s, z, t) ds' \end{aligned} \quad (4.13)$$

The first term of this expression is the rate of birth due to aggregation. The birth rate depends on the numbers of smaller particles that can aggregate to form a larger particle of solid volume s , as well as the aggregation kernel, β , describing the likelihood of aggregation between any two particles. The second term describes the depletion rate of particles as they aggregate into larger particles. All aggregation events were assumed to involve two colliding particles.

As the particles aggregate, the gas and liquid volumes also transfer to the larger particle. Equations 4.14 and 4.15 balance the transfer of liquid and gas due to aggregation.

$$\begin{aligned} \mathfrak{R}_{liq,agg}(s, z, t) = & \\ & \frac{1}{2} \int_0^s \beta(s', s - s', z, t) F(s', z, t) F(s - s', z, t) [l(s', z, t) + l(s - s', z, t)] ds' \\ & - l(s, z, t) F(s, z, t) \int_s^\infty \beta(s, s' - s, z, t) F(s' - s, z, t) ds' \end{aligned} \quad (4.14)$$

$$\begin{aligned} \mathfrak{R}_{gas,agg}(s, z, t) = & \\ \frac{1}{2} \int_0^s \beta(s', s - s', z, t) F(s', z, t) F(s - s', z, t) [g(s', z, t) + g(s - s', z, t)] ds' & \\ - g(s, z, t) F(s, z, t) \int_s^\infty \beta(s, s' - s, z, t) F(s' - s, z, t) ds' & \end{aligned} \quad (4.15)$$

Experimental results show that the product granule size distribution has a strong dependence on the liquid-to-solid ratio (El Hagrasy et al., 2013). To model this effect, two liquid-dependent aggregation kernels were considered. The first kernel, proposed by Madec et al. (2003), is given in Equation 4.16.

$$\beta(s, s', z, t) = \beta_0(V + V') \left[\left(\frac{LC + LC'}{2} \right)^\alpha \left(1 - \frac{LC + LC'}{2} \right)^\gamma \right]^\alpha \quad (4.16)$$

This kernel includes both a size and liquid dependence. It contains three adjustable parameters: a rate coefficient, β_0 , and two exponents describing the degree of liquid dependence, α and γ . The parameter γ describes how the aggregation rate reaches a maximum at an optimal liquid content. For the purposes of this study, γ was fixed at zero, and the liquid content was assumed to be much lower than the optimal value at all liquid-to-solid ratios. This assumption is supported by the experimental data, as the d_{25} value increases significantly with the liquid-to-solid ratio over the entire range.

The second kernel considered was proposed by Wauters (2001) and is given in Equation 4.17.

$$\beta(s, s', z, t) = \beta_0 P(s, s', z, t) \quad (4.17)$$

Here, β_0 is an adjustable coefficient, and P has a value of one or zero, depending on the properties of the colliding granules. The granules are divided into four classes: small and wet, large and wet, small and dry, and large and dry. Small and wet granules can aggregate with any granule, while large and wet granules can aggregate with all granules that are not large and dry. Small and dry granules can only aggregate with wet granules, and large and dry granules only aggregate with small and wet granules. The threshold values to determine what size is large and what liquid content is wet are adjustable parameters, denoted as d_{large} and LC_{wet} , respectively. Their values were estimated from experimental data.

4.3.5 Breakage

The net breakage rate is given by Equation 4.18, where b is the distribution of the fragment particles and K_{break} is the breakage kernel. A uniform breakage distribution was assumed.

$$\mathfrak{R}_{break}(s, z, t) = \int_s^{\infty} b(s', s) K_{break}(s', z, t) F(s', z, t) ds' - K_{break}(s, z, t) F(s, z, t) \quad (4.18)$$

The analogous equations for the transfer of liquid and gas due to breakage are shown in Equations 4.19 and 4.20. It was assumed that the fraction of liquid or gas in each fragment is proportional to its size.

$$\begin{aligned} \mathfrak{R}_{liq,break}(s, z, t) = \int_s^{\infty} b(s', s) K_{break}(s', z, t) F(s', z, t) \frac{sl(s', z, t)}{s'} ds' \\ - K_{break}(s, z, t) F(s, z, t) l(s, z, t) \end{aligned} \quad (4.19)$$

$$\begin{aligned} \mathfrak{R}_{gas,break}(s, z, t) = \int_s^{\infty} b(s', s) K_{break}(s', z, t) F(s', z, t) \frac{sg(s', z, t)}{s'} ds' \\ - K_{break}(s, z, t) F(s, z, t) g(s, z, t) \end{aligned} \quad (4.20)$$

A size dependent breakage kernel was used, as shown in Equation 4.21 (Pandya and Spielman, 1983). This kernel contains two adjustable parameters that were estimated: a rate coefficient, P_1 , and an exponent describing the size dependence, P_2 . The shear rate, G_{shear} , was assumed to be the same in all experiments, and its value was lumped into P_1 .

$$K_{break}(s, z, t) = \frac{1}{2} G_{shear} P_1 (V(s, z, t))^{P_2} \quad (4.21)$$

4.3.6 Multiple solid components

In addition to the 2-D model, a 3-D model was developed to simulate the API as a second solid component. The resulting PBM is given in Equation 4.22.

$$\begin{aligned} \frac{dF(s_1, s_2, z, t)}{dt} = \mathfrak{R}_{agg}(s_1, s_2, z, t) + \mathfrak{R}_{break}(s_1, s_2, z, t) \\ + \dot{F}_{in}(s_1, s_2, z, t) - \dot{F}_{out}(s_1, s_2, z, t) \end{aligned} \quad (4.22)$$

Here, s_1 represents the solid volume of excipient, per particle, while s_2 represents that of the API. The solid composition, x is then given by Equation 4.23.

$$x = \frac{s_2}{s_1 + s_2} \quad (4.23)$$

The aggregation kernel presented in Equation 4.16 was modified with a composition dependent term, Ψ , as proposed by Matsoukas et al. (2009), shown in Equation 4.24.

$$\Psi(x, x') = \exp[-a_{AB}(x + x' - 2xx')] \quad (4.24)$$

This term was used as a multiplicative factor to account for attractive or repulsive interactions between the API and excipient. The adjustable coefficient a_{AB} determines the attraction or repulsion between the two components. If a_{AB} is positive, the components are more likely to aggregate with other particles of their own kind, and the API and excipient are repulsive. A value of zero indicates no interaction, and a negative value means that the API and excipient have attractive interactions. For this study, multi-component experiments were not performed, and a_{AB} was used to simulate hypothetical interactions. In future work, a_{AB} can be estimated for various materials.

For these simulations, 90% by mass of the primary particles were excipient particles with the experimentally measured initial size distribution. The remaining 10% were API particles with the same initial size distribution as the excipient particles.

4.3.7 Numerical method

The solid volume grid was discretized to reduce the partial differential equations (PDEs) to a system of coupled ordinary differential equations (ODEs). Because the experimentally produced granules were much larger than the feed particles, a nonlinear grid was used to span this size gap. The per-particle volume of solid, s , in each bin, n , was determined from Equation 4.25

$$s(n) = s(1) \times 1.7^{n-1} \quad (4.25)$$

where $s(1)$ is the volume of solid in the first bin, fixed at $1.67e - 15m^3$, and there were 35 bins of solid volume in each compartment. Since a non-linear grid was used, most daughter particles from aggregation and breakage have solid volumes that fall between bins. The cell average method was used to allocate these particles (Kumar et al., 2006; Chaudhury et al., 2013a).

The coupled ODEs were solved using first-order Euler integration with a variable step size. The step size was selected at each step such that the net reduction in particles of a single bin is no greater than 20% in each time step, and the step size is no greater than 0.25 seconds. This approach was used to avoid numerical instabilities and obey the Courant-Friedrichs-Lewy condition (Ramachandran and Barton, 2010). The twin-screw granulator was simulated from start-up to 35 seconds, at which point a steady state has been reached.

To confirm that the model is internally consistent, the conservation of the total solid and liquid volumes was confirmed. To verify this observation, the total volumes of solid and liquid within the granulator at $t = 35s$ were calculated and compared to the integral of the net difference between the inlet and outlet flow rates over this time period. The percent difference between the expected and observed volumes of solid and liquid in the granulator at $t=35$ s were $7.0e - 13\%$ and $1.8e - 12\%$, respectively. This observation demonstrates the closure of the first moment of the PBM. When the grid was changed to contain 30 bins instead of 35, these percent differences became $2.8e - 13\%$ and $8.6e - 13\%$, respectively, demonstrating that the closure of the first moment is independent of the grid in this model.

4.3.8 Parameter estimation and validation

Experimental data was used to estimate the unknown parameters in the model, including three in the consolidation rate expression (c , γ , and ϵ_{min}), two in the breakage kernel (P_1 and P_2), and two or three in each aggregation kernel (β_0 and α) or (β_0 , d_{large} , and LC_{wet}). Parameter estimation was performed separately for each aggregation kernel, resulting in seven fitted parameters when using the Madec kernel and eight fitted parameters when using the Wauters kernel.

Of the five experimental runs, three were used for parameter estimation, with liquid-to-solid ratios of 0.15, 0.25, and 0.35. The remaining two runs were used to validate the calibrated model. The model was fitted to experimental measurements for the size distributions and the porosity of the 1-1.4 mm size class. Rather than fitting the model to all points on the size distribution, values for d_{25} , d_{50} , and d_{75} were used in order to focus on the product size class and limit the number of data points, reducing the complexity of the objective function. A complex objective function may have many local minima, resulting in a more difficult or less successful optimization. By post-processing the size distribution data, key information about the magnitude and spread of the distribution (d_{25} , d_{50} , and d_{75}) were used to fit the data. Furthermore, in many industrial processes, the product size range is of primary importance for subsequent downstream operations, so the focus was on this range. Consequently, twelve experimental data points (three experiments with four product attributes) were used to fit seven (Madec kernel) or eight (Wauters kernel) parameters. Additionally, the rate expressions were rewritten to decouple some of the parameters. Reported parameter values are based on the original rate expression.

The unknown parameters can be separated into two categories: size-related parameters (P_1 , P_2 , β_0 , α , d_{large} , and LC_{wet}) and porosity-related parameters (c , γ , and ϵ_{min}). Although the subprocesses of consolidation, aggregation, and breakage can have interactive effects on each other, it was observed that the first group of parameters greatly affect the size distribution, and the second set affect the porosity. To take advantage of this behavior, an iterative process was used to estimate these subsets individually before performing the overall optimization. The porosity-related parameters were estimated first while holding the size-related parameters constant. Subsequently, the aggregation and breakage parameters were estimated separately using the d_{25} , d_{50} , and d_{75} values. This cycle was repeated until no more improvement was observed, and an overall optimization was performed to fine-tune the parameter values.

The Nelder-Mead simplex optimization method was used to minimize the objective function, Φ , shown in Equation 4.26.

$$\Phi(\mathbf{X}) = \sum_{ij} \frac{(f_{ij}(\mathbf{X}) - y_{ij})^2}{\sigma_j^2} \quad (4.26)$$

A weighted least squares objective function was used, where \mathbf{X} is the set of unknown parameters, i is the set of experimental runs, and j is the set of measured variables. f and y represent the predicted and measured values for each data point, respectively, and σ is a weighting factor for each measurement. Based on the appearance of the experimental data, values of σ for d_{25} , d_{50} , and d_{75} were fixed at 25, 50, and $75\mu m$, respectively, and that of the porosity was fixed at 0.05. These values were selected based on the relative magnitudes of the variables compared to each other in order to scale the differences between the experimental and simulated results to approximately the same magnitude.

The coefficient of determination (R_j^2) was calculated for each measurement set according to Equation 4.27, where \bar{y}_j is the average measured value of all experimental runs.

$$R_j^2 = 1 - \frac{\sum_i (f_{ij}(\mathbf{X}) - y_{ij})^2}{\sum_i (\bar{y}_j - y_{ij})^2} \quad (4.27)$$

4.4 Results and discussion

4.4.1 Experimental results

Figure 4.2 shows the experimental particle size distributions for the feed particles and product granules at each liquid-to-solid ratio (El Hagrasy et al., 2013). The distributions show a decrease in primary particles as larger granules appear. The liquid-to-solid ratio has a large effect on the product size distributions, as an increase in liquid addition rate corresponds to a higher frequency of large particles and a decrease in primary particles. Additionally, at lower liquid-to-solid ratios, the product distributions are wider, while at higher liquid-to-solid ratios, the distributions are narrower. At low liquid addition rates, a wide distribution can occur because the liquid is not distributed evenly on the particles. Some particles are dryer and unable to aggregate, while wetter particles will form large granules.

4.4.2 Parameter estimation and predictive modeling

In order to quantitatively represent these trends in the simulations, the unknown rate parameters were estimated using this experimental data for two separate liquid-dependent

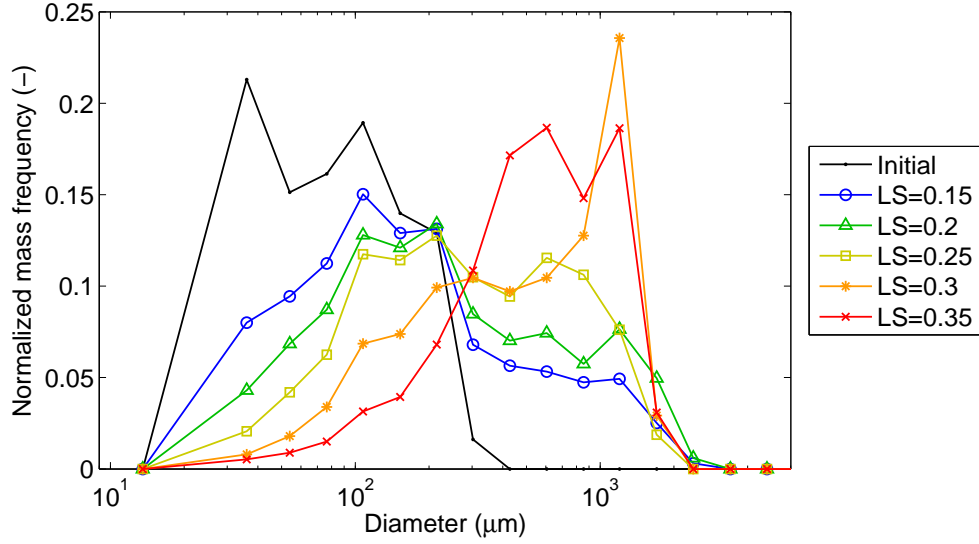


Figure 4.2: Experimental size distributions of initial blend and product at various liquid-to-solid ratios (El Hagrasy et al., 2013).

aggregation kernels. The initial and final values for each parameter are presented in Table 4.1.

Table 4.1: Parameter estimation results: Initial and final values of unknown parameters.

| Parameter | Initial Value | Final Value | |
|---|---------------|-------------|-----------|
| | | Madec | Wauters |
| Aggregation rate coefficient, β_0 ($\frac{1}{m^3\text{-particle-s}}$) | $1e-5$ | $1.26e-6$ | - |
| Aggregation liquid dependency exponent, α (-) | 0 | 1.23 | - |
| Aggregation rate coefficient, β_0 ($\frac{1}{\text{particle-s}}$) | $1e-6$ | - | $7.78e-6$ |
| Minimum diameter large particle, d_{large} (μm) | 200 | - | 48.7 |
| Minimum liquid content of wet particle, LC_{wet} (-) | 0.1 | - | 0.0764 |
| Breakage rate coefficient, P_1 (-) | 1 | 79.7 | 0.521 |
| Breakage size dependency exponent, P_2 (-) | 1 | 1.17 | 0.947 |
| Consolidation rate coefficient, c (1/s) | 0.1 | 0.596 | 0.596 |
| Consolidation liquid dependency exponent, γ (-) | 0.1 | 3.68 | 3.68 |
| Minimum porosity, ϵ_{min} (-) | 0.3 | 0.507 | 0.507 |

Using these values, the remaining two experimental runs were simulated. Figure 4.3 shows the measured values of d_{25} , d_{50} , and d_{75} along with those fitted using the Madec kernel. The interpolated results show strong agreement with the experimental data. The d_{25} values have the strongest fit to the data, with R^2 equal to 0.982, while the model tends to overestimate the d_{50} value by approximately $50\mu m$. For both the d_{25} and d_{50} values,

the data points that were predicted with the calibrated model fall in line with those used in parameter estimation. The model is successful at predicting these values within this experimental design space.

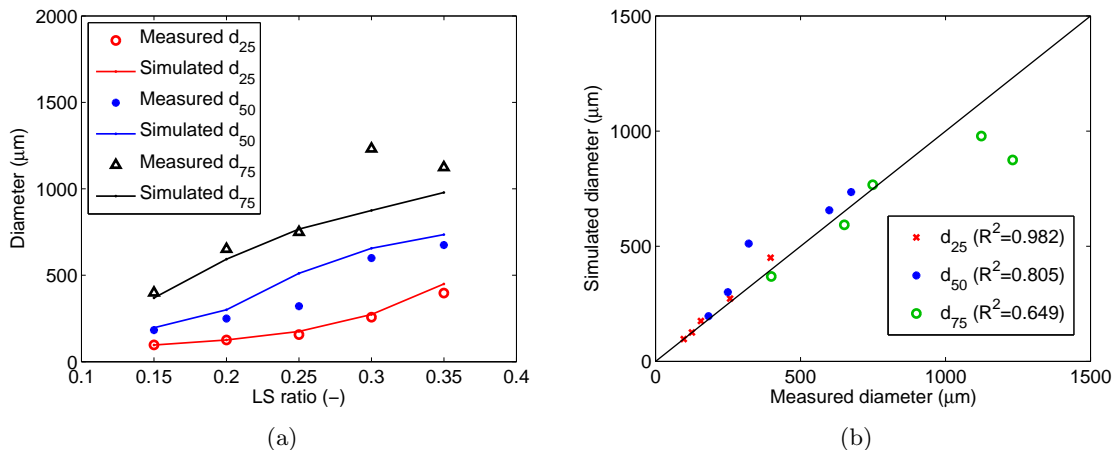


Figure 4.3: Experimental and model fitted and predicted d_{25} , d_{50} , and d_{75} values (a) versus liquid-to-solid ratio and (b) predicted versus measured. Predicted values based on Madec kernel.

In contrast, the simulations at high liquid-to-solid ratios predicted d_{75} values lower than those experimentally observed, resulting in R^2 equal to 0.649. The greatest error is observed is found in the data point at a liquid-to-solid ratio of 0.3. The experimental d_{75} value is greater than that of the liquid-to-solid ratio of 0.35, and may be an outlier in the data.

Figure 4.4 shows the measured and predicted size descriptors when using the Wauters kernel. Similar to the Madec kernel, the fitted and predicted d_{25} and d_{50} values strongly matched the experimental data. However, this model fails to match the d_{75} value of the distributions, with an R^2 value of only 0.423. This can be attributed to the lack of size dependence in this kernel. As a result of this lack of fit, the Madec kernel was found to describe this process better. Thus, the remaining results are based on the Madec kernel.

In Figure 4.5, the experimental and fitted particle size distributions using the Madec kernel are presented for the liquid-to-solid ratios that were used to fit the model. While the results show some differences, many of the peaks in the data match. A slight overestimation of the frequency of fine particles is observed, along with an underrepresentation of larger particles. Additionally, the model predicts narrower and higher peaks than measured.

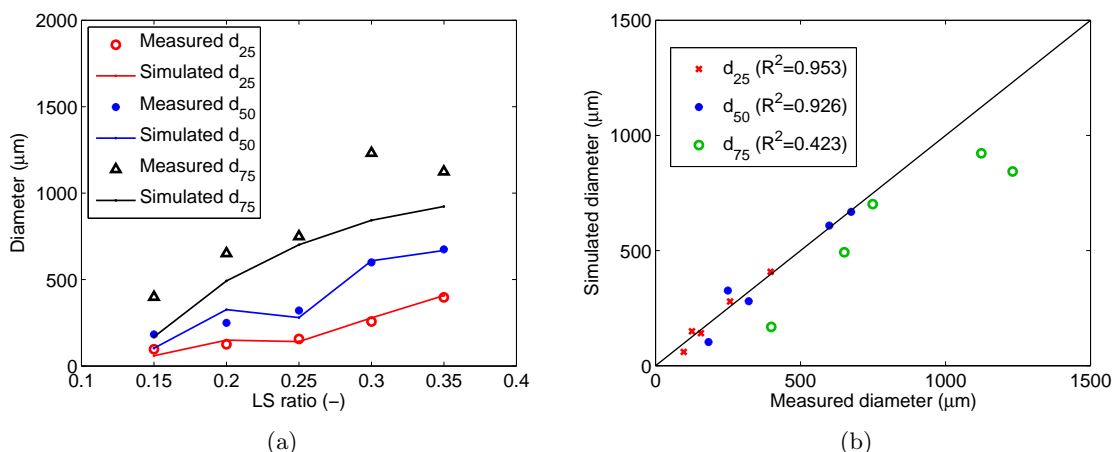


Figure 4.4: Experimental and model fitted and predicted d_{25} , d_{50} , and d_{75} values (a) versus liquid-to-solid ratio and (b) predicted versus measured. Predicted values based on Wauters kernel.

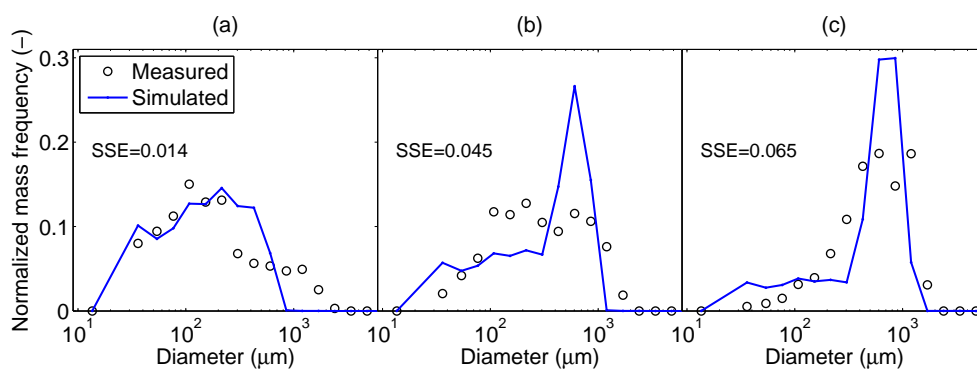


Figure 4.5: Measured and fitted steady-state product size distributions of runs used in parameter estimation, at liquid-to-solid ratios of (a) 0.15, (b) 0.25, and (c) 0.35.

Figure 4.6 shows the purely predictive size distributions of the remaining liquid-to-solid ratios. Like the fitted distributions, these plots show greater peaks, and discrepancies at the upper and lower bounds. These differences may indicate an inability of the model to represent high frequencies of very large granules. In order to improve the model, future work will focus on using DEM to obtain particle flux data and collision frequencies. Additionally, more mechanistic kernels can be developed and tested against these empirical rate expressions.

In Figure 4.7, the measured and predicted porosity values are presented for the 1-1.4 mm

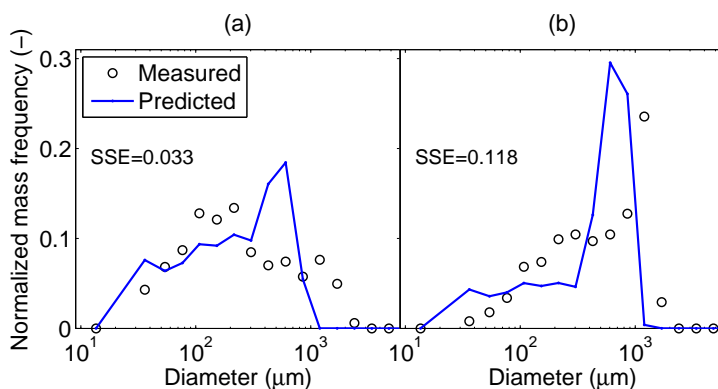


Figure 4.6: Measured and predicted steady-state product size distributions of runs used in validation, at liquid-to-solid ratios of (a) 0.2 and (b) 0.3.

product size range. A reduced porosity is observed at higher liquid-to-solid ratios, which can be attributed to the greater mobility of the particles in liquid and higher collision frequency. The predicted porosity strongly fits the experimental data, with an R^2 value of 0.984, indicating that the consolidation rate model was successful in describing these trends. An empirical parameter was used to quantify the effect of liquid-to-solid ratio on the consolidation rate, and a more mechanistic approach can be taken to develop a better understanding of this observation.

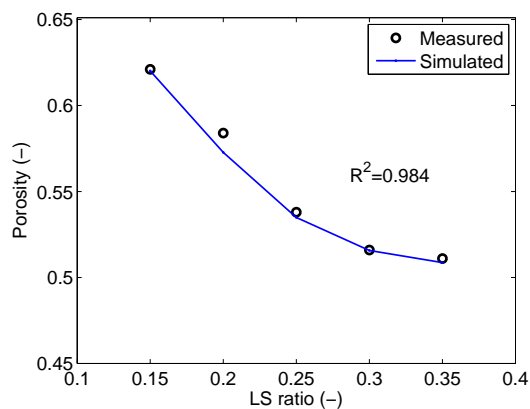


Figure 4.7: Measured and predicted or fitted porosity of granules in the 1-1.4 mm size class.

4.4.3 Sensitivity analysis of adjustable parameters

To further investigate the effects of the adjustable parameters on the results of the simulation, a sensitivity study was performed. The values of the adjustable parameters were changed by +/- 5% of the estimated values, and the simulated results were compared. Figure 4.8(a) shows the effect of four adjustable parameters on the median diameter for a liquid-to-solid ratio of 0.25. The aggregation rate coefficient had the largest effect on the median diameter, and a greater aggregation rate resulted in larger granules. Similarly, an increase in the breakage rate coefficient resulted in smaller product granules. The minimum porosity also affects the median diameter. An increase in the minimum porosity results in more porous granules, which can hold more internal liquid. Less liquid is available on the surface for aggregation, and smaller granules are produced. The consolidation rate constant had a minor effect on the product size, as an increase in the consolidation rate results in less porous particles and more external liquid.

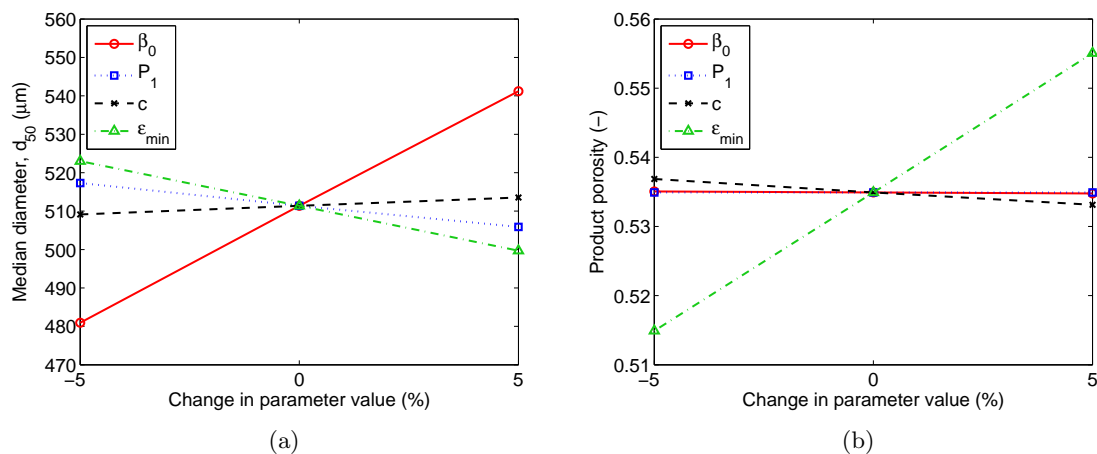


Figure 4.8: Effect of changes in adjustable parameter values on (a) median diameter and (b) porosity of 1-1.4 mm size class for a liquid-to-solid ratio of 0.25.

Similarly, Figure 4.8(b) shows the effects of these parameters on the porosity of the 1-1.4 mm size class for a liquid-to-solid ratio of 0.25. The aggregation and breakage rate coefficients do not significantly affect the product porosity. An increase in the consolidation rate coefficient results in a less porous product, while an increase in the minimum porosity has the opposite effect.

Figure 4.9 shows the effects of the liquid dependency exponents on the median product diameter and porosity for a range of liquid-to-solid ratios. In Figure 4.9(a), a decrease in the liquid dependence exponent in the aggregation rate kernel, α , results in larger granules since the overall aggregation rate decreases. Further, the liquid-to-solid ratio has a reduced effect on the median diameter as the value of α decreases. The exponent describing the liquid dependence of the consolidation rate, γ , has a similar effect on the product porosity. In Figure 4.9(b), an increase in γ increases the effect of the liquid-to-solid ratio on the product porosity, particularly when the liquid-to-solid ratio is low.

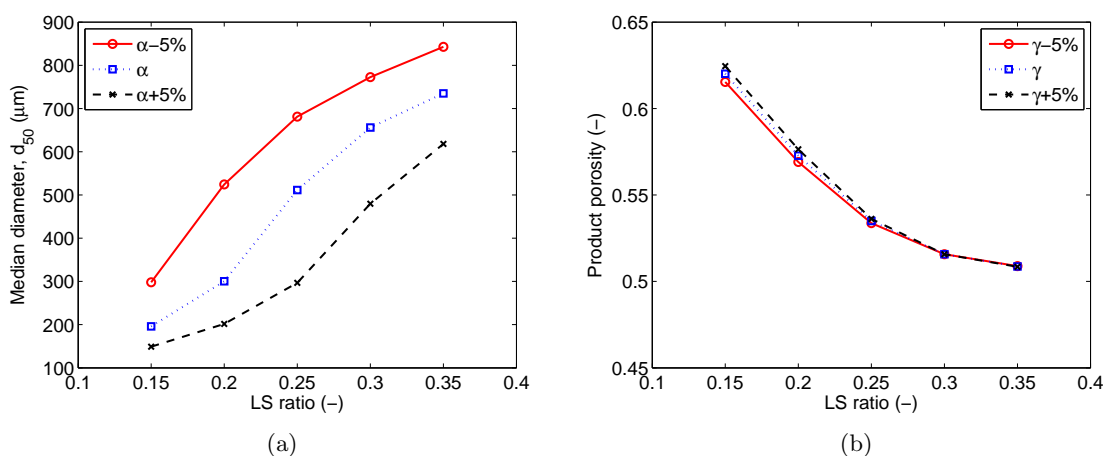


Figure 4.9: Effect of changes in adjustable exponents describing liquid dependence of (a) aggregation rate on the median diameter and (b) consolidation rate on the porosity of the 1-1.4 mm size class.

4.4.4 Simulated dynamic behavior

Figure 4.10 shows the start-up behavior of the size enlargement process. In Figure 4.10(a), the median product diameter is shown over time. After liquid addition begins at five seconds, the median diameter increases, and a steady state is reached within about 25 seconds, regardless of the liquid to solid ratio. Because the residence time within the granulator is short, a steady state can be reached quickly. Figure 4.10(b) shows the median diameter during start-up at different axial positions in the granulator. At 4 cm from the start of the liquid addition zone, the liquid is being added to the particles, and the median diameter increases slightly. Most of the size enlargement occurs in the wet-massing zone,

where the median diameter nearly doubles in less than 10 cm.

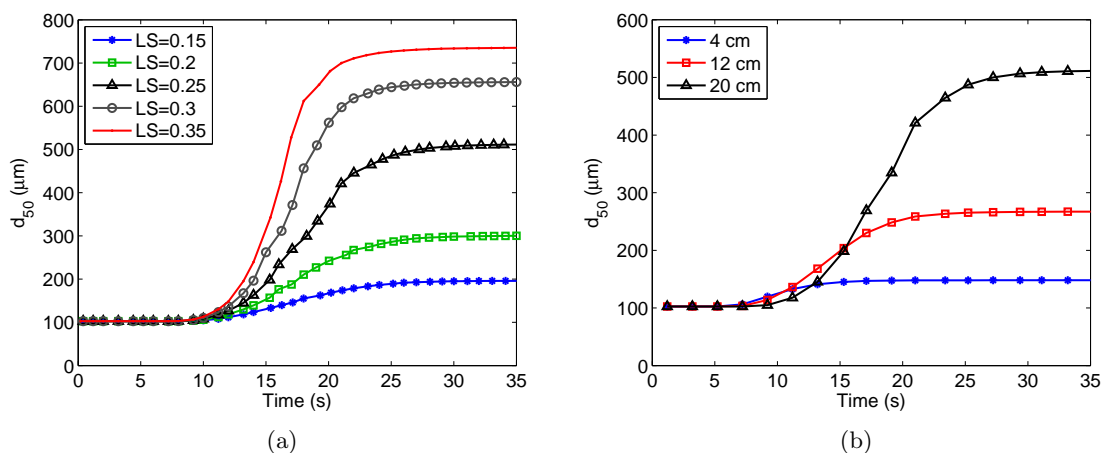


Figure 4.10: Simulated dynamic behavior of median diameter from start-up to steady state (a) of product at various liquid-to-solid ratios and (b) at various axial locations within the granulator with a liquid-to-solid ratio of 0.3.

4.4.5 Multi-component interactions

In Figure 4.11, the simulated effects of multi-component interactions are presented. The average composition for the size class of 0.15-1.5 mm is shown for the cases of no interaction ($a_{AB} = 0$), attraction ($a_{AB} < 0$) and repulsion ($a_{AB} > 0$). In the cases with repulsion, the API mass fractions in the higher size class were lower than expected, which would result in a final dosage form with less API in a real system. The composition for the case with no interaction is approximately 10%, equal to the overall mass fraction of API in the system. For simulations of attraction between the API and excipient, the larger particles were likely to have a greater API mass fraction than the overall system. In these cases, granules with higher mass fractions of API are more likely to aggregate with excipient particles, resulting in a greater API mass fraction within larger size classes. Future work will involve evaluating the composition of each sieve fraction to identify these interactions.

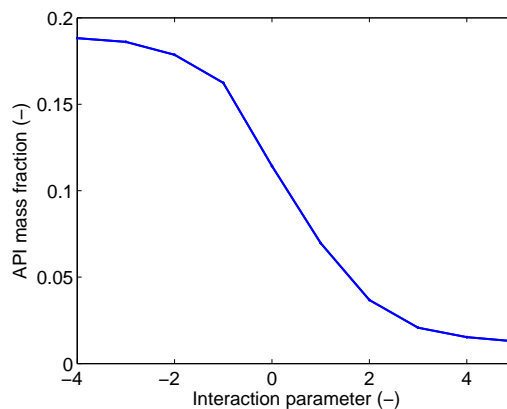


Figure 4.11: Average composition of 0.5-1.5 mm size class versus interaction parameter.

4.5 Summary

A 2-D PBM for a continuous wet granulation process was presented, and unknown rate parameters were estimated using experimental size distributions and porosities. Using the model, the effect of the liquid-to-solid ratio was quantified, and the calibrated model was then used as a predictive tool within the experimental space. Two liquid-dependent aggregation kernels were used, and the more appropriate kernel was selected. The results show strong agreement with experimental data, but have some discrepancies in the size distributions at very large and very small particle sizes.

Many powder processes are poorly understood, and their operation is based mainly on heuristic data. A model-based approach can be taken to develop a better understanding of powder processes and implement QbD. By developing and validating predictive models, the CQAs can be linked to process parameters and material properties, reducing the number of experiments needed to characterize a process. In this study, the effect of the liquid-to-solid ratio on the CQAs of granule porosity and PSD was characterized for a TSG process. By defining a target range for the CQAs, a validated model can be used to define the design space of the process and implement QbD. Predictive models can also facilitate process optimization and model-based control.

Specific Aim III

Development of a multi-scale model using bi-directional coupling of discrete element modeling and population balance modeling

The PBM cannot predict mechanistic behavior related to material properties, process parameters, and equipment geometry. Discrete element modeling (DEM) can be used to capture particle-scale information such as collision behavior and velocity distributions. In this aim, a multi-scale model is proposed and demonstrated, taking advantage of the combined capabilities of PBM and DEM.

The goals of this specific aim are to:

- Design an algorithm for bi-directional coupling between the PBM and DEM, using PBM to update the distribution of particles within the granulator, and DEM to feed particle-scale information to the PBM.
- Implement mechanistic rate expressions by creating links between the DEM results and the PBM rate kernels for aggregation, breakage, and consolidation.
- Develop computationally-efficient techniques to transfer data between the models.

These works were originally published in:

- Barrasso, D., Ramachandran, R., 2015a. Multi-scale modeling of granulation processes: Bi-directional coupling of PBM with DEM via collision frequencies. *Chemical Engineering Research and Design* 93, 304–317
- Barrasso, D., Eppinger, T., Pereira, F. E., Aglave, R., Debus, K., Bermingham, S. K., Ramachandran, R., 2015b. A multi-scale, mechanistic model of a wet granulation process using a novel bi-directional PBM-DEM coupling algorithm. *Chemical Engineering Science* 123, 500 – 513

Chapter 5

Multi-scale modeling of granulation processes: Bi-directional coupling of PBM with DEM via collision frequencies

Wet granulation is a complex particle design process often operated inefficiently in industrial applications. Enhanced process understanding is required to facilitate design, control, and optimization. In this study, a hybrid multi-scale model is presented using a bi-directional coupling approach between DEM and PBM. The hybrid model takes into account particle collision frequencies and liquid distribution, providing a framework suitable for the complex sub-processes in wet granulation. The effect of particle size distribution on the collision frequency function was demonstrated, indicating the need for a multi-scale model. Results of the hybrid model show an increase in particle size over time from an average diameter of 0.98 mm to 2.5 mm, which qualitatively agrees with experimental trends observed during the liquid addition and wet massing stages. Two-dimensional distributions in particle size and liquid fraction are also presented incorporating the key effect of liquid distribution the evolution of granule PSD.

5.1 Background

To meet build a more scientific understanding of powder processes and implement Quality-by-Design, a model-based approach has been proposed, where empirical and mechanistic models are developed and validated using experimental data (Glaser et al., 2009; Ramachandran and Chaudhury, 2012). Validated models can then be used as predictive tools to aid in design, model-based control, and optimization. Various modeling approaches have been employed for granulation. Data-driven models include response surface methodology (RSM) and artificial neural networks (ANN) (Ranjbarian and Farhadi, 2013a; Behzadi et al., 2005). These models use data from existing or experimental processes, and have limited ability to

predicting process behavior beyond the experimental space. Population balance models (PBM) provide a more fundamental framework for tracking changes in particle properties over time, though they require rate expressions and empirical parameters that cannot easily be measured. Discrete element modeling (DEM) is more mechanistic, tracking particles as they move through space and collide. However, DEM by itself does not account for aggregation or other rate processes involved in wet granulation. Further, computational fluid dynamics (CFD) can also be used to determine drag forces resulting from fluid flow, which are significant in fluid bed granulation processes. Along with DEM, these forces can be used to determine particle fluxes.

In this study, a multi-scale model is presented, solving a two-dimensional PBM within a DEM simulation, focusing on systems such as high-shear, twin-screw, and drum granulation, which do not incorporate an air flow stream (such as in fluid bed granulation). As a result, CFD aspects can be neglected.

5.1.1 Comparison of PBM and DEM

While the PBM framework is largely empirical, DEM simulates particle-scale behavior. DEM inherently determines spatial effects, such as segregation and particle flux. Additionally, liquid binder droplet distribution has been simulated using DEM, representing binder droplets as solid particles that can merge with powder particles on contact (Goldschmidt et al., 2003). Further, each collision is treated as a separate event, and collision properties such as frequency, relative velocity, and particle properties can be extracted from the results for use in mechanistic kernels.

A critical difference between PBM and DEM is the treatment of the rate processes. DEM must be coupled with an additional model to simulate rate processes such as aggregation, consolidation, and breakage. Previously, aggregation has been represented by cohesion of spherical particles on contact, which result in agglomerates of spheres (Tardos et al., 1997). This approach is computationally intensive but provides insight into granule morphology. Alternatively, particles that coalesce can be replaced with a larger spherical particle by applying a conservation of mass (Goldschmidt et al., 2003). In this sense, DEM is used as

a simulation tool for solving a PBM. Both approaches require the aggregation criteria to be defined.

Some recent studies involve coupling of a PBM with DEM. In a study by Reinhold and Briesen (2012), DEM is coupled concurrently to a 1-D PBM to account for aggregation. Similarly, Dosta et al. (2013) performed multi-scale modeling of a granulation process using a 1-D PBM to generate size distributions and DEM to simulate particle-scale behavior. Additionally, Wang et al. (2012) simulated a ball milling process using DEM to obtain collision and dissipation energies, which were used in a PBM to simulate breakage.

Coupling DEM with other modeling tools is a subject of interest. Many models have been developed using DEM coupled with CFD for particle-fluid interaction in fluidized-bed granulation processes (Fries et al., 2011, 2013; Jajcevic et al., 2013). However, fewer studies integrate PBM and DEM simulations. One-way coupling has been used to incorporate powder flow data into compartmental PBMs for various powder processes (Sen and Ramachandran, 2013; Freireich et al., 2011; Sen et al., 2012; Li et al., 2013). Other models use DEM-generated coalescence kernels within a PBM (Liu and Litster, 2002; Gantt and Gatzke, 2006). With drastic particle size changes, as found in granulation, a two-way coupling approach may provide additional data as the particle size distribution (PSD) can effect large-scale behavior.

The two approaches for representing size enlargement due to aggregation within a DEM simulation have been presented, effectively solving the PBM using DEM (Goldschmidt et al., 2003; Tardos et al., 1997). A third approach is presented here, collecting collision and particle data from a DEM simulation over a specified time interval and applying a PBM to update the size distribution within the DEM. This two-way coupling approach requires collisions to be counted and stored, but does not require immediate action, reducing the computational expense of each collision. Additionally, the dynamic DEM data can be used to generate a reduced order model, replacing the expensive DEM step.

5.1.2 Objectives

The purpose of this study is to develop a coupled PBM-DEM model for wet granulation processes, with the following objectives:

- Demonstrate the limitations of PBM and DEM when used independently to model granulation processes.
- Present a hybrid PBM-DEM model using two-way coupling to transfer data related to collision frequencies and size and liquid distribution.
- Propose a framework for future work to incorporate additional sub-processes and complexities within the hybrid model.

5.2 Model development

5.2.1 Population balance model

A two-dimensional PBM was used to track the PSD over time during granulation, using solid and liquid volume as internal coordinates. The general form of this equation is given by

$$\frac{\partial}{\partial t} F(s, l, t) + \frac{\partial}{\partial l} \left[F(s, l, t) \frac{dl}{dt} \right] = \mathfrak{R}_{agg}(s, l, t), \quad (5.1)$$

where s and l represent the volumes of solid and liquid per particle, respectively. This equation includes the rate processes of liquid addition (represented by the partial derivative with respect to l) and aggregation (\mathfrak{R}_{agg}). In the hybrid model, liquid addition is simulated using DEM, so it must be omitted from the PBM. The PBM becomes

$$\frac{\partial}{\partial t} F(s, l, t) = \mathfrak{R}_{agg}(s, l, t). \quad (5.2)$$

The net aggregation rate consists of the depletion of smaller particles as they aggregate ($\mathfrak{R}_{agg,form}$) and the formation of larger granules ($\mathfrak{R}_{agg,dep}$), as shown in Equation 5.3.

$$\mathfrak{R}_{agg}(s, l, t) = \mathfrak{R}_{agg,form}(s, l, t) - \mathfrak{R}_{agg,dep}(s, l, t) \quad (5.3)$$

The expressions for these rates are given in Equations 5.4 and 5.5.

$$\mathfrak{R}_{agg,form}(s, l, t) = \frac{1}{2} \int_0^s \int_0^l \beta(s - s', l - l', s', l', t) F(s - s', l - l', t) F(s', l', t) dl' ds' \quad (5.4)$$

$$\mathfrak{R}_{agg,dep}(s, l, t) = \int_0^\infty \int_0^\infty \beta(s, l, s', l', t) F(s', l', t) F(s, l, t) dl' ds' \quad (5.5)$$

Here, $\beta(s, l, s', l', t)$ is the aggregation kernel, describing the rate of aggregation as it depends on the properties of the two colliding particles and time. The aggregation kernel can be broken into two factors: the collision frequency, C , and the collision efficiency, Ψ , shown in Equation 5.6.

$$\beta(s, l, s', l', t) = C(s, l, s', l', t) \Psi(s, l, s', l') \quad (5.6)$$

The collision frequency describes the rate of collision between particles as a function of particle properties. It has previously been demonstrated using DEM that particle size affects the collision frequency (Gantt et al., 2006).

The time dependency of the collision frequency is included to account for the effects of the current state of the system on the aggregation rate. For example, the PSD may affect the collision frequency. To test this hypothesis, DEM simulations were performed using different PSDs, and the collision frequency was calculated. The results of this investigation are presented in this study, confirming the effect of PSD on the collision frequency.

In the hybrid model, all collisions are recorded using DEM to calculate the collision frequency in real time. Based on the total number of collisions between each particle N_{coll} during the time interval Δt , the collision frequency can be determined from Equation 5.7, which normalizes the collision rate by the number of particles (Gantt et al., 2006).

$$C(s, l, s', l', t) = \frac{N_{coll}(s, l, s', l', t)}{F(s, l, t) F(s', l', t) \Delta t} \quad (5.7)$$

The collision efficiency describes the likelihood that two colliding particles will aggregate. Coalescence is determined by particle properties, such as size, surface liquid, and porosity, as well as collision properties, such as relative velocity (Gantt et al., 2006). Mechanistic

expressions have been developed to assess whether collisions will occur using particle-scale models. DEM simulations can be used to assess the collision properties and develop empirical expressions for the collision efficiency (Gantt et al., 2006). However, the effects of process parameters and material properties on the collision behavior is unknown.

In this study, a simple expression for the collision efficiency is used, as shown in Equation 5.8, adapted from Biggs et al. (2003).

$$\Psi(s, l, s', l') = \begin{cases} \Psi_0 & LC(s, l) \geq LC_{min} \text{ or } LC(s', l') \geq LC_{min} \\ 0 & LC(s, l) < LC_{min} \text{ and } LC(s', l') < LC_{min} \end{cases} \quad (5.8)$$

Here, LC is the particle liquid content, given by $LC(s, l) = \frac{l}{s+l}$, and LC_{min} is the minimum liquid content required for coalescence. This expression states that if either of the colliding particles have a liquid content greater than a minimum value, coalescence can occur upon collision. Ψ_0 is a rate constant defining the probability of coalescence for all collisions that meet the liquid content criterion. The values for LC_{min} and Ψ_0 are given in Table 5.1. Future work will involve coupling the DEM results to the PBM to determine the collision efficiency in addition to the frequency.

5.2.2 Discrete element model

Simulations were performed using EDEM 2.5 Academic Simulator (DEM Solutions) on an Intel Core i7-2600 CPU processor (3.4 GHz) with 16 GB of RAM. A User Defined Library (UDL) was created using C++ to implement the PBM and custom liquid addition model within the simulation. The UDL was written to enable multi-threading, and the simulations were performed with 4 cores.

A batch drum granulator was selected for its simple geometry (Poon et al., 2009). The equipment was modeled as a horizontal cylinder, and the dimensions and rotational speed are listed in Table 5.1. Four baffles were created as thin, flat plates along the granulator wall to agitate the particles. The model can be extended to simulate more complex equipment, such as those with impellers or screws (high-shear, twin-screw), as well as those with spatial inhomogeneities.

Table 5.1: Parameters and initial conditions for simulation. Values for parameters used in DEM simulations* were taken from Dubey et al. (2011).

| Parameter | Value |
|--|------------------------------|
| Solid volume of first bin, $s(1)$ | 0.5 mm^3 |
| Liquid volume of first bin, $l(1)$ | 0.5 mm^3 |
| Initial number of powder particles | 15000 |
| Initial powder particle bin | [1, 0] |
| Initial liquid droplet bin | [0, 1] |
| Simulation time, t_{sim} | 10 s |
| PBM time interval size, Δt | 0.01 s, 0.1 s, 1 s |
| DEM time step | $1 \times 10^{-5} \text{ s}$ |
| DEM grid size | 2 mm |
| Liquid addition start time | 0.1 s |
| Liquid addition end time | 5.1 s |
| Total liquid-to-solid ratio, L/S | 0.33 |
| Drum diameter, D | 40 mm |
| Drum length, L | 60 mm |
| Baffle width | 4 mm |
| Number of baffles | 4 |
| Drum rotational speed | 60 RPM |
| Collision efficiency constant, Ψ_0 | 0.001 |
| Minimum liquid content for coalescence, LC_{min} | 0.15 |
| Poisson's ratio* | 0.25 |
| Shear modulus* | 2 MPa |
| Particle density | 1 g/cm^3 |
| Coefficient of restitution* | 0.1 |
| Coefficient of static friction* | 0.5 |
| Coefficient of rolling friction* | 0.01 |

Primary powder particles were defined to have a uniform volume of 0.5 mm^3 or approximately 1 mm in diameter. This size is much larger than the primary particles used in real granulation processes, in order to fill an acceptable fraction of the drum with 15,000 particles. Particle scaling is typical in DEM simulations, which have computational limitations. A greater number of particles increases the computational burden on DEM, and smaller particles require a smaller time step for contact detection. The particles are initially placed randomly throughout the drum and settle at the bottom before the start of liquid addition. Additional particle properties are listed in Table 5.1. Several properties relevant to the DEM simulation were selected from Dubey et al. (2011), and experimental studies are needed to fully characterize these material properties.

Liquid droplets were modeled as solid particles with the same properties as the primary powder particles. A cylindrical region of 8 mm in diameter was created as the liquid addition zone. This region spanned the length of the granulator and is centered 8 mm below the top of the granulator to prevent liquid creation in the baffle region. Liquid particles were created during the time interval of 0.1 s to 5.1 s , allowing the powder particles to settle before liquid addition begins. This time period is known as the liquid addition period of the granulation process. The wet massing period occurs after liquid addition ends, from 5.1 s to 10 s . An overall liquid-to-solid ratio of $1/3$ was used, and liquid particles were created at a rate of 1000 s^{-1} . Upon contact with a powder particle, the liquid droplet disappears, and the liquid volume of the powder particle increases. This event changes the liquid bin of the particle, eliminating the need to simulate liquid addition within the PBM. If a liquid particle collides with another liquid particle, they merge to create a larger droplet. Using DEM to simulate liquid addition allows for inhomogeneities in liquid distribution, an effect that is not inherent in the PBM.

Powder-powder and powder-wall collisions were simulated using the Hertz-Mindlin model as provided by EDEM. The Hertz-Mindlin model is a non-linear, elastic model that calculates the normal and tangential contact forces on each body. The governing equations of this model are presented in 9. This contact model was selected for its simplicity, but other non-cohesive contact models can be used within this hybrid model framework. Liquid-particle collisions, which resulted in immediate coalescence, were simulated to apply no contact force on the new particle.

All particle-particle collisions were recorded and counted according to the sizes of the colliding particles. A four-dimensional array containing the total number of collisions between particles in each solid and liquid bin was generated and used within the PBM. The collision count was reset to zero after each PBM iteration.

The simulations were run for a total time of 10 s , with a fixed DEM time step of $1 \times 10^{-5}\text{ s}$. The geometric grid was simulated using a cell size of 2 mm .

5.2.3 Bi-directional coupling

A multi-scale model was created in which the PBM and DEM transfer information during the simulation. A schematic of this approach is shown in Figure 5.1.

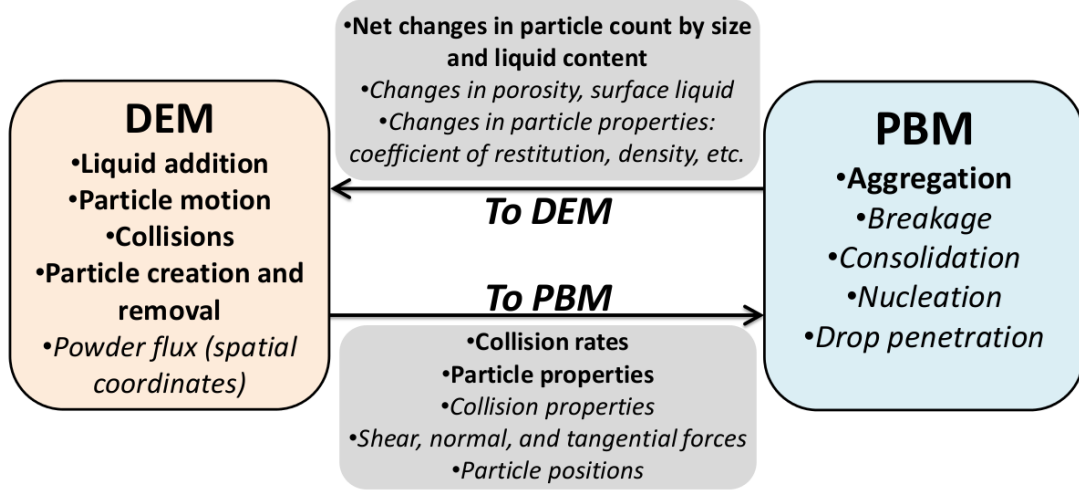


Figure 5.1: Schematic of multi-scale model and data transfer. In this study, the collision frequency and liquid addition behavior are considered to demonstrate the coupling algorithm. Remaining features will be presented in future work.

The PBM is used in the hybrid model to calculate the change in the number of particles of each solid and liquid volume over a set time interval. A linear grid with respect to volume was implemented. The initial particles were defined to be perfectly dry ($l = 0$), with a uniform initial solid volume, shown in Table 5.1, and liquid droplets contained no solid ($s = 0$), and had a uniform initial liquid volume. The initial volumes were used to space the bins equally along a grid. The fully discretized form of this model is given by Equation 5.9, which uses Euler integration to determine the change in the number of particles, ΔF , over the time interval.

$$\begin{aligned}
 \Delta F(s, l, t) = & \sum_{s'=0}^s \sum_{l'=0}^l N_{coll}(s-s', l-l', s', l', t) \Psi(s-s', l-l', s', l') \\
 & - \sum_{s'=0}^{s_{max}-s} \sum_{l'=0}^{l_{max}-l} N_{coll}(s, l, s', l', t) \Psi(s, l, s', l') \\
 & - \sum_{s'=0}^{s_{max}-s} \sum_{l'=0}^{l_{max}-l} N_{coll}(s', l', s, l, t) \Psi(s', l', s, l) \quad (5.9)
 \end{aligned}$$

s_{max} and l_{max} are the maximum solid and liquid volumes found in a particle within

the DEM simulation, which can change over time. These summations take advantage of the discrete nature of DEM, only performing calculations on particles that exist within the simulation. This approach circumvents the computational limitations of the grid size, as the maximum number of populated bins is a finite number less than the initial number of particles.

The number of collisions between each pair of bins over the time interval is recorded within the DEM simulation and transferred to the PBM. It should be noted that the number of particles in each bin, the normalized collision frequency, and the time interval size are not required to solve Equation 5.9 because they cancel out when combining Equations 5.4-5.7.

Each time the PBM is solved, a change in the particle distribution is calculated. To implement this change in DEM, particles are immediately destroyed or created. When ΔF is negative for a particular bin, particles must be destroyed. Particles within that bin are randomly selected and removed from the simulation.

Creating particles is more complex. When ΔF is positive, particles are created with the properties defined by the bin. A random position is assigned to the particle. Before creation, the new particle's position and size are checked against all other particles in the simulation to determine if there is overlap. A new position is attempted until the new particle does not overlap with any existing particles. This calculation requires the storage of each particle position and size at every step of the PBM. However, because the PBM is much less computationally demanding than the DEM, the effect on the total computation time is negligible. In simulations with a much greater number of particles or less available space, this computation may be inefficient.

Because DEM requires a discrete number of particles, fractional values of ΔF cannot be implemented. If the number of coalescence events between two bins, given by $N_{coll}\Psi$, is not a whole number, it must be rounded. A random number between zero and one is generated and compared to the decimal component of $N_{coll}\Psi$ to determine whether to round the number up or down to the nearest integer. While this rounding may have a small effect on the results, it is more representative of the discrete granulation process, where fractions of particles cannot exist.

The PBM is evaluated at specified time intervals, given by Δt . The time interval size was selected such that the randomly placed particles have ample time to settle and collide between PBM evaluations, minimizing the effect of their placement. Additionally, the time interval size must be small enough that the number of coalescing particles in a given bin is not greater than the number of existing particles. If each particle collides many times over a time interval, more than one coalescence event per particle may result. This requirement is an example of the Courant-Friedrichs-Lewy (CFL) condition, given by Equation 5.10

$$\frac{u \times \Delta t}{\Delta x} = C < 1, \quad (5.10)$$

where u is the velocity or growth rate, Δx is the grid spacing, and C is the Courant number (Ramachandran and Barton, 2010). Since this PBM does not include a growth rate, but instead includes a source term for the aggregation rate, the CFL condition can be adapted to form Equation 5.11.

$$-\frac{\mathfrak{R}_{agg} \times \Delta t}{F} = C < 1 \quad (5.11)$$

Three PBM time intervals were used to investigate these effects, as given in Table 5.1. A replicate simulation was performed with a PBM time interval of 0.1 s to demonstrate reproducibility and variation in the results due to random particle placement at the beginning and during the simulation.

5.3 Results and discussion

5.3.1 Effect of particle size distribution on collision rates

It has been reported that the collision rate is a function of particle size, and as a consequence various rate kernels have been proposed to capture this effect (Gantt et al., 2006; Tan et al., 2004; Darelus et al., 2005). However, no studies have captured the effect of the PSD on the collision frequency. Since the collision frequency is related to the packing of the particles and the interstitial space between large particles, the size distribution will affect the collision rate and its dependence on particle size. As the size distribution changes over time within the granulator, the collision frequency will also change, accounting for the temporal component

of the aggregation kernel, which traditionally has been lumped as an empirical constant that needs to be fitted from experimental data, thus limiting the predictive capability of the model.

To demonstrate the effect of the size distribution on the collision rate, DEM simulations were performed using four distributions, as presented in Figure 5.2. The collision rate, as a function of particle size, was determined independently for each distribution. Five particle types were defined with diameters between 1 *mm* and 5 *mm*. The number of particles of each size was varied to match the four distributions. The rotating drum granulator was filled with particles equaling a total volume 7500 *mm*³ according to the distributions presented. The particles were allowed to settle for 0.5 *s*. The number of collisions between each particle size during the 0.5 to 1.5 *s* interval was recorded. These totals were converted into normalized collision rates according to Equation 5.7. No size changes were implemented during these simulations.

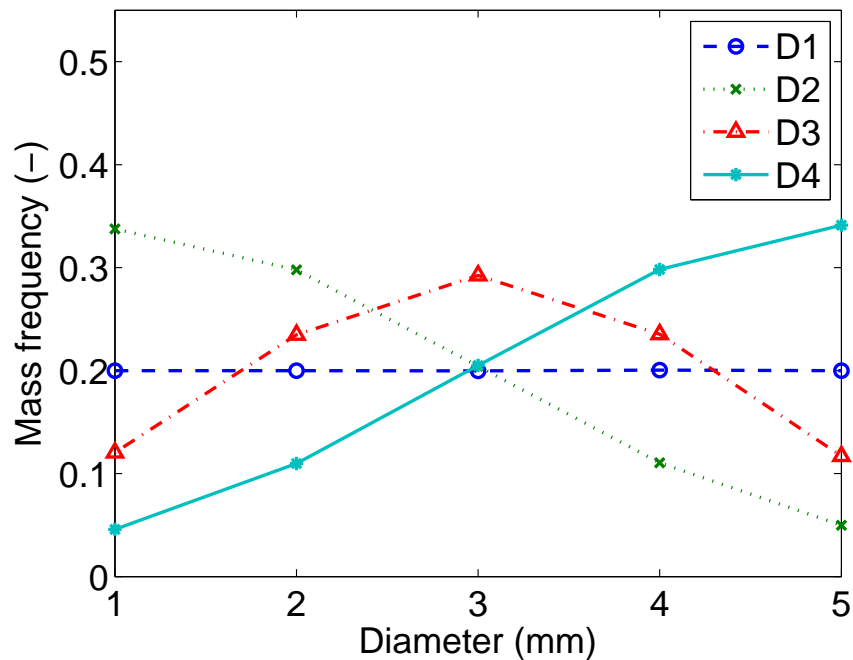


Figure 5.2: Size distributions used in DEM simulations to determine collision rates, from 1 – 5 *mm* in diameter.

The collision rates for each distribution are shown in Figure 5.3. In all cases, larger particles had greater collision rates than smaller particles. Small particles had lower collision

rates with other small particles than with larger particles. Particles of similar sizes were collided with each other less frequently than with particles of slightly different sizes, shown by the drop in collision rates along the axis of symmetry.

Despite these similarities, measurable differences are observed. The uniform size distribution (D1) showed similar trends as the size distribution with a greater frequency of medium-sized particles (D3). These distributions were the most similar, with the same median diameter. However, D3 shows lower collision frequencies between the largest particles and greater collision frequencies between medium-sized particles with large and small particles.

The skewed distributions showed greater differences. The distribution with a greater frequency of small particles (D2) showed lower collision frequencies overall, and the distribution with a greater frequency of large particles (D4) had greater collision frequencies. D2 shows strong size dependence, with larger particles colliding much more frequently than smaller particles. D4 showed a weaker size dependence, with large particles colliding with small particles most frequently, and particles of similar sizes colliding less often.

As the PSD develops within a granulator, the collision dynamics will also change. A PBM typically assumes that every particle can collide with every other particle, often at equal rates. Aggregation kernels can be used to account for the effects of size and other particle properties on the collision frequency and efficiency. However, no kernels describe the effects of the current size distribution on the aggregation rate. The effect of size on the collision frequency is dependent on the size distribution, and this interaction cannot be captured with a simple, size-dependent kernel. Because the collision frequency affects the aggregation rate, the temporal change in the size distribution is affected by the collision rate and, by extension, the current distribution.

To simulate this behavior within a process model, the collision rates must be updated in real time as the PBM is solved, demonstrating the need for bi-directional coupling of PBM with DEM. Because of the high computational expense of DEM, future approaches may involve developing a reduced order model to determine the effects of particle size and size distribution on the collision frequency.

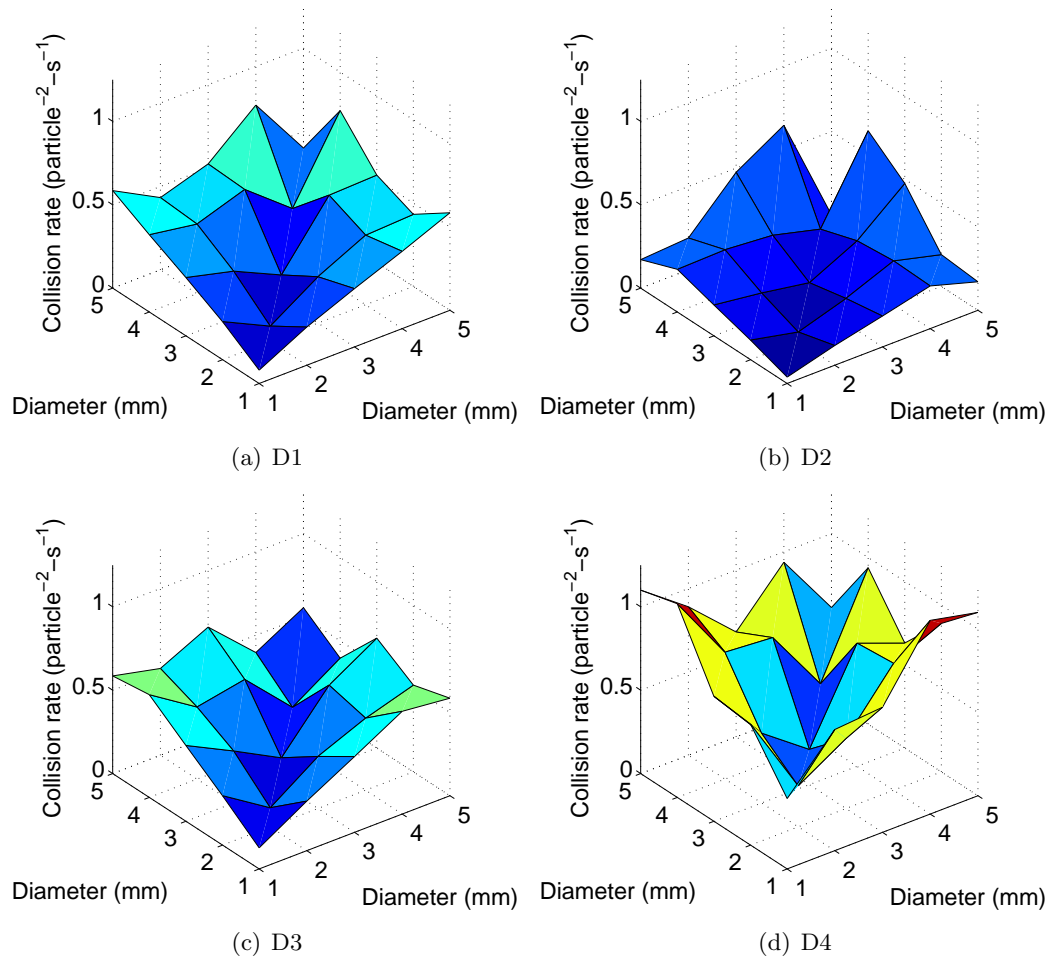


Figure 5.3: Collision frequency versus particle size for each distribution based on DEM simulations.

5.3.2 Hybrid model results

The fully-coupled hybrid model was used to simulate a simple rotating drum cylinder for a ten-second period. The simulation was completed in approximately six hours.

Figure 5.4 shows the conservation of solid and liquid volume over time. The total solid volume is constant over time, and the total liquid volume increases linearly during the liquid addition period but remains constant at all other times. These results support the validity of the numerical techniques used to solve the PBM and confirm the accuracy in implementing particle changes within the DEM.

Figure 5.5 shows the particles within the granulator at four different times, colored according to their liquid fraction for the simulation with a PBM time interval of 0.01 s .

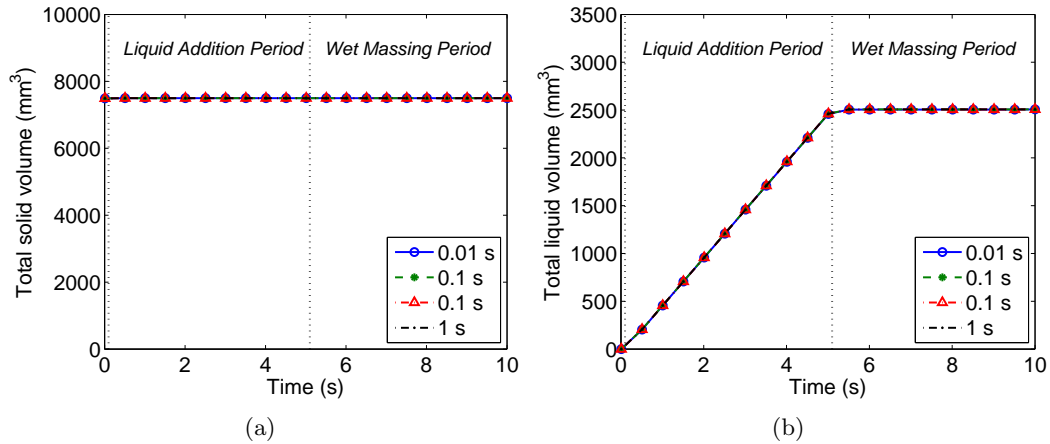


Figure 5.4: Total volumes of (a) solid and (b) liquid in the system over time for simulations of varying PBM time intervals. Replicate simulation performed at time interval of 0.1 s to show reproducibility.

Large particles develop over time as the particles aggregate. The largest particle present in the system at 5 s has a diameter of 2.76 mm and a liquid fraction of 0.36, corresponding to the PBM bin of [21, 12]. At 10 s, the largest particle has a diameter of 4.64 mm and a liquid fraction of 0.30, corresponding to the PBM bin of [100, 42].

The greatest liquid fraction of a powder particle decreases over time during the wet-massing period as aggregation occurs and wet particles merge with dryer particles. The greatest liquid fraction at 5 s is 0.75 for a particle of 1.44 mm in diameter. At 10 s, the greatest liquid fraction is 0.59 for a particle of 2.08 mm in diameter.

The average particle diameter increases from 0.98 mm to about 2.5 mm during the liquid addition and wet massing periods, as shown in Figure 5.6. This plot shows a discontinuous increase in average diameter for the simulation with the PBM time interval of 1 s, which can be attributed to the low frequency of PBM solution and particle replacement. Despite this result, all simulations resulted in approximately the same average diameter, presented in Table 5.2. The final $d_{4,3}$ of with a PBM time interval of 0.1 s were approximately 2.5% different than that of the PBM time interval of 0.01 s, suggesting that a PBM time interval of 0.1 s is sufficient to solve this model. The replicate simulations with a PBM time interval of 0.1 s resulted in slightly different average diameters, indicating some effect of the random placement of particles.

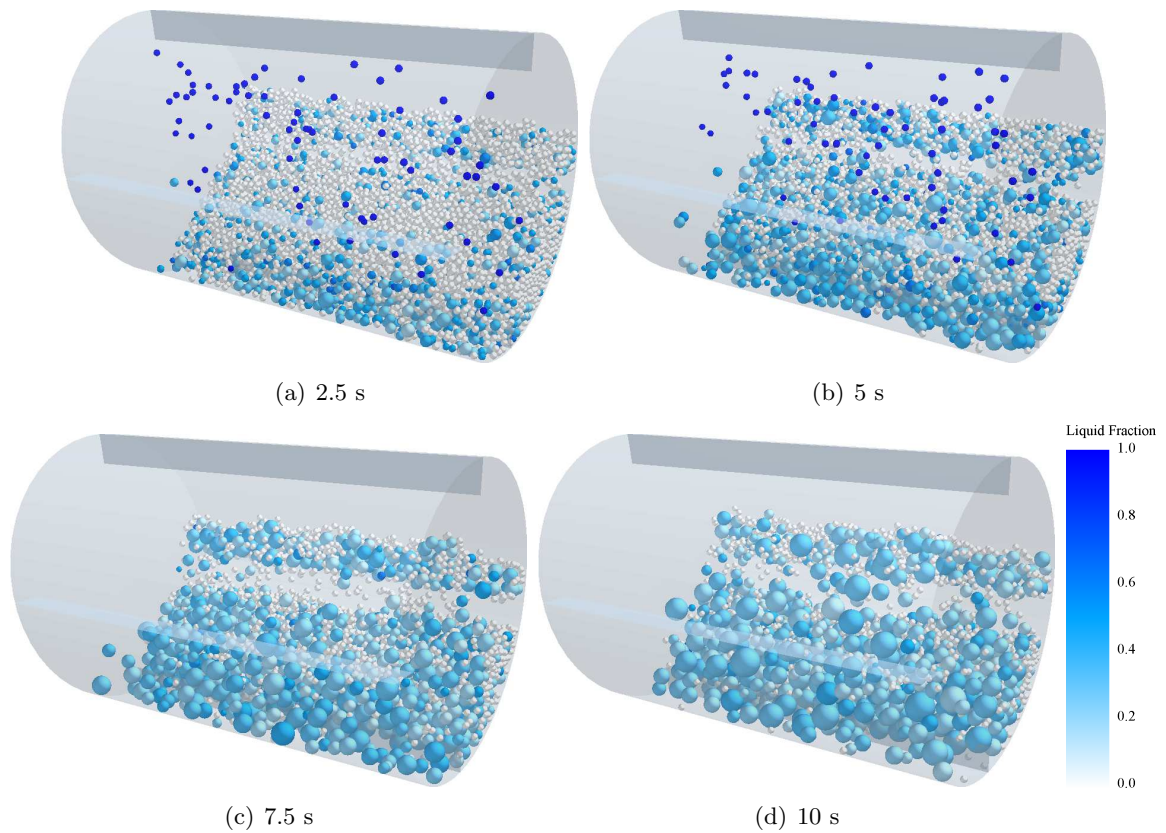


Figure 5.5: DEM image of particles at various times, colored by liquid fraction, using a PBM time interval of 0.01 s .

Table 5.2: Average diameter ($d_{4,3}$) after 10 seconds for simulations of varying PBM time intervals and percent error based on results of 0.01 s PBM time interval.

| PBM time interval (s) | $d_{4,3}(mm)$ | Percent error |
|-----------------------|---------------|---------------|
| 0.01 | 2.525 | - |
| 0.1 | 2.523 | 0.11 |
| 0.1 | 2.461 | 2.55 |
| 1 | 2.47 | 2.26 |

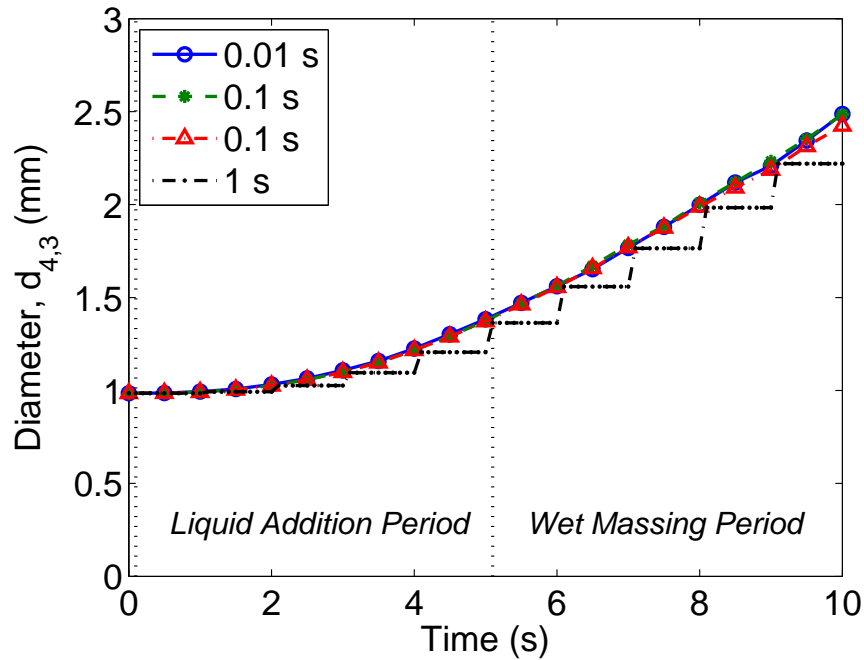


Figure 5.6: Average diameter ($d_{4,3}$) over time of the powder particles for simulations of varying PBM time intervals. Replicate simulation performed at time interval of 0.1 s to show reproducibility.

The average liquid fraction of each size class is shown in Figure 5.7. The average liquid fraction of the smallest particles increases during the liquid addition period, but decreases during the wet massing period as the wet particles aggregate and move to larger size classes. As particles form in each size class, the average liquid fractions of the larger size classes are high, a result of the wet particles aggregating. These values decrease over time as the large, wet particles aggregate with small, dry particles, reducing the average liquid content of the size class.

Figure 5.8 shows the PSDs at the end of each simulation. These distributions show that the simulation with the largest PBM time interval has a higher peak, or a lower frequency of very large and very small particles. This result can be attributed to numerical error. The PBM was only solved ten times in this simulation, limiting the opportunities for large particles to collide and aggregate with each other. The distributions for the smaller time intervals show more consistent results, suggesting that they are approaching an accurate solution.

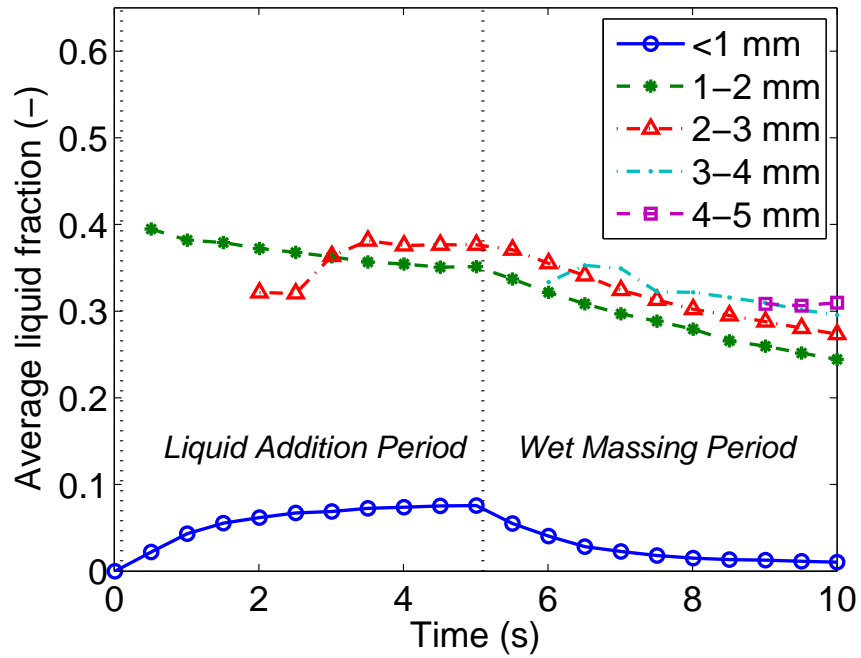


Figure 5.7: Average liquid fraction of powder particles over time for each size class, weighted by volume, for coupling time of 0.01 s.

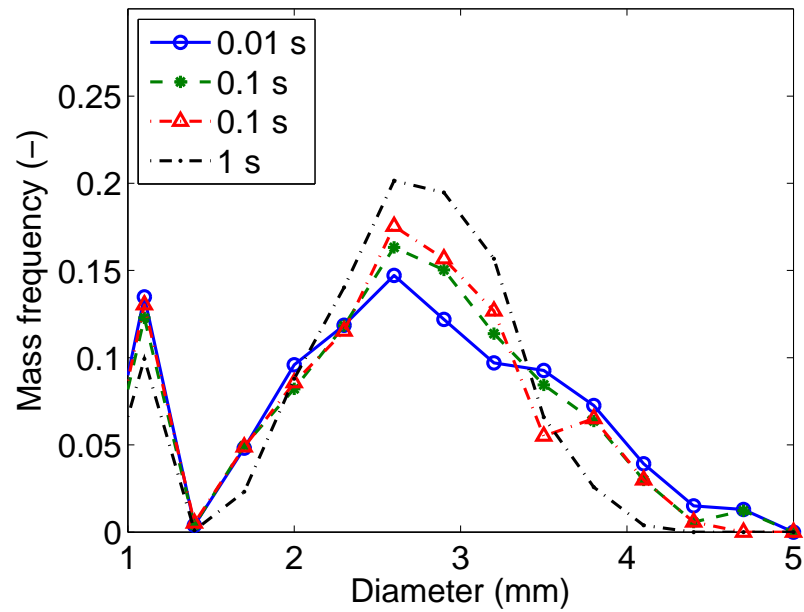


Figure 5.8: PSDs after 10 s for simulations of varying PBM time intervals. Replicate simulation performed at time interval of 0.1 s to show reproducibility.

The PSDs over time, presented in Figure 5.9, show a progression towards larger particles during granulation. An initially narrow size distribution widens over time to include larger particles. The mass frequency of smaller particles decreases, but many of the small particles still exist after ten seconds. This observation can be attributed to the inhomogeneous distribution of liquid, leaving many particles dry and unable to aggregate unless they collide with wet particles.

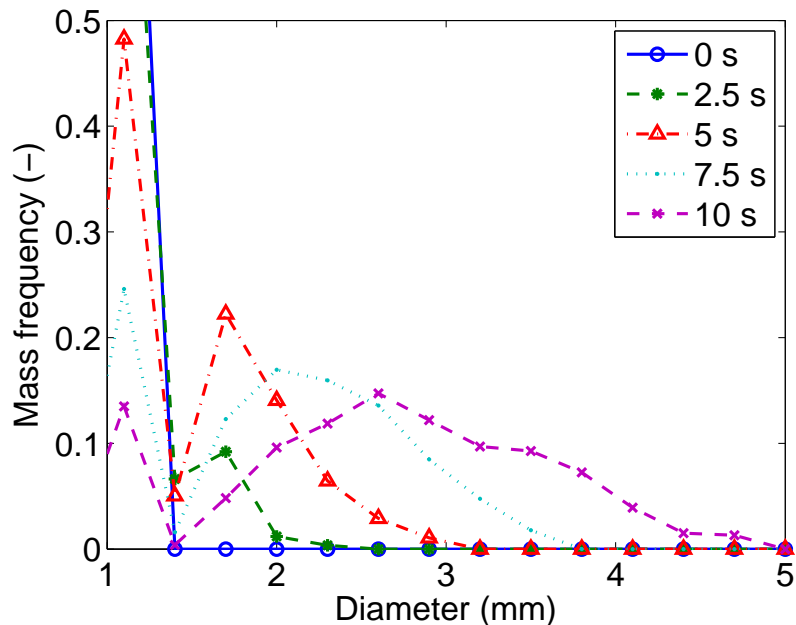


Figure 5.9: PSDs at various times using a PBM time interval of 0.01 s.

Two-dimensional particle distributions in size and liquid content support this explanation, as shown in Figure 5.10. The results show that even after ten seconds, the remaining small particles are completely dry. Additionally, during the liquid addition period, small, wet particles are present, but during the wet massing period, the only wet particles in the system are much larger. These results are consistent with the liquid-dependent collision efficiency used in the PBM.

The trends observed in this study are qualitatively consistent with experimental results. Experimental PSDs presented by Poon et al. (2009) are bimodal, with a shrinking frequency of primary particles over time and an increasing number of large particles. Ramachandran et al. (2008) also show bimodal PSDs that broaden over time, along with variations in the liquid binder content of different size classes. Additionally, the liquid addition and wet

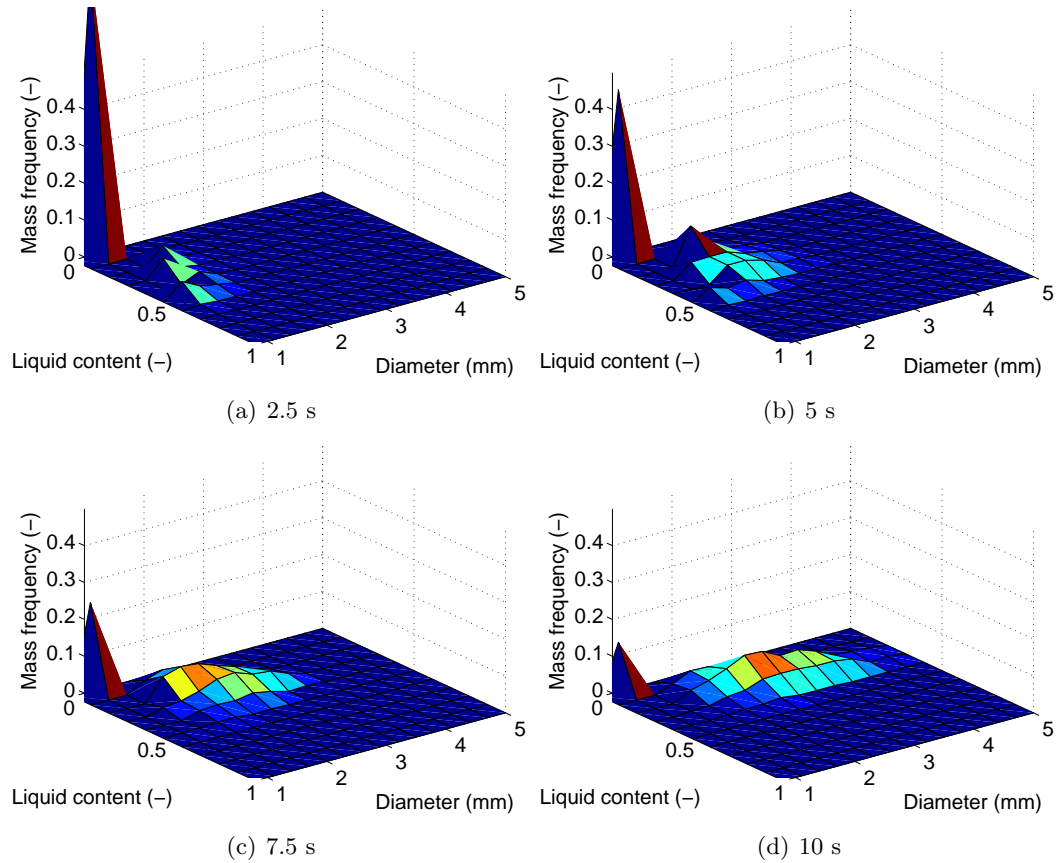


Figure 5.10: 2-D distributions of particle size and liquid content at various times using PBM time interval of 0.01 s.

massing dynamics observed by Pandey et al. (2013) agreed with the simulated results.

A more mechanistic expression for the collision efficiency, along with additional information transferred from the DEM, can be implemented within this framework. Future work is also needed to improve the liquid distribution model, accounting for the different sizes and properties of liquid droplets and the spatial inhomogeneities that persist during aggregation.

To simulate industrial systems, which are typically larger than those presented here, and finer particle sizes, which can be as small as $10\ \mu\text{m}$, many more particles must be simulated. The model will become more computationally expensive. The coded model can be optimized for better performance and simulated on a more advanced computer architecture to facilitate larger-scale simulations. Alternatively, reduced order models, such as artificial

neural networks, can be developed and trained using DEM data to replace the computationally expensive DEM. This approach still requires a limited number of DEM simulations for training, but can result in a much faster model suitable for iterative calculations and flowsheet modeling. Current research has involved developing reduced order models in place of DEM to couple with PBM (Barrasso et al., 2014).

5.4 Summary

In this study, a multi-scale model for wet granulation processes was presented using DEM and PBM techniques. Because PBMs rely on rate expressions, lumping all members of each class together, they have limited ability to capture the mechanistic behavior of particles in complex wet granulation processes. DEM can simulate dynamic particle-level behavior, tracking each individual particle and collision. However, DEM does not inherently simulate the sub-processes of granulation, such as aggregation and breakage. By coupling these models in real time, a hybrid modeling framework was developed.

The collision frequency between particles of different sizes was investigated. While the collision frequency is known to be dependent on particle size, the effect of the PSD had not been studied. It was demonstrated that the PSD significantly affects the shape and magnitude of the collision frequency function, accounting for the temporal dependence of the aggregation rate kernel. The collision frequency affects the aggregation rate kernel and influences the evolution of the PSD, demonstrating the need for bi-directional coupling between DEM and PBM.

A 2-D PBM was implemented within a DEM, accounting for simultaneous variations in particle size and liquid fraction. Initial particles were defined as powder or liquid, and liquid addition was handled within DEM, allowing for inhomogeneities in liquid distribution. Collision rates were recorded according to particle size and wetness, and this information was provided to the PBM at specified time intervals. The PBM calculated net changes in the number of particles, which were implemented in DEM by creating and removing particles.

The multi-scale model was successful in simulating particle size enlargement over time

resulting from liquid addition and aggregation. PSDs were determined, along with 2-D distributions in size and liquid fraction. Additionally, volume conservation was demonstrated, validating the numerical techniques of the model.

An empirical expression for the collision efficiency was used in this study. The collision efficiency has been shown to depend on the relative velocity of the colliding particles, their masses, and the surface liquid available on the particles. Within this multi-scale framework, these properties can be tracked and incorporated into a mechanistic expression for the collision efficiency. Additional particle properties, such as porosity and surface/internal liquid must be included, resulting in variable density and coefficient of restitution among the particles.

Liquid droplet distribution was simulated in this study, resulting in dry fine powder and wetter large particles. The current multi-scale model simulates processes in which the liquid droplets are of comparable size to the powder particles, as is observed in sprayers, and each liquid droplet only wets one particle. In some processes, a larger droplet can wet numerous particles, often resulting in nucleation. Additional work is needed to incorporate nucleation into the existing framework. Spatial coordinates or compartments can also be included within the PBM to ensure that changes in the number of particles are implemented in the region where the rate processes are occurring.

The additional rate processes of breakage and consolidation are typically modeled using empirical expressions in PBM. However, both of these sub-processes are affected by particle-particle and particle-wall collisions, and more mechanistic expressions can be developed using information from DEM simulations. The breakage rate depends on the forces exerted on each particle, information that is available from DEM. The consolidation rate also depends on impact forces. As particles collide with each other or equipment, they consolidate, resulting in a reduced porosity and an increased density.

Using the multi-scale framework, predictive models of wet granulation processes can be created, leading to a better understanding of the effects of material properties and process parameters on critical quality attributes. This detailed, model-based approach is necessary to accurately represent wet granulation processes and implement QbD in design, control,

and optimization of powder processes.

Chapter 6

A multi-scale, mechanistic model of a wet granulation process using a novel bi-directional PBM-DEM coupling algorithm

In this study, a novel mechanistic model for a wet granulation process is presented, combining the techniques of population balance modeling and discrete element methods to predict critical quality attributes of the granule product, such as porosity and size distribution. When applied to a twin screw granulation process, the model shows sensitivities to the screw element type and geometry, as well as material properties (binder viscosity, pore saturation) and process parameters (screw speed, liquid-to-solid ratio). Predicted trends are consistent with experimental observations in the literature. Using this modeling framework, a model-based approach can be used to implement Quality by Design, establishing a design space to transition towards a quantitative mechanistic understanding of wet granulation processes.

6.1 Background

Traditionally, models of wet granulation processes fall into one of two categories: process models or particle-scale models. Population balance modeling (PBM) is a process modeling framework that groups particles into classes based on their sizes and other properties, tracking changes in the number of particles in each class as they undergo rate processes, such as aggregation and breakage. PBMs have been used extensively to simulate wet granulation processes (Cameron et al., 2005; Verkoeyen et al., 2002). Multi-dimensional PBMs are particularly useful in tracking distributions of multiple particle properties, such as size, liquid content, and porosity, which can affect the aggregation and breakage rates in the system (Immanuel and Doyle III, 2005; Poon et al., 2008).

The development of accurate descriptions of aggregation and breakage rate expressions is an area of significant research. Many rate kernels are empirical and require estimation of unknown parameters from experimental data. Parameter estimation and validation have been performed for wet granulation processes, but these calibrated models have limited predictive capabilities outside of their experimental design spaces (Braumann et al., 2010; Ramachandran and Barton, 2010; Man et al., 2010; Chaudhury et al., 2014a; Barrasso et al., 2015a).

Mechanistic expressions have also been developed, describing aggregation (Darelius et al., 2005; Poon et al., 2008; Chaudhury et al., 2014b) and breakage (Ramachandran et al., 2009) rates. These expressions account for the effects of material properties, such as surface wetness, density, and yield strength. Since mechanistic expressions are based on particle-scale phenomena, such as individual collisions, they typically include terms for collision rates and particle velocities. This particle-scale information is not inherently known, and may depend on process parameters, equipment geometry, and material properties.

In contrast, discrete element modeling (DEM) is a particle-scale framework that tracks individual particles as they move through space and collide. Developed for soft spheres by Cundall and Strack (1979), this high-fidelity modeling tool provides the detailed particle-scale information that the PBM lacks, such as collision rates and velocity profiles, and is sensitive to process parameters, equipment geometry, and material properties. However, DEM does not inherently account for changes in particle size and other properties resulting from aggregation, breakage, consolidation, and liquid addition.

Because of the complementary advantages and limitations of each framework, efforts have been made to couple PBM and DEM. Ingram and Cameron (2005) discussed alternative multi-scale approaches for this problem, focusing on the information exchanged between the two frameworks and their integration. Most multi-scale studies involve one-directional coupling, where DEM data is collected and used within a PBM. Gantt et al. (2006) used DEM to evaluate mechanistic coalescence kernels for use in a PBM, and Bouffard et al. (2012) used DEM results to evaluate a spatial transfer in a compartmental PBM. Goldschmidt et al. (2003) used DEM simulations to solve a PBM, replacing small particles with

larger ones as they successfully coalesce. Additionally, Reinhold and Briesen (2012) developed a coupled PBM-DEM model for wet granulation, using DEM simulations to evaluate a mechanistic aggregation rate kernel. Recently, Barrasso and Ramachandran (2015a) implemented bi-directional coupling between PBM and DEM to evaluate collision frequencies and liquid distribution as a proof-of-concept, and Sen et al. (2014) combined this work with a computational fluid dynamics model to simulate fluidized bed granulation. Further, Barrasso et al. (2014) used DEM data to train an artificial neural network, which was then coupled with a PBM to capture collision rates as they depend on the impeller speed, particle size, and size distribution in the system.

Various types of equipment can be used for wet granulation, including high shear mixers, fluidized beds, and twin screw extruders. This study focuses on twin-screw granulation (TSG), which has potential advantages in continuous pharmaceutical manufacturing because of its low throughput, flexible design, and short residence time (El Hagrasy et al., 2013). However, the multi-scale modeling approach presented in this study can be applied to the general class of wet granulation systems.

In this study, a bi-directional coupling algorithm for PBM and DEM is presented and demonstrated for a twin-screw wet granulation process, developing a hybrid model to predict the effects of material properties, process parameters, and equipment geometry on the CQAs of the product.

6.1.1 Objectives

In order to predict the CQAs of a granulation process, a mechanistic process model is coupled to a particle-scale model. The purposes of this study are to:

- Present a mechanistic, two-dimensional PBM for a wet granulation process with sensitivities to material properties, process parameters, and particle-scale behavior.
- Develop an efficient bi-directional coupling algorithm, using DEM simulations to provide particle-scale data to the PBM.
- Determine the optimal settings for the model by characterizing the DEM simulation results.

- Apply the model to a twin-screw granulation process and demonstrate the model's sensitivity to equipment geometry, process parameters, and material properties on the CQAs of the product.

This work extends on previous models presented by Barrasso and Ramachandran (2015a) and Sen et al. (2014), incorporating mechanistic expressions for aggregation, breakage, and consolidation and evaluating these rates using particle velocity and collision data from DEM. Variations in particle properties, such as porosity and liquid content, are also accounted for in DEM simulations using empirical correlations for coefficients of restitution and Young's moduli.

6.2 Model development

A bi-directionally coupled model was designed to use particle-scale information from DEM simulations within a mechanistic PBM, which tracked changes in the particle size distribution, liquid content, and porosity. The hybrid model captures sensitivities of the product CQAs with respect to material properties, process parameters, and equipment geometries. An overall schematic of the model is presented in Figure 6.1. The model was applied to individual axial compartments in a TSG with no material inflow or outflow, treating the process as a batch system. Future work involves combining several compartments and quantifying flow behavior between them using DEM simulations to create a fully representative model of a continuous TSG.

6.2.1 Population balance model development

A detailed, two-dimensional PBM was developed and solved using gPROMS ModelBuilder 4.0 (Process Systems Enterprise). The resulting population balance equation (PBE), shown in Equation 6.1, tracks particle distributions with respect to size and liquid volume as the particles undergo aggregation, breakage, consolidation, and liquid addition. Nucleation and layering were omitted from this study to focus on the later stages of granulation after nuclei

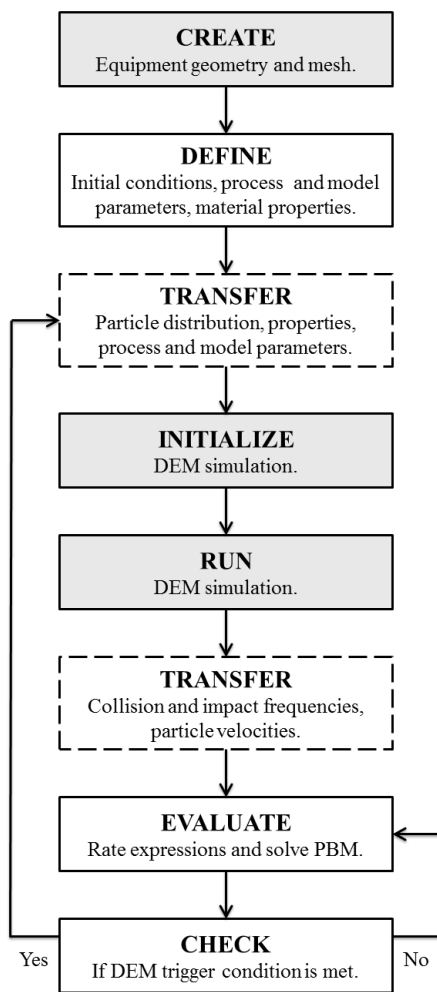


Figure 6.1: Schematic of bi-directional coupling approach. Boxes shaded in gray are executed in STAR-CCM+, and white, solid-lined boxes are executed in gPROMS Model-Builder. Dashed lines indicate data transfer across software platforms. Steps contained within the loop are fully automated, while steps outside the loop require user input.

have formed. In future work, these subprocesses will be incorporated into this framework.

$$\begin{aligned} \frac{\partial F}{\partial t} + \frac{\partial}{\partial V} \left(F \frac{dV}{dt} \right) + \frac{\partial}{\partial V_L} \left(F \frac{dV_L}{dt} \right) &= \mathfrak{R}_{agg} + \mathfrak{R}_{break} \\ F &= F(V, V_L, t) \end{aligned} \quad (6.1)$$

The particle volume is given by V , and the volume of liquid contained within or on the surface of the particle is given by V_L . The number of particles in each size and liquid class is given by F . The convective terms represent the change in the number of particles in each class due to consolidation and liquid addition, as the particles experience property changes and move throughout the 2-D grid. The aggregation and breakage source terms are given by \mathfrak{R}_{agg} and \mathfrak{R}_{break} .

In order to track the porosity of each class, the lumped parameter approach was used, assuming that all particles of the same size and wetness have the same porosity (Barrasso and Ramachandran, 2012; Barrasso et al., 2013b). The resulting PBE is given in Equation 6.2, where V_S is the volume of solid, per particle, in each class.

$$\begin{aligned} \frac{\partial FV_S}{\partial t} + \frac{\partial}{\partial V} \left(FV_S \frac{dV}{dt} \right) + \frac{\partial}{\partial V_L} \left(FV_S \frac{dV_L}{dt} \right) &= \mathfrak{R}_{S,agg} + \mathfrak{R}_{S,break} \\ V_S &= V_S(V, V_L, t) \end{aligned} \quad (6.2)$$

The remainder of the volume is occupied by pores. Here, the convective terms account for the transfer of solid as particles move along the grid due to consolidation and liquid addition. $\mathfrak{R}_{S,agg}$ and $\mathfrak{R}_{S,break}$ track the rates of change in the total solid volume in each class due to aggregation and breakage.

These four rate processes can strongly influence the CQAs of the product. Aggregation and breakage result in particle size changes, affecting the product size distribution. Further, the amount of liquid on the surface of the particles affects the rate at which aggregation occurs, so the amount and distribution of liquid binder influences the product size distribution. The consolidation rate determines the porosity of the product granules, affecting the strength and compatibility of the product granules. Additionally, the porosity will influence the breakage rate, as weaker particles break more easily, and the aggregation rate, as a decrease in porosity results in more liquid available on the surface of particles.

Using the 2-D PBM with the lumped parameter of pore volume, three particle properties are tracked: particle volume, liquid volume, and solid volume. From these three attributes, additional properties are evaluated. The volume of liquid associated with each particle was considered to be independent of the total volume, assuming that the liquid either occupies pore space or remains on the surface, outside of the particle. The total volume of the particle is composed of the solid volume and the pore volume (V_P), given by Equation 6.3. Assuming that all particles in the system are spherical, the particle diameter can be calculated based on the particle volume, or the first internal coordinate in the PBM (Equation 6.4). As shown in Equation 6.5, the porosity (ϵ) is the ratio of the pore volume to particle volume.

$$V = V_S + V_P \quad (6.3)$$

$$d = \left(\frac{6V}{\pi} \right)^{\frac{1}{3}} \quad (6.4)$$

$$\epsilon = \frac{V_P}{V} \quad (6.5)$$

The aggregation rate is strongly affected by the amount of liquid on the surface of particles (Ennis et al., 1991; Iveson et al., 2001). To capture this effect, a distinction is made between internal ($V_{L,int}$) and external ($V_{L,ext}$) liquid, as shown in Equations 6.6 and 6.7.

$$V_L = V_{L,int} + V_{L,ext} \quad (6.6)$$

$$V_{L,int} = \min(V_L, s^* V_P) \quad (6.7)$$

Liquid is assumed to penetrate the pore space instantly until a maximum fraction of the pore volume, given by s^* , is filled (Chaudhury et al., 2014b). Any additional liquid remains on the surface and contributes to aggregation. The value of s^* is presented in Table 6.1.

As shown in Equations 6.8 and 6.9, the wet (m_{wet}) and dry (m_{dry}) masses of each particle can be calculated based on the densities of the solid and liquid components, ρ_S and ρ_L , assuming vacant pore space has negligible mass.

$$m_{wet} = V_S \rho_S + V_L \rho_L \quad (6.8)$$

$$m_{dry} = V_S \rho_S \quad (6.9)$$

Table 6.1: Values of input parameters representing the base case.

| Parameter | Type | Value |
|--|-----------|-------------------------|
| Liquid-to-solid ratio ($L : S$) | process | 0.25 |
| End of liquid addition ($t_{liquid,stop}$) | process | 15 s |
| Batch time (t_{batch}) | process | 30 s |
| Screw speed | process | 240 RPM |
| Maximum pore saturation fraction (s^*) | material | 0.75 |
| Binder viscosity (μ) | material | 0.05 Pa s |
| Primary particle size (d_p) | material | 5 μm |
| Density of solid component (ρ_S) | material | 2000 kg m ⁻³ |
| Density of liquid component (ρ_L) | material | 1000 kg m ⁻³ |
| Consolidation rate constant (K_{cons}) | material | 0.005 |
| Surface asperity height (h_a) | material | 5 μm |
| Critical Stokes deformation number (St_{def}^*) | material | 0.2 |
| Coefficient of restitution slope, intercept (e_{slope}, e_0) | material | 0.5, 0.5 |
| Poisson's ratio | material | 0.2 |
| Ratio of Young's modulus to yield strength | material | 162 |
| Particle-particle coefficients of static, rolling friction | material | 0.35, 0.2 |
| Particle-wall coefficients of static, rolling friction | material | 0.16, 0.2 |
| Initial median diameter (d_{50}) | initial | 0.75 mm |
| Initial standard deviation of particle size | initial | 0.2 mm |
| Initial volume charge | initial | 1500 mm ³ |
| Initial porosity | initial | 0.6 |
| Number of grid points in each dimension (N, N_L) | model | 9, 10 |
| DEM settling, simulation times ($\Delta t_{settle}, \Delta t_{DEM}$) | model | 0.1 s, 0.25 s |
| Trigger condition: absolute change in L:S ratio | model | 0.05 |
| Trigger condition: relative change in $d_{4,3}$ | model | 10% |
| Implicit unsteady solver time step | model | 1e-4 s |
| Screw section length | equipment | 16 mm |
| Screw diameter | equipment | 16 mm |

The values for ρ_S and ρ_L are listed in Table 6.1.

Assuming that liquid is distributed evenly with respect to particle volume, the rate of liquid addition, per particle, is given by Equation 6.10.

$$\frac{dV_L}{dt} = \frac{\dot{L}_{in}V}{V_{total}} \quad (6.10)$$

\dot{L}_{in} is the total volumetric rate of liquid addition to the system and V_{total} is the total volume of particles in the system. Liquid was added between $t = 0\text{s}$ and $t = t_{liquid,stop}$. During this

period, the total liquid addition rate is given by Equation 6.11.

$$\dot{L}_{in} = \frac{(L : S)V_{S,total}}{t_{liquid,stop}} \quad (6.11)$$

$V_{S,total}$ is the total volume of solid in the system, and $L : S$ is the overall liquid-to-solid ratio. The values of these parameters are listed in Table 6.1.

As porous particles collide and deform, their porosity decreases, resulting in smaller, denser granules with a greater amount of surface liquid. The consolidation rate expression used in this study is based on that presented by Ennis et al. (1991) and Tardos et al. (1997), in which the degree of consolidation for a single collision depends on the viscous or deformation Stokes number. Based on this theory, the rate of change in the volume of a particle is given by Equation 6.12.

$$\frac{dV}{dt} = -K_{cons}V_P C_{impact} (1 - \exp(-St_{def})) \quad (6.12)$$

K_{cons} is a rate constant representing the fraction of pore space affected by a single collision, given in Table 6.1. The impact rate, in collisions per particle per second, is given by C_{impact} . The value for C_{impact} was evaluated using DEM to capture dependencies on the particle properties, equipment geometry, and process parameters, including particle-particle and particle-wall/screw collisions. It should be noted that particle-wall/screw collisions accounted for approximately 40% of all impacts for the base case in DEM simulations. St_{def} is Stokes deformation number, given by Equation 6.13.

$$St_{def} = \frac{\rho_S U_0^2}{2\tau_y} \quad (6.13)$$

U_0 is the particle velocity, and τ_y is the yield strength (Tardos et al., 1997; Iveson et al., 2001). The average particle velocity for each size and liquid class was obtained using DEM simulations, and the dynamic yield strength was approximated based on the porosity using Equation 6.14, where μ is the binder viscosity and d_p is the diameter of the primary particles, given in Table 6.1 (Van den Dries and Vromans, 2002).

$$\tau_y = \frac{9}{8} \frac{(1 - \epsilon)^2}{\epsilon^2} \frac{9\mu U_0}{16d_p} \quad (6.14)$$

Aggregation is a primary mechanism of particle growth in wet granulation processes. Collisions between wet particles can result in coalescence, effectively replacing two small particles with one larger particle. As shown in Equation 6.15, the net aggregation rate of a particular class is equal to the difference between the rates of formation ($\mathfrak{R}_{agg,form}$) and depletion ($\mathfrak{R}_{agg,dep}$) (Immanuel and Doyle III, 2005; Barrasso and Ramachandran, 2012).

$$\begin{aligned} \mathfrak{R}_{agg}(V, V_L, t) &= \mathfrak{R}_{agg,form}(V, V_L, t) - \mathfrak{R}_{agg,dep}(V, V_L, t) = \\ & \frac{1}{2} \int_0^V \int_0^{V_L} \beta(V - V', V_L - V'_L, V', V'_L, t) F(V - V', V_L - V'_L, t) F(V', V'_L, t) dV'_L dV' \\ & \quad - \int_0^\infty \int_0^\infty \beta(V, V_L, V', V'_L, t) F(V, V_L, t) F(V', V'_L, t) dV'_L dV' \end{aligned} \quad (6.15)$$

The aggregation rate kernel, $\beta(V, V_L, V', V'_L, t)$, describes the rate at which two particles in classes V, V_L and V', V'_L coalesce. Because the rate kernel can depend on particle porosity, which is tracked as a lumped parameter, its value can change over time as the particles consolidate. The aggregation rate kernel can be thought of as the product of the frequency of collisions between the two classes $C_{collision}$ and the probability that a collision will result in coalescence Ψ , as shown in Equation 6.16 (Gantt et al., 2006; Barrasso and Ramachandran, 2015a).

$$\beta(V, V_L, V', V'_L, t) = C_{collision}(V, V', t) \Psi(V, V_L, V', V'_L, t) \quad (6.16)$$

The collision frequency was evaluated on a per-particle basis using DEM simulations, which reported the number of collisions between any two size classes. For the purposes of this study, it was assumed that the collision frequency is independent of liquid content, and all collisions between two size classes were counted equally regardless of their liquid classes.

The collision efficiency was estimated based on the Stokes criterion for Type I coalescence, which states that a collision is successful if the viscous Stokes number associated with the collision, St_v , is less than the critical Stokes number of the particles, St_v^* , given by

Equations 6.17 and 6.18 (Iveson et al., 2001).

$$St_v = \frac{8\tilde{m}U}{3\pi\tilde{d}^2\mu} \quad (6.17)$$

$$St_v^* = \left(1 + \frac{1}{e}\right) \log\left(\frac{h}{h_a}\right) \quad (6.18)$$

The harmonic mean masses and diameters of the two particles are given by \tilde{m} and \tilde{d} , and the collision velocity is given by U . e is the coefficient of restitution, h is the thickness of the liquid on the surface of the particle, equal to $\frac{dV_{L,ext}}{6V}$, and h_a is the height of the surface asperities, given in Table 6.1 (Liu et al., 2000). Based on this criterion, a critical velocity, U_{crit} can be determined below which all collisions result in coalescence, as shown in Equation 6.19

$$U_{crit} = \left(1 + \frac{1}{e}\right) \log\left(\frac{h}{h_a}\right) \frac{3\pi\tilde{d}^2\mu}{8\tilde{m}} \quad (6.19)$$

The collision efficiency was evaluated from a collision velocity distribution, $p(U)$, as presented in Equation 6.20.

$$\Psi = \int_0^{U_{crit}} p(U)dU \quad (6.20)$$

Based on an examination of DEM results, the collision velocity distribution between any two particle classes was assumed to obey a log-normal distribution, shown in Equation 6.21, where U_0 and sd_U are the mean and standard deviation of the velocity, respectively.

$$p(U) = \frac{1}{U\sqrt{2\pi}\sigma} \exp\left[-\frac{(\ln U - \mu)^2}{2\sigma^2}\right] \quad (6.21)$$

$$U_0 = e^{\mu - \sigma^2/2} \quad (6.22)$$

$$sd_U^2 = (e^{\sigma^2} - 1)e^{2\mu + \sigma^2} \quad (6.23)$$

The mean and standard deviation of the collision velocity for any two classes were assumed to be equal to the average values of the particles in those classes. The particle velocities for each class and their standard deviations were obtained from DEM simulations.

Similarly, the net breakage rate was evaluated for each class from the formation and

depletion terms, as shown in Equation 6.24.

$$\begin{aligned} \mathfrak{R}_{break}(V, V_L, t) &= \mathfrak{R}_{break,form}(V, V_L, t) - \mathfrak{R}_{break,dep}(V, V_L, t) = \\ &\int_V^\infty \int_{V_L}^\infty b(V', V'_L, V, V_L) K_{break}(V', V'_L, t) F(V', V'_L, t) dV' dV'_L \\ &\quad - K_{break}(V, V_L, t) F(V, V_L, t) \end{aligned} \quad (6.24)$$

The rate of breakage, per particle, in each class is given by $K_{break}(V, V_L, t)$, and the number of fragment particles forming into class V, V_L from a single breakage event of V', V'_L is given by $b(V', V'_L, V, V_L)$.

A simple breakage distribution function was assumed, stating that all breakage events result in two particles of equal size and liquid volume, as presented in Equation 6.25.

$$b\left(V', V'_L, \frac{V'}{2}, \frac{V'_L}{2}\right) = 2 \quad (6.25)$$

For all other values of V and V_L , $b = 0$.

The breakage rate kernel was evaluated based on a Stokes criterion, where an impact will result in breakage if the associated Stokes deformation number is greater than a critical Stokes deformation number, St_{def}^* (Tardos et al., 1997; Iveson et al., 2001). By combining this criterion with Equations 6.13 and 6.14 and solving for the velocity, a critical breakage velocity (U_{break}) is determined, above which breakage will occur, as shown in Equation 6.26.

$$U_{break} = \frac{2St_{def}^*}{\rho_S} \frac{9(1-\epsilon)^2}{8\epsilon^2} \frac{9\mu}{16d_p} \quad (6.26)$$

Various values for St_{def}^* have been reported in the literature, ranging from 0.01 to 0.2 (Van den Dries and Vromans, 2002; Liu et al., 2009; Smith et al., 2010). The value used in this study is listed in Table 6.1.

As with aggregation, a log-normal impact velocity was assumed based on the average particle velocity of each class obtained from DEM simulations. Shown in Equation 6.27, the breakage kernel is equal to the product of the impact rate and the fraction of those impacts resulting in breakage, evaluated from the velocity distribution function.

$$K_{break} = C_{impact} \int_{U_{break}}^\infty p(U) dU \quad (6.27)$$

The initial particle size distribution was assumed to follow a log-normal mass distribution, with a fixed median diameter (d_{50}), standard deviation, and total volume. These values, along with the initial porosity, are listed in Table 6.1. All particles were assumed to be dry initially, with negligible liquid volume.

To solve this PBM, the two internal coordinates were discretized to form a 2-D grid. The volume coordinate was discretized into N classes, with the diameter (in mm) of each class i defined in Equation 6.28. The liquid volume coordinate was divided into N_L classes, where the smallest class represents negligible liquid volume, and the remaining classes have liquid volumes equal to those of the volume grid. Finite difference methods were used to evaluate the convective terms for consolidation and liquid addition on the discretized grid. The aggregation and breakage source terms were evaluated using the cell average technique (Chaudhury et al., 2013a; Barrasso and Ramachandran, 2012). The resulting system of algebraic and ordinary differential equations were solved using the differential-algebraic numerical solvers in gPROMS, which uses a backwards differentiation formula for dynamic integration. The values for N and N_L are provided in Table 6.1.

$$d(i) = 0.5 \exp\left(\frac{i-1}{4}\right) \text{ mm} \quad (6.28)$$

Throughout this PBM, mechanistic rate expressions call for additional data to describe particle velocity and collision behavior. For example, the particle velocity distribution affects the aggregation, breakage, and consolidation rates. At greater velocities, breakage and consolidation occur, while aggregation is favored at lower velocities. Additionally, the rates of collisions between any two particle sizes influences their aggregation rates, and the impact frequency is used in breakage and consolidation rate expressions. The values for these parameters may depend on equipment geometry (screw element configuration, impeller design), material properties (density, coefficient of restitution), process parameters (screw/impeller speed), and the state of the system (size distribution, liquid fraction). To evaluate this particle-scale behavior, the PBM is coupled with DEM simulations.

6.2.2 Discrete element method simulations

DEM simulations were performed using STAR-CCM+ v9.02 (CD-adapco). A 3-D CAD model was created in STAR-CCM+ for an axial section of a twin-screw granulator based on the EuroLab 16mm TSG (Thermo Fisher Scientific). The length of the section and the screw diameter are listed in Table 6.1. As shown in Figure 6.2, two screw element types were modeled: a block of mixing elements and a feed screw. The screws were rotated at a fixed speed, and a sliding interface was created to resolve the boundary between the screw space and the wall. A periodic interface was created from the axial boundaries of the TSG section to allow particles that exit the section to enter from the other side. This geometry was meshed using the polyhedral mesher and embedded thin mesher models in STAR-CCM+, resulting in approximately 40,000 volume cells to capture the geometric details of the equipment. The implicit unsteady solver was used with a fixed time step, as given in Table 6.1, and the DEM solver uses a variable time step to sub-step the simulation as the particles move, balancing accuracy, stability, and computational expense.

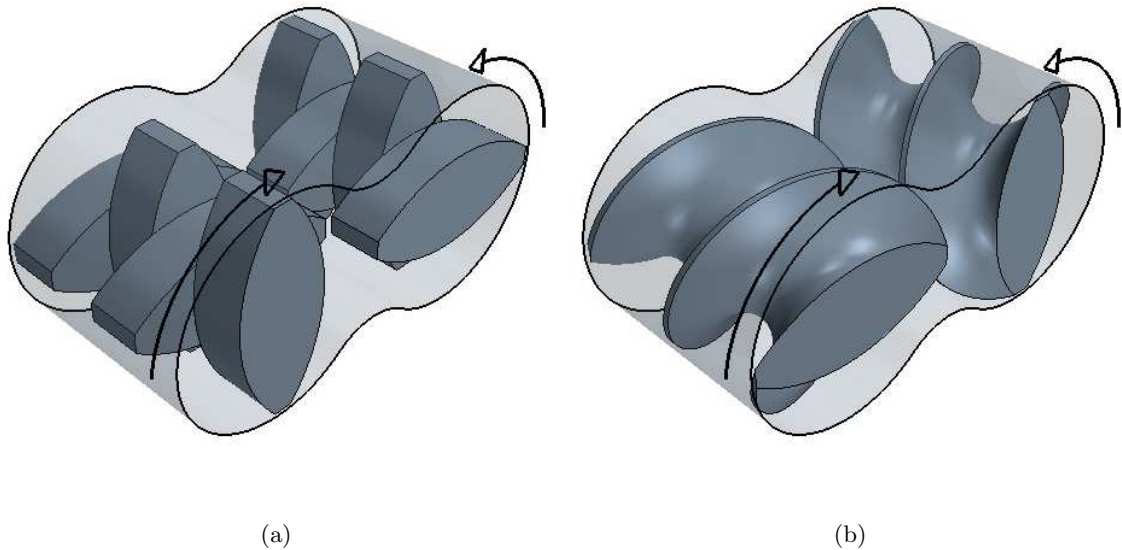


Figure 6.2: 3-D CAD models of axial section of a twin-screw granulator with (a) feed screw elements and (b) mixing elements. Arrows indicate direction of screw rotation.

Spherical particles were created to represent each of the classes in the PBM, specifying the properties of size, density, Young's modulus, and Poisson's ratio. The size and density are provided directly by the PBM. The Young's modulus was estimated based on the yield

strength for each class (Equation 6.14). A constant ratio of the Young's modulus to yield stress was assumed, using the value presented by Hassanpour and Ghadiri (2004) for lactose. The Poisson's ratio was assumed to be constant and equal for all particle types. The values for these parameters are presented in Table 6.1.

The Hertz-Mindlin contact model was used as implemented in STAR-CCM+ to resolve particle-particle and particle-wall collisions based on three interaction coefficients: restitution, static friction, and rolling friction (CD-adapco, 2014). The coefficient of restitution (e) is a measure of the ratio of rebound to impact velocities and has been shown to depend on the liquid content of the particles at low velocities (Iveson and Litster, 1998; Mangwandi et al., 2007). A linear dependence on liquid content was assumed, as shown in Equation 6.29, where e_0 and e_{slope} are the intercept and slope of the coefficient of restitution, respectively.

$$e = e_0 - e_{slope} \frac{L_{ext}}{L_{ext} + V} \quad (6.29)$$

For particle-particle collisions, this equation is evaluated based on the average external liquid fraction of the two particle types. Constant and equal coefficients of static and rolling friction were used, and their values were chosen based on those used by Hassanpour and Ghadiri (2004) and Ai et al. (2011), as presented in Table 6.1.

Four pieces of information are obtained from the DEM simulations and used within the PBM: the average (U_0) and standard deviation (s_U) of the particle velocity for each size/liquid class, the impact frequency (C_{impact}) of each particle size class, and the collision frequency ($C_{collision}$) between any two particle size classes. The collision and impact frequencies are reported on a per-particle and per-second basis, as determined from Equations 6.30 and 6.31.

$$C_{impact}(i) = \frac{N_{impact}(i)}{F(i)\Delta t_{DEM}} \quad (6.30)$$

$$C_{collision}(i, j) = \frac{N_{collision}(i, j)}{F(i)F(j)\Delta t_{DEM}} \quad (6.31)$$

$N_{impact}(i)$ is the number of collisions between particles of size class i and any other particles or the wall during the time interval Δt_{DEM} . $N_{collision}(i, j)$ is the number of collisions between particles of size classes i and j (Gantt et al., 2006; Barrasso and Ramachandran,

2015a). Here, $F(i)$ represents the total number of particles in size class i , regardless of liquid content.

The number of collisions between any pair of particle types (or the wall) is estimated based on the trajectory of their number of contacts over time. If the number of contacts increases over a time step, the additional contacts are considered new collisions and are added to a running total. If the number of contacts decreases or stays constant, it is assumed that no new collisions occur over that time step. The number of impacts is calculated from the collision data. To evaluate the particle velocity, the mean and standard deviation of the particle velocity for each class are tracked over time, and the average values during the interval are calculated from these trajectories.

It must be noted that if there are no particles present in a particular class, the DEM simulation has no data for that class to provide to the PBM. As particles form in these classes, reasonable approximations are used in place of missing data until the next DEM simulation is performed. The maximum collision and impact frequencies are used for any empty classes, since those classes are typically the largest particles, which collide more frequently. The mean and standard deviation of the velocity for all particles is used for the empty classes.

The previously described particle properties and interaction coefficients can have a profound impact on particle and collision scale behavior. Freireich et al. (2009) found that both the collision frequency and impact velocity distributions are sensitive to the coefficient of restitution and the particle stiffness. At greater stiffnesses, collisions occur more frequently and at lower velocities. This observation suggests that stiffer particles will aggregate at a greater rate than less stiff particles, since they will collide more often and with a greater efficiency.

Freireich et al. (2009) also found that the coefficient of restitution affects the collision frequency and velocity distribution. At greater coefficients of restitution, collision frequencies and impact velocities are increased, resulting in more breakage and consolidation. Although the collision frequency is increased, aggregation rates are reduced because the average velocities increases and the critical velocities decreases.

6.2.3 Bi-directional coupling of PBM and DEM

As particles take up liquid, aggregate, and consolidate, their properties change, and the particle-scale behavior is affected. To account for these changes, a bi-directional coupling algorithm was developed, combining particle-scale information from DEM with the process-scale PBM. The PBM tracks changes in particle size distributions and properties, and DEM simulations are performed when significant changes are observed to obtain new collision and velocity data. DEM is more computationally expensive than PBM, and limiting the use of DEM can drastically reduce the computation time. By triggering DEM simulations intermittently, a fraction of the process time is required to obtain meaningful information to use within the PBM. To implement this strategy, all results from the DEM simulations are reported as rates per particle so they can be used in the PBM as the system changes.

A schematic of this coupling algorithm is shown in Figure 6.1. Prior to the start of the simulation, the equipment geometry is created and meshed in STAR-CCM+. Values for all material properties, process parameters, initial conditions, and model settings are defined in gPROMS. The simulation is then executed from the gPROMS user interface, and the bi-directional coupling algorithm is implemented automatically. A DEM simulation must be performed initially to obtain values for the collision and velocity data.

The gPROMS Foreign Process Interface (FPI) was used to transfer information to STAR-CCM+, execute DEM simulations, and import DEM results into the PBM. A custom FPI was written using C++ to accomplish these tasks. First, the FPI writes the process parameters, particle distributions, material properties, and model settings to files. A summary of the data transferred across the two software platforms is presented in Table 6.2.

The FPI then executes a command to run a simulation in STAR-CCM+ using a custom Java macro. From the Java macro, the files created by the FPI are read and necessary changes are made to the STAR-CCM+ simulation. Process parameters (e.g. screw speed) and model settings (e.g. Δt_{settle} , Δt_{DEM}) are adjusted. A particle type is created for each class that contains one or more particles and values for the material properties are set. Interactions are defined between each pair of particle classes and between each class and

Table 6.2: Data exchanged between gPROMS and STAR-CCM+.

| gPROMS to STAR-CCM+ |
|---|
| Number of classes in each dimension (N, N_L) |
| Number of particles in each class (F) |
| Diameter (d), density (ρ), Young's modulus and Poisson's ratio of each class |
| Coefficients of restitution (e), static and rolling friction for each pair of classes, wall |
| DEM time intervals for settling, simulation ($\Delta t_{settle}, \Delta t_{DEM}$) |
| Screw speed |
| STAR-CCM+ to gPROMS |
| Average particle velocity of each size/liquid class (U_0) |
| Standard deviation of the particle velocity of each size/liquid class (sd_U) |
| Collision frequency of each pair of size classes ($C_{collision}$) |
| Impact frequency of each size class (C_{impact}) |

the equipment, defining the values for the coefficients of restitution and friction for each interaction.

Particles are inserted at random locations in the equipment to achieve the particle distribution specified by the PBM, rounding to the nearest whole numbers as needed, and the DEM simulation runs for a brief interval to allow particles to settle. After the particles settle, monitors are created to track the number of contacts between each pair of particles and the average velocity of each particle type. Finally, the full DEM simulation is executed, and results are processed to export collision frequencies, impact rates, and average velocities. These values are written to a file to be read by gPROMS.

After the DEM simulation is complete, the FPI reads the results file and updates the values for collision and velocity data in the PBM. The PBM is then solved until a significant change in the system is observed. When this criterion is met, the PBM pauses and the FPI is executed to run a new DEM simulation and obtain new values for these parameters. This cycle continues until the desired batch time is reached.

Trigger criteria were set to require updated DEM simulations when a significant change is observed in the PBM results. These criteria are met if either the absolute change in the total liquid fraction in the system or the relative change in the volume-average diameter ($d_{4,3}$) exceeds a set value. The values for these trigger conditions are presented in Table 6.1, and further discussion on the selection of these values can be found in Sections 6.3.1

and 6.3.2.

All simulations presented in this study were performed using eight CPUs on an Intel Xeon E5-2687W, 3.1 GHz processor with 128 GB of RAM.

6.3 Results and discussion

6.3.1 Characterizing the DEM simulations

Because DEM is much more computationally intensive than the PBM, it is advantageous to limit the DEM simulations while maintaining accuracy by adjusting the frequency with which the DEM simulations are called from the PBM and the amount of time simulated during iteration. DEM simulations were performed independently from the PBM to select these values.

At the start of each iteration, the particles are inserted randomly and allowed to settle for Δt_{settle} before results are collected over an interval of Δt_{DEM} . A DEM simulation was performed using the initial distribution of the base case in the mixing element geometry. Figure 6.3 shows trajectories of the average and standard deviation of the particle velocity and number of contacts over time for particles of 1 mm in diameter. Dry particles of various sizes are randomly inserted into the system, with a median diameter of 1.5 mm and a standard deviation of 0.5 mm. All other parameter values are based on the base values presented in Table 6.1. The mixing element is initially stationary and begins to rotate at 0.05 s. The values of the critical DEM results stabilize after 0.1 s and fluctuate mildly thereafter. Based on these results, values of 0.1 s and 0.25 s were chosen for Δt_{settle} and Δt_{DEM} , respectively, collecting data from one full screw revolution.

To determine the appropriate trigger criteria, an understanding must be developed relating the particle size and property distributions to the outcomes from DEM. Simulations were performed to demonstrate the effects of particle wetness, porosity, and size distribution on the average particle velocity and collision rate.

As shown in Figure 6.4, DEM simulations were performed using the base conditions with four different median diameters to illustrate how the collision and velocity data can change as the system evolves. The impact frequency of small particles increases as the median

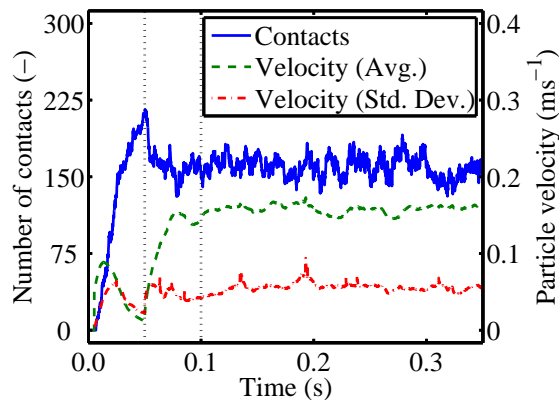


Figure 6.3: Time trajectories from DEM simulation showing number of contacts between 1-mm particles with particles of the same size, and the average and standard deviation of the velocity of 1-mm particles. Particles are added at time=0 s with a median diameter of 1.5 mm and a standard deviation of 0.5 mm. Dotted lines indicate start of rotation of the screw and start of data collection, respectively.

diameter increases, while that of the larger particles decreases. The size distribution also has a slight effect on the average particle velocity, which increases with average particle size. These results support the need for bi-directional coupling of PBM and DEM, since the particle-scale data from DEM depends on the state of the system, which changes throughout the process. A replicate simulation was performed for the median diameter of 1.5 mm, demonstrating the reproducibility of the data. Further, the liquid content and porosity of the particles moderately affects the collision and velocity data, as shown in Figure 6.5. DEM simulations were performed for a single size distribution ($d_{50}=1.5$ mm, std. dev.=0.5 mm) for three liquid-to-solid ratios and two porosities. Wetter particles have lower coefficients of restitution than drier particles, leading to a decrease in collision and impact frequencies, particularly for larger particles. No significant effect of wetness on particle velocity was observed. Similarly, a decrease in porosity results in a denser particle with a greater Young's modulus, resulting in slightly greater collision and impact frequencies.

Based on these results, a new DEM simulation was performed when the average diameter in the system, according to the PBM, changes by more than 10%. A change in the liquid content has a small but noticeable effect on the results, so an additional DEM trigger condition was set to run a new DEM simulation if the overall liquid fraction changes by more than 0.05.

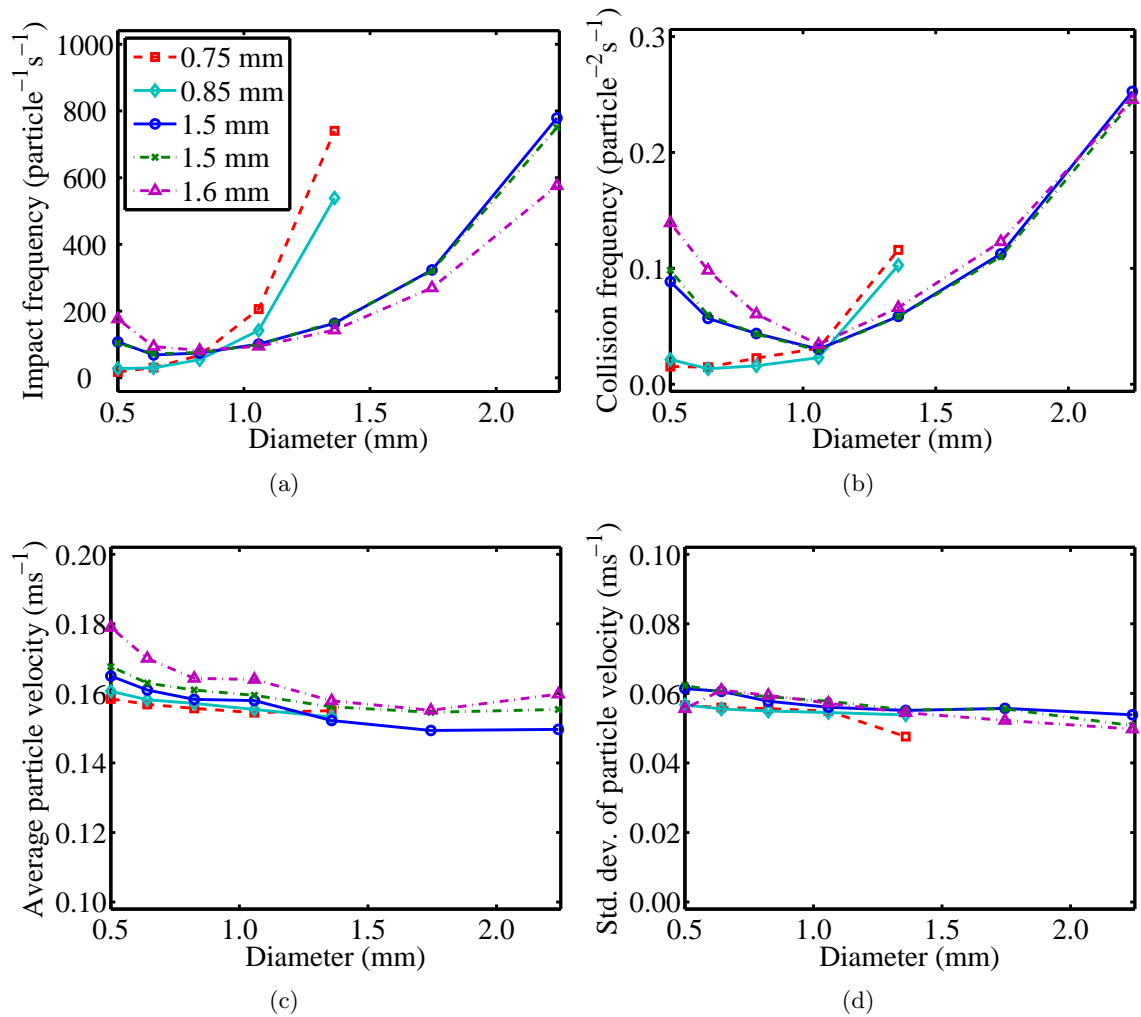


Figure 6.4: DEM results showing the effects of size distribution on (a) impact frequency, (b) collision frequency with 1-mm particles, (c) average particle velocity, and (d) standard deviation of particle velocity for each size class. Median diameters are listed in the legend. The standard deviation of the diameter is fixed at 0.2 mm for the smallest two simulations and 0.5 mm for the larger simulations.

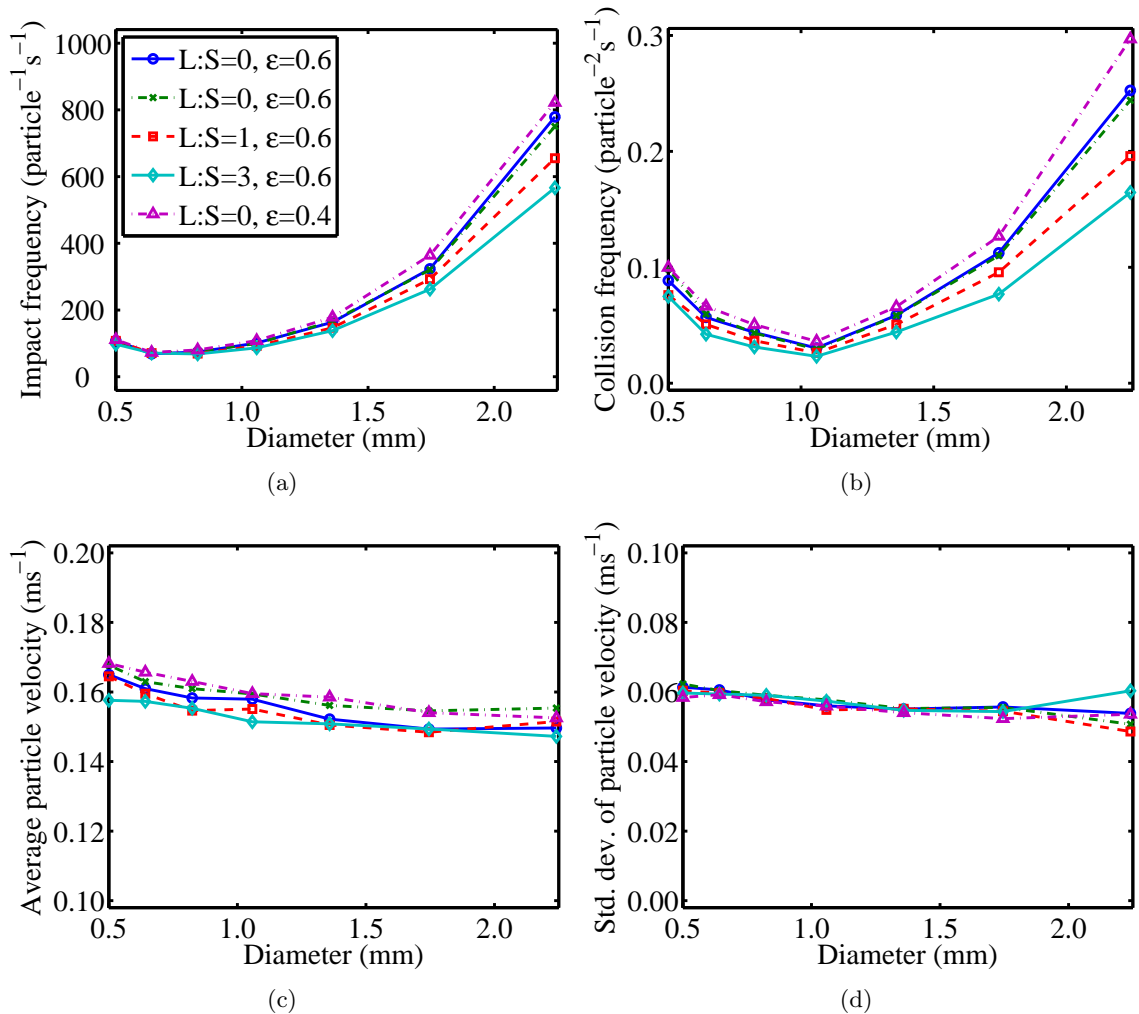


Figure 6.5: DEM results showing the effects of particle wetness and porosity on (a) impact frequency, (b) collision frequency with 1-mm particles, (c) average particle velocity, and (d) standard deviation of particle velocity for each size class.

Finally, DEM simulations were performed to identify the effects of the equipment geometry and screw speed on the particle-scale behavior, as shown in Figure 6.6. The same size distribution was simulated for dry particles using the mixing elements and the feed screw geometries at two different screw speeds. The mixing element resulted in greater velocities and collision frequencies than the feed screw as well as a greater variability in the particle velocity. Due to the greater velocities, the mixing element is expected to facilitate more breakage and consolidation than the feed screw. The broader velocity distribution observed in the mixing element may also result in more aggregation since a fraction of the particles are moving slowly enough to coalesce. For both the mixing element and the feed screw, an

increased rotational speed results in greater average velocities.

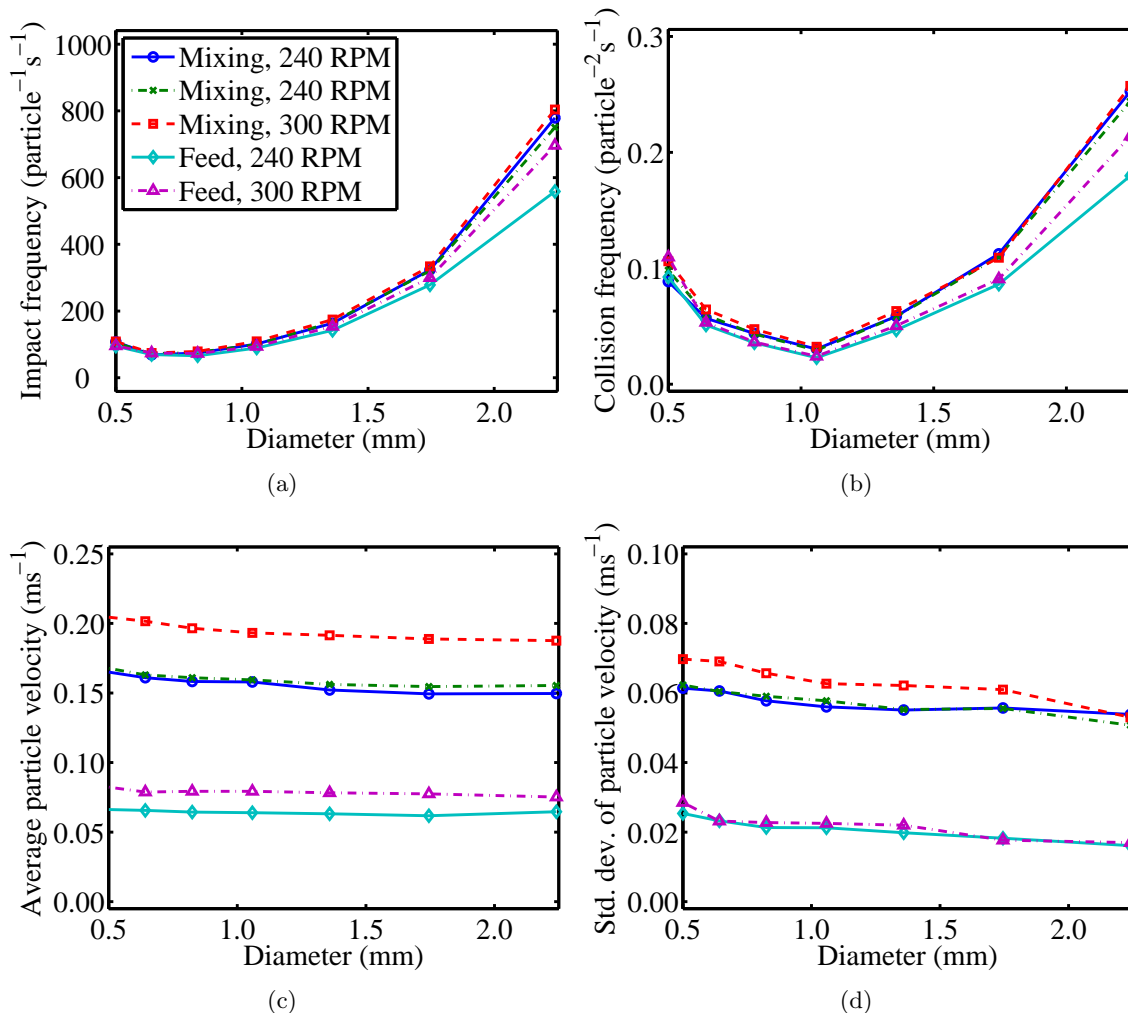


Figure 6.6: DEM results showing the effects of screw element type and rotational speed on (a) impact frequency, (b) collision frequency with 1-mm particles, (c) average particle velocity, and (d) standard deviation of particle velocity for each size class.

The data obtained from the DEM simulations showed clear sensitivities to the particle properties, process parameters, and equipment geometry. This particle-scale behavior is captured using DEM and transferred to the PBM, forming a predictive model that can identify the effects of these variables on the CQAs of the product.

6.3.2 PBM-DEM simulations: Base case

The results of the coupled PBM-DEM simulations are summarized in Table 6.3. Two PBM-DEM simulations were performed for the base case in the mixing element geometry.

During each simulation, STAR-CCM+ was called 11 times to update the DEM collision and velocity data, resulting in 3.85 s of physical time simulated in DEM. These simulations were solved in 13.1 hours. As DEM is more computationally intensive than the PBM, the majority of this time was spent running the DEM simulations. For all coupled simulations, the PBM steps in the simulation were solved in a total of approximately 5 minutes. By simulating only 3.85 s of the total 30-s process in DEM, the computation time is reduced by approximately 87%. If the computation time scales according to the DEM simulation time, the full 30-s simulation would take 4.5 days. Figure 6.7 (a-c) shows snapshots of the

Table 6.3: Summary of results of coupled PBM-DEM simulations.

| | Simulation | DEM iterations | Comp. time (hr) | Final $d_{4,3}$ (mm) |
|----|---|-----------------------|------------------------|--|
| 1 | Base case | 11 | 13.1 | 1.51 |
| 2 | Base case replicate | 11 | 13.1 | 1.57 |
| 3 | L:S trigger=0.035, $d_{4,3}$ trigger=7% | 15 | 15.4 | 1.51 |
| 4 | L:S trigger=0.1, $d_{4,3}$ trigger=15% | 6 | 8.4 | 1.44 |
| 5 | 300 RPM | 11 | 15.9 | 1.58 |
| 6 | Feed screw | 7 | 6.8 | 0.94 |
| 7 | Feed screw, 300 RPM | 7 | 7.2 | 0.99 |
| 8 | $L : S=0.2$ | 8 | 7.5 | 1.19 |
| 9 | $\mu=0.04$ Pa s | 11 | 13.4 | 1.61 |
| 10 | $s^*=0.85$ | 8 | 8.9 | 0.99 |

DEM simulations at the beginning, middle, and end of the process. These images show a wide variation in particle velocity as the mixing elements agitate the particles. Additionally, larger granules appear as the particles aggregate and form granules.

In Figure 6.8, simulated product size distributions and evolution of the average size, porosity, and total external liquid volume are presented for the base case. Throughout the process, the size distribution widens to include larger particles, while the frequency of small particles increases. This result suggests that aggregation is dominant over breakage. Some small particles remain, either due to a lack of external liquid available for aggregation or breakage and attrition of larger particles. A minimal increase in the average diameter is observed over the first 10 seconds, but as sufficient liquid is added and the particles consolidate, liquid appears on the surface and aggregation begins to occur. Aggregation continues

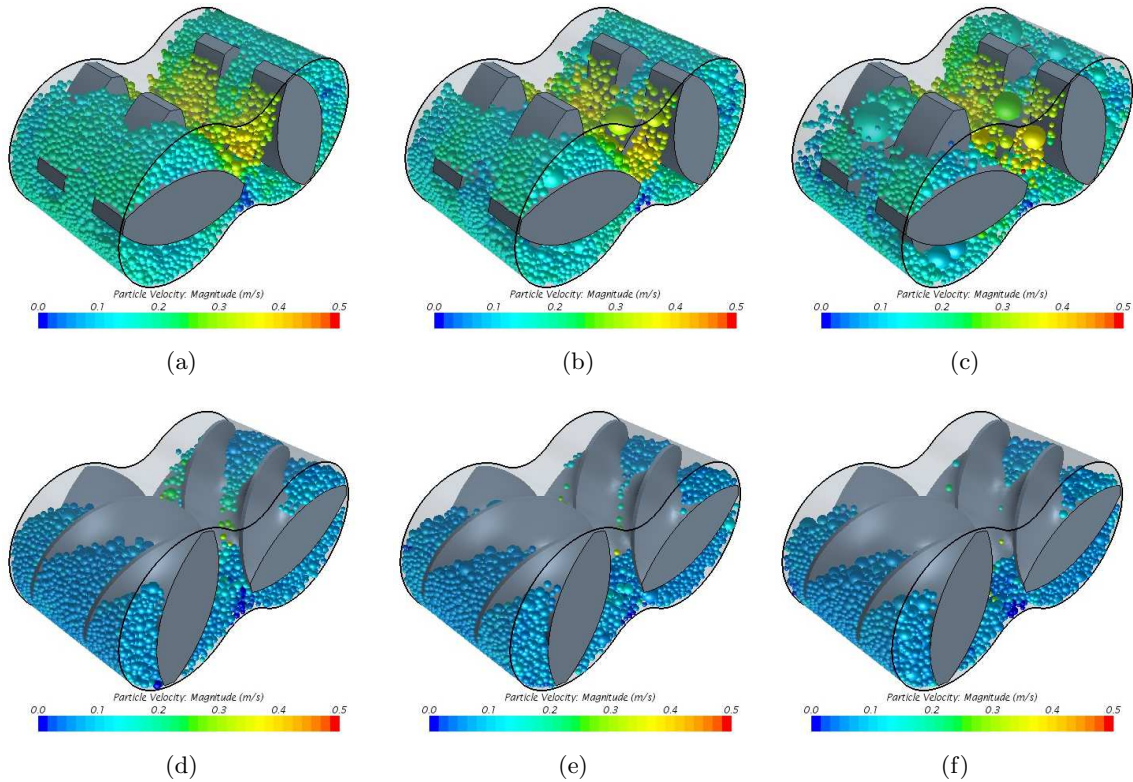


Figure 6.7: Snapshots of the DEM simulations for the base case with mixing elements (a-c) and feed screws (d-f) at times of approximately 0, 15, and 30 seconds, respectively.

after the liquid addition period is complete. Initially, the average porosity decreases slowly, but consolidation rates increase as larger granules appear and deform.

Further, the total volume of external liquid increases during the liquid addition period, and decreases as the liquid addition period ends. This observation can be attributed to the aggregation of wet particles with porous dry particles. As a wet particle and a dry particle coalesce, the pore space available for internal liquid increases, and excess liquid enters the pores in the dry particle, reducing the amount of external liquid. The total volume of external liquid then increases due to consolidation, which squeezes the internal liquid onto the surface of the particles.

Figure 6.8 also shows those results for a replicate simulation of the base case and two simulations with modified DEM trigger criteria. The results of the replicate simulation demonstrate reproducibility of the coupled model, suggesting that the DEM iterations contained sufficient numbers of particles and were simulated for a long enough interval to

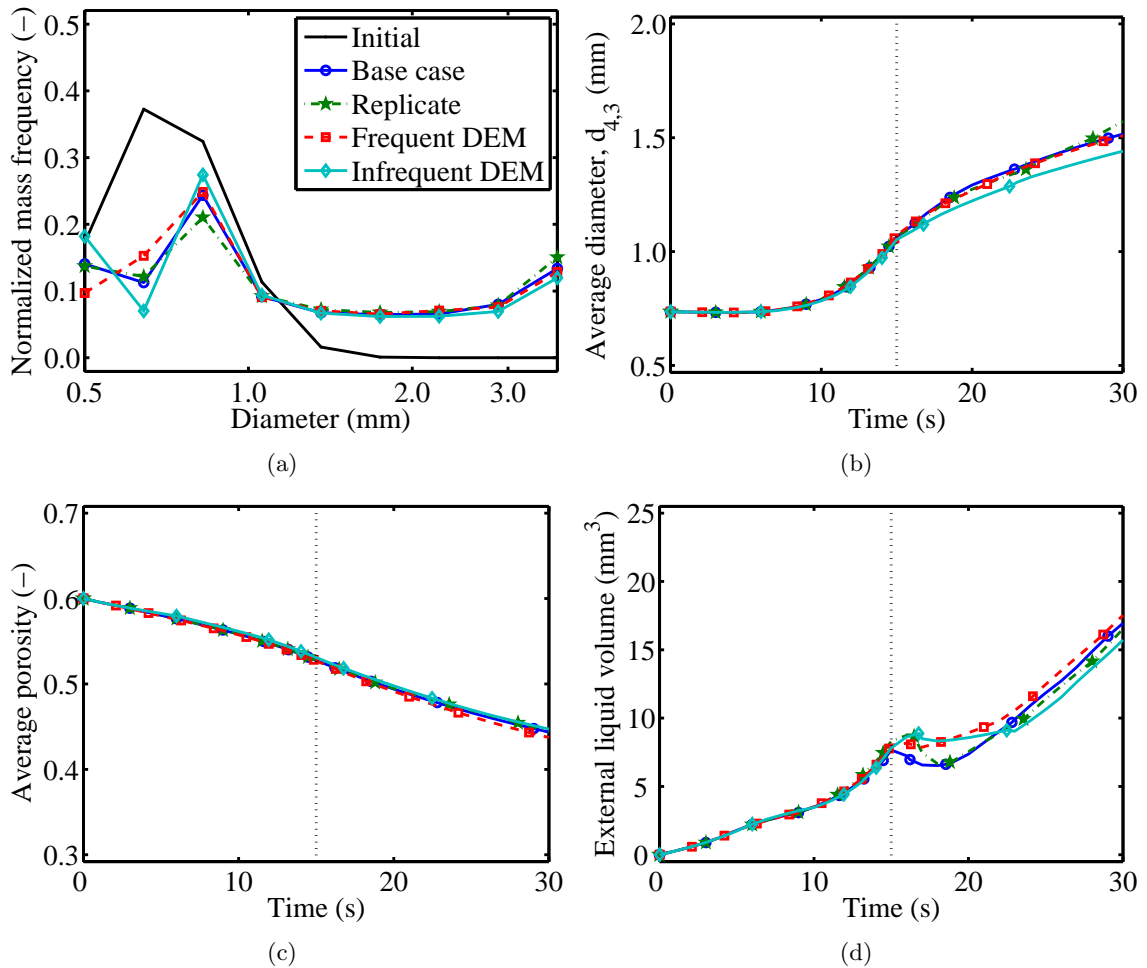


Figure 6.8: PBM-DEM results for the base case and a replicate simulation showing (a) the product size distribution, (b) the average diameter over time, (c) the average porosity over time, and (d) the total volume of external liquid over time. The points on time plots indicate DEM iterations. Vertical lines denote the end of the liquid addition period.

produce reliable data throughout the simulation.

The DEM criteria were tightened to perform DEM simulations when the liquid-to-solid ratio changes by 0.035 or when the average diameter changes by 7%. Under these conditions, 15 DEM iterations were performed throughout the process, resulting in a longer computation time. However, the results are roughly the same, suggesting that the initial trigger criteria were sufficient to capture the dynamic behavior of the process. Minor differences are observed in the product size distribution in the lower size classes and in the amount of surface liquid shortly after the liquid addition period ends.

Further, the DEM criteria were loosened to trigger a DEM simulation when the liquid-to-solid ratio changes by 0.1 or when the average diameter changes by 15%. The coupled model used 6 DEM iterations and was solved in 8.4 hours. Results show a similar evolution in the average velocity and external liquid volume, but a slightly smaller average diameter. This observation suggests that the coupling frequency affects the results, further indicating a need for bi-directional coupling between the two modeling frameworks.

6.3.3 PBM-DEM simulations: Sensitivity analysis

Additional PBM-DEM simulations were performed to assess the model's sensitivity to equipment geometry, process parameters, and material properties. Snapshots of DEM simulations in the mixing element and the feed screw for a rotational speed of 240 RPM are shown in Figure 6.7.

To evaluate the model's ability to capture realistic trends, the results are compared to two experimental studies that used the co-rotating TSG (16mm Prism Euro Lab TSG, Thermo Fisher Scientific), similar to the screw element geometries used in DEM simulations. Dhenge et al. (2012) granulated a formulation of α -lactose monohydrate, microcrystalline cellulose, and crosscarmellose sodium using water or a 6% hydroxypropylcellulose solution as the granulating liquid. The screw elements consisted of conveying elements and kneading blocks at a 60° pitch, and the rotation rate of the screw was fixed at 400 RPM. The effects of the liquid-to-solid ratio, binder viscosity, and powder feed rate on the size, strength, and shape of the product granules were observed.

In another study, El Hagrasy et al. (2013) granulated a formulation of α -lactose monohydrate, microcrystalline cellulose, and crosscarmellose sodium using hydroxypropylmethyl cellulose as the binder. The effects of lactose grade, liquid-to-solid ratio, and binder distribution method on the product size distribution and porosity were analyzed, at a constant screw speed of 400 RPM. Screw elements consisted of conveying blocks and kneading elements with a 60° pitch.

From Figure 6.7, it is evident that the simulated velocities in the feed screw are lower and more uniform than those in the mixing elements. Figure 6.9 shows results for two

geometries (mixing elements and feed screws) at two rotational speeds. These results show a strong sensitivity to the equipment geometry. In the feed screw, where velocities and collision rates are reduced, a smaller size change is observed. Little consolidation occurs, resulting in a lower amount of external liquid available for aggregation. Although the particle velocity is lower in the feed screw, favoring aggregation, the critical aggregation velocity is reduced without the presence of surface liquid. The greater degree of consolidation in the mixing elements is consistent with the experimental findings of Dhenge et al. (2012), who determined that the kneading elements promoted consolidation and breakage.

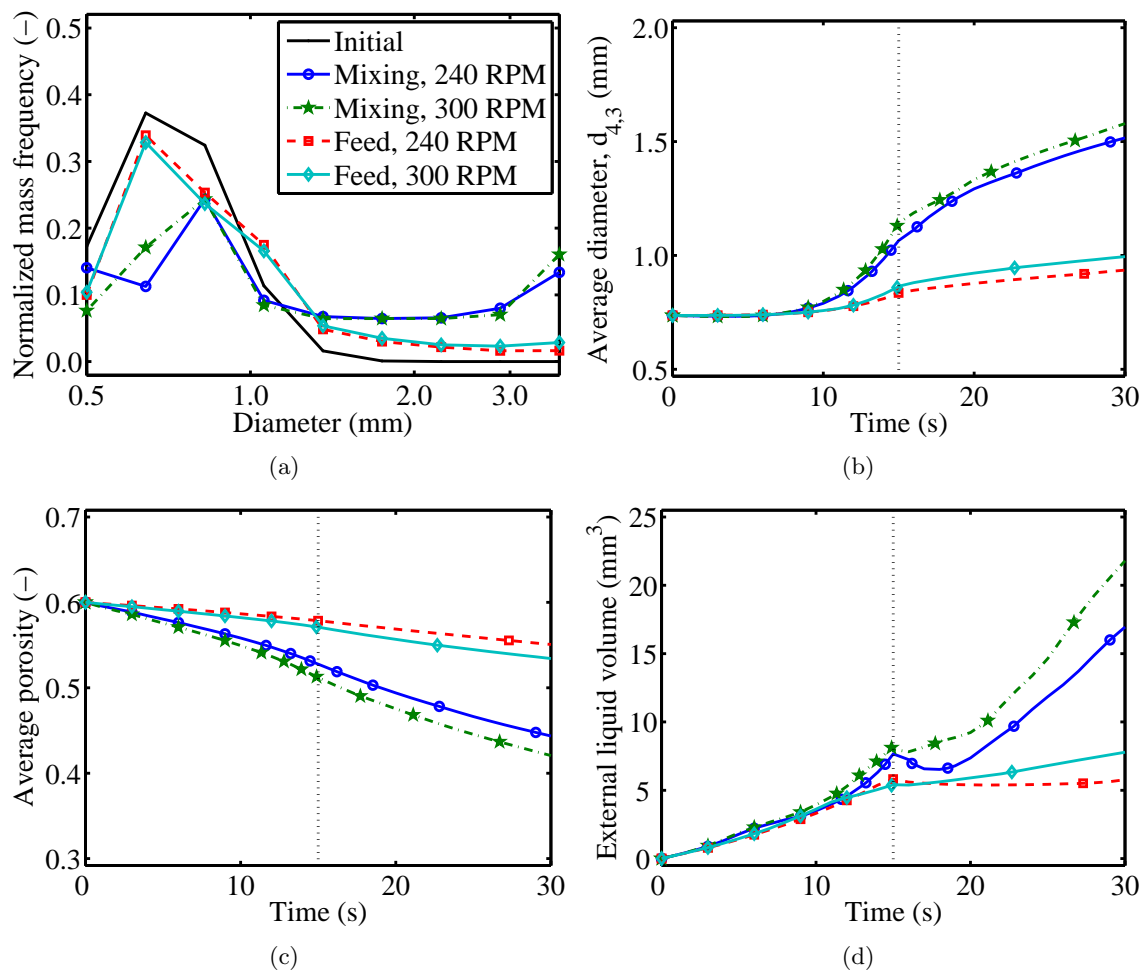


Figure 6.9: PBM-DEM results showing effects of equipment geometry and screw speed on (a) the product size distribution, (b) the average diameter over time, (c) the average porosity over time, and (d) the total volume of external liquid over time. The points on time plots indicate DEM iterations. Vertical lines denote the end of the liquid addition period.

Similarly, the screw speed affected the CQAs of the product in both geometries. At a higher screw speed, more consolidation occurred, resulting in a greater amount of surface liquid and slightly larger granules. These results demonstrate the sensitivity of the PBM to the results of the DEM simulations. Further, the CQAs of the product, as predicted by the PBM, are affected by changes in the screw speed and the equipment geometry via the DEM simulations. The PBM-DEM model captures these effects, while PBM and DEM by themselves do not, demonstrating the predictive value of the coupled model.

The liquid-to-solid ratio, binder viscosity, and maximum pore saturation fraction were also varied, and their effects on the CQAs were predicted, as shown in Figure 6.10. Simulations showed that a decrease in the liquid-to-solid ratio resulted in smaller particles, consistent with the experimental observations of Dhenge et al. (2012) and El Hagrasy et al. (2013), who observed a decrease in the fraction of fine powder particles with an increase in the liquid-to-solid ratio. Since fewer large granules form, less consolidation occurs, further reducing the amount of surface liquid available. The greater porosity observed at the lower liquid-to-solid ratio is consistent with experimental results of El Hagrasy et al. (2013).

An increase in the maximum pore saturation fraction, or the amount of liquid the pores can hold internally, resulted in much smaller granules due to a reduction in the surface liquid. Further research is needed to characterize this material property for a particular powder as an input to the model.

Finally, a reduction in the binder viscosity produced larger granules of a lower porosity. While the aggregation rate increases with viscosity, the consolidation rate decreases due to an increase in granule strength. Because of the additional consolidation that occurs at the lower viscosity, a greater amount of surface liquid is available, and larger granules are formed. The effects of binder viscosity on the aggregation and consolidation rates are competing, and the direction of these trends may depend on other factors, such as the total amount of liquid in the system. In addition, an increase in the amount of small particles is also observed at the lower viscosity, resulting in a bimodal distribution. This observation can be attributed to the reduction in the strength of the particles, resulting in more breakage. Dhenge et al. (2012) similarly observed a reduction in consolidation and breakage with an

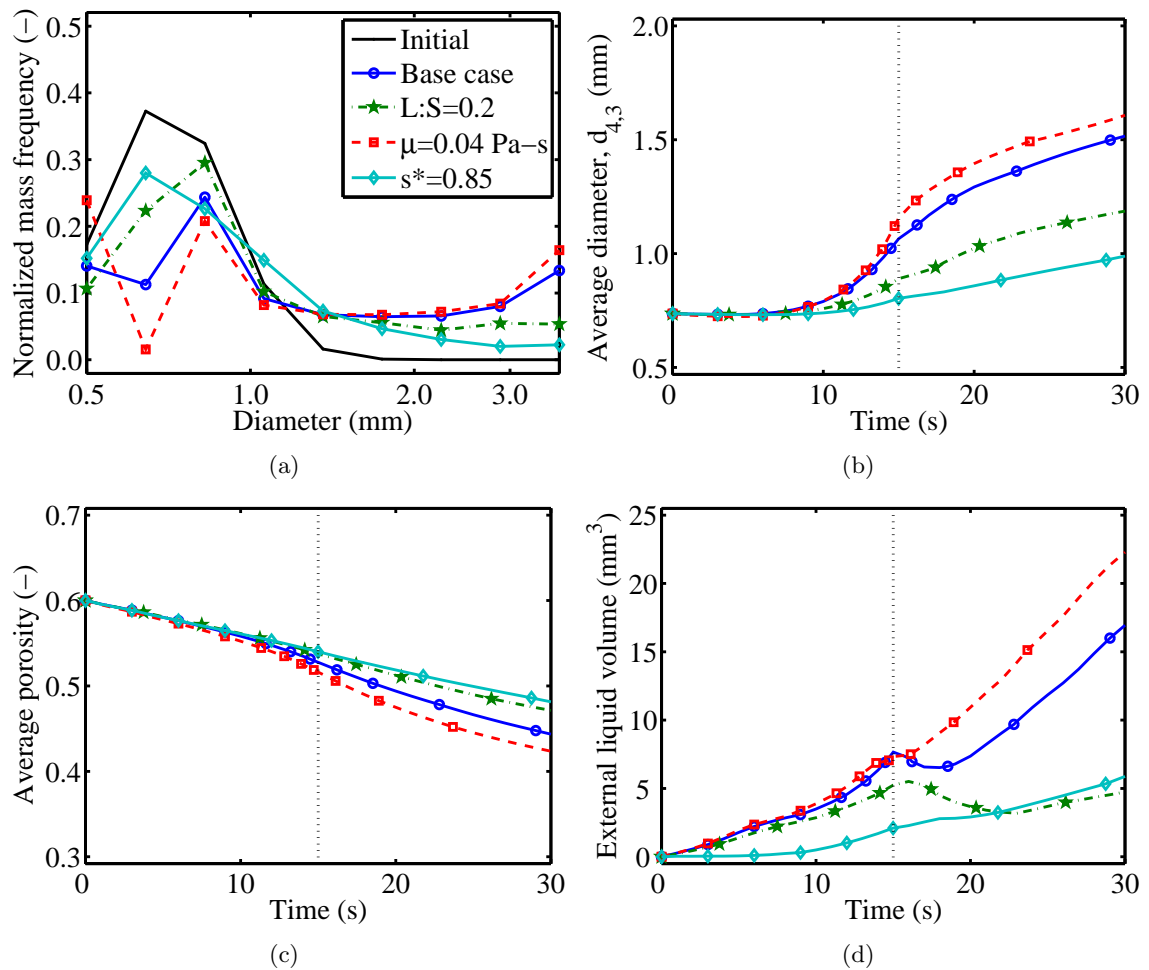


Figure 6.10: PBM-DEM results showing effects of the liquid-to-solid ratio, binder viscosity, and maximum pore saturation fraction on (a) the product size distribution, (b) the average diameter over time, (c) the average porosity over time, and (d) the total volume of external liquid over time. The points on time plots indicate DEM iterations. Vertical lines denote the end of the liquid addition period.

increase in binder viscosity.

The sensitivity of the CQAs to these material properties suggests that additional experimental work should focus on characterizing powders, with particular emphasis on their strength, surface properties, and ability to absorb liquid. Further, the effects of these properties on the key inputs to DEM, such as the coefficients of restitution and friction, Poisson's ratio, and Young's modulus, should be investigated.

6.4 Summary

A multi-scale model was developed and applied to a twin screw wet granulation process with mechanistic representations of aggregation, breakage, and consolidation. The model combines PBM and DEM techniques to predict the effects of equipment geometry, material properties, and process parameters on the CQAs of the product, building a knowledge space for QbD.

Results were reproducible and consistent with experimental trends. The screw element configuration determined the dominant rate processes and strongly influenced the product attributes, with mixing elements resulting in more aggregation, breakage, and consolidation than the feed screw, forming larger, denser particles. The model also demonstrated sensitivities to screw speed, liquid-to-solid ratio, and material properties.

During design and scale-up, process engineers typically struggle to characterize the effects of process and design parameters on quality attributes, often relying on rules of thumb or simplistic scale-up methods. By establishing the sensitivities of the product quality to the process design, this work addresses the problem from a fundamental perspective, laying out a path for QbD and scale-up.

Future work will involve enhancing the model to account for the presence of fine powder particles and the mechanisms of nucleation and layering. Additionally, spatial compartments and particle flow can be included to simulate a more realistic process. Qualitative and quantitative validation with experimental results can then be performed, along with a thorough characterization of the relevant material properties.

Specific Aim IV

Applications of multi-scale models to simulate realistic wet granulation processes

In previous aims, it has been demonstrated that multi-dimensional and multi-scale models are necessary to simulate wet granulation processes. With these added complexities, the computational demand of the model increases drastically. Further, in simulating realistic processes, model validation is necessary to ascertain the accuracy of predicted behavior. This aim focuses on simulating realistic processes by finding practical solutions to computational limitations and by qualitatively validating multi-scale models.

The goals of this specific aim are to:

- Develop and validate an ROM in place of computationally-intensive DEM simulations.
- Use a computationally-efficient multi-scale model to simulate a realistic continuous wet granulation process.
- Qualitatively validate the multi-scale mechanistic model by comparing predicted trends with experimental observations.

These works were originally published in:

Barrasso, D., Tamrakar, A., Ramachandran, R., 2014. A reduced order PBM-ANN model of a multi-scale PBM-DEM description of a wet granulation process. *Chemical Engineering Science* 119, 319 – 329

Barrasso, D., Ramachandran, R., 2015b. Qualitative assessment of a multi-scale, compartmental PBM-DEM model of a continuous twin-screw wet granulation process, In review

Chapter 7

A reduced order PBM-ANN model of a multi-scale PBM-DEM description of a wet granulation process

Wet granulation is a particle design process, often used in the pharmaceutical, consumer product, food, and fertilizer industries. A better process understanding is needed to improve process design, control, and optimization. Predominantly, two modeling frameworks are implemented to simulate granulation processes: population balance modeling (PBM) and discrete element methods (DEM). While PBM simulates changes in the number of particles in each size class due to rate processes such as aggregation, DEM tracks each particle individually, with the abilities to simulate spatial variations and collect mechanistic data. In this bi-directional coupled approach, the computational expenditure of the full model is overwhelmed by the high-fidelity DEM algorithm that needs to solve a set of ODEs for each and every particle being handled in the system for very small time intervals. To mitigate this computational inefficiency, reduced order modeling (ROM) is used to replace the computationally expensive DEM step. An artificial neural network (ANN) was trained using DEM results to relate particle size, size distribution, and impeller speed to the collision frequency. Results showed a high correlation between the trained ANN predictions and DEM-generated data. The ANN was coupled with a PBM as a key component of the aggregation rate kernel. The coupled model showed a different development of average particle size and size distribution over time from that of a constant aggregation rate kernel. In addition, the coupled model demonstrated sensitivity to the impeller speed via the ANN rate kernel. When compared with the fully coupled PBM-DEM model for accuracy and computation time savings, the hybrid PBM-ANN model demonstrated excellent agreement with DEM simulations at fractions of the original computational time.

7.1 Background

Modeling of particulate systems is of critical importance within the chemical and pharmaceutical industries, and yet it remains relatively poorly understood. Traditionally, the pharmaceutical industry has implemented a Quality by Testing (QbT) approach to product manufacturing which involves sampling the products of empirically designed processes and rejecting out-of-specification batches. In recent years, in a move from batch to continuous processes, the industry has redoubled its efforts to focus on a Quality by Design (QbD) practice to improve controllability, scalability, and protability. The QbD approach aims to better understand and define the design space and operating parameters that will result in quality products and has elevated the urgency to establish robust particulate system models (Yu, 2008). To develop practical and predictive models of pharmaceutical processes, an effective model-based approach has been proposed in which mathematical process models are developed and validated using experimental data (Glaser et al., 2009; Ramachandran and Chaudhury, 2012). For the highly complex process of wet granulation, which is governed by the rate processes of wetting and nucleation, aggregation and consolidation, and breakage and attrition (Iveson et al., 2001), empirical models have limited applicability outside the space of the calibration data set (Barrasso et al., 2015a; Chaudhury et al., 2014a). To overcome these limitations, a multi-scale modeling approach in which mechanistic information from a DEM model is provided to the PBM via a reduced order model (ROM).

7.1.1 Reduced order models and artificial neural networks

One of the main issues with using a computationally complex model such as a DEM simulation is its inefficiency while being used for overall system analysis which entails iterative calculations. DEM simulations have a high computational cost because they solve a set of ODEs for each and every particle being handled in the system for very small time intervals (usually around $1e-6$ seconds) while also tracking their interactions and spatial movement (Boukouvala et al., 2013; Hassanpour et al., 2007). Iterative calculations required for system optimization or parameter estimation will thus take a significantly large amount of time

because the base model calculations are protracted themselves. This computational inefficiency poses a significant computational challenge to implementing a multi-scale coupled model using PBM and DEM. While a simple PBM can simulate a full process in seconds or minutes, a DEM simulation can take hours or days of computation time, depending on the choice of software and hardware, to solve for only a few seconds of physical time. This problem is exacerbated with large numbers of particles and small particle sizes, often the case in particulate processes (Ketterhagen et al., 2009).

In order to deal with this issue, three popular, computationally-economical approaches are usually implemented as an alternative for modeling the entire granulation system: periodic section DEM simulation, simulation of larger and fewer particles and reduced order models (ROMs). In the periodic section approach, taking advantage of the symmetric geometry of a granulator, simulations of a segment of the granulator are performed rather than the entire system. Since DEM calculations scale non-linearly with the number of particles, running multiple smaller simulations of the entire system is computationally faster than simulating the entire system itself Dubey et al. (2011); Gao et al. (2012). Another common approach to reduce the DEM calculation time is to mimic the original granulation system in DEM with a system with fewer but larger particles. This reduction entails adjusting the particle densities to maintain similar momentum exchange between particles; however, additional sensitivity studies on the effect of particle size on the powder dynamics needs to be performed before such reduction can be made (Hassanpour et al., 2011). The final alternative approach is to develop ROMs through data fitting techniques to replace the computationally intensive, high-fidelity DEM models. Even though a smaller system of particles are being simulated in the periodic section approach, the fact that DEM algorithm needs to be implemented multiple times for system analysis necessitates investigation into drastically faster reduced order modeling techniques. Various data fitting techniques are available in literature that have been used to replace full scale models including response surface methodology (RSM) (Boukouvala et al., 2010a; Jia et al., 2009; Ranjbarian and Farhadi, 2013b), Kriging method (Gao et al., 2012; Jia et al., 2009; Ranjbarian and Farhadi, 2013b), high dimensional model representations (HDMR) (Banerjee et al., 2010; Banerjee and Ierapetritou, 2004), and artificial neural networking (ANN) (Boukouvala et al., 2010b;

Basheer and Hajmeer, 2000; Kumar Akkisetty et al., 2010). Developing such reduced order models not only provide a quantitatively accurate description of the system dynamics which are far less computationally taxing than the original models but also provide a means by which the system dynamics can be readily interpreted for process simulation and optimization purposes (Lucia et al., 2004). In this study, reduced order models are investigated to replace the DEM simulations.

The main challenge with developing ROMs for DEM simulations, however, is to accurately capture the inherent intricacies of the particles interacting with other particles and its surroundings. DEM simulations are designed to calculate the elastic, plastic and frictional forces between particles and walls in order to track individual particle motion and deformation. The governing system equations - Newton's laws of physics and supplemental contact models - must therefore be solved for each particle in the simulation taking into account the effects of neighboring particles/wall/impeller blades in the particular space at that particular time. The commotion of the system dynamics is further exacerbated due to the random nature in the calculations imbued by the application of a contact detection step to identify nearby particles or walls for each discrete particle (Boukouvala et al., 2013; Hassanpour et al., 2007). The complexity in these particle movements, which introduces noise, non-linearity, and discontinuities in the distributed parameter profiles increases the difficulty of a data-driven ROM to accurately predict the dynamic nature of the interactions between particles. Thus, a ROM technique that will not just lower the computational expense of the system model but also retain the original model's fidelity is desired.

Artificial neural networks (ANNs), in particular, are popular modeling techniques to address similarly complex problems and are used extensively to develop empirical process models (Basheer and Hajmeer, 2000). ANNs mimic the learning systems of the brain, using a trained set of weighted neurons to predict output values from input data. In pharmaceutical science, ANNs can be used to model analytical data, molecular drug design, modeling pharmacokinetic and pharmacodynamics profiles, optimizing manufacturing processes (Agatonovic-Kustrin and Beresford, 2000), and to model pharmaceutical unit operations (Kumar Akkisetty et al., 2010). In a previous study, Kumar Akkisetty et al. (2010) used

an ANN within a PBM to represent the breakage kernel in an industrial milling process. ANNs are particularly well suited for modeling non-linear problems and can be evaluated rapidly, making them a suitable candidate to model DEM data within a PBM.

7.1.2 Objectives and approach

DEM modeling can provide useful mechanistic information to comparatively semi-empirical PBMs. Simulating DEM models of multi-scale and multi-dimensional wet granulation processes is a computationally expensive procedure that is not feasible for practical purposes of optimization, control or flowsheet modeling. An alternative to running DEM simulations is to develop a reduced order model (ROM) that will substitute the intensive calculations of DEMs with faster black box models. The ROM investigated in this study utilizes the data generated from DEM models to train an artificial neural network (ANN) which is used within a PBM. A schematic of this approach is shown in Figure 7.1. The objectives of this study are to:

- Present a one-dimensional PBM for a batch wet granulation process representing the aggregation rate kernel as the product of the collision frequency and efficiency.
- Characterize the effects of particle size, size distribution, and impeller speed on the collision frequencies in a batch granulator using DEM.
- Based on the results from DEM simulations, train ANNs to predict the collision frequency from some or all of the following: colliding particle sizes and number frequencies, overall size distribution, and impeller speed.
- Compare the accuracies of the ANNs to predict the collision frequencies from their subsets of input variables and select the optimal ANN configuration.
- Perform simulations using a hybrid PBM-ANN for a dynamic, size, size distribution, and impeller speed-dependent aggregation kernel, and compare the results of the hybrid model to those of the uncoupled PBM.
- Compare the hybrid PBM-ANN results to those of a fully coupled PBM-DEM model for accuracy and computation time savings.

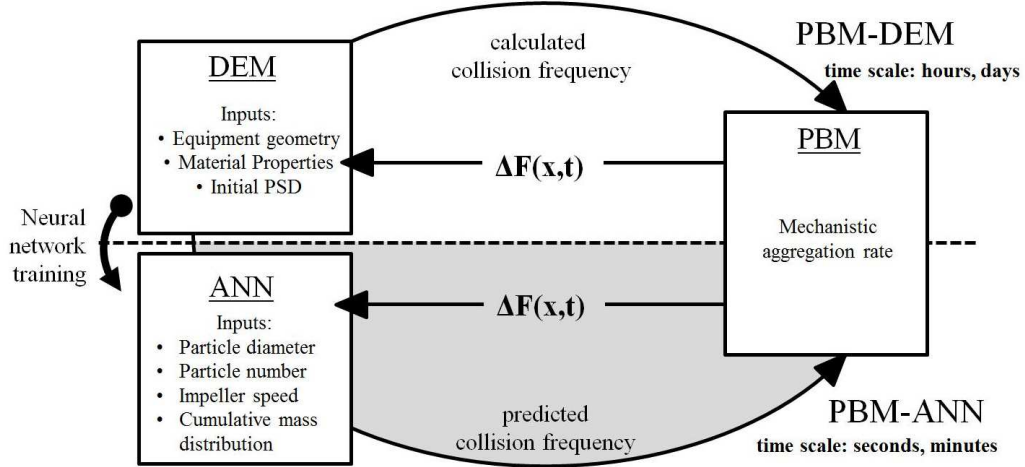


Figure 7.1: Schematic of bi-directional coupled PBM-DEM model (top) and PBM-ANN reduced order model (bottom).

7.2 Model development

7.2.1 Population balance model development

A one-dimensional PBM was developed, tracking distributions in particle size over time due to aggregation. The rate of change of the number of particles, F , as a function of particle size (x), is given in Equation 7.1 (Ramkrishna, 2000),

$$\frac{\partial F(x, t)}{\partial t} = \mathfrak{R}_{agg}(x, t) \quad (7.1)$$

where \mathfrak{R}_{agg} is the net aggregation rate source term, defined in Equation 7.2.

$$\mathfrak{R}_{agg}(x, t) = \frac{1}{2} \int_0^x \beta(x - x', x', t) F(x - x', t) F(x', t) dx' - \int_0^\infty \beta(x, x', t) F(x, t) F(x', t) dx' \quad (7.2)$$

The aggregation rate constant between any two size classes (x) and (x') is given by $\beta(x, x')$. A linear grid with respect to volume was implemented to discretize the size domain. The discretized form of this PBM is given in Equation 7.3, where i is the index of the bin and

N is the total number of bins, given in Table 7.1.

$$\frac{dF(x, t)}{dt} = \frac{1}{2} \sum_{j=1}^{i-1} \beta(i-j, j, t) F(i-j, t) F(j, t) - \sum_{j=1}^{N-i} \beta(i, j, t) F(i, t) F(j, t) \quad (7.3)$$

Table 7.1: Parameter values used in PBM simulations.

| Parameter | Value |
|---|-------------------------|
| Number of bins (N) | 125 |
| Volume of first bin (V_0) | 4.19e-12 m ³ |
| Diameter of first bin ($d(1)$) | 200 μ m |
| Initial number of particles in first bin ($F(1)$) | 1e5 |
| Batch time | 180 s |
| Integration time step | 0.25 s |
| Collision efficiency (Ψ) | 0.03 % |

The volume (V) and diameter (d) of the particles in each bin are given by Equations 7.4 and 7.5, where V_0 is the volume of the first bin. The size of all initial particles was equal to that of the first bin, and the initial number of particles is given in Table 7.1, along with the volume of the first bin.

$$V(i) = V_0 i \quad (7.4)$$

$$d(i) = \left(\frac{6V_0 i}{\pi} \right)^{1/3} \quad (7.5)$$

Several aggregation rate kernels have been proposed in the literature, including dependencies on size (Cameron et al., 2005), liquid content (Madec et al., 2003), and composition (Matsoukas et al., 2009). The aggregation rate can be represented as the product of the collision frequency (C) and the collision efficiency (Ψ) between two particle classes, as shown in Equation 7.6 (Gantt et al., 2006).

$$\beta(x, x', t) = C(x, x', t) \Psi(x, x') \quad (7.6)$$

The collision efficiency represents the likelihood or probability that a single collision will result in coalescence. This value depends on the sizes, masses, and surface liquid of the colliding particles, as well as their relative velocities (Gantt et al., 2006; Liu and

Litster, 2002). For the purposes of this study, a constant size-independent collision efficiency was assumed in order to focus the investigation on the collision frequency. The value for the collision efficiency, given in Table 7.1, was tuned to provide a realistic particle size distribution.

The collision frequency is the rate at which collisions occur between two bins per particle in each class. As shown in Equation 7.7, the collision frequency can be calculated from the number of collisions (N_C) between the two classes over a time interval (Δt) and the number of particles in each class (Gantt et al., 2006; Barrasso and Ramachandran, 2015a).

$$C(x, x', t) = \frac{N_C(i, j, t)}{F(i, t)F(j, t)\Delta t} \quad (7.7)$$

In order to estimate the collision frequency, DEM simulations can be performed, and the number of collisions can be counted. It has previously been demonstrated and is shown here that the particle size distribution in the system affects the collision frequency functions (Barrasso and Ramachandran, 2015a). Because of this effect, a single DEM simulation is not sufficient to characterize the aggregation kernel, which may change over time as the state of the system changes. Bi-directional coupling between PBM and DEM has been proposed and demonstrated (Barrasso and Ramachandran, 2015a). However, these detailed models are limited by their computational expense. Further, process parameters, such as impeller speed, may affect the collision frequency and should be considered in the aggregation rate kernel.

In this study, DEM simulations were performed to gather data relating particle size, size distribution of the system, and impeller speed to the collision frequency. An ANN was trained and validated using the results from the DEM simulations to describe the collision frequency as a function of these input parameters. The resulting aggregation kernel, which is a function of particle sizes (i, j), distribution ($F(x, t)$) and impeller speed (v) is given in Equation 7.8.

$$\beta(i, j, v, F(x, t)) = C(i, j, v, F(x, t))\Psi \quad (7.8)$$

Because this kernel depends on the state of the system, or the current particle size

distribution, denoted by $F(x)$, it changes over time, resulting in a dynamic aggregation rate kernel. Traditionally, aggregation kernels lump the effects of the collision frequency and efficiency, often assuming a constant value for the collision frequency. These kernels often fail to account for operating conditions. In this work, a more mechanistic expression for the collision frequency is obtained, first with DEM, and these effects are captured using an ANN.

The PBM was solved for a total batch time of 3 minutes using MATLAB. First-order explicit Euler integration was used to solve the resulting system of ordinary differential equations.

7.2.2 Discrete element method

To generate the training data set for ANN development, DEM simulations were performed, tracking the collision frequency of particles in the system. In a batch granulator with a four-blade impeller, fifteen particle distributions were simulated at three impeller speeds. Collision rates between particles were recorded according to the sizes of the colliding particles. EDEM 2.5 (DEM Solutions) was used to perform the DEM simulations in this study.

As shown in Figure 7.2(a), the geometry for a batch granulator with an impeller was created in EDEM. The walls of the tank were represented by a vertical cylinder, and four impeller blades were created to agitate particles at the bottom of the tank. The dimensions of the geometry and rotational speeds of the impeller are listed in Table 7.2. All particles were created in random locations above the impeller at a rate of $1e6$ particles/s until the specified number of particles was created. Figure 7.2(b) shows a snapshot of a DEM simulation with particles.

The standard Hertz-Mindlin contact model was used, and the values for material properties and contact parameters are shown in Table 7.2. These parameters were obtained from previous literature studies with applications for granular systems (Barrasso and Ramachandran, 2015a; Dubey et al., 2011).

In order to develop a high-performance ANN that can accurately predict the nonlinear relationships between the collision frequencies, the physical state of the particulate system (i.e. particle size and distribution) and the process conditions (impeller speed), the ANN

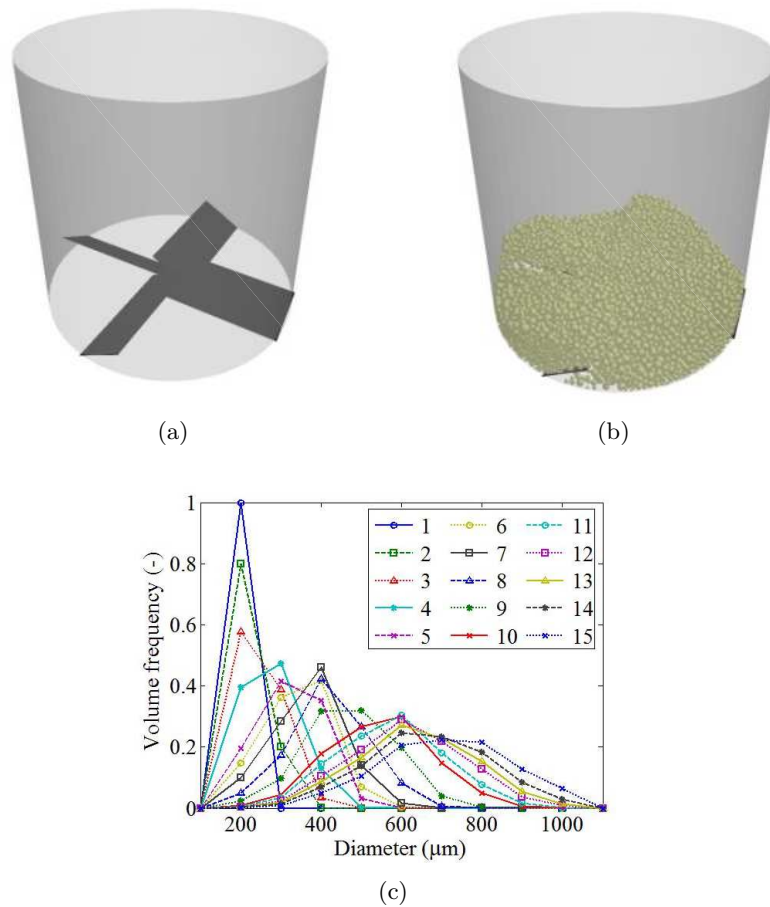


Figure 7.2: (a) Equipment geometry, (b) snapshot of DEM simulation, and (c) size distributions simulated in DEM as obtained from PBM.

Table 7.2: Parameter values and equipment geometry used in DEM simulations.

| Parameter | Value |
|--|---------------------|
| Poisson's ratio | 0.25 |
| Shear modulus | 2 MPa |
| Coefficient of restitution | 0.1 |
| Coefficients of static, rolling friction | 0.5, 0.01 |
| Density | 1 g/cm ³ |
| Grid cell size | 1 mm |
| Fixed time step | 5e-6 s |
| Total DEM simulation time | 10 s |
| Tank diameter | 40 mm |
| Tank height | 40 mm |
| Blade width | 8 mm |
| Blade angle | 30 ° |

training process must use a substantial DEM dataset. This dataset not only needs to capture the relation among the selected input and output variables but must also encompass most realistic scenarios.

A simple method to generate such a diverse dataset with varying particle size distribution and particle sizes is to record the freeze-frame particle distribution of a population balance model at various points in time. Since the particle number and sizes are being continuously modified, the distributions with different timestamps essentially behave as different states of granulation system with different effects between the input and output variables. For this study, fifteen different particle size distributions were generated using the PBM presented in Section 7.2.1, assuming a constant and uniform collision frequency of 0.01 collisions/particle²-s. The 125 bins in the population balance model were first grouped into nine particle classes, ranging from 200 to 1000 μm , which typically describes the size range of interest in a granulation process. The normalized mass frequencies in each of these nine classes were then calculated over time, and the distributions were selected based on the mass frequency of the smallest class. The selected fifteen distributions were isolated from the PBM results when the relative mass frequency of the smallest size class reached the following values: 1, 0.8, 0.6, 0.4, 0.2, 0.15, 0.1, 0.05, 0.025, 0.01, 0.0075, 0.005, 0.004, 0.003, and 0.002. The resulting distributions created by this method are illustrated in Figure 7.2(c).

To accurately represent each of the fifteen distributions selected through the above process, nine corresponding spherical particle types were created in EDEM with different diameters representing each of the nine particle size classes. The number of particles in each class was varied for each simulation according to the distributions obtained from the PBM. Thus, fifteen realistic particle distribution scenarios were created in EDEM. Each of these distributions was simulated once with an impeller speed of 60 RPM and again with an impeller speed of 30 RPM or 90 RPM. The high and low impeller speeds were alternated for odd and even numbered distributions. The number of collisions between all particle types over a ten-second interval was recorded, and the collision frequency was calculated according to Equation 7.7. Figure 7.3 illustrates the collision frequencies recorded between

each particle size classes (denoted by the two diameter axes for the colliding particles) for three different simulations. The collision frequency values for all distributions are provided in Figure 7.4(a). Simulations were performed on a Dell Precision T1650 desktop using four

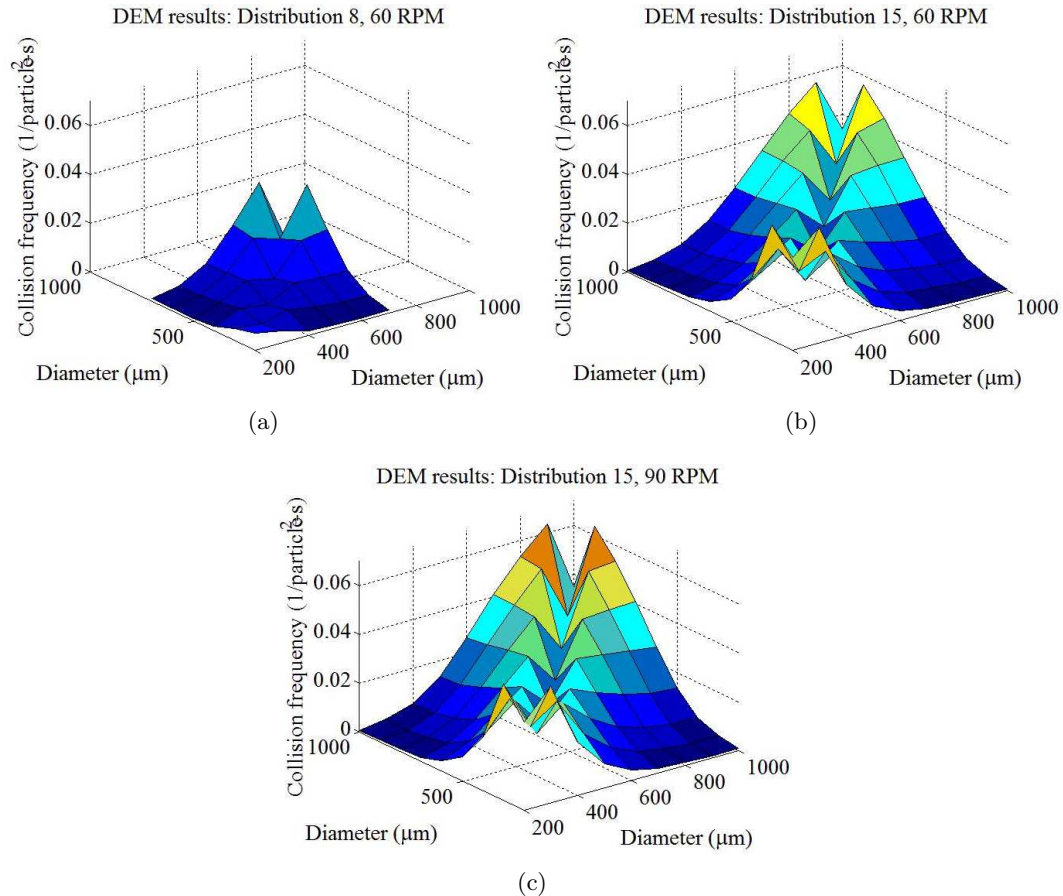


Figure 7.3: DEM collision frequency results for (a) distribution 8 at 60 RPM and distribution 15 at (b) 60 RPM and (c) 90 RPM.

Intel Core i7-3770 (3.4GHz) processors with 32GB RAM. The fixed DEM time step and grid cell size are given in Table 7.2, and each distribution was simulated for a total time of 10 seconds. The computation time for these simulations ranged from 4 days for the first distribution, which contained 100,000 particles, to 2.5 hours for the fifteenth distribution, which contained 3,500 particles.

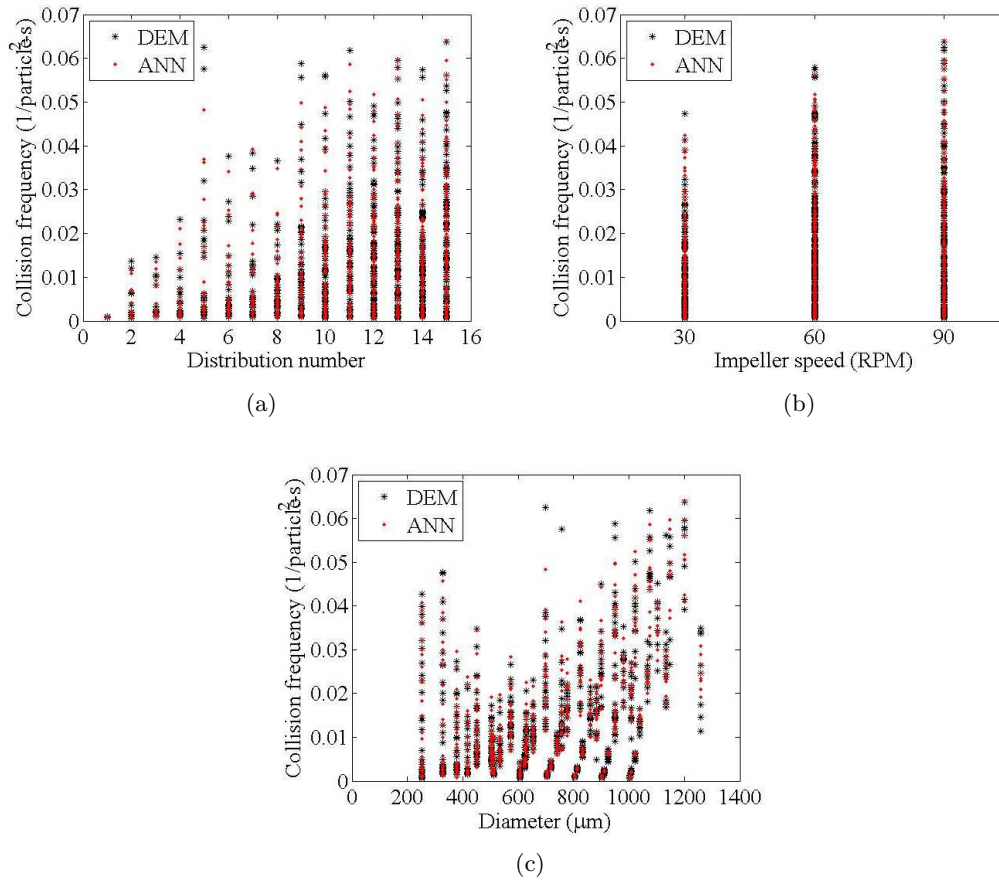


Figure 7.4: DEM results and ANN predictions versus (a) distribution number, (b) impeller speed, and (c) aggregate particle diameter.

7.2.3 Artificial neural network architecture and training techniques

The datasets obtained from the DEM simulations were used to generate an ROM, relating inputs of particle sizes, size distribution, and impeller speed to collision frequencies. Since the DEM algorithm produces noisy, non-linear and discontinuous data, an artificial neural network (ANN), which is a type of universal functional approximation that is capable of accurately modeling non-linear functions, was chosen as a suitable ROM. The ANN parameters are fitted using general data-driven, self-adaptive methods hence they are well suited for problems whose underlying principles are unknown or difficult to specify but for which there are sufficient data or observations (Zhang et al., 1998).

The ANN developed in this study is used in providing the collision frequency values of the aggregation rate kernel (C parameter in Equation 7.6) for the PBM. In order to

investigate the dependency of collision frequency on the particle size (PS), size distribution (SD) and impeller speed (IS), four alternative ANNs were generated from the DEM dataset that exploited different combination of these parameters as inputs. These ANNs represent four types of aggregation kernels- the PS and IS dependent kernel (ANN 1), the SD and IS dependent kernel (ANN 2), the PS and SD dependent kernel (ANN 3) and the comprehensive PS, SD and IS dependent kernel (ANN 4). By observing the performance quality of the each ANN, the dependence of collision frequency on the three parameters can be determined. For instance, if ANN 1 which only considers the PS and IS data displays as good an agreement with the DEM simulation as ANN 4 which considers all parameters, then the effect of SD is minimal in developing a ROM kernel. Similarly, if ANN 1, ANN 2 and ANN 3, which only consider binary combinations, show poorer ANN performance than ANN 4, the secondary effects between these parameters are significant. The inputs and outputs of each ANN are listed in Table 7.3. By using various inputs for these ANNs, the kernels can be compared for their ability to capture physical behavior using only a subset of inputs. For example, when omitting the impeller speed from the input dataset, the ANN may perform more poorly, indicating that the impeller speed has a significant effect on the collision frequency and must be considered in the aggregation rate kernel. All four ANNs had a single output: the square root of the collision frequency. The square root transformation was used to ensure that data points of lower collision frequencies were predicted accurately and no negative collision frequencies would be predicted.

The first ANN only considers the sizes of the two colliding particles, denoted as A and B, and the impeller speed, resulting in a size- and impeller speed-dependent aggregation rate kernel. This ANN does not consider the state of the system (the size distribution), and results in a kernel that is not dynamic. The second ANN considers the size distribution and impeller speed, but not the particle size. Although the rate kernel resulting from this ANN treats all particles in the system equally (the collision frequency is irrespective of the particle size), the kernel is considered dynamic in nature because it is dependent on the particle size distribution within the granulator. The third ANN includes the sizes of A and B and the size distribution of the system, as well as the normalized number frequency of the classes A and B in particular, resulting in a dynamic rate kernel that does not account for impeller

Table 7.3: Four ANN alternatives for describing collision frequencies.

| ANN | Dependencies | No. of inputs | Inputs |
|-----|---|---------------|---|
| 1 | Particle size, impeller speed | 3 | Diameters of A and B, impeller speed |
| 2 | Size distribution, impeller speed | 10 | CSD of nine classes, impeller speed |
| 3 | Particle size, size distribution | 13 | Diameters of A and B, normalized number frequencies of A and B, CSD of nine classes |
| 4 | Particle size, size distribution, impeller speed, | 14 | Diameters of A and B, normalized number frequencies of A and B, CSD of nine classes, impeller speed |

speed. Finally, the fourth ANN represents the full kernel, with size, size distribution, and impeller speed dependencies. This ANN uses the sizes of the two particles involved in the collision as well as their relative number frequency of these particles in the system. The cumulative mass frequencies of the nine size classes are also provided as inputs, and the single output is the square root of the collision frequency for the two particles.

All ANNs were structured to contain a single hidden layer of 10 neurons, which was determined to have the best fit for all distributions. The available input and corresponding target data from the DEM simulations were divided into three subsets: training (70% of data), validation (15%), and test sets (15%) through a randomization algorithm. The training dataset is used for computing the gradient and updating the network weights and biases to teach the network. The validation set is used for monitoring the performance of the training process. The training continues as long as the network continues improving on the validation set (i.e. the validation error is decreasing). The mean-squared errors for both training and validation subsets are calculated over different epochs, or iterations, of training. Finally, the test subset provides an independent measure of network accuracy. Resampling the available dataset through this randomized holdout method ensures that mutually independent samples of input/target datasets are being used to improve and test the ANN developed (Flexer, 1996).

The ANNs in this study were generated using the neural network toolbox in MATLAB using the Levenberg-Marquardt (LM) training algorithm. Since the objective of the study was to test the computational efficiency of using ANN in place of DEM, the LM training algorithm, which is the fastest back-propagation algorithm, was sufficient to reduce the computational time. The target values specified were the square-roots of the collision frequencies generated in DEM simulations. The resulting output of the ANNs represented the estimated square root of the collision frequency, and as such, these values were squared before use in the PBM to invert the square root transform and retain their physical meaning.

7.2.4 Bi-directionally coupled PBM-DEM model

A bi-directionally coupled PBM-DEM model was implemented as presented in (Barrasso and Ramachandran, 2015a) to assess the accuracy and computation time savings of the PBM-ANN model. The PBM described in Section 7.2.1 was solved within the DEM simulations using a custom model to count collisions, calculate net changes in the size distribution, and create and remove particles from the simulation. The number of collisions between any two particle size classes was enumerated for 0.25-second time intervals, equal to the time step used in Euler integration to solve the PBM-ANN model, at which point the DEM simulation pauses to solve the PBM. The collision frequencies are then calculated and used in the aggregation rate kernel to determine the net changes in the number of particles in each class. These net changes are achieved by deleting particles, selected randomly, or creating new particles in the space above the impeller. The DEM simulation proceeds for the next time interval to calculate a new collision frequency. The PBM-DEM simulations use the geometry and parameter values presented in Section 7.2.2.

Due to the large computational expense of implementing the fully-coupled PBM-DEM model with initial particle size distribution of 105 total particles, only a fraction of a 3-minute granulation process was simulated. Size distributions from the PBM-ANN models were collected at $t=100$ seconds, at which point significant aggregation would have already occurred to decrease the total particle count, and used as the starting distributions for the PBM-DEM model. The PBM-DEM model was then simulated for the subsequent 10

seconds; the resulting size distributions were compared to those obtained from continuing the PBM-ANN model until $t=110$ seconds. Similar PBM-DEM and PBM-ANN comparisons were simulated for impeller speeds of 60 RPM and 90 RPM. Since these 10-second PBM-DEM simulations was solved in approximately one day, a full three-minute simulation would require approximately three weeks if the number of particles in the system remained constant. However, in the initial stages of granulation, the number of particles in the system is much greater, drastically increasing the computational expense. As a result, the three-minute simulation of the PBM-DEM model would likely require months to solve for this system.

7.3 Results and discussion

7.3.1 Particle size distributions and collision rate functions from DEM

The DEM simulations showed that the collision frequency of any two classes depends on the sizes of those classes, the impeller speed, and the size distribution of the particles in the system. Figure 7.3 shows surface plots of collision frequency versus particle sizes for three simulations using various particle size distributions and impeller speeds.

In general, larger particles collide more frequently than smaller particles - a trend which is prominently noticeable from the steeply rising surface height for larger diameters in Figure 7.3. Additionally, when comparing between impeller speeds with the same size distribution (Figures 7.3(b) and 7.3(c)), the collision frequency increases at larger impeller speeds. These effects are demonstrated more clearly in Figure 7.4, which plots all of the collision frequency data points versus the size distribution number (from Figure 7.2(c)), the impeller speed, and the size of the aggregate particle. From Figure 7.4(a), DEM results show that when the distribution number increases, such as when the average particle size is growing and the particle size distribution is widening, collision frequencies also increase. This trend suggests that the physical state of the system has a significant influence on the collision frequency, and that a dynamic aggregation rate needs to be considered when developing a population balance model. It is also evident from Figure 7.4(b) that an increase in impeller speed results in slightly greater collision frequencies, which can be attributed to the increased

agitation of the system. Furthermore, the behavior of larger particles engaging in more frequent collisions is also discernible from Figure 7.4(c).

Because the collision frequency data from both DEM and ANN simulations are overlaid in Figure 7.4, similar pattern of the aforementioned effects of the particle size and distribution on collision frequencies are observable for both ANN and DEM simulations.

7.3.2 ANN training and predictability

The performance of a neural network developed can be measured by plotting the regression of the square root of the collision frequencies predicted by the ANN (known as the output) versus those calculated by DEM simulations (known as targets). The coefficient of determination (R^2) values for the regression plots of the four neural networks are listed in Table 7.4 for the training, validation, and testing subsets, in addition to the overall value.

Table 7.4: Coefficients of determination (R^2) for each ANN, by data set.

| ANN | Training | Validation | Testing | Overall |
|-----|----------|------------|---------|---------|
| 1 | 0.7859 | 0.7167 | 0.8516 | 0.7810 |
| 2 | 0.1057 | 0.1360 | 0.1220 | 0.1121 |
| 3 | 0.8657 | 0.8393 | 0.8871 | 0.8643 |
| 4 | 0.9780 | 0.9715 | 0.9600 | 0.9751 |

These results show that the accuracy of the fourth ANN is much higher than that of the first three. Two conclusions can be drawn from this observation; either, the architecture is insufficient to describe the input-target relationships for the first three ANNs, or the inputs used for these ANNs are not extensive enough to describe the target collision frequencies generated from the DEM simulations. Based on the results of the DEM simulations, shown in Figure 7.4, it is clear that the impeller speed, particle size, and size distribution affect the collision frequency. As a result, the fourth ANN was selected as the optimal ANN for use in the aggregation rate kernel, and all subsequent results are based on this ANN.

The regression plots for the ANN are shown in Figure 7.5, and an overlay of the effects plots for the target and output collision frequencies is shown in Figure 4. The ANN predictions show strong correlation to the target values, or DEM results, suggesting that

the training was successful and the ANN captures the trends observed. The validation and testing data sets were also strongly correlated, suggesting that the ANN is not over-fitting the data and has predictive capabilities beyond the data points used in training. Based on the overlay of the effects plot (Figure 7.4) the ANN captures the overall relationships between the input and target variables.

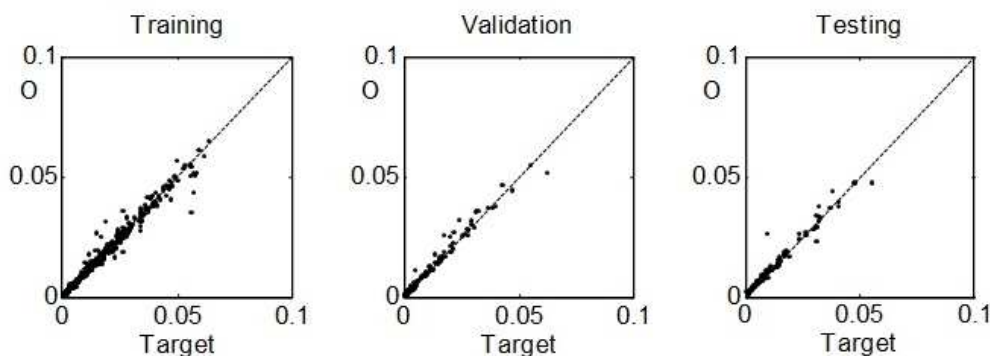


Figure 7.5: Regression plots for ANN 4. Target values are collision frequencies, in collisions/particle²-s, from DEM results. Output values are the corresponding predicted collision frequencies from ANN.

Figure 7.6 shows the ANN-predicted collision frequency as a function of the sizes of the colliding particles for the three distributions and impeller speeds shown in Figure 7.3. These plots show similar shapes trends to those from the DEM data sets (Figure 7.3).

7.3.3 PBM-ANN simulation results

The ANN thus developed provides a dynamic collision frequency function which is dependent on particle size and distribution, and impeller speed to the PBM. When combined with the constant collision efficiency, the ANN-based function completes the aggregation rate kernel. To use the PBM-ANN model, the ANN was evaluated at every time step during the PBM simulation to determine a predicted collision frequency between each pair of bins based on their diameters and number frequencies, the overall size distribution of the system, and the impeller speed. Figure 7.7 shows the results of the uncoupled PBM and PBM-ANN models.

Figure 7.7(a) shows the average volume-mean diameter ($d_{4,3}$) over time for the constant

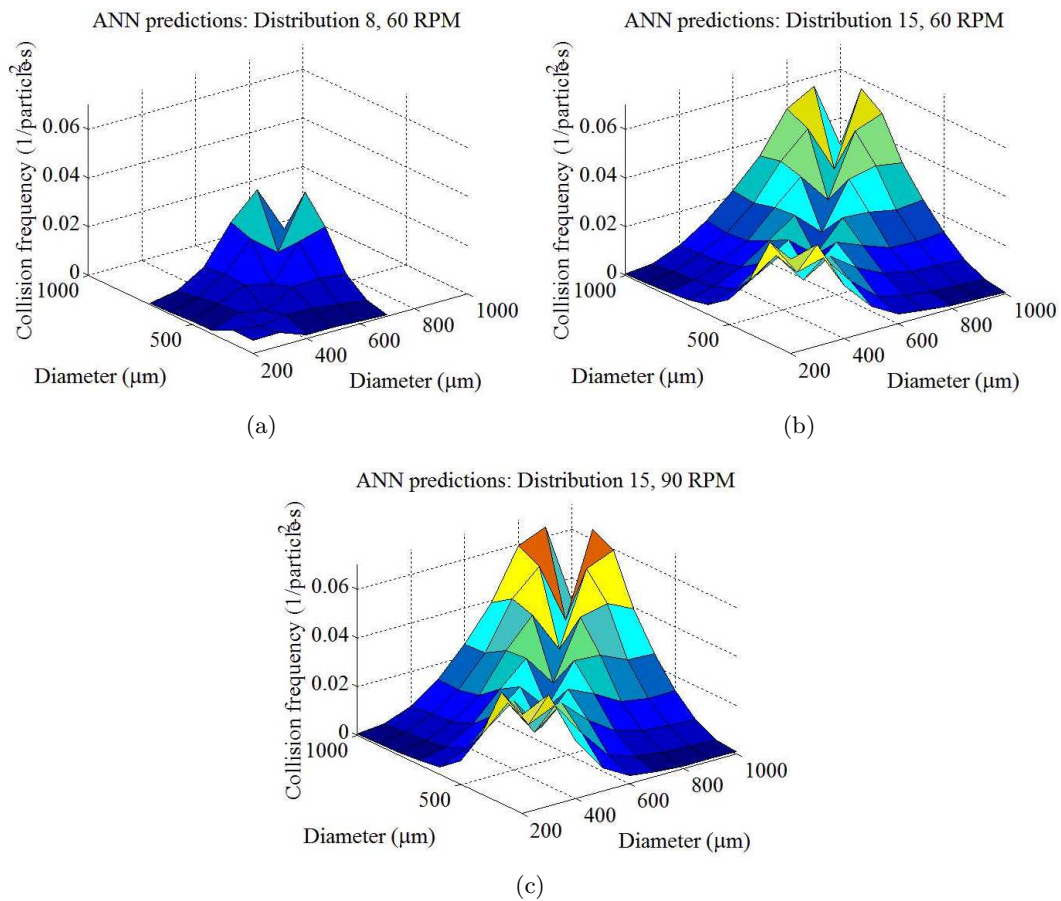


Figure 7.6: ANN collision frequency predictions for (a) distribution 8 at 60 RPM and distribution 15 at (b) 60 RPM and (c) 90 RPM.

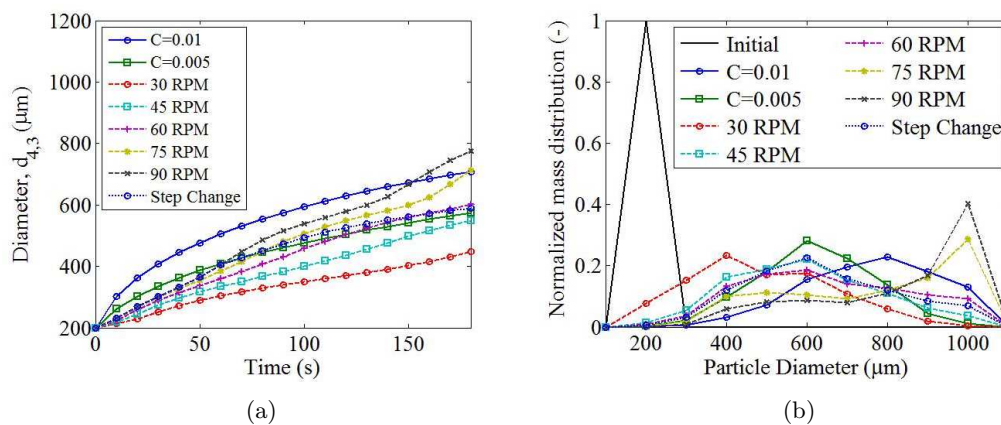


Figure 7.7: PBM results for two constant collision frequencies (in 1/particle²-s) and PBM-ANN results for five impeller speeds and a step change in impeller speed from 90 RPM to 30 RPM at 60 seconds, (a) $d_{4,3}$ vs. time and (b) particle size distributions after 180 seconds.

and dynamic collision frequencies. The constant collision frequencies resulted in sharp increases in size initially, but the size starts to level off after the first minute. However, in the simulations using the dynamic and size-dependent collision frequency (via ANN), the size increase is more gradual initially, but steadier throughout the process. This result can be attributed to the size and size distribution dependencies of the aggregation rate kernel when using the ANN. As was demonstrated in DEM simulations illustrated in Figures 7.3 and 7.4, the collision frequencies of particles in granulation processes are functions of the physical state of the system rather than being constant values. Thus, using the ANN-based kernel for accurately captures this dynamic aggregation behavior.

Figure 7.7 also demonstrates the effect of impeller speed on the granulation process. The PBM-ANN was simulated at five impeller speeds ranging from 30 to 90 RPM and with a step change in impeller speed from 90 to 30 RPM at 60 seconds. Greater impeller speeds result in larger particles due to the increase in collision frequency.

In the step change simulation, the particle size initially increases quickly. When the impeller speed is reduced at 60 seconds, the aggregation rate reduces. This result demonstrates the ability of the PBM-ANN model to respond to changes in a process parameter, which may be useful in process design, control, and optimization.

By using the ANN, the computation times of the multi-scale simulations were drastically reduced compared to those of a full PBM-DEM model. While the DEM simulations required hours or days to solve only 10 seconds of simulation, the PBM-ANN model was solved in approximately 15 seconds. In comparison, the uncoupled PBM was solved in less than one second. The increase in computation time when using the ANN can be attributed to the evaluation of the ANN based on the current input parameters at each time step. Additionally, the calculation of some of those input parameters (such as particle size distribution) was not required at every time step in the uncoupled PBM since they had no impact on the results. Unlike the full PBM-DEM model, the 15-second PBM-ANN simulation can be used for iterative calculations, such as parameter estimation, optimization, and model-based control.

7.3.4 Comparison of PBM-DEM and PBM-ANN results

A fully coupled PBM-DEM model was simulated for 10 seconds to assess the computation time savings and accuracy of the hybrid PBM-ANN model. Figure 7.8 shows the initial ($t=100$ s) and final ($t=110$ s) size distributions generated from the PBM-ANN and PBM-DEM models for two impeller speeds. As seen in Figure 7.8(a), the PBM-ANN and PBM-DEM simulations for the impeller speed of 60 RPM showed similar size changes over the 10-s interval and nearly identical final size distributions, with an R^2 value of 0.993. The final size distributions obtained from the two models at 90 RPM (Figure 7.8(b)) showed similar accuracy with R^2 value of 0.963, however, the PBM-DEM simulation showed slightly larger particles. The minor discrepancy between the PBM-DEM and PBM-ANN in these figures may primarily be due to noise and interpolation error introduced while running the PBM-DEM simulations at much shorter intervals. For the coupled PBM-DEM model, the DEM simulations were performed for very short time intervals (0.25 seconds), successively followed by the update in particle size distribution calculated by PBM. The collision frequency calculated by DEM for these shorter intervals contain more noise which amasses as the simulation proceeds. The PBM-ANN model, on the other hand, employs the collision frequency predictions from the ANN developed using 10-second DEM simulations. The collision frequencies used at each time interval is an interpolation by the ANN and thus, is slightly different from the collision data shown by DEM.

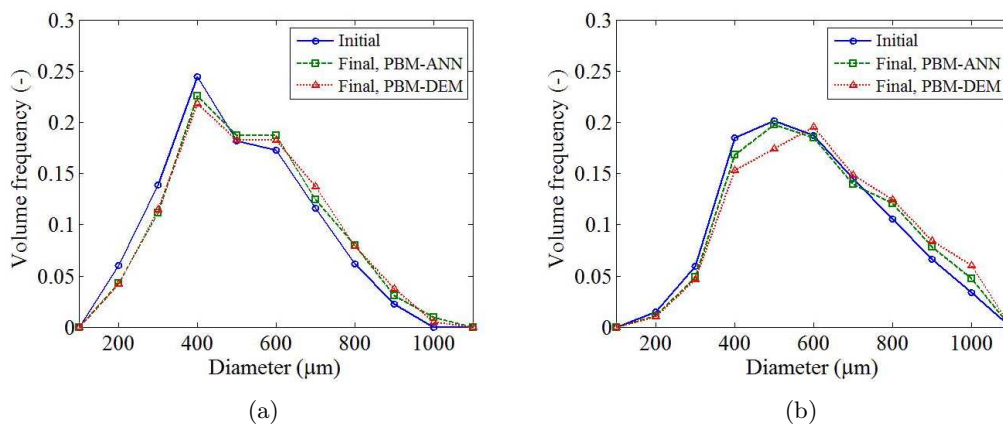


Figure 7.8: Particle size distributions obtained from the PBM-ANN and PBM-DEM models over a 10 second interval for impeller speeds of (a) 60 RPM and (b) 90 RPM. Initial size distributions were obtained from the PBM-ANN models at $t=100$ s.

Using 4 processors, the PBM-DEM model was solved in approximately 12 and 20 hours for the 60 RPM and 90 RPM simulations, respectively. Because the aggregation rate is slower at the smaller impeller speed, the initial size distribution (at $t=100$ s) for the 60 RPM simulation contained more particles than that of the 90 RPM simulation, explaining the difference in computation time. Had the PBM-DEM model used the initial distribution at $t=0$ s, the initial number of particles in the system would have been 100,000, drastically increasing the computational expense. Further, to simulate the full 180 seconds of process time, the coupled model would require months to solve. In contrast, the PBM-ANN model is able to capture key trends and can be solved in seconds, and is a good alternative for calculating end-point and dynamic distributions.

7.4 Summary

The QbD approach to solving complex problems in science and engineering demands a model-based method to understand process design and parameters. For a highly complex process of wet granulation, developing a predictive model that is dependable beyond the space of calibration data set is critical in aiding process control and optimization. A multi-scale model where the mechanistic information from a DEM model is provided to the empirical PBM calculations can be used to simulate multi-dimensional wet granulation processes. Simulating DEM models, however, is a computationally taxing procedure and one that is not very feasible for practical purposes of optimization, control or flowsheet modeling.

An alternative to running DEM simulations is to develop a ROM that will substitute the intensive calculations of DEMs for a faster approach of black box models. The reduced order model investigated in this study utilizes DEM results to train an artificial neural network (ANN) which can relate particle size, size distribution, and impeller speed to the collision frequency. The trained ANN showed a high predictive ability with respect to DEM generated data. A coupled PBM-ANN bi-directional model was subsequently developed using ANN predictions as a key component of the aggregation rate kernel. The coupled model showed a different development of average particle size and size distribution over

time from that of a constant aggregation rate kernel. In addition, the coupled model demonstrated sensitivity to the impeller speed via the ANN rate kernel. Further, the PBM-ANN model showed similar size changes over a 10-second interval to those of the fully coupled PBM-DEM model. The computational time required to solve the PBM-ANN model was observed to be drastically lower than that of the full PBM-DEM model, illustrating its potential for dynamic or iterative calculations. This approach can be extended to more detailed PBM models, incorporating particle-scale flux and velocity data from DEM to evaluate mechanistic rate expressions in the PBM.

Chapter 8

Qualitative assessment of a multi-scale, compartmental PBM-DEM model of a continuous twin-screw wet granulation process

Wet granulation processes play a crucial role in solid oral dosage manufacturing processes. However they are often designed empirically with poor efficiency. To implement Quality-by-Design, a more scientific understanding is desired to predict the effects of process and equipment design and material properties on the rate mechanisms governing wet granulation processes. In this study, a multi-dimensional compartmental population balance model of a twin screw granulation process is coupled with discrete element method simulations to evaluate mechanistic rate expressions describing aggregation, breakage, consolidation, and particle flow. Steady-state results are presented for various configurations of the screw elements. The effects of screw element configuration on product size distribution, porosity, and liquid distribution are presented and compared with experimental trends described in literature. Simulated results are consistent with experimental findings, demonstrating the model's qualitative ability to predict the effects of screw element design and configuration on the particle-scale phenomena and process outcomes.

8.1 Background

High shear and fluid bed granulators are traditionally used for batch and continuous wet granulation processes. However, as pharmaceutical manufacturing processes shift from the traditional batch operation towards a more modern continuous framework, twin screw wet granulation has shown particular potential for its reduced throughput, design flexibility, and short residence time (El Hagrasy et al., 2013). Using a twin screw extruder, large, porous granules are formed from fine powder after drop addition of a liquid binder. Characterizing

the mechanisms of twin screw granulation (TSG), particularly with respect to screw element design and configuration, is an area of significant importance and experimental research (Dhenge et al., 2012; Vercruyssen et al., 2012; El Hagrasy et al., 2013; El Hagrasy and Litster, 2013; Lee et al., 2013; Kumar et al., 2014; Sayin et al., 2015).

The transition to continuous pharmaceutical manufacturing operations coincides with efforts to implement Quality-by-Design (QbD), which is a risk management approach whereby processes and products are designed to meet required quality and safety specifications so long as they are operated within a known design space which is a function of process parameters, material properties, and equipment geometry (U.S. Food and Drug Administration, 2006, 2009). Substantial process understanding is required to define the design space of a process, particularly relating process outcomes, such as size distributions and content uniformity metrics, to input variables, such as material grade or impeller speed. Using a model-based approach, these relationships can be understood and predicted, thus facilitating QbD.

To model particulate processes such as wet granulation, two techniques are often used independently. Population balance modeling (PBM) groups the particles into classes based on their properties and uses differential equations to track the number of particles in each class as they undergo rate changes, such as growth, agglomeration, and breakage. In contrast, discrete element method (DEM) simulations are used to track individual particles as they move through space, colliding with other particles and equipment. Newton's laws of physics are used to evaluate particle motion from the resulting forces.

PBM is more often used to simulate wet granulation processes, often capturing multi-dimensional distributions in properties such as size, liquid content, and porosity (Verkoeijen et al., 2002; Cameron et al., 2005; Immanuel and Doyle III, 2005; Poon et al., 2008). However, these models typically rely on empirical fitting of unknown parameters, with little predictive capabilities beyond an experimental design space (Braumann et al., 2010; Ramachandran and Barton, 2010; Chaudhury et al., 2014a; Barrasso et al., 2015a). DEM captures particle-scale behavior, but does not inherently relate these events to the process-scale changes in particle size and other properties (Barrasso and Ramachandran, 2015a;

Barrasso et al., 2015b). Further, DEM is computationally expensive, requiring more computing power as the number of particles is increased and as their sizes are decreased.

Significant research interest lies in combining these two methods. Early work in this area focused on using DEM simulations to solve a PBM, replacing small particles with larger ones as they collide and merge (Goldschmidt et al., 2003; Ingram and Cameron, 2005; Barrasso and Ramachandran, 2015a; Sen et al., 2014). Other studies focused on using DEM simulations to evaluate mechanistic rate kernels in the PBM (Gantt et al., 2006; Reinhold and Briesen, 2012) or spatial transfer between compartments (Bouffard et al., 2012). Alternatively, DEM data was used to train a surrogate model in the form of an artificial neural network to use within a PBM (Barrasso et al., 2014). Most recently, Barrasso et al. (2015b) developed a bi-directional coupling algorithm between PBM and DEM simulations and demonstrated the technique for single compartments of a twin screw granulator. Despite this progress, a complete model for a continuous twin screw granulation has not been presented with sensitivities to screw element configuration, material properties, and process parameters. This work aims to address this gap.

8.1.1 Objectives

In this work, a multi-scale model is presented and implemented for a continuous TSG process using PBM and DEM techniques based on the framework developed by Barrasso et al. (2015b). The following aims are addressed:

- The two-dimensional, compartmental PBM tracks particle size, liquid content, and porosities throughout the granulator, accounting for particle flow, nucleation, agglomeration, breakage, layering, consolidation, and liquid addition. An additional mass balance equation is developed to track the mass of fine powder particles in the system.
- DEM simulations are used to obtain compartmental residence time data, particle velocities, and collision rates. This particle-scale information is used to evaluate transfer rates between compartments in addition to mechanistic aggregation, consolidation, and breakage rate expressions, forming a scientifically meaningful model.

- The predictive power of the model is demonstrated, and the model is assessed qualitatively by comparison with experimentally observed trends, particularly those reported by El Hagrasy and Litster (2013). The implications of the predictive model for QbD are discussed.

8.2 Population balance model development

In order to model this system, the continuous TSG was divided into four axial compartments, and flow along the granulator was simulated by transferring particles into and out of each compartment based on a residence time model and DEM simulations. The four-compartment model is based on the experimental set-up used by El Hagrasy and Litster (2013), and further details are provided in Section 8.2.2. A 2-D PBM was solved in each compartment, tracking distributions in particle size and liquid content, and the lumped parameter approach was used to track porosity changes, based on the technique presented by Barrasso and Ramachandran (2012), assuming that all particles in a compartment belonging to a given size and liquid class have the same porosity. A separate mass balance was implemented to track fine powder particles, which were treated as a separate phase from the granulated material. Mechanistic expressions were used to evaluate aggregation, breakage, and consolidation rate expressions, using the bi-directional coupling technique presented by Barrasso et al. (2015b) to obtain collision and velocity data from DEM simulations. Nucleation and layering mechanisms were added to the model to represent the formation of granules from fine powder. For all simulations, a steady state is reached, and steady-state results are presented in this study. Figure 8.1 describes this algorithm in more detail.

The compartmental approach was implemented as previously demonstrated in Barrasso et al. (2013b) and Barrasso et al. (2015a) in order to capture size and liquid distributions along the length of the granulator. In each of four axial compartments, a 2-D PBM was solved, tracking changes in particle size and liquid content distributions as due to wetting, nucleation, aggregation, breakage, layering, and consolidation. Equation 8.1 shows the general population balance equation for this model, where F is the number of particles as

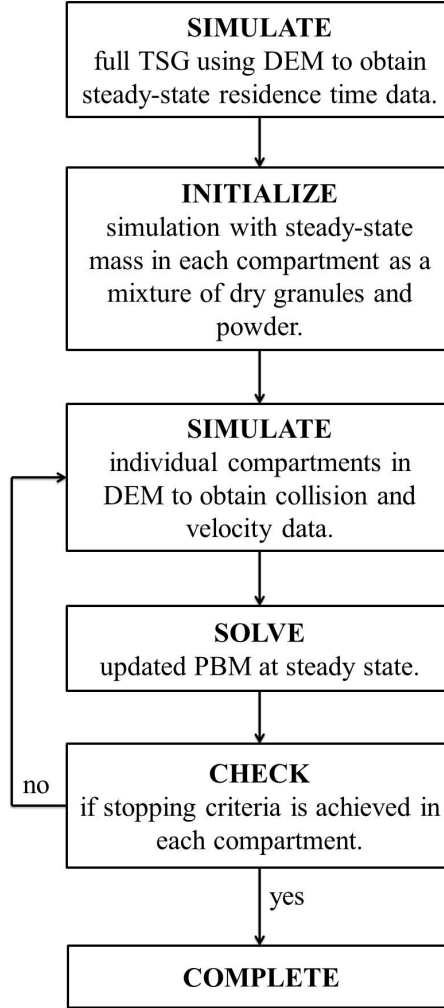


Figure 8.1: Flowchart of coupled PBM-DEM modeling approach.

a function of particle volume (V), liquid volume (V_L), compartment (x), and time (t).

$$\frac{\partial F}{\partial t} + \frac{\partial}{\partial V} \left(F \frac{dV}{dt} \right) + \frac{\partial}{\partial V_L} \left(F \frac{dV_L}{dt} \right) = \mathfrak{R}_{nuc} + \mathfrak{R}_{agg} + \mathfrak{R}_{break} + \dot{F}_{in} - \dot{F}_{out}$$

$$F = F(V, V_L, x, t) \quad (8.1)$$

\mathfrak{R}_{nuc} , \mathfrak{R}_{agg} , and \mathfrak{R}_{break} are source terms representing the net rates of change due to nucleation, aggregation, and breakage, respectively, and \dot{F}_{in} and \dot{F}_{out} are the transfer rates of particles into and out of the compartment. The growth terms account for changes in particle size and liquid content due to layering and consolidation ($\frac{\partial}{\partial V} (F \frac{dV}{dt})$) and liquid addition ($\frac{\partial}{\partial V_L} (F \frac{dV_L}{dt})$), where $\frac{dV}{dt}$ and $\frac{dV_L}{dt}$ are the rates of particle volume growth and liquid volume growth in each bin.

To monitor the porosity of each particle, the per-particle solid volume (V_S) of each bin was tracked using the lumped parameter approach presented by Barrasso and Ramachandran (2012), as shown in Equation 8.2.

$$\begin{aligned} \frac{\partial FV_S}{\partial t} + \frac{\partial}{\partial V} \left(FV_S \frac{dV}{dt} \right) + \frac{\partial}{\partial V_L} \left(FV_S \frac{dV_L}{dt} \right) &= \mathfrak{R}_{S,nuc} + \mathfrak{R}_{S,agg} \\ &+ \mathfrak{R}_{S,break} + \mathfrak{R}_{S,layer} + \dot{F}_{in} V_{S,in} - \dot{F}_{out} V_S \\ V_S &= V_S(V, V_L, x, t) \end{aligned} \quad (8.2)$$

The source terms $\mathfrak{R}_{S,nuc}$, $\mathfrak{R}_{S,agg}$, and $\mathfrak{R}_{S,break}$ track the transfer of solid volume during nucleation, aggregation, and breakage, and the growth terms account for changes in the total solid volume in each bin as the distribution changes due to layering, consolidation, and liquid addition. $\mathfrak{R}_{S,layer}$ accounts for the addition of fine powder to the granule phase due to layering. $V_{S,in}$ is the per-particle solid volume of the inlet stream of each compartment. As in Equation 8.1, the partial derivatives represent the consolidation, layering, and liquid addition mechanisms.

To represent all of the material in the granulator, a distinction is made between granules and fine powder. Equations 8.1 and 8.2 are applied only to granules after they are formed from the nucleation of fine powder. It is assumed that the fine powder and granulated material are two distinct phases that only interact during nucleation, as liquid droplets merge with fine powder to form granule nuclei, and layering, as fine powder accumulates on the surfaces of wet granules. A separate mass balance, given by Equation 8.3, is used to track the mass of fine powder (m_p) in each compartment as it changes due to nucleation, layering, and powder flow.

$$\begin{aligned} \frac{dm_p}{dt} &= \dot{m}_{p,in} - \dot{m}_{p,out} - D_{m_p,layer} - D_{m_p,nuc} \\ m_p &= m_p(x, t) \end{aligned} \quad (8.3)$$

The inflow and outflow of fine powder in each compartment are given by $\dot{m}_{p,in}$ and $\dot{m}_{p,out}$, and $D_{m_p,layer}$ and $D_{m_p,nuc}$ represent the depletion of fines due to layering and nucleation, respectively. In this model, it is assumed that fine particles are not created from granule attrition, only consumed by the granulation process.

8.2.1 Particle properties

Based on the 2-D grid and the lumped parameter of the solid volume, additional granule properties can be calculated. The pore volume, V_P , is the difference between the total and solid volumes for each bin, as shown in Equation 8.4, and the intra-granular porosity, ϵ , is given by Equation 8.5.

$$V_P = V - V_S \quad (8.4)$$

$$\epsilon = \frac{V_P}{V} \quad (8.5)$$

Changes in particle porosity are evaluated in the model by tracking the total solid volume and the particle volumes using Equations 8.1 and 8.2.

The diameter, d , of each granule is based on the total volume, assuming all granules are spherical, according to Equation 8.6.

$$d = \left(\frac{6V}{\pi} \right)^{\frac{1}{3}} \quad (8.6)$$

The PBE framework does not rely on the assumption that all particles are spherical. However, the DEM simulations implement particles as spheres due to a lack of understanding of the mechanisms governing shape. Further, the particle theory used to derive the mechanistic rate kernels for breakage and agglomeration may rely on this assumption. This assumption may be a source of error in quantitative comparison with experimental results, but should not affect the qualitative trends of the model.

The total liquid volume is the sum of internal and external liquid, where internal liquid ($V_{L,int}$) occupies some of the pore space, and external liquid ($V_{L,ext}$) remains on the surface of the granule to induce layering and aggregation. The volume of internal liquid in each granule is equal to the product of the pore volume and the maximum pore saturation fraction (s^*), if sufficient liquid is present, as shown in Equation 8.8.

$$V_L = V_{L,int} + V_{L,ext} \quad (8.7)$$

$$V_{L,int} = \min(V_L, s^* V_P) \quad (8.8)$$

If there is not sufficient liquid to saturate the pores, all of the liquid is considered internal.

The value for s^* is listed in Table 8.1. A hypothetical value was presumed for these calculations, and further experimental characterization is required to obtain a more accurate measure of pore saturation.

Table 8.1: Values for material properties, process parameters, equipment geometry specifications, and model settings used in simulations.

| Parameter | Type | Value |
|--|-----------|---|
| Maximum pore saturation fraction (s^*) | material | 0.6 |
| Density of solid component (ρ_S) | material | 2000 kg m ⁻³ |
| Density of liquid component (ρ_L) | material | 1000 kg m ⁻³ |
| Binder viscosity (μ) | material | 0.05 Pa s |
| Primary particle size (d_p) | material | 5 μ m |
| Coefficient of restitution slope, intercept (e_{slope}, e_0) | material | 0.5, 0.5 |
| Inlet powder feed rate ($m_{p,in}$) | process | 4 kg h ⁻¹ |
| Liquid binder addition rate (\dot{L}_{in}) | process | 0.6 kg h ⁻¹ |
| Powder bed porosity (ϵ_{bed}) | material | 0.65 |
| Liquid droplet diameter | material | 1.5 mm |
| Surface asperity height (h_a) | material | 5 μ m |
| Critical Stokes deformation number (St_{def}^*) | material | 0.2 |
| Consolidation rate constant (K_{cons}) | material | 2e – 3 |
| Layering rate constant (K_{layer}) | material | 2e – 3 mm ⁻² s ⁻¹ |
| Particle-particle coefficients of static, rolling friction | material | 0.35, 0.2 |
| Particle-wall coefficients of static, rolling friction | material | 0.16, 0.2 |
| Poisson's ratio | material | 0.2 |
| Ratio of Young's modulus to yield strength | material | 162 |
| Implicit unsteady solver time step | model | 1e – 4 s |
| Screw speed | process | 600 RPM |
| Granulator length (total, per compartment) | equipment | 96 mm, 24 mm |
| Screw diameter | equipment | 16 mm |
| DEM initialization time | model | 0.1 s |
| DEM simulation time (Δt_{DEM}) | model | 0.25 s |
| DEM trigger condition: relative change in $d_{4,3}$ | model | 10% |

From the solid and liquid volumes, the wet (m_{wet}) and dry (m_{dry}) granule masses can be calculated, according to Equations 8.9 and 8.10, where ρ_S and ρ_L are the solid and liquid densities, respectively, given in Table 8.1.

$$m_{wet} = V_S \rho_S + V_L \rho_L \quad (8.9)$$

$$m_{dry} = V_S \rho_S \quad (8.10)$$

The solid density is assumed to be constant as the model only considers one solid component.

The yield strength (τ_y) was evaluated according to Equation 8.11 as a function of granule porosity, average particle velocity (U_0), and primary particle size (d_p) (Van den Dries and Vromans, 2002; Barrasso et al., 2015b).

$$\tau_y = \frac{9}{8} \frac{(1 - \epsilon)^2}{\epsilon^2} \frac{9\mu U_0}{16d_p}, \quad (8.11)$$

The primary particle size is listed in Table 8.1, and the average particle velocity was obtained from DEM simulations.

Using the correlation presented by Barrasso et al. (2015b), the coefficient of restitution (e) between any two particle types was assumed to be linearly dependent on the external liquid fraction, as shown in Equation 8.12.

$$e = e_0 - e_{slope} \frac{V_{L,ext}}{V_{L,ext} + V} \quad (8.12)$$

The intercept (e_0) and slope (e_{slope}) are given in Table 8.1, and $V_{L,ext}$ is determined from Equations 8.7 and 8.8. The true relationship between particle properties and the coefficient of restitution is unknown, and these values were selected as realistic approximations based on the work of Mangwandi et al. (2007).

8.2.2 Compartments and flow

In the PBM, the TSG was represented as four well-mixed axial spatial compartments in series, as shown in Figure 8.2. The powder feed and liquid binder are introduced in the first compartment, and the product exits from the last compartment. Similar to the techniques

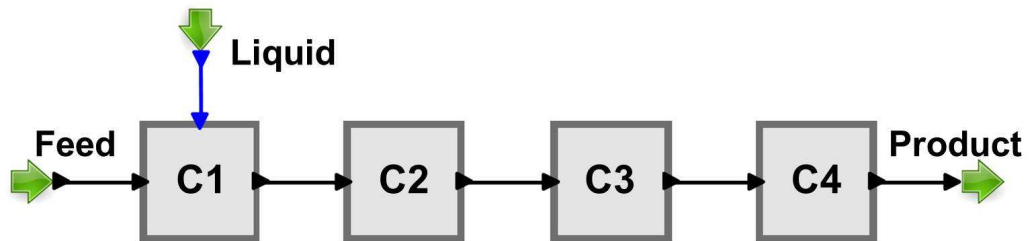


Figure 8.2: Schematic of four-compartment model of the TSG, with powder feed and liquid added to the first compartment (C1) and product exiting the fourth compartment (C4).

used in Barrasso et al. (2013b) and Barrasso et al. (2015a), the flow rate out of each

compartment is described by a residence time function, as shown in Equation 8.13.

$$\dot{F}_{out}(V, V_L, x, t) = \frac{F(V, V_L, x, t)}{\tau(x)} \quad (8.13)$$

$\tau(x)$ is the average residence time in compartment x , and \dot{F}_{out} is the flow rate of granules of each size and liquid class exiting the compartment. The average residence times depend on equipment geometry and process parameters, and they were estimated using DEM simulations, as described in Section 8.3.2. The inlet flow rates are equal to the outlet flow rates of the previous compartments.

$$\dot{F}_{in}(V, V_L, x, t) = \dot{F}_{out}(V, V_L, x - 1, t) \quad (8.14)$$

Similarly, the outlet mass flow rates of fine powder particles are given by Equation 8.15, and the inlet flow rates by Equation 8.16.

$$\dot{m}_{p,out}(x, t) = \frac{m_p(x, t)}{\tau(x)} \quad (8.15)$$

$$\dot{m}_{p,in}(x) = \dot{m}_{p,out}(x - 1) \quad (8.16)$$

It should be noted that the feed is pure powder, with no granules. The powder feed rate ($\dot{m}_{p,in}(1)$) is listed in Table 8.1.

8.2.3 Liquid addition

As droplets of liquid binder are added to the system, they either form new granule nuclei by interacting with fine particles or they increase the liquid content of existing granules. To represent these subprocesses, the total liquid addition rate, \dot{L}_{in} , is broken into two terms: the rate of liquid addition to the fine powder, $\dot{L}_{in,powder}$, and the rate of liquid addition to the granules, $\dot{L}_{in,granules}$, as shown in Equation 8.17.

$$\dot{L}_{in}(x) = \dot{L}_{in,powder}(x, t) + \dot{L}_{in,granules}(x, t) \quad (8.17)$$

The value used for the total liquid addition rate, by volume, is listed in Table 8.1, and liquid is only added in the first axial compartment. The liquid properties, such as viscosity, affect

the agglomeration and consolidation rates of the particles.

The fraction of liquid added to the fine powder is assumed to be equal to its volume fraction, or the ratio of the total volume of powder, $V_{total,powder}$, to the total volume of granules and powder, $V_{total,granules} + V_{total,powder}$. This assumption is used to allocate liquid to the fines or the granules. Liquid that is added to fine powder forms nuclei, while liquid added to granules increases their wetness. It seems that the total volume makes more sense for fine powder, while the surface area makes more sense for granules. Either way, this assumption should have little effect on the model results and is mainly used to conserve mass and reduce the nucleation rate as the fines fraction approaches zero.

$$\frac{\dot{L}_{in,powder}(x,t)}{\dot{L}_{in}(x)} = \frac{V_{total,powder}(x,t)}{V_{total,granules}(x,t) + V_{total,powder}(x,t)} \quad (8.18)$$

The volume of powder is calculated from the mass of powder, solid density, and bed porosity (ϵ_{bed}), as shown in Equation 8.19, and the volume of granules is determined from the granule size distribution in the compartment, shown in Equation 8.20.

$$V_{total,powder}(x,t) = \frac{m_p(x,t)}{\rho_S(1 - \epsilon_{bed})} \quad (8.19)$$

$$V_{total,granules}(x,t) = \sum F(V, V_L, x, t)V \quad (8.20)$$

The rate of increase in the liquid volume, per granule, is determined from the total granule liquid addition rate according to Equation 8.21 and used to evaluate the growth terms in Equations 8.1 and 8.2.

$$\frac{dV_L}{dt}(V, V_L, x, t) = \frac{\dot{L}_{in,granules}(x,t)V}{V_{total,granules}(x,t)} \quad (8.21)$$

Equation 8.21 assumes that the liquid is distributed uniformly in each compartment, and each granule takes up liquid at a rate proportional to its volume.

The liquid addition rate to the fine powder particles is then used to evaluate the nucleation rate.

8.2.4 Nucleation

As droplets are added to the system, granule nuclei form when droplets come into contact with fine powder particles. It is assumed that each droplet that reaches the fine particles forms a single saturated granule of volume V_{nuc} and liquid volume $V_{L,nuc}$. The rate of nuclei formation, \mathfrak{R}_{nuc} is equal to the rate of droplet addition to the powder fines, as shown in Equation 8.22.

$$\mathfrak{R}_{nuc}(V_{nuc}, V_{L,nuc}, x, t) = \frac{\dot{L}_{in,powder}(x, t)}{V_{droplet}} \quad (8.22)$$

$V_{droplet}$ is the volume of a single liquid droplet, assumed to be constant and spherical, with a diameter listed in Table 8.1. The liquid volume of the nucleus is equal to that of the droplet ($V_{L,nuc} = V_{droplet}$). The nuclei volume is determined from Equation 8.23, which assumes that each nucleus is fully saturated with liquid and has a porosity equal to that of the bed. This assumption is consistent with a droplet penetrating a porous bed and forming a nuclei, similar to the theory presented in Iveson et al. (2001).

$$V_{nuc} = \frac{V_{L,nuc}}{s^* \epsilon_{bed}} \quad (8.23)$$

During nucleation, solid material is transferred from the fine powder phase to the granule phase. This process is captured in Equations 8.24 and 8.25. The depletion rate of fine powder particles is equal to the product of the nucleation rate and the mass of solid associated with each nucleus, as shown in Equation 8.24.

$$D_{m_p,nuc}(x, t) = \frac{\dot{L}_{in,powder}(x, t)}{V_{droplet}} (1 - \epsilon_{bed}) V_{nuc} \rho_S \quad (8.24)$$

The rate of solid formation in the granule phase is similarly calculated according to Equation 8.25.

$$\mathfrak{R}_{S,nuc}(V_{nuc}, V_{L,nuc}, x, t) = \frac{\dot{L}_{in,powder}(x, t)}{V_{droplet}} (1 - \epsilon_{bed}) V_{nuc} \quad (8.25)$$

8.2.5 Aggregation

The subprocess of aggregation was modeled using the approach presented by Barrasso et al. (2015b), where the total aggregation rate is given by Equation 8.26.

$$\begin{aligned} \mathfrak{R}_{agg}(V, V_L, x, t) = & - \int_0^\infty \int_0^\infty \beta(V, V_L, V', V'_L, x, t) F(V, V_L, x, t) F(V', V'_L, x, t) dV'_L dV' \\ & \frac{1}{2} \int_0^V \int_0^{V_L} \beta(V - V', V_L - V'_L, V', V'_L, x, t) F(V - V', V_L - V'_L, x, t) F(V', V'_L, x, t) dV'_L dV' \end{aligned} \quad (8.26)$$

The rate kernel, β , describes the rate at which particles of different sizes and liquid contents coalesce. A mechanistic rate kernel is used, represented by the product of the collision frequency, $C_{collision}$, and the collision efficiency, Ψ , as shown in Equation 8.27 (Gantt et al., 2006).

$$\beta(V, V_L, V', V'_L, x, t) = C_{collision}(V, V', x, t) \Psi(V, V_L, V', V'_L, x, t) \quad (8.27)$$

The collision efficiency is the number of collisions per second between any two particle sizes, on a per-particle basis. It is evaluated independently for each compartment using bi-directionally coupled DEM simulations, as described in Section 8.3.3.

The collision frequency is the fraction of collisions that result in successful coalescence. Based on the Stokes criterion, this value is equal to the fraction of collisions that have relative velocities below a critical velocity (U_{crit}), as shown in Equation 8.28, where $p(U)$ is the probability distribution of the collision velocity (Barrasso et al., 2015b).

$$\Psi(V, V_L, V', V'_L, x, t) = \int_0^{U_{crit}} p(U) dU \quad (8.28)$$

The critical velocity is calculated from Equation 8.29, where h is the average height of the surface liquid, h_a is the height of the surface asperities, μ is the binder viscosity, and \tilde{d} and \tilde{m} are the harmonic means of the particle diameters and masses, respectively (Iveson et al., 2001; Barrasso et al., 2015b).

$$U_{crit}(V, V_L, V', V'_L, x, t) = \left(1 + \frac{1}{e}\right) \log\left(\frac{h}{h_a}\right) \frac{3\pi\tilde{d}^2\mu}{8\tilde{m}} \quad (8.29)$$

The surface liquid height is determined from the external liquid volume, where $h = L_{ext}d/6V$ (Liu et al., 2000).

A log-normal probability distribution was assumed to describe the distribution in particle velocity, as shown in Equation 8.30, where μ_U and σ_U are parameters describing the mean and variance of the velocity.

$$p(U) = \frac{1}{U\sqrt{2\pi}\sigma_U} \exp\left[-\frac{(\ln U - \mu_U)^2}{2\sigma_U^2}\right] \quad (8.30)$$

$$U_0 = e^{\mu_U - \sigma_U^2/2} \quad (8.31)$$

$$sd_U^2 = (e^{\sigma_U^2} - 1)e^{2\mu_U + \sigma_U^2} \quad (8.32)$$

μ_U and σ_U were calculated from the mean and standard deviation of the particle velocity, U_0 and sd_U , obtained from DEM simulations. In this study, $p(U)$ was calculated for each compartment, assuming that all particle types have the same velocity distribution. This assumption is supported by the prior work of Barrasso et al. (2015b). Bi-directional coupling with DEM was implemented to capture dependencies on liquid content, density, fill level, and size distribution.

The source term tracking the change in the solid volume in each bin due to aggregation, $\mathfrak{R}_{S,agg}$, was evaluated using the techniques presented in Barrasso and Ramachandran (2012) and Barrasso et al. (2015b).

8.2.6 Breakage

The net rate of formation due to breakage in each bin, \mathfrak{R}_{break} is given by Equation 8.33, where b is the fragment distribution function, and K_{break} is the breakage rate kernel.

$$\begin{aligned} \mathfrak{R}_{break}(V, V_L, x, t) = & -K_{break}(V, V_L, x, t)F(V, V_L, x, t) \\ & \int_V^\infty \int_{V_L}^\infty b(V', V'_L, V, V_L)K_{break}(V', V'_L, x, t)F(V', V'_L, x, t)dV'dV'_L \end{aligned} \quad (8.33)$$

A simple fragment distribution was assumed such that all breakage events result in two equally sized particles with equal liquid volumes, as shown in Equation 8.34.

$$b\left(V, V_L, \frac{V}{2}, \frac{V_L}{2}\right) = 2 \quad (8.34)$$

Although this assumption may not be accurate, there is little in the literature describing fragment size distributions in a granulator. In future work, the model can be enhanced by implementing a more physical fragment distribution model.

A mechanistic breakage rate kernel, presented in Barrasso et al. (2015b), was implemented using an approach similar to that of aggregation. A size-dependent rate of particle-particle and particle-wall impacts, C_{impact} , was determined from DEM simulations, and the probability of successful breakage was evaluated based on the particle velocity distribution. The product of these terms is the breakage rate, as shown in Equation 8.35.

$$K_{break}(V, V_L, x, t) = C_{impact}(V, x, t) \int_{U_{break}}^{\infty} p(U) dU \quad (8.35)$$

U_{break} is the critical breakage velocity, above which an impact results in breakage (Tardos et al., 1997; Iveson et al., 2001). It is calculated based on the Stokes deformation criterion, as shown in Equation 8.36, where St_{def}^* is the critical Stokes deformation number, listed in Table 8.1.

$$U_{break}(V, V_L, x, t) = \frac{2St_{def}^*}{\rho_S} \frac{9(1-\epsilon)^2}{8} \frac{9\mu}{\epsilon^2} \frac{1}{16d_p} \quad (8.36)$$

8.2.7 Consolidation and layering

In addition to the event-driven subprocesses of nucleation, aggregation, and breakage, two subprocesses result in gradual changes in particle size. As granules collide and deform, they consolidate, resulting in a decrease in porosity and total volume. Similarly, fine powder particles adhere to granules with surface liquid, resulting in an increase in total volume and solid volume. The net rate of change in particle volume, $\frac{dV}{dt}$, is given by Equation 8.37, where $\frac{dV}{dt}_{cons}$ and $\frac{dV}{dt}_{layer}$ are the rates of change in particle volume due to consolidation and layering, respectively.

$$\frac{dV}{dt} = \frac{dV}{dt}_{cons} + \frac{dV}{dt}_{layer} \quad (8.37)$$

A mechanistic consolidation rate expression was used as implemented by Barrasso et al. (2015b) based on the theories proposed by Ennis et al. (1991) and Tardos et al. (1997). As shown in Equation 8.38, the rate of decrease in particle size is a function of the per-particle

pore volume, impact frequency, Stokes deformation number (St_{def}), and a rate coefficient (K_{cons}).

$$\frac{dV}{dt}_{cons}(V, V_L, x, t) = -K_{cons}V_P C_{impact} (1 - \exp(-St_{def})) \quad (8.38)$$

Unlike empirical models for consolidation, which can require up to three unknown or fitted parameters, this mechanistic kernel only has one adjustable parameter in K_{cons} (Barrasso et al., 2015a). The presumed value for K_{cons} is given in Table 8.1.

The Stokes deformation number is a particle property depending on the solid density, yield strength, and particle velocity, as shown in Equation 8.39.

$$St_{def}(V, V_L, x, t) = \frac{\rho_S U_0^2}{2\tau_y}, \quad (8.39)$$

Both the impact rate, as a function of particle size, and the average particle velocity were obtained from DEM simulations.

Layering was modeled as an increase in granule size as fine powder particles adhere to wet surfaces. The rate of increase in the solid volume of a granule ($\frac{dV_S}{dt}_{layer}$) was assumed to be proportional to the granule surface area and the volume of powder fines in the compartment, as shown by Equation 8.40, where K_{layer} is an adjustable rate constant.

$$\frac{dV_S}{dt}_{layer}(V, V_L, x, t) = \frac{K_{layer}\pi d^2 m_p}{\rho_S} \quad (8.40)$$

Further experimental work is needed to characterize the value of the adjustable rate constant, and a presumed value was used as listed in Table 8.1. This value has little effect on qualitative trends, but a more thorough tuning approach would be required for quantitative validation. Only granules with surface liquid experienced layering, and the layering rate for all other granules was fixed at zero. As a result, an increase in consolidation, which results in excess surface liquid, induces layering.

As the solid volume of the granule increases, the total volume also rises. The initial porosity of the layered region was taken to be that of the powder bed. The increase in total granule volume due to layering ($\frac{dV}{dt}_{layer}$) relates to that of the solid volume according to

Equation 8.41.

$$\frac{dV_S}{dt}_{layer} = \frac{dV}{dt}_{layer} (1 - \epsilon_{bed}) \quad (8.41)$$

While the change in volume is accounted for directly in the growth terms of Equations 8.1 and 8.2, the transfer of solid from the fine powder phase to the granule phase must be considered in a source term in Equation 8.2. The resulting expression for the birth of solid in the granule phase ($\mathfrak{R}_{S,layer}$) is given by Equation 8.42.

$$\mathfrak{R}_{S,layer}(V, V_L, x, t) = F \frac{dV_S}{dt}_{layer} \quad (8.42)$$

Finally, the depletion of fine powder ($D_{m_p,layer}$) is given by Equation 8.43.

$$D_{m_p,layer}(x, t) = \rho_S \int_0^\infty \int_0^\infty F \frac{dV_S}{dt}_{layer} dV dV_L \quad (8.43)$$

Equations 8.42 and 8.43 are closely related and are consistent with a conservation of mass.

8.2.8 Numerical techniques

A 2-D grid of granule and liquid volume was formed by discretizing the two internal coordinates. The granule volume grid was discretized into 9 bins according to Equation 8.44, where d is the granule diameter and i is the index of each bin.

$$d(i) = 0.5 \exp\left(\frac{i-1}{4}\right) \text{ mm} \quad (8.44)$$

The liquid volume grid was discretized into 10 bins, with the first bin representing dry particles and the remaining bins with liquid volumes equal to those of the volume grid.

The growth terms in Equations 8.1 and 8.2 were evaluated using finite difference methods, while the source terms of aggregation, nucleation, and breakage were allocated using the cell-average technique (Chaudhury et al., 2013a; Barrasso and Ramachandran, 2012), resulting in a system of algebraic and ordinary differential equations.

The model was written and solved using gPROMS ModelBuilder 4.0, which uses a dynamic explicit integration technique. Although only steady-state results are reported, the model was solved dynamically until a steady state was reached in all simulations.

8.3 Discrete element method simulations and coupling to PBM

DEM simulations were used for two purposes: to obtain residence time information in each axial compartment in the screw, and to collect collision and velocity data in each compartment. Prior to the evaluation of the PBM, DEM simulations were performed on the whole screw to estimate a residence time for each compartment, and these values were assumed to be independent of particle size and properties. Bi-directional coupling was used to evaluate collision and velocity data in each compartment as the PBM was solved, as demonstrated by Barrasso et al. (2015b).

STAR-CCM+v9.06 was used to perform all DEM simulations, using the implicit unsteady solver with a fixed time step given in Table 8.1 and a variable sub-step to resolve particle contacts. Simulations were performed using four cores of an Intel Core i7-2600, 3.4 GHz processor with 16 GB of RAM.

The Hertz-Mindlin contact model was used as implemented in STAR-CCM+ to evaluate forces due to particle-particle and particle-wall contacts. A unique particle type was created for each volume bin in the PBM, and the density and coefficient of restitution of each particle type was determined from the average liquid content (based on Equation 8.12) and density of the particles of that size. Constant values were used for the coefficients of static and rolling friction and the material Poisson's ratio, as listed in Table 8.1 (Hassanpour and Ghadiri, 2004; Ai et al., 2011). The Young's modulus was assumed to be proportional to the yield strength, as presented by Hassanpour and Ghadiri (2004), using the ratio observed for lactose given in Table 8.1.

Fine particles were omitted from DEM simulations for several reasons. First, these particles are more influenced by cohesive interactions and drag forces than granules, so the assumptions in standard contact models are less applicable to the fine particles. Including them in the DEM simulations would not necessarily be any more accurate than omitting them. Second, they are very small in comparison to the granules, making the DEM simulations impossible to solve in a reasonable amount of time. Finally, the PBM as established requires little information about fine particles and their contact and velocity behavior. While including the fines in DEM simulations may moderately affect the granule

packing and velocities, these effects were assumed to be negligible.

8.3.1 Screw element geometries and configurations

CAD geometry was developed in STAR-CCM+ to represent axial compartments of a twin-screw granulator based on the 16mm Prism EuroLab TSG (Thermo Fisher Scientific). Four element types were modeled, as shown in Figure 8.3, including one conveying element (CE) compartment and three compartments of kneading elements (KEs), with various offset angles. Each KE compartment consists of 6 KEs. The length of each compartment and the screw diameter are listed in Table 8.1. The polyhedral mesher and embedded thin mesher models in STAR-CCM+ were used to generate meshes for these compartments. A sliding interface was created between the screws and the walls to allow for rotation of the screws, which was applied at a constant rate, as listed in Table 8.1. For single-compartment simulations, periodic boundaries were applied to each end of the compartment, effectively representing an infinitely long screw.

To simulate a four-compartment screw, these compartments were aligned horizontally and arranged in various configurations, allowing particles to move naturally from one compartment to another. Eight screw configurations were simulated as listed in Table 8.2. Figure 8.4 shows four of these configurations. In all cases, the first two compartments consisted of CEs, followed by one CE compartment and one KE compartment (denoted by “short”) or two KE compartments (denoted by “long”). An additional configuration was simulated comprising only CEs. All offset angles were oriented in the forward direction except for one configuration in which the KEs were offset counter to the CEs. Prior to the first compartment, a small section of CEs was added for particle creation, and an outlet was created to allow the particles to exit the fourth compartment.

8.3.2 Multi-compartment simulations and residence times

In order to determine the flow behavior within each screw configuration, DEM simulations were performed on the screw configurations, and the average residence time in each axial compartment was calculated at steady state. A four-compartment TSG was modeled in

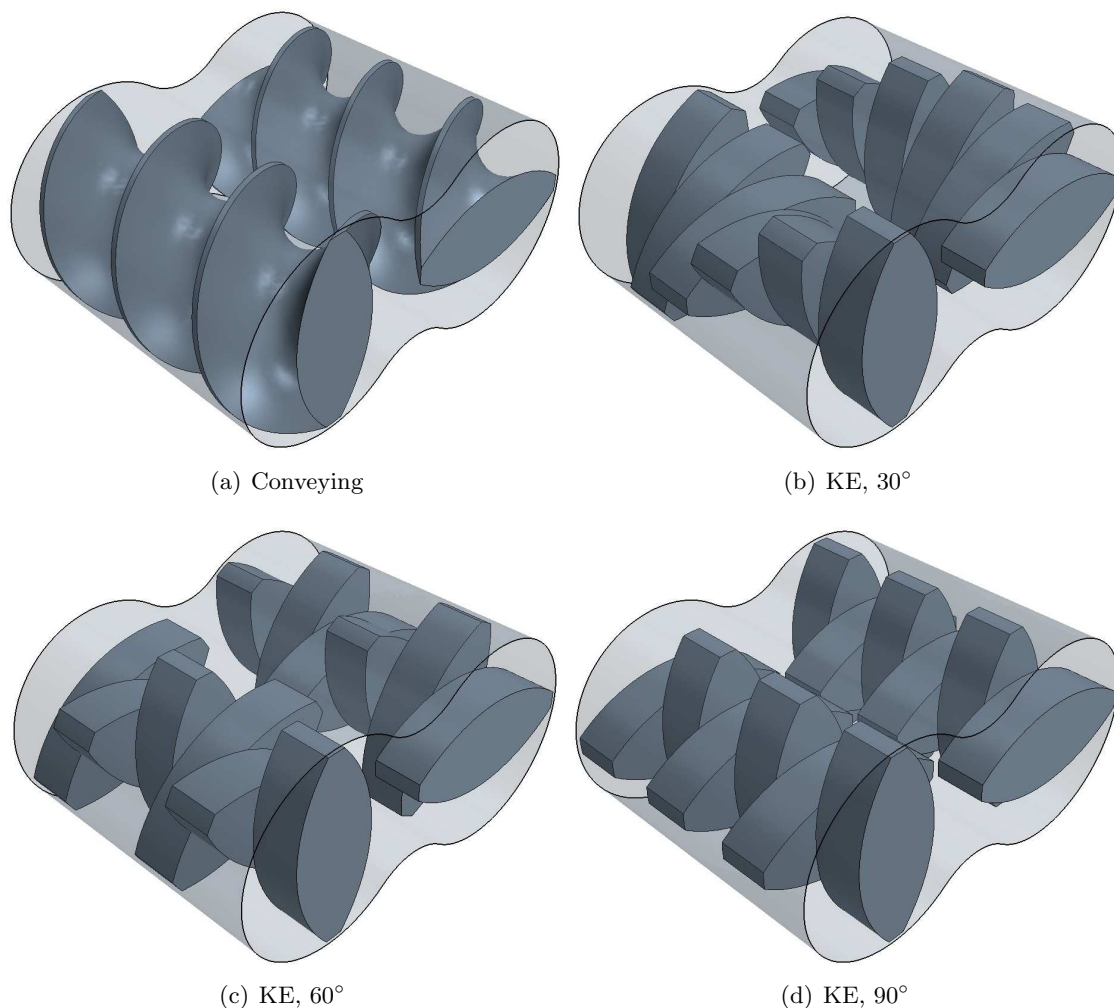
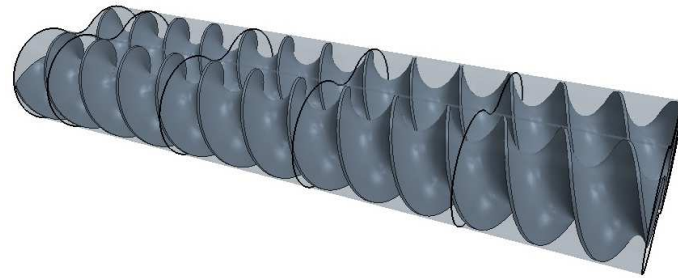


Figure 8.3: Geometries of individual screw sections of conveying elements and kneading elements of 30°, 60°, and 90° offsets.

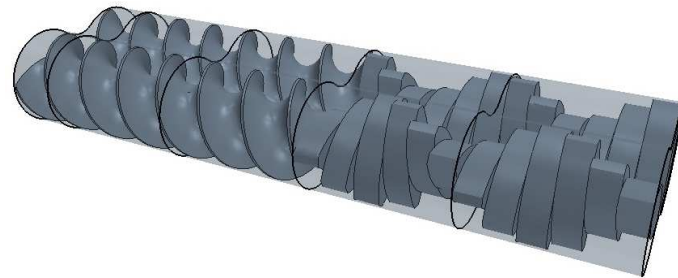
STAR-CCM+. Particles were generated with a lognormal size distribution at a mass flow rate of 4 kg/hr at the inlet end of the granulator, and particles were allowed to exit through the outlet. An initial charge of 1000 particles was applied to allow the system to reach a steady state in a shorter amount of time than if it were empty. Particle properties were set to those of dry particles with a porosity equal to the bed porosity. The average total mass of particles in each compartment was evaluated during the interval from five to ten seconds, during which a quasi-steady state is maintained. From these values, the average residence time for each compartment was estimated, assuming minimal back mixing, using Equation



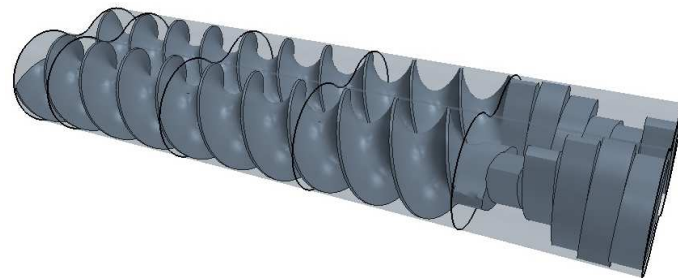
(a) 1. Conveying



(b) 2. 30°, short



(c) 5. 30°, long



(d) 8. 30°, short, reverse

Figure 8.4: Examples of screw element configurations for residence time DEM simulations. Black lines indicate compartment boundaries. Particles are created in the narrow section on the left end and exit through the right end. Numbers correspond to configurations listed in Table 8.2.

Table 8.2: Screw element configurations simulated in PBM-DEM framework. Short and long refer to the length of the KE block. Element type for each compartment denoted by CE (conveying element) or KE offset angle. R denotes reverse configuration. All KEs are offset in forward configuration unless otherwise noted.

| Configuration | No. of KE | Compartment | | | |
|-----------------------|-----------|-------------|----|-----|------|
| | | 1 | 2 | 3 | 4 |
| 1 Conveying | 0 | CE | CE | CE | CE |
| 2 30°, short | 6 | CE | CE | CE | 30° |
| 3 60°, short | 6 | CE | CE | CE | 60° |
| 4 90°, short | 6 | CE | CE | CE | 90° |
| 5 30°, long | 12 | CE | CE | 30° | 30° |
| 6 60°, long | 12 | CE | CE | 60° | 60° |
| 7 90°, long | 12 | CE | CE | 90° | 90° |
| 8 30°, short, reverse | 6 | CE | CE | CE | 30°R |

8.45.

$$\tau(x) = \frac{m(x)}{4 \text{ kg/hr}} \quad (8.45)$$

These average residence times are used as inputs to the PBM in Equations 8.13 and 8.15, assuming they do not depend on the current state of the system, only on the geometry and fixed process parameters and properties.

This assumption allows for a one-directional coupling of the residence time DEM simulations to the PBM, drastically reducing the computational demand and simplifying the problem. In a real system, the particle size distribution and properties vary along the length of the granulator, and each compartment contains a different set of particles and properties. Because the particles are exchanged between compartments in the DEM simulation, the compartment-specific size and property distributions cannot be held constant. By assuming that the residence time in each compartment only depends on the geometry and fixed parameters (such as screw speed and feed rate), a constant particle size distribution can be used for all compartments, while the mass hold up in each compartment is allowed to vary. Using this framework as a starting point, additional complexities can be added, such as a size and liquid content dependence on the residence time in each compartment.

8.3.3 Single-compartment simulations and bi-directional coupling

To obtain contact and velocity data for each compartment, a bi-directional coupling strategy was implemented based on the framework presented by Barrasso et al. (2015b). Figure 8.1 outlines the algorithm. First, each compartment is filled with a mass of granules equal to the steady-state mass obtained from the multi-compartment simulations using the same particle size distribution using 9 particle types representing different sizes. Collision and velocity data from this simulation are used to initialize the PBM, which is solved to reach a steady state. After a steady state is reached, new DEM simulations are performed on each compartment, this time using the particle distributions and properties obtained from PBM simulations to define each size class. The number of particles in each size class, their densities, coefficients of restitution, and Young's moduli are transferred and used as inputs for the DEM simulations. New collision and velocity data are obtained, and the PBM is again solved to reach a steady state. The cycle continues until two sequential PBM iterations result in an average particle size within 10% of each other for each compartment, based on the volume-weighted average diameter ($d_{4,3}$). Previously published work details the numerical verification of the algorithm (Barrasso et al., 2015b).

To initialize each DEM simulation, the particles are created in random positions and allowed to settle for a specified time interval. The simulation continues for a second time interval (Δt_{DEM}), collecting data on the number of collisions between each pair of particle size classes ($N_{collision}$) and between each size class and the wall. These values are used to evaluate the per-particle collision ($C_{collision}$) and impact (C_{impact}) rates, as shown in Equations 8.46 and 8.47.

$$C_{collision}(i, j) = \frac{N_{collision}(i, j)}{F(i)F(j)\Delta t_{DEM}} \quad (8.46)$$

$$C_{impact}(i) = \frac{N_{impact}(i)}{F(i)\Delta t_{DEM}} \quad (8.47)$$

The number of impacts (N_{impact}) in each size class is similar to the number of collisions, but does not consider the properties of the other body involved in the collision. Thus, it is the sum of all collisions for that size class, including those with the wall. These collision

and impact rates are used in the aggregation, breakage, and consolidation rate expressions in the PBM. The time intervals are listed in Table 8.1.

The average and standard deviations of the particle velocities are also obtained from DEM simulations and used in the aggregation, breakage, and consolidation rate expressions within the PBM. For this study, these velocities were collected as size-independent values.

When multiple compartments were simulated during a single iteration, they were executed in parallel to utilize all of the available processors.

8.4 Results and discussion

Steady-state results are presented for the residence time DEM simulations and the coupled PBM-DEM model. These results are compared qualitatively to experimental trends observed in the literature. By qualitatively verifying the predictive power of the model, relative conclusions can be made to facilitate process design. For example, the effects of changing the shapes of the screw elements can be investigated to optimize the desired rate mechanisms prior to construction of new equipment. While the results may not quantitatively match experimental values, the model provides useful insight into the process behavior. Further, to quantitatively validate the model, copious experimental work is needed to characterize material properties whose values are approximated for this study.

In a previous study, the effects of liquid viscosity, liquid to solid ratio, and other material properties on product attributes in a single compartment batch model were compared to experimental trends and demonstrated consistent behavior (Barrasso et al., 2015b). In this study, qualitative assessment will focus on the effects of screw element configuration on product size distribution, fraction of fine powder, and liquid distribution. Simulated results are compared to the experimental work of El Hagrasy and Litster (2013), which used similar parameters and configurations to those in this study.

El Hagrasy and Litster (2013) investigated the effect of screw configuration on the rate processes occurring in a twin screw granulation process, examining the product size, shape, and liquid distribution. A formulation containing α -lactose monohydrate (Pharmatose

200M, 73.5%), microcrystalline cellulose (Avicel PH101, 20%), hydroxypropyl methylcellulose (Hypromellose, 5%), and croscarmellose sodium (Ac-Di-Sol, 1.5%) was fed into a co-rotating twin screw granulator (16mm Prism EuroLab TSG, Thermo Fisher Scientific) at a rate of 4 kg/hr. The liquid binder comprised of 0.1% (w/w) nigrosin dye in distilled water at a baseline liquid to solid ratio of 0.15. Sieve analysis was used to characterize the product size distributions, and a UV/Vis spectroscopic method was used to measure the dye content in each size class.

8.4.1 Residence time results

Figure 8.5 shows snapshots of DEM simulations for two screw configurations at steady state, where particles are colored according to their compartments. From this graphic, the inhibition of flow by KEs can be observed visually, as a greater amount of granules are held up in the KEs and the compartments preceding them.

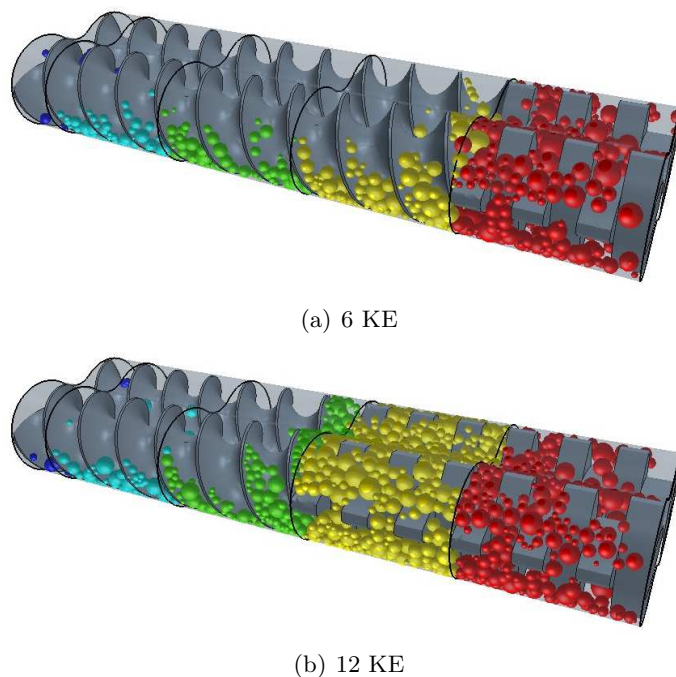


Figure 8.5: Snapshots of DEM simulations after a steady state is reached for configurations with a 90° offset angle of (a) 6 and (b) 12 KEs. Particles are colored according to their compartment.

Based on the steady-state hold up obtained from these DEM simulations, the average

residence time for each compartment in each configuration was evaluated, as shown in Figure 8.6. The configuration consisting of all CEs showed nearly equal residence times in each compartment, indicating that there is no preference for one compartment over another. In contrast, all KE configurations had some variations in residence time along the length of the granulator, suggesting that KEs inhibit particle flow. Further, the offset angle affects the residence time, particularly in the compartments preceding and containing the KEs. An increase in the offset angle results in a greater inhibition of flow and higher residence times. The 30° and 60° configurations have CE characteristics, but do not behave as ideal CEs. That is, these elements convey the material forward and induce flow. This result is partly consistent with the findings of El Hagrasy and Litster (2013), who stated that the 60° offset angle is expected to have the shortest residence time, while these simulations suggest that the KE block with a 30° offset angle is the most like the CE. One possible source of error is the one-way coupling between residence time DEM simulations and the fully-coupled PBM-DEM model. The evolving granule properties in each screw element are not accounted for and may affect their residence times. From Figure 8.6 (a) and (b), the effect of the number of KEs on the residence time in each compartment can be observed. Increasing the number of KEs drastically increases the residence time in each compartment as the conveying behavior is reduced. In configurations with 12 KEs, or two KE compartments, the first compartments of KEs had greater residence times than the second. This observation can be explained by the effects of KE compartments on the preceding compartment. The first KE compartment is followed by another KE compartment, which inhibits flow out of the block, increasing its residence time. In contrast, the second KE compartment is followed by an open end, which does not inhibit flow. Strong effects of offset angle on residence times are observed when 12 KEs are present; the first KE compartment with a 90° offset angle has nearly twice the residence time of that of the 60° offset angle.

Figure 8.6 (c) shows the effect of KE direction on residence time for the 30° offset angle. The configuration with 6 KEs offset by 30° in the reverse direction (counter to the CEs) has a greater residence time than the forward configuration, indicating that the reverse configuration eliminates the conveying characteristics of the 30° offset KEs.

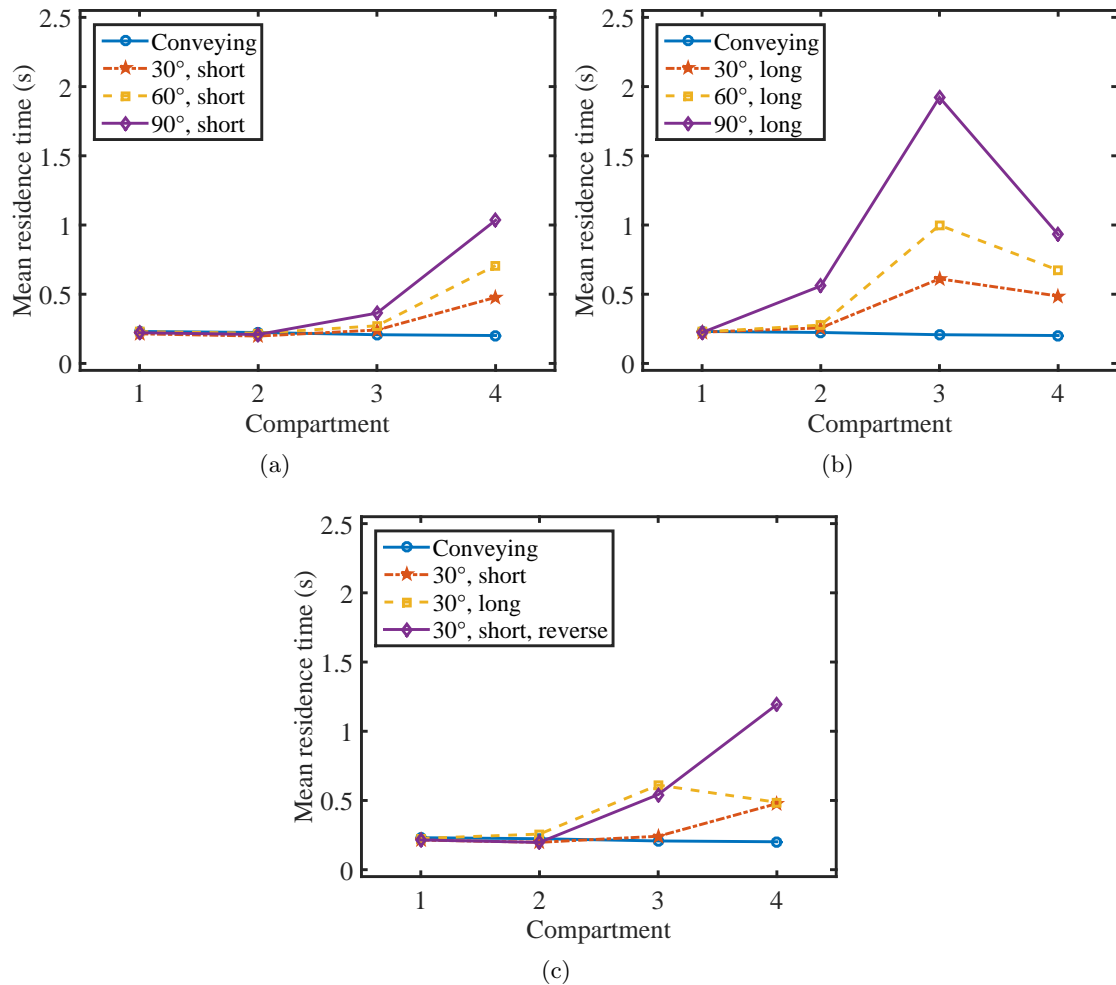


Figure 8.6: Average residence time in each compartment based on steady-state DEM simulations of the full screw for conveying screw and configurations with (a) 6 KE, (b) 12 KE, and (c) 30° offset angle.

8.4.2 PBM-DEM simulations: Mechanisms by compartment

Using the results of the residence time DEM simulations as inputs to the model, two-way coupled PBM-DEM simulations were performed for each screw configuration. Computation time for these simulations ranged from four to fifteen hours depending on the number of DEM iterations required and the number of particles in each compartment. Three to five DEM iterations were required for all cases, and typically the KEs required more iterations than the CEs since little size changes were observed in the CEs. Results are presented for the steady-state granule size distribution and porosity, mass fraction of ungranulated fine powder, and liquid distribution. Additionally, a replicate simulation was performed for the

90° configuration with 6 KEs, demonstrating reproducible results.

Figure 8.7 shows snapshots of the final DEM iteration for the fourth compartments of the configurations with 6 KEs at various offset angles. It is clear from these images that the three offset angles have different granule fill levels. The 30° offset contains the least material, while the 90° offset contains the most. This observation can be attributed to the different residence times in each compartment determined from the DEM simulations of the full screw, where a greater residence time results in a larger hold up. Additionally, the fine powder particles are not represented in the DEM simulations, and a greater mass fraction of fine powder will result in fewer granules.

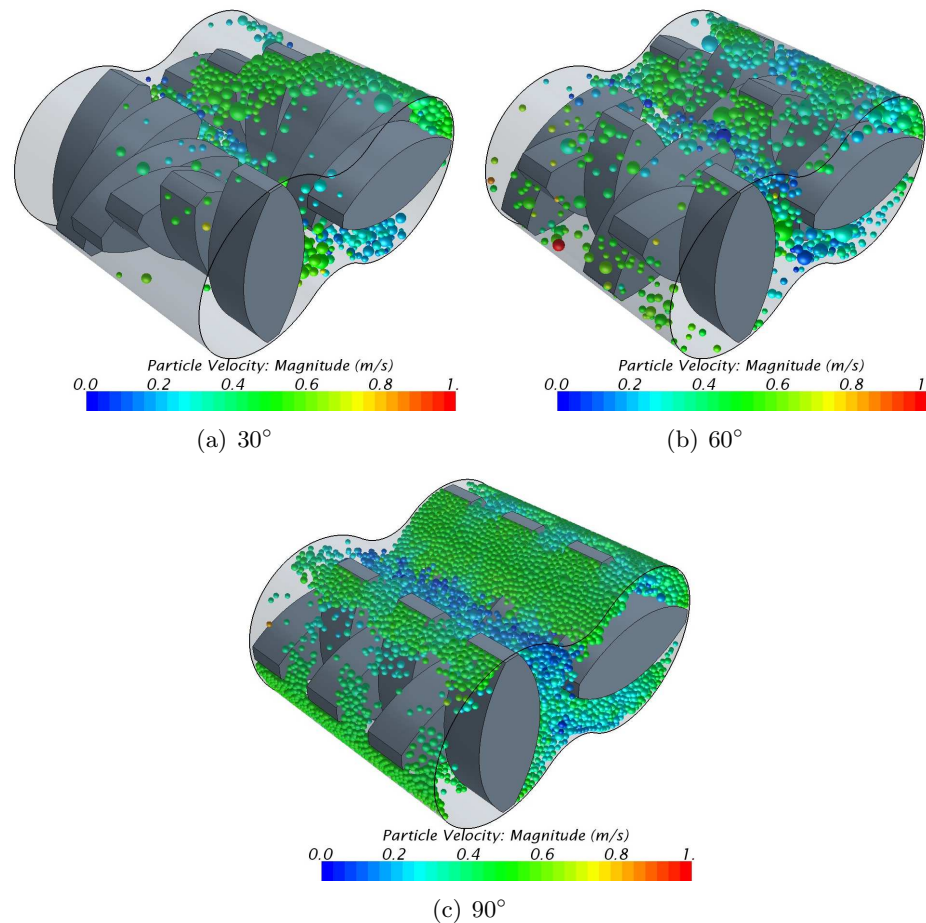


Figure 8.7: Snapshots of the fourth compartment after the final DEM iteration for configurations with 6 KEs and various offset angles. Particles are colored according to their velocities.

Figure 8.7 also shows different size distributions in each offset angle, demonstrating

the model's ability to capture effects of the equipment geometry. Using this capability, various design parameters can be tested, such as offset angle, barrel size, and KE shape, for their effects on process outcomes. By qualitatively assessing the model, confidence can be established that the predicted trends will match realistic behavior.

In Figure 8.8, the average granule diameter, mass fraction of fine powder, and average granule porosity are shown in each compartment for the conveying and 6-KE configurations along with the product size distributions. In the first compartment, drop nucleation occurs, creating large, porous granules from the fine powder. The configuration consisting of all CEs shows minimal size changes beyond the first compartment, suggesting that coalescence and breakage are not dominant in CEs. Rather, drop nucleation is the dominant mechanism in these elements. This result matches the experimental observations of El Hagrasy and Litster (2013), who stated that in CEs, "agglomerates are formed by drop granulation as the liquid is dripped into the barrel producing bimodal size distribution of ungranulated fines and wet agglomerates." The product size distribution for this configuration, shown in Figure 8.8 (d), is clearly bimodal, with the first peak representing ungranulated fine powder, and the second showing wet nuclei. El Hagrasy and Litster (2013) also found that some layering and coalescence may occur in the CEs at high liquid-to-solid ratios. These subtle changes are apparent in the simulated results, where the granule size increases slightly along the length, and the mass fraction of fine powder is reduced. In all simulations, the CEs have little effect on the particle sizes and their properties, and it is not until the KEs are reached that measurable changes occur.

In the KEs, breakage is a dominant rate mechanism, characterized by a large reduction in particle size, as seen in Figure 8.8. El Hagrasy and Litster (2013) also drew this conclusion experimentally. They also noted that less breakage occurs in the 30° offset KEs than in the 90° configuration, explaining that the 30° offset angle has conveying characteristics and provides a path for particle flow. This observation is consistent with our results, which show larger particles in the 30° configuration than in the 90° configuration. The simulated size distribution of the 30° configuration has a broad second mode with a greater mean size than that of the 90° configuration. These results can also be explained by the conveying

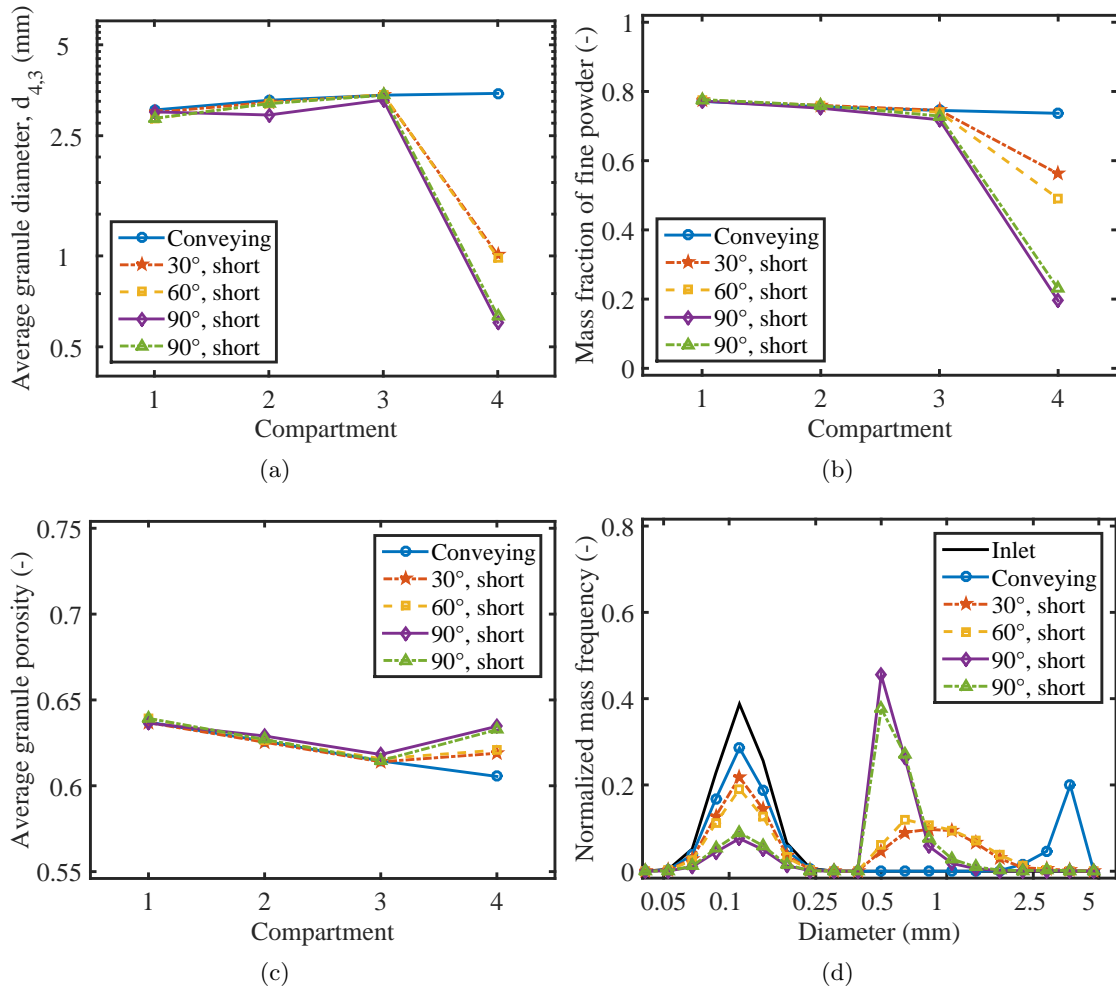


Figure 8.8: (a) Average granule diameter, (b) mass fraction of fine powder, and (c) average granule porosity in each compartment and (d) product size distributions at steady state simulated by PBM-DEM model for conveying screw and configurations with 6 KE. Fine powder particles are represented as having a log-normal distribution with a mean size of 0.1 mm and a standard deviation of 0.025 mm.

characteristics of the 30° offset KEs, which have a reduced residence time than the 90° offset KEs, subjecting the particles to fewer breakage events.

El Hagrasy and Litster (2013) concluded that the 60° configuration has characteristics similar to conveying elements, with minimal breakage or other events, explaining that poor mixing results from a smooth passageway through the center channel. Still, some breakage must occur in this section as the experimentally observed size distributions show a reduction in fine powder and smaller granules than that of the all-CE configuration. Simulated results show that the 60° configuration produces granules similar to those of the 30° configuration.

Although the 60° configuration has a much greater residence time than the 30° configuration, a similar total amount of breakage occurs in each, suggesting that the breakage rates are lower in the 60° offset KEs than in the 30° offset KEs. The similarity in the total amount of breakage is likely coincidental as the combined effects of residence time and breakage rate produce similar size distributions. This result is best explained by the images of DEM simulations in each, shown in Figure 8.7, where particles in the 30° offset KEs are trapped by the closely arranged KEs and smeared against the wall, resulting in more collisions. In contrast, particles in the 60° offset KEs are able to pass through the gaps between adjacent KEs, reducing their impact and breakage rates. Additionally, the 60° configuration has noticeable differences from the 30° configuration, particularly with respect to liquid distribution, discussed in Section 8.4.5.

Figure 8.8 (b) shows the effect of KE offset angle on the mass fraction of ungranulated fine powder. The fraction of fine powder particles decreases as the offset angle increases, which can be attributed to the increased residence time that allows for more layering to occur. Additionally, the increased amount of layering observed with greater offset angles can be explained by the increased breakage rates in these configurations. El Hagrasy and Litster (2013) found that breakage events induce layering by increasing the wet surface area of the fragments that can pick up dry fine powder. The same effect is captured in the model, where an increase in wet granule surface area results in an greater layering rate.

However, El Hagrasy and Litster (2013) noted that the bimodal peaks begin to merge in the 90° configuration as fine particles are generated as breakage occurs. Although simulated results show a less bimodal distribution in this configuration, the model does not capture an increase in fine particles during breakage. As a result, El Hagrasy and Litster (2013) observed an increase in the mass of fine powder in the 90° configuration, while the simulated results do not show this behavior. Further, a better, more mechanistic understanding of the fragment distribution would greatly improve the model, which relies on the simple assumption that all breakage events result in two equal particles.

In all cases, little consolidation occurs. Twin screw granulation is known to produce more porous particles than traditional high-shear and fluid bed granulation (Dhenge et al.,

2012; Lee et al., 2013; Sayin et al., 2015). While the average granule porosity decreases slightly in the CEs, it increases in the KEs as breakage induces layering, as seen in Figure 8.8 (c). In the model, fines were assumed to deposit on the surface of the granules with a porosity equal to the bed porosity, returning the granule porosity to that of the original nuclei. This hypothesis is supported by Figures 8.8(c), 8.9(c), and 8.10(c), where in all cases, an increase in porosity is accompanied by a decrease in fine particles. Additional experimental data is needed to validate or improve this assumption, though these minor porosity changes have little practical consequence.

8.4.3 PBM-DEM simulations: Effect of number of kneading elements

Steady-state results for configurations with 12 KEs are shown in Figure 8.9. In these simulations, both the third and fourth compartments comprised of KEs. For the 30° configuration, simulated results show an increase in the number of KEs corresponds to a decrease in granule size and a reduction in the mass fraction of fine powder particles, consistent with experimental trends observed by El Hagrasy and Litster (2013). These results can be attributed to the greater residence time in the KEs, providing a longer time for breakage, consolidation, and layering. Additionally, the greater residence time in the first KE compartment results in an increased hold up, causing more collisions and further increasing breakage and consolidation rates. Consequently, the granules in this compartment are, on average, smaller than those of the first KE compartment in the 6 KE configurations.

The 60° configuration showed similar simulated results to the 30° configuration, with slightly larger granules produced by the 60° configuration. El Hagrasy and Litster (2013) found that the number of KEs has little effect on the granule size distribution for the 60° configuration. In contrast, the simulated results predicted smaller particles and a reduced fraction of fine powder with 12 KEs than with 6 KEs. El Hagrasy and Litster (2013) postulated that much of the breakage occurs at the transition from CEs to KEs, suggesting that the dominant breakage mechanism is particle-equipment interaction. The model treats particle-particle and particle-equipment interactions equally. Further work is needed to characterize these mechanisms independently.

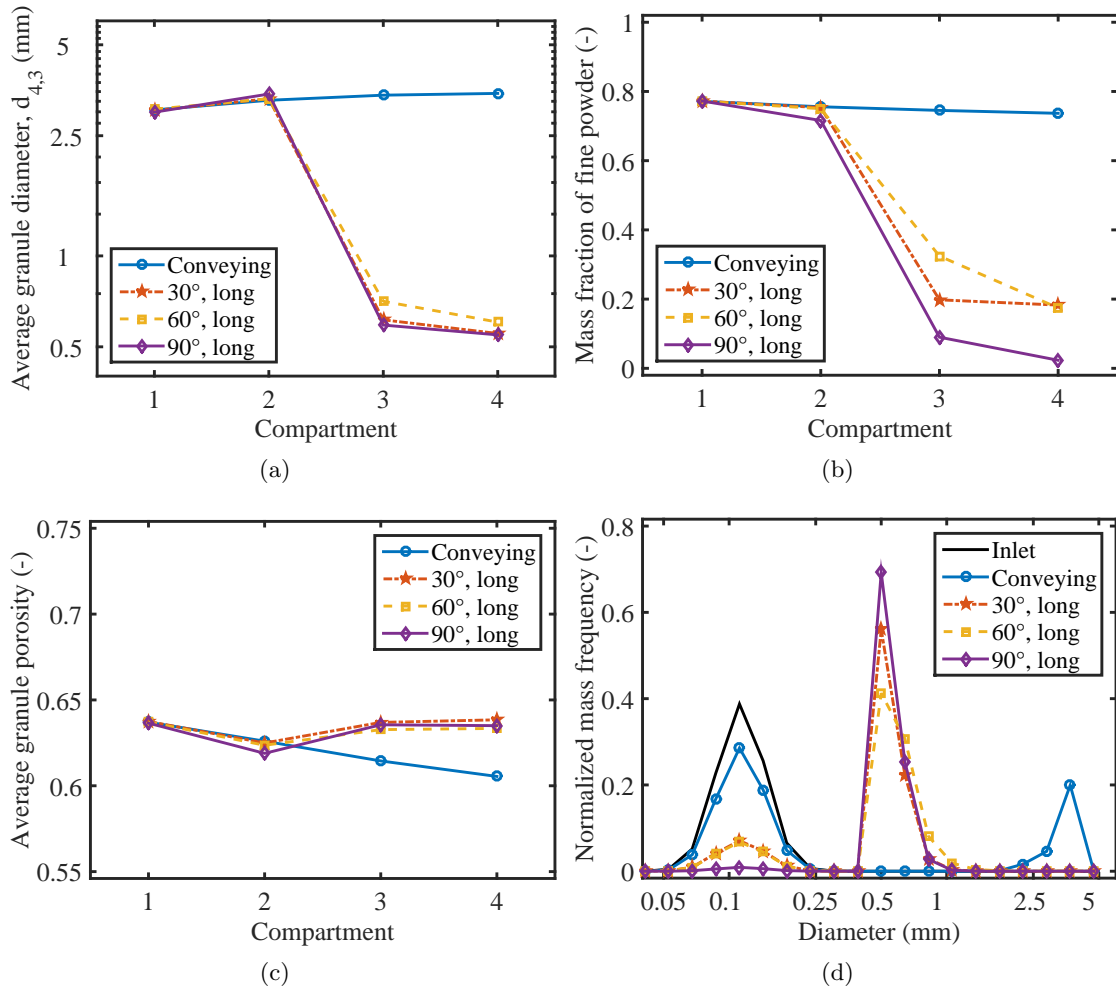


Figure 8.9: (a) Average granule diameter, (b) mass fraction of fine powder, and (c) average granule porosity in each compartment and (d) product size distributions at steady state simulated by PBM-DEM model for conveying screw and configurations with 12 KE. Fine powder particles are represented as having a log-normal distribution with a mean size of 0.1 mm and a standard deviation of 0.025 mm.

However, the 60° configuration with 12 KEs resulted in larger particles than the 30° configuration despite the greater residence time in the 60° KEs. This result suggests that less breakage is occurring in the 60° configuration, and the effect of the number of KEs on the extent of breakage is lessened for the 60° configuration than the 30° configuration. The weaker effect of the number of KEs can be attributed to the pathway for particles to move between KEs in the 60° configuration, which results in fewer particle impacts and opportunities for breakage. Because the trends for this configuration are consistent, the

disagreement between experimental and simulated observations can be attributed to quantitative differences between the simulated values for some of the material properties and their true values which are not easily measured, such as the yield strength and coefficient of restitution, which greatly influence aggregation and breakage.

The simulated results for the 90° configuration show similar effects of the number of KEs on the process outcomes, with a reduction in fine powder and a decrease in granule size. While El Hagrasy and Litster (2013) observed an increase in fine powder when more KEs are used in this configuration, they explain the result by the creation of fine powder particles during breakage, an effect not captured by the model. It is clear from this discrepancy that future work is needed to account for broad fragment distributions during breakage, resulting in an additional exchange of material from the granule phase to the fine powder phase.

8.4.4 PBM-DEM simulations: Reverse configuration

For offset angles less than 90° , the direction of the offset affects flow. When the KEs are oriented in the forward direction, they move the particles in the same direction as the CEs, resulting in conveying characteristics. In the reverse configuration, the KEs push the particles in the opposite direction of the flow, eliminating their conveying characteristics and increasing residence times. It should be noted that in the reverse configuration, the two-way coupling of single-compartment DEM simulations are the same as those of the forward configuration. It is assumed that the rate mechanisms, such as breakage and aggregation, do not depend on the direction of flow because the model decouples flow from the other rate processes.

Figure 8.10 shows the effect of KE orientation of the 30° configuration on process outcomes. The greater residence time in the reverse configuration results in more breakage, producing smaller granules and reducing the mass fraction of fine powder. El Hagrasy and Litster (2013) also found an increase in breakage and layering in the reverse configuration, attributing the difference to the narrow passageway for the particles. They state that “the main passage for the material from CE is through smearing against the barrel wall, leading to shear-elongation of the wet agglomerates.” While the model captures the inhibited

passageway, it does not account for shear elongation and the direction of flow.

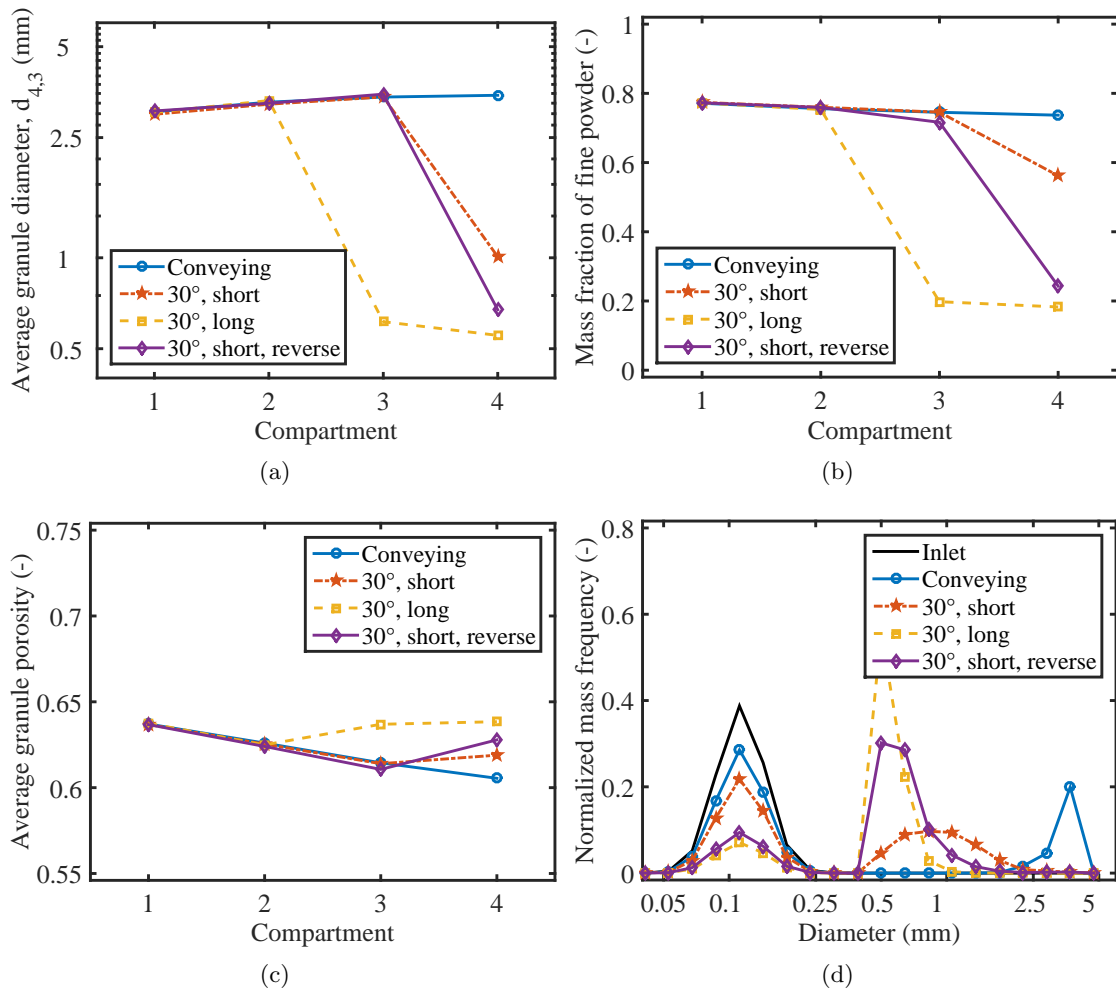


Figure 8.10: (a) Average granule diameter, (b) mass fraction of fine powder, and (c) average granule porosity in each compartment and (d) product size distributions at steady state simulated by PBM-DEM model for conveying screw and configurations with 30° offset angle. Fine powder particles are represented as having a log-normal distribution with a mean size of 0.1 mm and a standard deviation of 0.025 mm.

8.4.5 PBM-DEM simulations: Liquid distribution

Figure 8.11 shows the liquid distribution for each configuration at steady state, indicating the average liquid mass fraction in each size class of the product particles. Because of the model's design, no liquid is present in the fine powder phase. In future work, a broad breakage distribution can be used to transfer fragment particles to the fine powder phase. In this case, the wetness of the powder phase should be considered. In the granule phase, there

is a strong correlation between particle size and wetness, with larger particles containing larger amounts of liquid, in general, regardless of screw configuration. El Hagrasy and Litster (2013) also found a positive correlation between particle size and liquid content, attributing this dependence to the nucleation rate mechanism, resulting in large wet nuclei. As breakage and layering occur, the liquid is distributed across the fragment particles, weakening the size-dependence. The largest particles exhibited a slight decrease in liquid content. These large particles were likely formed from the layering of dry fine particles onto slightly smaller wet particles, resulting in a lower overall liquid content.

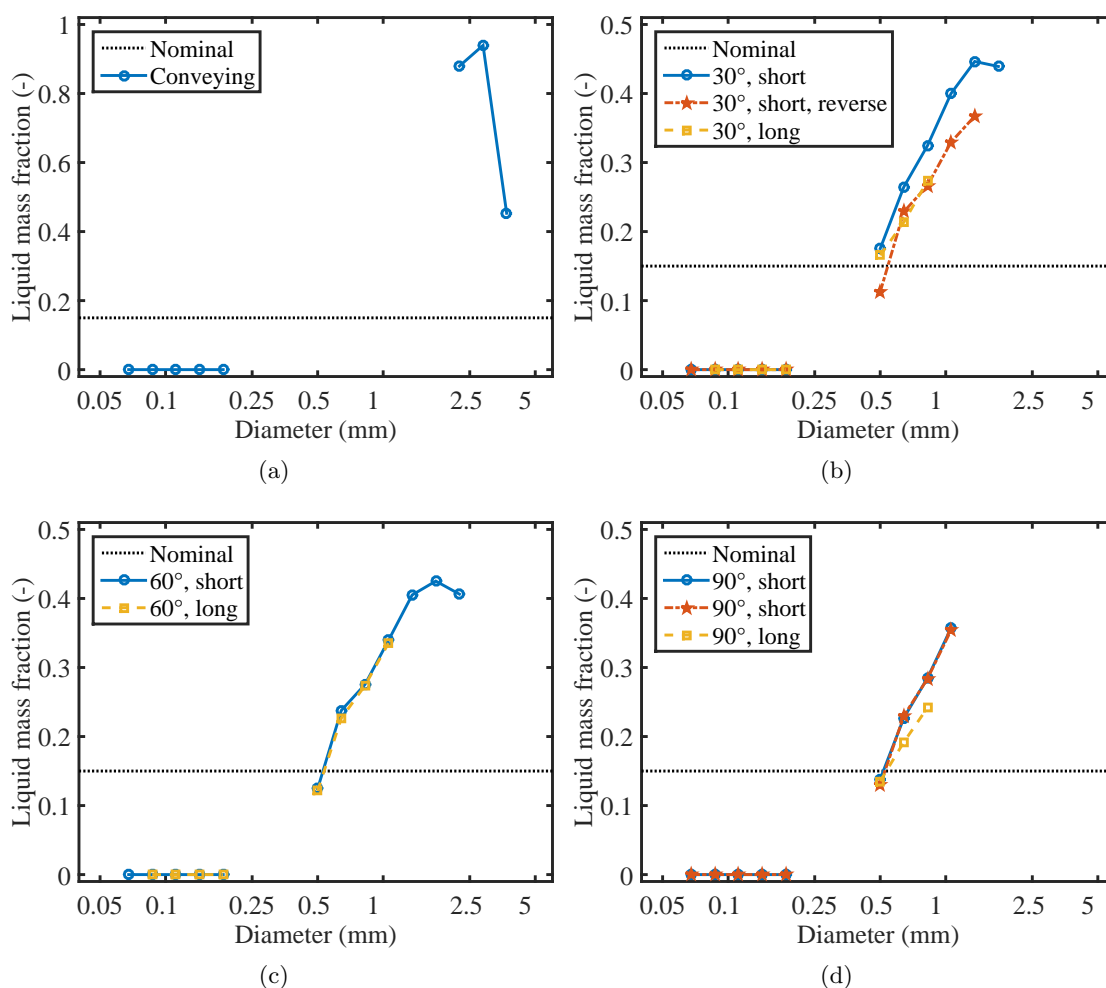


Figure 8.11: Steady-state product liquid mass fraction in each size class for configurations of (a) all conveying elements, (b) 30° offset angle, (c) 60° offset angle, and (d) 90° offset angle. Values only shown for size classes with mass fractions making up >1% of the total product mass.

Simulated results for the conveying configuration support this theory, with the poorest

liquid distribution of all simulations, as seen in Figure 8.11 (a). Minimal breakage occurs after nucleation, resulting in large, wet granules containing all of the liquid. El Hagrasy and Litster (2013) also observed the poorest liquid distribution in this configuration.

Shown in Figure 8.11 (b), liquid distribution in the 30° configuration is also poor, but improves when the number of KEs increases from 6 to 12. This finding is consistent with that of El Hagrasy and Litster (2013), who attributed it to the longer residence time for breakage, consolidation, and growth. Further, the 30° reverse configuration shows improved liquid distribution over the forward configuration, due to the greater amount of breakage and layering in this section. However, no clear dependence of liquid content on particle size was observed experimentally for the reverse configuration, but a positive correlation was predicted from the simulations. This discrepancy is likely a result of the narrow breakage distribution used in the simulations and the lack of any wetness in the fine powder phase.

The 60° configuration also resulted in a poor predicted distribution of liquid, as shown in Figure 8.11 (c), but unlike the 30° configuration, the liquid distribution was unchanged as the number of KEs was increased from 6 to 12. This unusual result matches experimental findings exactly. El Hagrasy and Litster (2013) observed no effect of the number of KEs on the liquid distribution for this configuration and attributed this fact to the poor mixing in the 60° offset KEs. In the model, a possible mechanism for liquid distribution is coalescence followed by breakage, allowing wet granules to transfer some of their liquid to dry particles. Because there is less particle-particle interaction in the 60° configuration than the 30° configuration, minimal coalescence occurs. El Hagrasy and Litster (2013) also suggest that most of the breakage in the 60° configuration occurs at the transition from the CEs to the KEs, so the length of the KE section has little effect on the product. While this might be true, the compartment model does not account for this possibility.

Lastly, the 90° configuration shows a better liquid distribution than the 30° configuration, as presented in Figure 8.11 (d), consistent with experimental results, and the liquid distribution improves with an increase in the number of KEs. However, the size dependence of the liquid content was not eliminated at greater numbers of KEs. A better understanding

of the fragment size distribution may improve the model's ability to predict the liquid distribution accurately and quantitatively. Further, the model does not consider particle-particle liquid transfer in the absence of aggregation and breakage. This mechanism is typically omitted from models of wet granulation, and a more scientific understanding of its behavior is needed to quantify it.

8.5 Summary

In this study, a multi-dimensional compartment PBM for a continuous twin screw wet granulation process was presented. DEM simulations were used to obtain residence time information for each compartment, and mechanistic expressions for aggregation, breakage, and consolidation rate processes were evaluated using a two-way coupling algorithm to gather collision and velocity information from DEM simulations. Steady-state results were presented for various screw configurations, demonstrating the effects of the number of KEs and their offset angles on the key mechanisms governing the process. In most cases, the simulated results were compared qualitatively to the experimental observations of El Hagrasy and Litster (2013), and the predicted trends were consistent with the empirical observations. Where differences were observed between simulated and experimental results, mechanisms were postulated, suggesting future enhancements for the model and identifying critical steps in the wet granulation process.

Findings showed that little occurs in the CEs of the screw aside from drop nucleation and some layering of fine powder onto the wet surfaces of the granules. Breakage dominates in the KEs, forming smaller granules from the large, wet nuclei and inducing additional layering. KEs also serve to distribute liquid. Screw element offset angle influences the residence time in each compartment, with forwardly-oriented angles causing conveying characteristics in the KE sections. Additionally, the offset angle affects the granule-granule interactions and mixing, with implications for liquid distribution.

To improve the model, a better representation of fine powder particles in DEM simulations is desired in order to capture the interaction of these particles with larger granules. A more mechanistic understanding of the fragment distribution of breakage events is needed

to quantitatively capture the broad size distributions observed experientially. Finally, extensive material characterization is needed to improve the correlations between particle porosity, liquid content, and size and the critical DEM input parameters, such as the coefficients of restitution, Poisson's ratio, and Young's modulus.

Still, the qualitative predictability of the model is useful for design applications, and the model in its current form can be used to evaluate alternative screw element designs a priori. A novel feature of the model is the ability to predict the effects of geometric design parameters on the particle-scale mechanisms and subsequent process outcomes. Because of its inherent ability to capture this behavior, this multi-scale modeling framework shows strong potential as a tool to advance Quality-by-Design.

Chapter 9

Conclusions and future perspectives

In industry, powder processes are often operated empirically and inefficiently. Design stages are facilitated by substantial and costly experimentation, and quality products are assured by testing product properties and rejecting material that does not meet specifications. Through this work, model-based approaches are developed and explored to further the understanding of the complex phenomena that drive wet granulation processes.

Traditional chemical process modeling, which has been used in industry for decades, often relies on thermodynamic relationships and first-principles concepts to describe process behavior. In contrast, powder processes are not driven by well-established thermodynamic laws but by complex mechanisms that are poorly understood. As a result, powder process modeling is less advanced than chemical process modeling, and developing useful models of powder processes is an area of ongoing research.

Population balance modeling is used as a general framework for powder process modeling. This technique captures changes in property distributions as particles undergo various rate processes, such as growth, coalescence, and breakage. PBMs have been employed previously to model granulation processes, though they are often overly simplified and based on empirical descriptions of phenomena.

In this work, more detailed PBMs are developed to capture realistic process behavior. Multi-dimensional PBMs, which track distributions in more than one property, are implemented and compared to lower-dimensional models. Although these high-order models are computationally intensive, they are well suited for wet granulation processes, which involve interdependent phenomena of solid, liquid, and gas phases. By implementing a lumped-parameter approach, multiple components can be tracked in a lower-dimensional

model, and a balance can be found between computational speed and model accuracy. Further, compartmental approaches are employed to incorporate powder flow into the PBM framework, enabling spatial inhomogeneities to be described.

With this framework, a PBM describing a twin-screw wet granulation process was calibrated and validated using experimental data. Parameter estimation was performed to evaluate unknown parameters in empirical expressions that describe the rate mechanisms of aggregation, breakage, and consolidation. The resulting model has predictive capabilities within the experimental design space, quantitatively describing the effects of process parameters on product attributes. However, these empirical models have limited applicability beyond the ranges of experimental conditions.

The main limitation of the PBM approach is its inability to inherently predict the effects of process parameters and material properties on particle-scale phenomena driving the process. To improve these models, a more detailed understanding of spatial inhomogeneities and collision-scale interactions is required. Discrete element modeling precisely addresses these needs, simulating individual particles as they move through complex geometries and collide.

The unique capabilities of DEM techniques are combined with the process-scale PBM to create a novel multi-scale powder process modeling framework. Two approaches are developed and compared to meet this goal. First, a PBM is solved within a DEM simulation, effectively changing the size distribution throughout the process. While this technique served as a proof-of-concept, it exacerbated the computational needs of DEM and exposed limitations in custom capabilities of commercially-available DEM software.

In the second multi-scale approach, the PBM was used to drive the simulation, calling upon short DEM simulations to gather particle-scale data as needed to evaluate mechanistic rate expressions. Through this computationally-efficient technique, a PBM of variable complexity can be enhanced with DEM simulations as the two models are solved independently. Further, this framework demonstrated inherent sensitivities to process inputs not possible with the PBM alone.

Additional considerations in applying these models to realistic processes were also addressed. First, a reduced order model of the expensive DEM step was created using an artificial neural network, creating a PBM-ANN model that can be rapidly evaluated for a high-shear wet granulation process, for potential use in iterative calculations, such as parameter estimation and optimization.

Finally, the PBM-DEM model was applied to a compartmental twin screw wet granulation process, predicting the driving mechanisms as they depend on screw element geometry. Results were qualitatively consistent with experimentally observed trends, demonstrating the models ability to evaluate various design configurations without experimental calibration.

Although this powerful tool qualitatively matches experimental observations, it highlights some of the limitations of DEM techniques, both computationally and scientifically. DEM lacks validated descriptions of complex physics, such as particle deformation and multi-phase interactions. Further, DEM is computationally expensive, particularly when simulating realistically large numbers of fine particles.

In summary, modeling tools were advanced to meet two unique objectives: a quantitative description of a granulation process, valid within an experimental design space, and a qualitative tool with inherent capabilities to assess cause and effect relationships between process inputs and outputs.

Through this work, several areas of future interest were identified. First and foremost, solids process modeling has been demonstrated as a useful tool in understanding powder process behavior. Process-scale models can be advanced by using a more rigorous approach, incorporating mechanistic theory into sophisticated PBM frameworks. Using these tools to design, control, and optimize industrial processes is an area with great potential implications.

Additionally, the computational and scientific limitations of DEM techniques can be improved by implementing more detailed and accurate particle physics and multi-phase interactions with a strong emphasis on parallel computing and scalability. Validating DEM

simulations is also an area requiring attention in order to bring these techniques into mainstream use.

Process modeling tools are relatively new to the pharmaceutical industry, in part due to the lack of reliable solids process models. As efforts are taken to implement Quality-by-Design and transition to continuous manufacturing operations, a renewed focus is placed on efficiency, risk analysis, robustness, and process understanding. The approaches demonstrated here for wet granulation processes can be applied to other unit operations to understand the effects of key process inputs on product attributes. Further, these models can be integrated using flowsheet modeling tools to create a more complete process understanding for design, control, and optimization.

Appendix A

Cell average technique and model order reduction

The cell average method was extended to four dimensions in order to assign born particles to the appropriate bins. Since a non-linear grid was used, two aggregating particles form a daughter particle that may not have the same solid, liquid, or gas volumes described by the points on the grid. These particles fall between bins, and a fraction of each is assigned to the neighboring bins. In the 4-D model, 16 bins describe all of the combinations of high and low bins neighboring a cell.

For aggregation, the particle birth and depletion rates are calculated using Equations 2.6 and 2.7. The particle birth rate does not describe the number of particles forming in bin (h, i, j, k) . Instead, it represents the formation of particles with component volumes that fall between this bin and the next largest bin in each dimension. To determine the neighboring bins for each daughter particle, the component volumes of that particle are calculated, and the indices corresponding to the neighboring bins are found, as shown for the first solid component in Equations 9.1-9.3.

$$s_{1,agg}(s_{1,a}, s_{1,b}) = s_{1,a} + s_{1,b} \quad (9.1)$$

$$s_1(h) < s_{1,agg} \quad (9.2)$$

$$s_1(h + 1) > s_{1,agg} \quad (9.3)$$

In these equations, $s_{1,a}$ and $s_{1,b}$ are the volumes of the first solid component in each of two aggregating particles, and $s_{1,agg}$ is the volume of the first solid component in the aggregate particle. The indices h and $h + 1$ correspond to the bins directly lower and higher than the aggregate particle. The same technique can be used to determine these indices for gas, liquid, and the second solid component. The sixteen neighboring bins are represented by every combination of h or $h + 1$, i or $i + 1$, j or $j + 1$ and k or $k + 1$. The total number

of particles forming in the cell described by the lowest neighboring bin h, i, j, k must be calculated, as shown in Equation 9.4

$$\mathfrak{R}_{agg}^{form}(h, i, j, k) = \sum_a \sum_b \beta(a, b)F(a)F(b), \quad (9.4)$$

where a and b are the set of all bin indices that satisfy the conditions listed in Equations 9.5 and 9.6 for all four components.

$$(s_1(h), s_2(i), l(j), g(k)) \leq (s_1, s_2, l, g)_a + (s_1, s_2, l, g)_b \quad (9.5)$$

$$(s_1(h+1), s_2(i+1), l(j+1), g(k+1)) > (s_1, s_2, l, g)_a + (s_1, s_2, l, g)_b \quad (9.6)$$

In order to conserve volume, the total amount of each component aggregating into this cell is calculated from the birth rate, as demonstrated for the first solid component in Equation 9.7, where $s_{1,agg}^{total}$ is the total volume of solid aggregating into this cell.

$$s_{1,agg}^{total}(h, i, j, k) = \sum_a \sum_b \beta(a, b)F(a)F(b)(s_{1,a} + s_{1,b}) \quad (9.7)$$

The average volume of the each component per particle is then calculated for each cell. The cell average volume for the first solid component (s_1^{CA}) is given in Equation 9.8.

$$s_{1,CA}(h, i, j, k) = \frac{s_{1,agg}^{total}(h, i, j, k)}{\mathfrak{R}_{agg}^{form}(h, i, j, k)} \quad (9.8)$$

After repeating this procedure for each component, the particles aggregating into the cell are allocated into the neighboring bins. The fraction of particles (f) forming in a neighboring bin is given by Equation 9.9, where h^{nb} , i^{nb} , j^{nb} , and k^{nb} are the indices of the neighboring bin. This equation is used for each of the sixteen neighboring bins. The total number of particles assigned to each bin $\mathfrak{R}_{agg,CA}$ is given by Equation 9.10.

$$f(h^{nb}, i^{nb}, j^{nb}, k^{nb}) = \left(\frac{s_1(h+1) - s_1(h) - |s_1(h^{nb}) - s_1^{CA}(h)|}{s_1(h+1) - s_1(h)} \right) \times \left(\frac{s_2(i+1) - s_2(i) - |s_2(i^{nb}) - s_2^{CA}(i)|}{s_2(i+1) - s_2(i)} \right) \times \left(\frac{l(j+1) - l(j) - |l(j^{nb}) - l^{CA}(j)|}{l(j+1) - l(j)} \right) \times \left(\frac{g(k+1) - g(k) - |g(k^{nb}) - g^{CA}(k)|}{g(k+1) - g(k)} \right) \quad (9.9)$$

$$\mathfrak{R}_{agg,CA}(h^{nb}, i^{nb}, j^{nb}, k^{nb}) = f(h^{nb}, i^{nb}, j^{nb}, k^{nb}) \times \mathfrak{R}_{agg}^{form}(h, i, j, k) \quad (9.10)$$

Reduced order population balance equations were developed from the 4-D model by

lumping one or more parameters into the remaining distributions. The governing equations for these models are presented.

The population balance equation for 3-D model with a lumped solid component volume is given in Equation 9.11, and the solid balance equation is shown in Equation 9.12, where S_2 is the total solid volume in each bin.

$$\frac{\partial}{\partial t} F(s_1, l, g, t) + \frac{\partial}{\partial l} \left[F(s_1, l, g, t) \frac{dl}{dt} \right] + \frac{\partial}{\partial g} \left[F(s_1, l, g, t) \frac{dg}{dt} \right] = \mathfrak{R}_{agg} + \mathfrak{R}_{break} \quad (9.11)$$

$$\frac{\partial}{\partial t} [S_2(s_1, l, g, t)] = \mathfrak{R}_{agg,solid} + \mathfrak{R}_{break,solid} \quad (9.12)$$

The aggregation and breakage rates were similarly modified, and new equations were developed to track the solid component volume during these processes, as shown in Equations 9.13-9.16.

$$\begin{aligned} \mathfrak{R}_{agg}(s_1, l, g, t) = & \\ \frac{1}{2} \int_0^{s_1} \int_0^l \int_0^g \beta(s_1 - s'_1, l - l', g - g', s'_1, l', g', t) & F(s_1 - s'_1, l - l', g - g', t) F(s'_1, l', g', t) dg' dl' ds'_1 \\ - F(s_1, l, g, t) \int_0^\infty \int_0^\infty \int_0^\infty \beta(s_1, l, g, s'_1, l', g', t) & F(s'_1, l', g', t) dg dl ds_1 \end{aligned} \quad (9.13)$$

$$\begin{aligned} \mathfrak{R}_{agg,solid}(s_1, l, g, t) = & \\ \frac{1}{2} \int_0^{s_1} \int_0^l \int_0^g \beta(s_1 - s'_1, l - l', g - g', s'_1, l', g', t) & F(s_1 - s'_1, l - l', g - g', t) F(s'_1, l', g', t) \\ \times (s_2(s_1 - s'_1, l - l', g - g', t) + s_2(s'_1, l', g', t)) & dg' dl' ds'_1 \\ - S_2(s_1, l, g, t) \int_0^\infty \int_0^\infty \int_0^\infty \beta(s_1, l, g, s'_1, l', g', t) & F(s'_1, l', g', t) dg dl ds_1 \end{aligned} \quad (9.14)$$

$$\begin{aligned} \mathfrak{R}_{break}(s_1, l, g, t) = \int_{s_1}^\infty \int_l^\infty \int_g^\infty K_{break}(s'_1, l', g', t) & b(s'_1, l', g', s_1, l, g) F(s'_1, l', g', t) dg' dl' ds'_1 \\ - K_{break}(s_1, l, g, t) F(s_1, l, g, t) \end{aligned} \quad (9.15)$$

$$\begin{aligned} \mathfrak{R}_{break,solid}(s_1, l, g, t) = & \\ V(s_1, l, g, t) \int_{s_1}^\infty \int_l^\infty \int_g^\infty K_{break}(s'_1, l', g', t) & b(s'_1, l', g', s_1, l, g) \frac{S_2(s'_1, l', g', t)}{V(s'_1, l', g', t)} dg' dl' ds'_1 \\ - K_{break}(s_1, l, g, t) G(s_1, l, g, t) \end{aligned} \quad (9.16)$$

The analogous equations for the 3-D model with lumped liquid binder volume are presented in Equations 9.17-9.22, where L is the total volume of liquid in each bin.

$$\frac{\partial}{\partial t} F(s_1, s_2, g, t) + \frac{\partial}{\partial g} \left[F(s_1, s_2, g, t) \frac{dg}{dt} \right] = \mathfrak{R}_{agg} + \mathfrak{R}_{break} \quad (9.17)$$

$$\frac{\partial}{\partial t} [L(s_1, s_2, g, t)] = F(s_1, s_2, g, t) \frac{dl}{dt} + \mathfrak{R}_{agg,liq} + \mathfrak{R}_{break,liq} \quad (9.18)$$

$$\begin{aligned} \mathfrak{R}_{agg}(s_1, s_2, g, t) &= \frac{1}{2} \int_0^{s_1} \int_0^{s_2} \int_0^g \beta(s_1 - s'_1, s_2 - s'_2, g - g', s'_1, s'_2, g', t) \\ &\quad \times F(s_1 - s'_1, s_2 - s'_2, g - g', t) F(s'_1, s'_2, g', t) dg' ds'_2 ds'_1 \\ &\quad - F(s_1, s_2, g, t) \int_0^\infty \int_0^\infty \int_0^\infty \beta(s_1, s_2, g, s'_1, s'_2, g', t) F(s'_1, s'_2, g', t) dg ds_2 ds_1 \end{aligned} \quad (9.19)$$

$$\begin{aligned} \mathfrak{R}_{agg,liq}(s_1, s_2, g, t) &= \\ \frac{1}{2} \int_0^{s_1} \int_0^{s_2} \int_0^g \beta(s_1 - s'_1, s_2 - s'_2, g - g', s'_1, s'_2, g', t) &F(s_1 - s'_1, s_2 - s'_2, g - g', t) F(s'_1, s'_2, g', t) \\ &\quad \times (l(s_1 - s'_1, s_2 - s'_2, g - g', t) + l(s'_1, s'_2, g', t)) dg' ds'_2 ds'_1 \\ &\quad - L(s_1, s_2, g, t) \int_0^\infty \int_0^\infty \int_0^\infty \beta(s_1, s_2, g, s'_1, s'_2, g', t) F(s'_1, s'_2, g', t) dg ds_2 ds_1 \end{aligned} \quad (9.20)$$

$$\begin{aligned} \mathfrak{R}_{break}(s_1, s_2, g, t) &= \\ \int_{s_1}^\infty \int_{s_2}^\infty \int_g^\infty K_{break}(s'_1, s'_2, g', t) b(s'_1, s'_2, g', s_1, s_2, g) &F(s'_1, s'_2, g', t) dg' ds'_2 ds'_1 \\ &\quad - K_{break}(s_1, s_2, g, t) F(s_1, s_2, g, t) \end{aligned} \quad (9.21)$$

$$\begin{aligned} \mathfrak{R}_{break,liq}(s_1, s_2, g, t) &= \\ V(s_1, s_2, g, t) \int_{s_1}^\infty \int_{s_2}^\infty \int_g^\infty K_{break}(s'_1, s'_2, g', t) b(s'_1, s'_2, g', s_1, s_2, g) &\frac{L(s'_1, s'_2, g', t)}{V(s'_1, s'_2, g', t)} dg' ds'_2 ds'_1 \\ &\quad - K_{break}(s_1, s_2, g, t) L(s_1, s_2, g, t) \end{aligned} \quad (9.22)$$

For the 2-D model, additional equations were developed to evaluate the second lumped parameter. The population balance is given by Equation 9.23, while the liquid and gas

volume balances are given by Equations 9.24 and 9.25, respectively.

$$\frac{\partial}{\partial t} F(s_1, s_2, t) = \mathfrak{R}_{agg} + \mathfrak{R}_{break} \quad (9.23)$$

$$\frac{\partial}{\partial t} [L(s_1, s_2, t)] = F(s_1, s_2, t) \frac{dl}{dt} + \mathfrak{R}_{agg,liq} + \mathfrak{R}_{break,liq} \quad (9.24)$$

$$\frac{\partial}{\partial t} [G(s_1, s_2, t)] = F(s_1, s_2, t) \frac{dg}{dt} + \mathfrak{R}_{agg,gas} + \mathfrak{R}_{break,gas} \quad (9.25)$$

Similarly, new equations were developed for the aggregation and breakage terms to track both lumped parameters during these processes, as shown in Equations 9.26-9.31.

$$\begin{aligned} \mathfrak{R}_{agg}(s_1, s_2, t) &= \frac{1}{2} \int_0^{s_1} \int_0^{s_2} \beta(s_1-s'_1, s_2-s'_2, s'_1, s'_2, t) F(s_1-s'_1, s_2-s'_2, t) F(s'_1, s'_2, t) ds'_2 ds'_1 \\ &\quad - F(s_1, s_2, t) \int_0^{\infty} \int_0^{\infty} \beta(s_1, s_2, s'_1, s'_2, t) F(s'_1, s'_2, t) ds_2 ds_1 \end{aligned} \quad (9.26)$$

$$\begin{aligned} \mathfrak{R}_{agg,liq}(s_1, s_2, t) &= \frac{1}{2} \int_0^{s_1} \int_0^{s_2} \beta(s_1-s'_1, s_2-s'_2, s'_1, s'_2, t) F(s_1-s'_1, s_2-s'_2, t) F(s'_1, s'_2, t) \\ &\quad \times (l(s_1-s'_1, s_2-s'_2, t) + l(s'_1, s'_2, t)) ds'_2 ds'_1 \\ &\quad - L(s_1, s_2, t) \int_0^{\infty} \int_0^{\infty} \beta(s_1, s_2, s'_1, s'_2, t) F(s'_1, s'_2, t) ds_2 ds_1 \end{aligned} \quad (9.27)$$

$$\begin{aligned} \mathfrak{R}_{agg,gas}(s_1, s_2, t) &= \frac{1}{2} \int_0^{s_1} \int_0^{s_2} \beta(s_1-s'_1, s_2-s'_2, s'_1, s'_2, t) F(s_1-s'_1, s_2-s'_2, t) F(s'_1, s'_2, t) \\ &\quad \times (g(s_1-s'_1, s_2-s'_2, t) + g(s'_1, s'_2, t)) ds'_2 ds'_1 \\ &\quad - G(s_1, s_2, t) \int_0^{\infty} \int_0^{\infty} \beta(s_1, s_2, s'_1, s'_2, t) F(s'_1, s'_2, t) ds_2 ds_1 \end{aligned} \quad (9.28)$$

$$\begin{aligned} \mathfrak{R}_{break}(s_1, s_2, t) &= \int_{s_1}^{\infty} \int_{s_2}^{\infty} K_{break}(s'_1, s'_2, t) b(s'_1, s'_2, s_1, s_2) F(s'_1, s'_2, t) ds'_2 ds'_1 \\ &\quad - K_{break}(s_1, s_2, t) F(s_1, s_2, t) \end{aligned} \quad (9.29)$$

$$\begin{aligned} \mathfrak{R}_{break,liq}(s_1, s_2, t) &= V(s_1, s_2, t) \int_{s_1}^{\infty} \int_{s_2}^{\infty} K_{break}(s'_1, s'_2, t) b(s'_1, s'_2, s_1, s_2) \frac{L(s'_1, s'_2, t)}{V(s'_1, s'_2, t)} ds'_2 ds'_1 \\ &\quad - K_{break}(s_1, s_2, t) L(s_1, s_2, t) \end{aligned} \quad (9.30)$$

$$\begin{aligned} \mathfrak{R}_{break,gas}(s_1, s_2, t) &= V(s_1, s_2, t) \int_{s_1}^{\infty} \int_{s_2}^{\infty} K_{break}(s'_1, s'_2, t) b(s'_1, s'_2, s_1, s_2) \frac{G(s'_1, s'_2, t)}{V(s'_1, s'_2, t)} ds'_2 ds'_1 \\ &\quad - K_{break}(s_1, s_2, t) G(s_1, s_2, t) \end{aligned} \quad (9.31)$$

In the 1-D model, the only distributed parameter is the volume of the first solid component. The remaining parameters are only distributed with respect to this volume. There are four equations each for the population and volume balances (Equations 9.32-9.35), aggregation functions (Equations 9.36-9.39), and breakage functions (Equations 9.40-9.43).

$$\frac{\partial}{\partial t} F(s_1, t) = \mathfrak{R}_{agg} + \mathfrak{R}_{break} \quad (9.32)$$

$$\frac{\partial}{\partial t} [S_2(s_1, t)] = \mathfrak{R}_{agg, solid} + \mathfrak{R}_{break, solid} \quad (9.33)$$

$$\frac{\partial}{\partial t} [L(s_1, t)] = F(s_1, t) \frac{dl}{dt} + \mathfrak{R}_{agg, liq} + \mathfrak{R}_{break, liq} \quad (9.34)$$

$$\frac{\partial}{\partial t} [G(s_1, t)] = F(s_1, t) \frac{dg}{dt} + \mathfrak{R}_{agg, gas} + \mathfrak{R}_{break, gas} \quad (9.35)$$

$$\begin{aligned} \mathfrak{R}_{agg}(s_1, t) &= \frac{1}{2} \int_0^{s_1} \beta(s_1 - s'_1, s'_1, t) F(s_1 - s'_1, t) F(s'_1, t) ds'_1 \\ &\quad - F(s_1, t) \int_0^{\infty} \beta(s_1, s'_1, t) F(s'_1, t) ds_1 \end{aligned} \quad (9.36)$$

$$\begin{aligned} \mathfrak{R}_{agg, solid}(s_1, t) &= \frac{1}{2} \int_0^{s_1} \beta(s_1 - s'_1, s'_1, t) F(s_1 - s'_1, t) F(s'_1, t) (s_2(s_1 - s'_1, t) + s_2(s'_1, t)) ds'_1 \\ &\quad - S_2(s_1, t) \int_0^{\infty} \beta(s_1, s'_1, t) F(s'_1, t) ds_1 \end{aligned} \quad (9.37)$$

$$\begin{aligned} \mathfrak{R}_{agg, liq}(s_1, t) &= \frac{1}{2} \int_0^{s_1} \beta(s_1 - s'_1, s'_1, t) F(s_1 - s'_1, t) F(s'_1, t) (l(s_1 - s'_1, t) + l(s'_1, t)) ds'_1 \\ &\quad - L(s_1, t) \int_0^{\infty} \beta(s_1, s'_1, t) F(s'_1, t) ds_1 \end{aligned} \quad (9.38)$$

$$\begin{aligned} \mathfrak{R}_{agg, gas}(s_1, t) &= \frac{1}{2} \int_0^{s_1} \beta(s_1 - s'_1, s'_1, t) F(s_1 - s'_1, t) F(s'_1, t) (g(s_1 - s'_1, t) + g(s'_1, t)) ds'_1 \\ &\quad - G(s_1, t) \int_0^{\infty} \beta(s_1, s'_1, t) F(s'_1, t) ds_1 \end{aligned} \quad (9.39)$$

$$\mathfrak{R}_{break}(s_1, t) = \int_{s_1}^{\infty} K_{break}(s'_1, t) b(s'_1, s_1) F(s'_1, t) ds'_1 - K_{break}(s_1, t) F(s_1, t) \quad (9.40)$$

$$\begin{aligned} \mathfrak{R}_{break, solid}(s_1, t) &= V(s_1, t) \int_{s_1}^{\infty} K_{break}(s'_1, t) b(s'_1, s_1) \frac{S_2(s'_1, t)}{V(s'_1, t)} ds'_1 \\ &\quad - K_{break}(s_1, t) S_2(s_1, t) \end{aligned} \quad (9.41)$$

$$\begin{aligned} \Re_{break,liq}(s_1, t) = & V(s_1, t) \int_{s_1}^{\infty} K_{break}(s'_1, t) b(s'_1, s_1) \frac{L(s'_1, t)}{V(s'_1, t)} ds'_1 \\ & - K_{break}(s_1, t) L(s_1, t) \end{aligned} \quad (9.42)$$

$$\begin{aligned} \Re_{break,gas}(s_1, t) = & V(s_1, t) \int_{s_1}^{\infty} K_{break}(s'_1, t) b(s'_1, s_1) \frac{G(s'_1, t)}{V(s'_1, t)} ds'_1 \\ & - K_{break}(s_1, t) G(s_1, t) \end{aligned} \quad (9.43)$$

Appendix B

Hertz-Mindlin contact model

The Hertz-Mindlin contact model was used to calculate the normal and tangential forces on particles during collisions. This model was provided as a standard contact model in EDEM. The governing equations for the normal and tangential forces, F_n and F_t , resulting from a collision are given in Equations 9.44 and 9.45, respectively (Solutions, 2013).

$$F_n = \frac{4}{3}E^*\sqrt{R^*}\delta_n^{\frac{3}{2}} - 2\sqrt{\frac{5}{6}}\beta\sqrt{S_n m^*}v_n^{rel} \quad (9.44)$$

$$F_t = \min[\mu_s F_n, -S_t \delta_t - 2\sqrt{\frac{5}{6}}\beta\sqrt{S_t m^*}v_t^{rel}] \quad (9.45)$$

The equivalent Young's and shear moduli are given by E^* and G^* , respectively, and R^* and m^* are the equivalent radius and mass. δ represents the overlap in the normal or tangential direction, and v^{rel} is the relative velocity. The coefficient of static friction is given by μ_s . S_n and S_t are the normal and tangential stiffness, given by Equations 9.46 and 9.47.

$$S_n = 2E^*\sqrt{R^*\delta_n} \quad (9.46)$$

$$S_t = 8G^*\sqrt{R^*\delta_n} \quad (9.47)$$

Finally, β is a function of the coefficient of restitution, e , as given by Equation 9.48.

$$\beta = \frac{\ln e}{\ln^2 e + \pi^2} \quad (9.48)$$

Acknowledgment of previous publications

The work presented in this dissertation represents original research by the author. The individual chapters presented here have previously appeared in prior publications of which the author of this dissertation is the first author. Parts of these publications have been modified to avoid redundancy and improve readability in this form. Portions of these works were also used in Chapter 1: Introduction.

The following publications were used as chapters in this thesis with the permission of the original publishers and co-authors:

- Barrasso, D., Ramachandran, R., 2012. A comparison of model order reduction techniques for a four-dimensional population balance model describing multi-component wet granulation processes. *Chemical Engineering Science* 80, 380 – 392
- Barrasso, D., Walia, S., Ramachandran, R., 2013b. Multi-component population balance modeling of continuous granulation processes: A parametric study and comparison with experimental trends. *Powder Technology* 241, 85 – 97
- Barrasso, D., El Hagrasy, A., Litster, J. D., Ramachandran, R., 2015a. Multi-dimensional population balance model development and validation for a twin screw granulation process. *Powder Technology* 270, Part B, 612 – 621
- Barrasso, D., Ramachandran, R., 2015a. Multi-scale modeling of granulation processes: Bi-directional coupling of PBM with DEM via collision frequencies. *Chemical Engineering Research and Design* 93, 304–317
- Barrasso, D., Eppinger, T., Pereira, F. E., Aglave, R., Debus, K., Bermingham, S. K., Ramachandran, R., 2015b. A multi-scale, mechanistic model of a wet granulation process using a novel bi-directional PBM-DEM coupling algorithm. *Chemical Engineering Science* 123, 500 – 513
- Barrasso, D., Tamrakar, A., Ramachandran, R., 2014. A reduced order PBM-ANN model of a multi-scale PBM-DEM description of a wet granulation process. *Chemical Engineering Science* 119, 319 – 329
- Barrasso, D., Ramachandran, R., 2015b. Qualitative assessment of a multi-scale, compartmental PBM-DEM model of a continuous twin-screw wet granulation process, In review

Bibliography

- Agatonovic-Kustrin, S., Beresford, R., 2000. Basic concepts of artificial neural network (ANN) modeling and its application in pharmaceutical research. *Journal of Pharmaceutical and Biomedical Analysis* 22 (5), 717 – 727.
- Ai, J., Chen, J.-F., Rotter, J. M., Ooi, J. Y., 2011. Assessment of rolling resistance models in discrete element simulations. *Powder Technology* 206 (3), 269 – 282.
- Banerjee, I., Ierapetritou, M. G., 2004. Model independent parametric decision making. *Annals of Operations Research* 132 (1-4), 135–155.
- Banerjee, I., Pal, S., Maiti, S., 2010. Computationally efficient black-box modeling for feasibility analysis. *Computers & Chemical Engineering* 34 (9), 1515 – 1521.
- Barrasso, D., El Hagrasy, A., Litster, J. D., Ramachandran, R., 2015a. Multi-dimensional population balance model development and validation for a twin screw granulation process. *Powder Technology* 270, Part B, 612 – 621.
- Barrasso, D., Eppinger, T., Pereira, F. E., Aglave, R., Debus, K., Bermingham, S. K., Ramachandran, R., 2015b. A multi-scale, mechanistic model of a wet granulation process using a novel bi-directional PBM-DEM coupling algorithm. *Chemical Engineering Science* 123, 500 – 513.
- Barrasso, D., Oka, S., Muliadi, A., Litster, J. D., Wassgren, C., Ramachandran, R., 2013a. Population balance model validation and prediction of CQAs for continuous milling processes: toward QbD in pharmaceutical drug product manufacturing. *Journal of Pharmaceutical Innovation* 8 (3), 147–162.
- Barrasso, D., Ramachandran, R., 2012. A comparison of model order reduction techniques for a four-dimensional population balance model describing multi-component wet granulation processes. *Chemical Engineering Science* 80, 380 – 392.
- Barrasso, D., Ramachandran, R., 2015a. Multi-scale modeling of granulation processes: Bi-directional coupling of PBM with DEM via collision frequencies. *Chemical Engineering Research and Design* 93, 304–317.
- Barrasso, D., Ramachandran, R., 2015b. Qualitative assessment of a multi-scale, compartmental PBM-DEM model of a continuous twin-screw wet granulation process, In review.
- Barrasso, D., Tamrakar, A., Ramachandran, R., 2014. A reduced order PBM-ANN model of a multi-scale PBM-DEM description of a wet granulation process. *Chemical Engineering Science* 119, 319 – 329.
- Barrasso, D., Walia, S., Ramachandran, R., 2013b. Multi-component population balance modeling of continuous granulation processes: A parametric study and comparison with experimental trends. *Powder Technology* 241, 85 – 97.

- Basheer, I., Hajmeer, M., 2000. Artificial neural networks: fundamentals, computing, design, and application. *Journal of Microbiological Methods* 43 (1), 3 – 31.
- Behzadi, S. S., Klocker, J., Huttlin, H., Wolschann, P., Viernstein, H., 2005. Validation of fluid bed granulation utilizing artificial neural network. *International Journal of Pharmaceutics* 291 (1-2), 139 – 148.
- Biggs, C., Sanders, C., Scott, A., Willemse, A., Hoffman, A., Instone, T., Salman, A., Hounslow, M., 2003. Coupling granule properties and granulation rates in high-shear granulation. *Powder Technology* 130 (1-3), 162 – 168.
- Bilgili, E., Scarlett, B., 2005. Population balance modeling of non-linear effects in milling processes. *Powder Technology* 153 (1), 59 – 71.
- Borner, M., Peglow, M., Tsotsas, E., 2013. Derivation of parameters for a two compartment population balance model of wurster fluidised bed granulation. *Powder Technology* 238, 122 – 131.
- Bouffard, J., Bertrand, F., Chaouki, J., 2012. A multiscale model for the simulation of granulation in rotor-based equipment. *Chemical Engineering Science* 81, 106 – 117.
- Boukouvala, F., Dubey, A., Vanarase, A., Ramachandran, R., Muzzio, F. J., Ierapetritou, M., 2012a. Computational approaches for studying the granular dynamics of continuous blending processes, 2 - Population balance and data-based methods. *Macromolecular Materials and Engineering* 297 (1), 9–19.
- Boukouvala, F., Gao, Y., Muzzio, F., Ierapetritou, M. G., 2013. Reduced-order discrete element method modeling. *Chemical Engineering Science* 95, 12 – 26.
- Boukouvala, F., Muzzio, F. J., Ierapetritou, M. G., 2010a. Design space of pharmaceutical processes using data-driven-based methods. *Journal of Pharmaceutical Innovation* 5 (3), 119–137.
- Boukouvala, F., Muzzio, F. J., Ierapetritou, M. G., 2010b. Predictive modeling of pharmaceutical processes with missing and noisy data. *AIChE Journal* 56 (11), 2860–2872.
- Boukouvala, F., Niotis, V., Ramachandran, R., Muzzio, F. J., Ierapetritou, M. G., 2012b. An integrated approach for dynamic flowsheet modeling and sensitivity analysis of a continuous tablet manufacturing process. *Computers & Chemical Engineering* 42, 30 – 47.
- Boukouvala, F., Ramachandran, R., Vanarase, A., Muzzio, F. J., Ierapetritou, M. G., 2011. Computer aided design and analysis of continuous pharmaceutical manufacturing processes. In: E.N. Pistikopoulos, M. G., Kokossis, A. (Eds.), 21st European Symposium on Computer Aided Process Engineering. Vol. 29 of Computer Aided Chemical Engineering. Elsevier, pp. 216 – 220.
- Braumann, A., Kraft, M., Mort, P. R., 2010. Parameter estimation in a multidimensional granulation model. *Powder Technology* 197 (3), 196 – 210.
- Cameron, I., Wang, F., Immanuel, C., Stepanek, F., 2005. Process systems modelling and applications in granulation: a review. *Chemical Engineering Science* 60 (14), 3723 – 3750.

- Capece, M., Bilgili, E., Dave, R., 2011. Identification of the breakage rate and distribution parameters in a non-linear population balance model for batch milling. *Powder Technology* 208 (1), 195 – 204.
- CD-adapco, 2014. STAR-CCM+ v9.02 User Guide.
- Chaudhury, A., Barrasso, D., Pandey, P., Wu, H., Ramachandran, R., 2014a. Population balance model development, validation, and prediction of CQAs of a high-shear wet granulation process: Towards QbD in drug product pharmaceutical manufacturing. *Journal of Pharmaceutical Innovation* 9 (1), 53–64.
- Chaudhury, A., Kapadia, A., Prakash, A. V., Barrasso, D., Ramachandran, R., 2013a. An extended cell-average technique for a multi-dimensional population balance of granulation describing aggregation and breakage. *Advanced Powder Technology* 24 (6), 962 – 971.
- Chaudhury, A., Niziolek, A., Ramachandran, R., 2013b. Multi-dimensional mechanistic modeling of fluid bed granulation processes: An integrated approach. *Advanced Powder Technology* 24 (1), 113 – 131.
- Chaudhury, A., Wu, H., Khan, M., Ramachandran, R., 2014b. A mechanistic population balance model for granulation processes: Effect of process and formulation parameters. *Chemical Engineering Science* 107, 76 – 92.
- Chua, K. W., Makkawi, Y. T., Hounslow, M. J., 2013. A priori prediction of aggregation efficiency and rate constant for fluidized bed melt granulation. *Chemical Engineering Science* 98, 291 – 297.
- Cundall, P., Strack, O., 1979. Discrete numerical model for granular assemblies. *Geotechnique* 29 (1), 47–65.
- Darelius, A., Brage, H., Rasmuson, A., Bjrn, I. N., Folestad, S., 2006. A volume-based multi-dimensional population balance approach for modelling high shear granulation. *Chemical Engineering Science* 61 (8), 2482 – 2493.
- Darelius, A., Rasmuson, A., Bjrn, I. N., Folestad, S., 2005. High shear wet granulation modelling—a mechanistic approach using population balances. *Powder Technology* 160 (3), 209 – 218.
- Dhenge, R. M., Cartwright, J. J., Hounslow, M. J., Salman, A. D., 2012. Twin screw granulation: Steps in granule growth. *International Journal of Pharmaceutics* 438 (1-2), 20 – 32.
- Dhenge, R. M., Fyles, R. S., Cartwright, J. J., Doughty, D. G., Hounslow, M. J., Salman, A. D., 2010. Twin screw wet granulation: Granule properties. *Chemical Engineering Journal* 164 (2-3), 322 – 329.
- Dhenge, R. M., Washino, K., Cartwright, J. J., Hounslow, M. J., Salman, A. D., 2013. Twin screw granulation using conveying screws: Effects of viscosity of granulation liquids and flow of powders. *Powder Technology* 238, 77–90.
- Dosta, M., Antonyuk, S., Heinrich, S., 2013. Multiscale simulation of agglomerate breakage in fluidized beds. *Industrial & Engineering Chemistry Research* 52 (33), 11275–11281.

- Dubey, A., Sarkar, A., Ierapetritou, M., Wassgren, C. R., Muzzio, F. J., 2011. Computational approaches for studying the granular dynamics of continuous blending processes, 1 - DEM based methods. *Macromolecular Materials and Engineering* 296 (3-4), 290–307.
- El Hagrasy, A., Hennenkamp, J., Burke, M., Cartwright, J., Litster, J., 2013. Twin screw wet granulation: Influence of formulation parameters on granule properties and growth behavior. *Powder Technology* 238, 108 – 115.
- El Hagrasy, A., Litster, J., 2013. Granulation rate processes in the kneading elements of a twin screw granulator. *AIChE Journal* 59 (11), 4100 – 4115.
- Ennis, B. J., Tardos, G., Pfeffer, R., 1991. A microlevel-based characterization of granulation phenomena. *Powder Technology* 65 (1-3), 257 – 272.
- Faure, A., York, P., Rowe, R., 2001. Process control and scale-up of pharmaceutical wet granulation processes: a review. *European Journal of Pharmaceutics and Biopharmaceutics* 52 (3), 269 – 277.
- Flexer, A., 1996. Statistical evaluation of neural network experiments: Minimum requirements and current practice. *Cybernetics and Systems Research*, 1005–1008.
- Freireich, B., Li, J., Litster, J., Wassgren, C., 2011. Incorporating particle flow information from discrete element simulations in population balance models of mixer-coaters. *Chemical Engineering Science* 66 (16), 3592 – 3604.
- Freireich, B., Litster, J., Wassgren, C., 2009. Using the discrete element method to predict collision-scale behavior: A sensitivity analysis. *Chemical Engineering Science* 64 (15), 3407 – 3416.
- Fries, L., Antonyuk, S., Heinrich, S., Dopfer, D., Palzer, S., 2013. Collision dynamics in fluidised bed granulators: A DEM-CFD study. *Chemical Engineering Science* 86, 108 – 123.
- Fries, L., Antonyuk, S., Heinrich, S., Palzer, S., 2011. DEM-CFD modeling of a fluidized bed spray granulator. *Chemical Engineering Science* 66 (11), 2340 – 2355.
- Gantt, J. A., Cameron, I. T., Litster, J. D., Gatzke, E. P., 2006. Determination of coalescence kernels for high-shear granulation using DEM simulations. *Powder Technology* 170 (2), 53 – 63.
- Gantt, J. A., Gatzke, E. P., 2005. High-shear granulation modeling using a discrete element simulation approach. *Powder Technology* 156 (2-3), 195 – 212.
- Gantt, J. A., Gatzke, E. P., 2006. A stochastic technique for multidimensional granulation modeling. *AIChE Journal* 52 (9), 3067–3077.
- Gao, Y., Ierapetritou, M., Muzzio, F., 2011. Periodic section modeling of convective continuous powder mixing processes. *AIChE Journal* 58 (1), 69 – 78.
- Gao, Y., Muzzio, F. J., Ierapetritou, M. G., 2012. Optimizing continuous powder mixing processes using periodic section modeling. *Chemical Engineering Science* 80, 70 – 80.

- Gerstlauer, A., Motz, S., Mitrovic, A., Gilles, E.-D., 2002. Development, analysis and validation of population models for continuous and batch crystallizers. *Chemical Engineering Science* 57 (20), 4311 – 4327.
- Glaser, T., Sanders, C. F., Wang, F., Cameron, I. T., Litster, J. D., Poon, J. M.-H., Ramachandran, R., Immanuel, C. D., Doyle III, F. J., 2009. Model predictive control of continuous drum granulation. *Journal of Process Control* 19 (4), 615 – 622.
- Goldschmidt, M., Weijers, G., Boerefijn, R., Kuipers, J., 2003. Discrete element modelling of fluidised bed spray granulation. *Powder Technology* 138 (1), 39 – 45.
- Griffin, D. W., Mellichamp, D. A., Doherty, M. F., 2010. Reducing the mean size of API crystals by continuous manufacturing with product classification and recycle. *Chemical Engineering Science* 65 (21), 5770 – 5780.
- Hassanpour, A., Antony, S., Ghadiri, M., 2007. Effect of size ratio on the behaviour of agglomerates embedded in a bed of particles subjected to shearing: DEM analysis. *Chemical Engineering Science* 62 (4), 935 – 942.
- Hassanpour, A., Ghadiri, M., 2004. Distinct element analysis and experimental evaluation of the heckel analysis of bulk powder compression. *Powder Technology* 141 (3), 251 – 261.
- Hassanpour, A., Kwan, C., Ng, B., Rahmanian, N., Ding, Y., Antony, S., Jia, X., Ghadiri, M., 2009. Effect of granulation scale-up on the strength of granules. *Powder Technology* 189 (2), 304 – 312.
- Hassanpour, A., Tan, H., Bayly, A., Gopalkrishnan, P., Ng, B., Ghadiri, M., 2011. Analysis of particle motion in a paddle mixer using discrete element method (DEM). *Powder Technology* 206 (12), 189 – 194.
- Heinrich, S., Peglow, M., Ihlow, M., Henneberg, M., Morl, L., 2002a. Analysis of the start-up process in continuous fluidized bed spray granulation by population balance modelling. *Chemical Engineering Science* 57 (20), 4369 – 4390.
- Heinrich, S., Peglow, M., Morl, L., 2002b. Unsteady and steady-state particle size distributions in batch and continuous fluidized bed granulation systems. *Chemical Engineering Journal* 86 (1-2), 223 – 231.
- Hounslow, M. J., Pearson, J. M. K., Instone, T., 2001. Tracer studies of high-shear granulation: II Population balance modeling. *AIChE Journal* 47 (9), 1984–1999.
- Immanuel, C. D., Doyle III, F. J., 2005. Solution technique for a multi-dimensional population balance model describing granulation processes. *Powder Technology* 156 (2-3), 213 – 225.
- Ingram, G. D., Cameron, I. T., 2005. Formulation and comparison of alternative multiscale models for drum granulation. *Computer Aided Chemical Engineering* 20, 481 – 486.
- Iveson, S., Litster, J., 1998. Liquid-bound granule impact deformation and coefficient of restitution. *Powder Technology* 99 (3), 234 – 242.
- Iveson, S., Litster, J., Ennis, B., 1996. Fundamental studies of granule consolidation part 1: Effects of binder content and binder viscosity. *Powder Technology* 88 (1), 15 – 20.

- Iveson, S. M., 2002. Limitations of one-dimensional population balance models of wet granulation processes. *Powder Technology* 124 (3), 219 – 229.
- Iveson, S. M., Litster, J. D., Hapgood, K., Ennis, B. J., 2001. Nucleation, growth and breakage phenomena in agitated wet granulation processes: a review. *Powder Technology* 117 (1-2), 3 – 39.
- Jajcevic, D., Siegmund, E., Radeke, C., Khinast, J. G., 2013. Large-scale CFD-DEM simulations of fluidized granular systems. *Chemical Engineering Science* 98, 298 – 310.
- Jia, Z., Davis, E., Muzzio, F. J., Ierapetritou, M. G., 2009. Predictive modeling for pharmaceutical processes using kriging and response surface. *Journal of Pharmaceutical Innovation* 4 (4), 174–186.
- Kafui, K., Thornton, C., 2000. Numerical simulations of impact breakage of a spherical crystalline agglomerate. *Powder Technology* 109 (1-3), 113 – 132.
- Kayrak-Talay, D., Dale, S., Wassgren, C., Litster, J., 2013. Quality by design for wet granulation in pharmaceutical processing: Assessing models for a priori design and scaling. *Powder Technology* 240, 7 – 18.
- Keleb, E., Vermeire, A., Vervaet, C., Remon, J., 2004. Twin screw granulation as a simple and efficient tool for continuous wet granulation. *International Journal of Pharmaceutics* 273 (1-2), 183 – 194.
- Ketterhagen, W. R., am Ende, M. T., Hancock, B. C., 2009. Process modeling in the pharmaceutical industry using the discrete element method. *Journal of Pharmaceutical Sciences* 98 (2), 442–470.
- Kumar, A., Vercruyssen, J., Toiviainen, M., Panouillot, P.-E., Juuti, M., Vanhoorne, V., Vervaet, C., Remon, J. P., Gernaey, K. V., Beer, T. D., Nopens, I., 2014. Mixing and transport during pharmaceutical twin-screw wet granulation: Experimental analysis via chemical imaging. *European Journal of Pharmaceutics and Biopharmaceutics* 87 (2), 279 – 289.
- Kumar, J., Peglow, M., Warnecke, G., Heinrich, S., Morl, L., 2006. Improved accuracy and convergence of discretized population balance for aggregation: The cell average technique. *Chemical Engineering Science* 61 (10), 3327 – 3342.
- Kumar Akkisetty, P., Lee, U., Reklaitis, G. V., Venkatasubramanian, V., 2010. Population balance model-based hybrid neural network for a pharmaceutical milling process. *Journal of Pharmaceutical Innovation* 5 (4), 161–168.
- Lee, K., Kim, T., Rajniak, P., Matsoukas, T., 2008. Compositional distributions in multi-component aggregation. *Chemical Engineering Science* 63 (5), 1293 – 1303.
- Lee, K. T., Ingram, A., Rowson, N. A., 2013. Comparison of granule properties produced using twin screw extruder and high shear mixer: A step towards understanding the mechanism of twin screw wet granulation. *Powder Technology* 238, 91 – 98.
- Leuenberger, H., 2001. New trends in the production of pharmaceutical granules: batch versus continuous processing. *European Journal of Pharmaceutics and Biopharmaceutics* 52 (3), 289 – 296.

- Leuenberger, H., 2003. Scale-up in the 4th dimension in the field of granulation and drying or how to avoid classical scale-up. *Powder Technology* 130 (1-3), 225 – 230.
- Li, J., Freireich, B. J., Wassgren, C. R., Litster, J. D., 2013. Experimental validation of a 2-D population balance model for spray coating processes. *Chemical Engineering Science* 95, 360 – 365.
- Lian, G., Thornton, C., Adams, M. J., 1998. Discrete particle simulation of agglomerate impact coalescence. *Chemical Engineering Science* 53 (19), 3381 – 3391.
- Liu, L., Smith, R., Litster, J., 2009. Wet granule breakage in a breakage only high-hear mixer: Effect of formulation properties on breakage behaviour. *Powder Technology* 189 (2), 158 – 164.
- Liu, L. X., Litster, J. D., 2002. Population balance modelling of granulation with a physically based coalescence kernel. *Chemical Engineering Science* 57 (12), 2183 – 2191.
- Liu, L. X., Litster, J. D., Iveson, S. M., Ennis, B. J., 2000. Coalescence of deformable granules in wet granulation processes. *AIChE Journal* 46 (3), 529–539.
- Lucia, D. J., Beran, P. S., Silva, W. A., 2004. Reduced-order modeling: new approaches for computational physics. *Progress in Aerospace Sciences* 40 (12), 51 – 117.
- Madec, L., Falk, L., Plasari, E., 2003. Modelling of the agglomeration in suspension process with multidimensional kernels. *Powder Technology* 130 (1-3), 147 – 153.
- Man, P. L., Braumann, A., Kraft, M., 2010. Resolving conflicting parameter estimates in multivariate population balance models. *Chemical Engineering Science* 65 (13), 4038 – 4045.
- Mangwandi, C., Cheong, Y., Adams, M., Hounslow, M., Salman, A., 2007. The coefficient of restitution of different representative types of granules. *Chemical Engineering Science* 62 (1-2), 437 – 450.
- Maronga, S., Wnukowski, P., 1997. Modelling of the three-domain fluidized-bed particulate coating process. *Chemical Engineering Science* 52 (17), 2915 – 2925.
- Marshall Jr., C. L., Rajniak, P., Matsoukas, T., 2011. Numerical simulations of two-component granulation: Comparison of three methods. *Chemical Engineering Research and Design* 89 (5), 545 – 552.
- Marshall Jr., C. L., Rajniak, P., Matsoukas, T., 2013. Multi-component population balance modeling of granulation with continuous addition of binder. *Powder Technology* 236, 211–220.
- Matsoukas, T., Kim, T., Lee, K., 2009. Bicomponent aggregation with composition-dependent rates and the approach to well-mixed state. *Chemical Engineering Science* 64 (4), 787 – 799.
- Matsoukas, T., Marshall Jr., C. L., 2010. Bicomponent aggregation in finite systems. *Europhysics Letters* 92 (4), 46007.

- Mortier, S. T. F., Gernaey, K. V., Beer, T. D., Nopens, I., 2013. Development of a population balance model of a pharmaceutical drying process and testing of solution methods. *Computers & Chemical Engineering* 50, 39 – 53.
- Pandey, P., Tao, J., Chaudhury, A., Ramachandran, R., Gao, J. Z., Bindra, D. S., 2013. A combined experimental and modeling approach to study the effects of high-shear wet granulation process parameters on granule characteristics. *Pharmaceutical Development and Technology* 18 (1), 210–224.
- Pandya, J., Spielman, L., 1983. Floc breakage in agitated suspensions: Effect of agitation rate. *Chemical Engineering Science* 38 (12), 1983 – 1992.
- Pinto, M. A., Immanuel, C. D., Doyle III, F. J., 2007. A feasible solution technique for higher-dimensional population balance models. *Computers & Chemical Engineering* 31 (10), 1242 – 1256.
- Plumb, K., 2005. Continuous processing in the pharmaceutical industry: Changing the mind set. *Chemical Engineering Research and Design* 83 (6), 730 – 738.
- Poon, J. M.-H., Immanuel, C. D., Doyle III, F. J., Litster, J. D., 2008. A three-dimensional population balance model of granulation with a mechanistic representation of the nucleation and aggregation phenomena. *Chemical Engineering Science* 63 (5), 1315 – 1329.
- Poon, J. M.-H., Ramachandran, R., Sanders, C. F., Glaser, T., Immanuel, C. D., Doyle III, F. J., Litster, J. D., Stepanek, F., Wang, F.-Y., Cameron, I. T., 2009. Experimental validation studies on a multi-dimensional and multi-scale population balance model of batch granulation. *Chemical Engineering Science* 64 (4), 775 – 786.
- Portillo, P. M., Muzzio, F. J., Ierapetritou, M. G., 2007. Hybrid DEM-compartment modeling approach for granular mixing. *AIChE Journal* 53 (1), 119–128.
- Rajniak, P., Stepanek, F., Dhanasekharan, K., Fan, R., Mancinelli, C., Chern, R., 2009. A combined experimental and computational study of wet granulation in a wurster fluid bed granulator. *Powder Technology* 189 (2), 190 – 201.
- Ramachandran, R., Ansari, M. A., Chaudhury, A., Kapadia, A., Prakash, A. V., Stepanek, F., 2012. A quantitative assessment of the influence of primary particle size polydispersity on granule inhomogeneity. *Chemical Engineering Science* 71, 104 – 110.
- Ramachandran, R., Arjunan, J., Chaudhury, A., Ierapetritou, M., 2011. Model-based control-loop performance of a continuous direct compaction process. *Journal of Pharmaceutical Innovation* 6, 249–263.
- Ramachandran, R., Barton, P. I., 2010. Effective parameter estimation within a multi-dimensional population balance model framework. *Chemical Engineering Science* 65 (16), 4884 – 4893.
- Ramachandran, R., Chaudhury, A., 2012. Model-based design and control of a continuous drum granulation process. *Chemical Engineering Research and Design* 90 (8), 1063 – 1073.

- Ramachandran, R., Immanuel, C. D., Stepanek, F., Litster, J. D., Doyle III, F. J., 2009. A mechanistic model for breakage in population balances of granulation: Theoretical kernel development and experimental validation. *Chemical Engineering Research and Design* 87 (4), 598 – 614.
- Ramachandran, R., Poon, J. M.-H., Sanders, C. F., Glaser, T., Immanuel, C. D., Doyle III, F. J., Litster, J. D., Stepanek, F., Wang, F.-Y., Cameron, I. T., 2008. Experimental studies on distributions of granule size, binder content and porosity in batch drum granulation: Inferences on process modelling requirements and process sensitivities. *Powder Technology* 188 (2), 89 – 101.
- Ramkrishna, D., 2000. *Population Balances: Theory and Applications to Particulate Systems in Engineering*. Academic Press, San Diego.
- Ranjbarian, S., Farhadi, F., 2013a. Evaluation of the effects of process parameters on granule mean size in a conical high shear granulator using response surface methodology. *Powder Technology* 237, 186 – 190.
- Ranjbarian, S., Farhadi, F., 2013b. Evaluation of the effects of process parameters on granule mean size in a conical high shear granulator using response surface methodology. *Powder Technology* 237, 186 – 190.
- Reinhold, A., Briesen, H., 2012. Numerical behavior of a multiscale aggregation model–coupling population balances and discrete element models. *Chemical Engineering Science* 70, 165 – 175.
- Renzo, A. D., Maio, F. P. D., 2004. Comparison of contact-force models for the simulation of collisions in dem-based granular flow codes. *Chemical Engineering Science* 59 (3), 525 – 541.
- Reynolds, G., Biggs, C., Salman, A., Hounslow, M., 2004. Non-uniformity of binder distribution in high-shear granulation. *Powder Technology* 140 (3), 203 – 208.
- Reynolds, G. K., 2010. Modelling of pharmaceutical granule size reduction in a conical screen mill. *Chemical Engineering Journal* 164 (23), 383 – 392.
- Sayin, R., Hagrasy, A. E., Litster, J., 2015. Distributive mixing elements: Towards improved granule attributes from a twin screw granulation process. *Chemical Engineering Science* 125, 165–175.
- Schaber, S. D., Gerogiorgis, D. I., Ramachandran, R., Evans, J. M. B., Barton, P. I., Trout, B. L., 2011. Economic analysis of integrated continuous and batch pharmaceutical manufacturing: A case study. *Industrial & Engineering Chemistry Research* 50 (17), 10083–10092.
- Scott, A., Hounslow, M., Instone, T., 2000. Direct evidence of heterogeneity during high-shear granulation. *Powder Technology* 113 (1-2), 205 – 213.
- Sen, M., Barrasso, D., Singh, R., Ramachandran, R., 2014. A multi-scale hybrid CFD-DEM-PBM description of a fluid-bed granulation process. *Processes* 2 (1), 89–111.
- Sen, M., Ramachandran, R., 2013. A multi-dimensional population balance model approach to continuous powder mixing processes. *Advanced Powder Technology* 24 (1), 51 – 59.

- Sen, M., Singh, R., Vanarase, A., John, J., Ramachandran, R., 2012. Multi-dimensional population balance modeling and experimental validation of continuous powder mixing processes. *Chemical Engineering Science* 80, 349 – 360.
- Smith, R. M., Liu, L. X., Litster, J. D., 2010. Breakage of drop nucleated granules in a breakage only high shear mixer. *Chemical Engineering Science* 65 (21), 5651 – 5657.
- Solutions, D., 2013. EDEM 2.5 User Guide. DEM Solutions.
- Stepanek, F., Rajniak, P., Mancinelli, C., Chern, R., Ramachandran, R., 2009. Distribution and accessibility of binder in wet granules. *Powder Technology* 189 (2), 376 – 384.
- Tan, H., Goldschmidt, M., Boerefijn, R., Hounslow, M., Salman, A., Kuipers, J., 2004. Building population balance model for fluidized bed melt granulation: lessons from kinetic theory of granular flow. *Powder Technology* 142 (2-3), 103 – 109.
- Tardos, G. I., Khan, M. I., Mort, P. R., 1997. Critical parameters and limiting conditions in binder granulation of fine powders. *Powder Technology* 94 (3), 245 – 258.
- U.S. Food and Drug Administration, May 2006. Guidance for Industry: Q8 Pharmaceutical Development.
- U.S. Food and Drug Administration, November 2009. Guidance for Industry: Q8(R2) Pharmaceutical Development.
- Van den Dries, K., Vromans, H., 2002. Relationship between inhomogeneity phenomena and granule growth mechanisms in a high-shear mixer. *International Journal of Pharmaceutics* 247 (1-2), 167 – 177.
- Vercruyssen, J., Diaz, D. C., Peeters, E., Fonteyne, M., Delaet, U., Assche, I. V., Beer, T. D., Remon, J., Vervaet, C., 2012. Continuous twin screw granulation: Influence of process variables on granule and tablet quality. *European Journal of Pharmaceutics and Biopharmaceutics* 82 (1), 205 – 211.
- Verkoeijen, D., Pouw, G. A., Meesters, G. M. H., Scarlett, B., 2002. Population balances for particulate processes—a volume approach. *Chemical Engineering Science* 57 (12), 2287 – 2303.
- Vervaet, C., Remon, J. P., 2005. Continuous granulation in the pharmaceutical industry. *Chemical Engineering Science* 60 (14), 3949 – 3957.
- Vreman, A., Van Lare, C., Hounslow, M., 2009. A basic population balance model for fluid bed spray granulation. *Chemical Engineering Science* 64 (21), 4389 – 4398.
- Walker, G. M., 2007. Chapter 4 - drum granulation processes. In: A.D. Salman, M. H., Seville, J. (Eds.), *Granulation*. Vol. 11 of *Handbook of Powder Technology*. Elsevier Science B.V., pp. 219 – 254.
- Wang, F. Y., Cameron, I. T., 2002. Review and future directions in the modelling and control of continuous drum granulation. *Powder Technology* 124 (3), 238 – 253.
- Wang, M., Yang, R., Yu, A., 2012. DEM investigation of energy distribution and particle breakage in tumbling ball mills. *Powder Technology* 223, 83 – 91.

- Wauters, P., 2001. Modeling and mechanisms of granulation. Ph.D. thesis, Delft University of Technology, Delft, The Netherlands.
- Yang, R., Zou, R., Yu, A., 2003. Microdynamic analysis of particle flow in a horizontal rotating drum. *Powder Technology* 130 (13), 138 – 146.
- Yu, L. X., 2008. Pharmaceutical quality by design: product and process development, understanding, and control. *Pharmaceutical Research* 25 (4), 781–791.
- Zhang, G., Patuwo, B. E., Hu, M. Y., 1998. Forecasting with artificial neural networks: The state of the art. *International Journal of Forecasting* 14 (1), 35 – 62.